

WL-TR-97-2002



THERMAL MANAGEMENT RESEARCH STUDIES
VOLUME 2 - ROTATING HEAT PIPE

Rengasamy Ponnappan, Ph.D.
UES, Inc.
4401 Dayton-Xenia Road
Dayton, OH 45432-1894

17 September 1996

Final Report for the period: March 1991 - August 1996

Approved for public release, distribution unlimited.

19970523 160

AERO PROPULSION AND POWER DIRECTORATE

WRIGHT LABORATORY, AIR FORCE MATERIEL COMMAND
WRIGHT-PATTERSON AIR FORCE BASE, OH 45433-7251

ONE QUALITY INSPECTED A

NOTICE

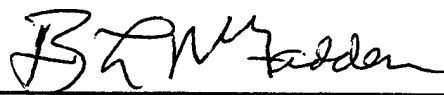
When Government drawings, specifications, or other data are used for any purpose other than in connection with a definitely Government-related procurement, the United States Government incurs no responsibility or any obligation whatsoever. The fact that the government may have formulated or in any way supplied the said drawings, specifications, or other data, is not to be regarded by implication, or otherwise in any manner construed, as licensing the holder, or any other person or corporation; or as conveying any rights or permission to manufacture, use, or sell any patented invention that may in any way be related thereto.

This report is releasable to the National Technical Information Service (NTIS). At NTIS, it will be available to the general public, including foreign nations.

This technical report has been reviewed and is approved for publication.



John E. Leland
Project Engineer
Mechanical Branch



B.L. McFadden,
Chief
Mechanical Branch



MICHAEL D. BRAYDICH, LT COL, USAF
CHIEF
Aerospace Power Division

IF YOUR ADDRESS HAS CHANGED, IF YOU WISH TO BE REMOVED FROM OUR MAILING LIST, OR IF THE ADDRESSEE IS NO LONGER EMPLOYED BY YOUR ORGANIZATION, PLEASE NOTIFY WL/POSL, WRIGHT-PATTERSON AFB, OH 45433-7103 TO HELP MAINTAIN A CURRENT MAILING LIST.

COPIES OF THIS REPORT SHOULD NOT BE RETURNED UNLESS RETURN IS REQUIRED BY SECURITY CONSIDERATIONS, CONTRACTUAL OBLIGATIONS, OR NOTICE ON A SPECIFIC DOCUMENT.

REPORT DOCUMENTATION PAGE

*Form Approved
OMB No. 0704-0188*

Public reporting burden for this collection of information is estimated to average 1 hour per response, including the time for reviewing instructions, searching existing data sources, gathering and maintaining the data needed, and completing and reviewing the collection of information. Send comments regarding this burden estimate or any other aspect of this collection of information, including suggestions for reducing this burden, to Washington Headquarters Services, Directorate for Information Operations and Reports, 1215 Jefferson Davis Highway, Suite 1204, Arlington, VA 22202-4302, and to the Office of Management and Budget, Paperwork Reduction Project (0704-0188), Washington, DC 20503.

1. AGENCY USE ONLY (Leave blank)			2. REPORT DATE		3. REPORT TYPE AND DATES COVERED		
			17 September 1996		Final March 1991 - August 1996		
4. TITLE AND SUBTITLE			5. FUNDING NUMBERS				
Thermal Management Research Studies Volume 2 - Rotating Heat Pipe			C F33615-91-C-2104 PE-62203F PR-3145 TA-20 WU-00				
6. AUTHOR(S)			7. PERFORMING ORGANIZATION NAME(S) AND ADDRESS(ES)				
Rengasamy Ponnappan, Ph.D.			UES, Inc. 4401 Dayton-Xenia Road Dayton, OH 45432-1894				
8. PERFORMING ORGANIZATION REPORT NUMBER			UES-255-TR-96-1 (Vol. 2)				
9. SPONSORING / MONITORING AGENCY NAME(S) AND ADDRESS(ES)			10. SPONSORING / MONITORING AGENCY REPORT NUMBER				
Aero Propulsion and Power Directorate Wright Laboratory Wright Laboratory, Air Force Materiel Command Wright-Patterson AFB, OH 45433-7251 POC: John Leland (937) 255-2922			WL-TR-97-2002				
11. SUPPLEMENTARY NOTES							
The other volumes of this report are: Volume 1 - Electronics Cooling (WL-TR-97-2011) Volume 3 - Heat Pipe in High-G Environment: Analysis, Design and Testing (WL-TR-96-2128)							
12a. DISTRIBUTION / AVAILABILITY STATEMENT			12b. DISTRIBUTION CODE				
Approved for public release; distribution is unlimited							
13. ABSTRACT (Maximum 200 words)							
This document presents a comprehensive account of the high speed rotating heat pipe (RHP) research performed in support of the more-electric airplane technology development. A literature review revealed that there are no studies done on RHP at rotational speeds above 12,000 rpm. New trends in advanced IPU (Integrated Power Unit) and IS/G (Integral Starter/Generator) type of systems require very high speeds up to 60,000 rpm in order to be directly coupled to the gas turbine engines used in aircraft. RHP technology may be a viable method for the thermal management of these power systems. RHP test articles have been designed, fabricated and tested successfully in the high speed test rig developed especially for this purpose. Water and methanol filled RHPs made of stainless steel were tested up to 30,000 rpm for the first time. Some deficiencies in the existing analytical modeling of the RHP performance were identified and improvement directions were initiated. Several unique design and testing scenarios, such as critical speed, and dynamic balancing aspects, non-contact temperature measurement, induction heating, oil-jet cooling, etc. are presented. Air-jet cooling of the RHP condenser looks attractive for low heat transport capacity applications as opposed to the oil jet cooling which requires rotary shaft seals.							
14. SUBJECT TERMS			15. NUMBER OF PAGES		16. PRICE CODE		
Rotating heat pipe, high speed, magnetic shaft-seals, ceramic ball bearings, critical speed, dynamic balancing, infra-red temperature sensor, induction heating, oil or air-jet cooling, thermal management of electric generator rotor			215				
17. SECURITY CLASSIFICATION OF REPORT		18. SECURITY CLASSIFICATION OF THIS PAGE		19. SECURITY CLASSIFICATION OF ABSTRACT		20. LIMITATION OF ABSTRACT	
UNCLASSIFIED		UNCLASSIFIED		UNCLASSIFIED		SAR	

TABLE OF CONTENTS

<u>SECTION</u>		<u>PAGE</u>
FOREWORD		
LIST OF ILLUSTRATIONS		v
LIST OF TABLES		x
NOMENCLATURE		xi
LIST OF APPLICABLE DOCUMENTS		xiv
1.0	INTRODUCTION	1
1.1	Literature Review	1
1.2	Current Problems	4
1.3	Electrical Machine Types and Thermal Loads	5
1.4	Cooling Techniques and Problems	5
1.5	Rotating Heat Pipe Solution	10
1.6	Scope of the Present Research	12
2.0	DESIGN AND ANALYSIS OF RHP	14
2.1	Design Requirements	14
2.2	Design Theory and Principles	15
2.2.1	Working Principle	15
2.2.2	Condenser Taper	17
2.2.3	Critical Speed	17
2.2.4	Choice of Materials	20
2.2.5	Fluid Inventory	21
2.2.6	Heat Transport Capacity	21
2.2.7	Wall ΔT and Thermal Expansion	24
2.3	LSRHP Design	24
2.3.1	Physical Dimensions	24
2.3.2	Design Heat Transport Capacity	24
2.4	HSRHP Design	28
2.4.1	Physical Dimension	28
2.4.2	Design Heat Transport Capacity	30
2.5	Numerical Analysis Modeling	30
2.5.1	Critical Evaluation of Selected Literature	30
2.5.2	Verification of Daniels and Al Jumaily Analysis	35
2.5.3	Summary of Findings and Suggested Future Course	37
3.0	EXPERIMENTAL WORK	40
3.1	Hardware Fabrication	40
3.1.1	LSRHP	40
3.1.2	HSRHP	44
3.1.3	Dynamic Balancing	55
3.1.4	External Surface Finish	55

TABLE OF CONTENTS (CONT'D.)

<u>SECTION</u>		<u>PAGE</u>
3.2	Test Set Up	57
3.2.1	Overall System Description	57
3.2.2	Drive and Mechanical Support System	64
3.2.3	Heating System	65
3.2.4	Cooling System	69
3.2.5	Instrumentation	75
3.3	Test Procedure	77
3.3.1	Test Configuration	77
3.3.2	Heat Balance Analysis - LSRHP	77
3.3.3	Reprocessing of LSRHP	81
4.0	RESULTS AND DISCUSSIONS	82
4.1	LSRHP - Early Tests	82
4.1.1	Heat Loss in Resistive Heater	82
4.1.2	Effect of Cooling Rate on Temperature Profile	84
4.1.3	Effect of Rotational Speed	88
4.1.4	Heat Transport Capacity	88
4.1.5	Overall Temperature Difference	93
4.1.6	Summary of Early Tests on LSRHP	95
4.2	LSRHP - Additional Tests	97
4.2.1	Axial Temperature Profiles	97
4.2.2	Fluid Distribution Model	99
4.2.3	Heat Transport Capacity	104
4.2.4	Comparison with Theory	104
4.2.5	Comparison of Water and Methanol LSRHPs	106
4.3	HSRHP Tests	115
4.3.1	Air Cooling Tests - Water and Methanol RHPs	115
4.3.2	Oil Spray Cooling Tests - Methanol RHP	120
4.4	Discussion on the Choice of Condenser Cooling	120
5.0	SUMMARY OF CONCLUSIONS AND RECOMMENDATIONS	131
5.1	Conclusions	131
5.2	Recommendations	132
6.0	REFERENCES	134
APPENDIX A - CRITICAL SPEED AND ROTOR DYNAMICS ANALYSIS		139
APPENDIX B - DRAWINGS OF RHP TEST RIG		176
APPENDIX C - RHP INERTIA AND TORQUE CALCULATION		184
APPENDIX D - DRAWINGS OF THE CONDENSER COOLING CHAMBER		188
APPENDIX E - UNCERTAINTY ANALYSIS		198

LIST OF ILLUSTRATIONS

<u>FIGURE</u>		<u>PAGE</u>
1	A Typical Permanent Magnet Machine Used in Aircraft Engine	6
2	Cross-sectional Views (Typical) of SRM and PM Machines	8
3	Rotating Heat Pipe Cooling Concept for Electric Motor or Generator	11
4	Geometry of the Rotating Heat Pipe (RHP)	16
5	RHP Critical Speed vs. Bearing Support Stiffness	19
6	Liquid Transport Factor for Various Fluids	23
7	LSRHP - Schematic Diagram of Overall Details	25
8	Theoretical Heat Transport Capacities of LSRHP	27
9	HSRHP - Modified Short Version RHP	29
10	Theoretical Heat Transport Capacities of HSRHP	29
11	Condensate Film Thickness	36
12	Free Surface Profile of Liquid Film Inside a Cylinder Under Rotation	37
13(a)	Fabrication Drawing of the LSRHP Unit	41
13(b)	Fabrication Drawing of the LSRHP Unit	42
14	Working Fluid Fill-station - A Schematic Diagram	43
15	Fabrication Drawing of the First HSRHP Unit - Assembly	46
16	Fabrication Drawing of the First HSRHP Unit - Taper Tube	47
17	Fabrication Drawing of the First HSRHP Unit - End-caps	48
18(a)	Fabrication Drawing of the <u>Modified HSRHP</u> - Overall Details	49
18(b)	Fabrication Drawing of the <u>Modified HSRHP</u> Unit - Assembly	50
18(c)	Fabrication Drawing of the <u>Modified HSRHP</u> Unit - Taper Tube	51

LIST OF ILLUSTRATIONS (CONT'D.)

<u>FIGURE</u>		<u>PAGE</u>
18(d)	Fabrication Drawing of the <u>Modified HSRHP</u> Unit - End-caps	52
19	Photographic View of the HSRHP with Magseal Ring	54
20(a)	Schematic Diagram of the Experimental Setup - LSRHP	58
20(b)	Schematic Diagram of the Experimental Setup - HSRHP	59
21	Photograph of the RHP Test Setup	61
22	Photograph of the Setup with Induction Heater in the Background	62
23	Photograph of the HSRHP Units and Parts of the Setup	63
24	RF Load-Coil Design (6 in. Coil)	68
25(a)	RF Load-Coil Calibration Equipment Layout	70
25(b)	Heat Generation on RHP vs. RF Power Control Voltage	70
26	Schematic Diagram of the Oil-Spray Cooling System	72
27	Calibration Source (0-300°C) for IR Sensor	78
28	IR Sensor Calibration Data	78
29	Heat Balance Representation	79
30	Heat Loss Data for Nichrome Heater	83
31	Effect of Cooling Rate on Temperature Profile (250 W)	85
32	Effect of Cooling Rate on Temperature Profile (750 W)	86
33	Temperature Profile at Constant Speed (1800 rpm) and Different Power Inputs for Mist Cooling	87
34	Effect of Rotational Speed on Temperature-Profile (Increasing Speed)	89
35	Effect of Rotational Speed on Temperature-Profile (Decreasing Speed) ...	90
36	Heat Transport Capacity Estimates and Losses ($Q V_s \Delta T_{He}$)	91

LIST OF ILLUSTRATIONS (CONT'D.)

<u>FIGURE</u>		<u>PAGE</u>
37	Heat Transport Capacity Estimates and Losses (Q_1 vs. Q_{loss} and Q_2)	92
38	Comparison of Theoretical and Experimental Values of Q for Various T_s at 3500 rpm	94
39	Overall Temperature Difference as a Function of Speed for Different Cooling and Heat Inputs	96
40	Temperature Profiles at Various Cooling Methods and Power Inputs	98
41	Temperature Profile for 1700 W at Various Speeds	100
42	Temperature Profile for 2000 W at Various Cooling Rates and Speeds	101
43	Temperature Profile for 2250 W at Various Speeds	102
44	Fluid Distribution Model for RHP	103
45	Comparison of Theoretical and Experimental Heat Transport Capacity of the LSRHP Test Articles No. 1 and No. 2	105
46	Performance of Water-RHP ($Q_{Transport} = 2250$ W)	107
47	Peak Performance of Methanol-RHP ($Q_{Transport} = 1200$ W)	108
48	Axial Temperature Profiles - Methanol-RHP (Various Cooling)	110
49	Axial Temperature Profiles - Water-RHP (Air Cooling)	111
50	Effect of Mist-Cooling Rate - Methanol-RHP 750 W; 4000 and 7000 rpm	113
51	Temperature Leveling Effect - Methanol-RHP 500 and 1000 W; 3000 - 7000 rpm	114
52	Axial Temperature Profile of Methanol-HSRHP: Air Cooling; 0 W	116
53	Axial Temperature Profile of Methanol-HSRHP: Air Cooling; 250 W	117
54	Axial Temperature Profile of Methanol-HSRHP: Air Cooling; 500 W	118

LIST OF ILLUSTRATIONS (CONT'D.)

<u>FIGURE</u>		<u>PAGE</u>
55	Axial Temperature Profile of Methanol-HSRHP: Air Cooling; 750 W	119
56	Axial Temperature Profile of Water-HSRHP: Air Cooling; 0 W	121
57	Axial Temperature Profile of Water-HSRHP: Air Cooling; 250 W	122
58	Axial Temperature Profile of Water-HSRHP: Air Cooling; 500 W	123
59	Axial Temperature Profile of Water-HSRHP: Air Cooling; 750 W	124
60	Axial Temperature Profile of Methanol-HSRHP; Oil-Spray Cooling; 0 W	125
61	Axial Temperature Profile of Methanol-HSRHP; Oil-Spray Cooling; 250 W	126
62	Axial Temperature Profile of Methanol-HSRHP; Oil-Spray Cooling; 500 W	127
63	Axial Temperature Profile of Methanol-HSRHP; Oil-Spray Cooling; 750 W	128
64	Axial Temperature Profile of Methanol-HSRHP; Oil-Spray Cooling; 922 W	129
A.1	Fill Tube as Cantilever Beam	140
A.2	Critical Speed Graph for Fill Tube	142
A.3	RHP as Simple Support Beam	142
A.4	Critical Speed Graph for RHP Tube	144
A.5	RHP as a Simple Rigid Rotor in Flexible Supports	145
A.6	HSRHP - Deflection in Free-Free Modes	154
A.7	HSRHP - Critical Speed Map	155
A.8	HSRHP - Mode Shapes at K=1.0E5	157

LIST OF ILLUSTRATIONS (CONT'D.)

<u>FIGURE</u>		<u>PAGE</u>
A.9	Response to Mode-1 Unbalance (Drive-end Bearing)	159
A.10	Response to Mode-1 Unbalance (Rotor Center)	160
A.11	Response to Mode-1 Unbalance (Opposite Drive-end Bearing)	161
A.12	Response to Mode-2 Unbalance (Drive-end Bearing)	162
A.13	Response to Mode-2 Unbalance (Rotor Center)	163
A.14	Response to Mode-2 Unbalance (Opposite Drive-end Bearing)	164
A.15	Revised HSRHP - Critical Speed Map	169
A.16	Revised HSRHP - Mode Shapes at K=1.0E5	170
A.17	Response to Mode-1 Unbalance (Drive-end Bearing) - Revised HSRHP ..	171
A.18	Response to Mode-1 Unbalance (Rotor Center) - Revised HSRHP	172
A.19	Response to Mode-1 Unbalance (Opposite Drive-end Bearing) - Revised HSRHP	173

LIST OF TABLES

<u>TABLE</u>		<u>PAGE</u>
1	Brushless Rotating Electrical Machine Types and Their Characteristics	7
2	RHP Design Preliminary Input Data	14
3	Critical Speed Analysis Data	20
4	LSRHP Inventory of Fluid-Comparison of Three Designs	22
5	LSRHP - Test Hardware Design and Test Parameters	26
6	HSRHP Design: Revised Input Data	28
7	HSRHP - Test Hardware Design and Test Parameters	31
8	HSRHP - Filling Process-Log Summary	56
9	Balancing Data of the HSRHPs at 3500 rpm	57
10	Evolution of RHP Test Articles and Tests	82
A.1	Summary of Rotor Model	151
A.2	Bearing Stiffness vs. Speed at 25 lb. Axial Preload	152
A.3	Summary of Response to Unbalance Analysis	166
A.4	Summary of Revised Rotor Model	168

NOMENCLATURE

A	Area, m ²
a_a	Axial component of the centrifugal acceleration, m/s ²
c	Clearance between the RHP and heater, m
c_p	Specific heat of working fluid, kJ/kg °C
d	Diameter of rotor shaft, m
E	Modulus of elasticity, lb/in. ²
F	Radiation shape factor
g	Acceleration due to gravity, m/s ²
G	Ratio of induced acceleration to g
h	Heat transfer coefficient, W/m ² °C
h_{fg}, \bar{h}_{fg}	Latent heat of vaporization, kJ/kg
I	Section modulus of inertia, in. ⁴
k	Thermal conductivity, W/m °C
K	Bearing stiffness, lb/in.
L	Length, m; span between bearing supports, in.
N	Rotational speed, rpm
N_L	Liquid transport factor
Nu	Nusselt number
$Q_1 \dots Q_4$	Heat flow rate, W Eq. (8)
q	Heat flux density, W/m ²
r,R	Minimum and maximum inner radii of condenser (Fig. 4), m
r_m	Mean radius of taper section $(r+R)/2$, m
r_i, r_o	Inner and outer radii of heater insulation, m
R_1	Inner radius of heater, m
T	Temperature °C
Ta	Taylor number (Eq. 15)
T_{1-2} , etc.	Average temperature, $(T_1+T_2)/2$
ΔT_{AB}	Temperature difference between A and B, °C
$\Delta T_{A,B}$	Temperature difference across A at B, °C (Ref Fig. 29)

NOMENCLATURE (CONT'D.)

Greek Symbols

α	Half cone angle of taper
α_w	Absorptance of RHP wall
ϵ	Emittance
δ	Liquid film thickness
ρ	Density, kg/m ³
$\Delta T_{f,c}$	Temperature difference, $T_s - T_w$, °C
μ	Dynamic viscosity, Ns/m ²
σ	Stefan-Boltzmann constant, W/m ² k ⁴
ν	Kinematic viscosity, m ² /s
ω	Angular velocity, $(2\pi N)/60$, rad/s

Subscript

a	Adiabatic
c	Condenser
e	Evaporator
f	Fluid
H	Heater
S	Saturation
v	Vapor
w	Wall
ss	Stainless steel
avg	Average
cond	Conduction
conv	Convection
insu	Insulation
Rad	Radiation

NOMENCLATURE (CONT'D.)

Abbreviations

APU	Auxiliary power unit
EBW	Electron beam welding
IPU	Integrated power unit
HSRHP	High speed rotating heat pipe
IS/G	Integral starter/generator
LSRHP	Low speed rotating heat pipe
MEA	More electric aircraft
PAO	Poly alfa olefin
PM	Permanent magnet
RF	Radio frequency
RHP	Rotating heat pipe
RTD	Resistance thermometer detector
RTS	Rotating thermo syphon
RPM	Revolutions per minute
SCFH	Standard cubic feet per hour
SRM	Switched reluctance machine
TIG	Tungsten inert gas welding

APPLICABLE DOCUMENTS

1. R. Ponnappan, J.E. Leland, and J.E. Beam, "Rotating Heat Pipe for Cooling of Rotors in Advanced Generators", AIAA 94-2033, 6th AIAA/ASME Joint Thermophysics and Heat Transfer Conference, Colorado Springs, CO, 20-24 June 1994.
2. R. Ponnappan, J.E. Leland, and J.E. Beam, "Thermal Management Issues of Rotors in Rotating Electrical Machines", SAE 942184, Aerotech '94, Los Angeles, CA, 3-6 October 1994.
3. R. Ponnappan, J.E. Leland, and J.E. Beam, "Experimental Results of a High-Speed On-Axis Rotating Heat Pipe", 9th International Heat Pipe Conference, Albuquerque, NM, 1-5 May 1995.
4. R. Ponnappan, and J.E. Leland, "High Speed Rotating Heat Pipe for Aircraft Applications", SAE 951437, Aerospace Atlantic conference, Dayton, Ohio, 23-25 May 1995.
5. R. Ponnappan, J.E. Leland and J.E. Beam, "Comparison of Performance Results for Water and Methanol Rotating Heat Pipes", AIAA 96-0477, 34th Aerospace Sciences Meeting, January 1996, Reno, NV.
6. M.A. Streby, R. Ponnappan, J.E. Leland and J.E. Beam, "Design and Testing of a High Speed Rotating Heat Pipe", paper no.96301, IECEC-96, Washington DC, August 11-16, 1996.
7. R. Ponnappan, "System Safety and Hazard Analysis Report - Preliminary Hazard Analysis" for Thermal Management Research Contract No. F33615-91-c-2104. Final Report to WL/POOS, WPAFB, November 1996.

FOREWORD

This final technical report was prepared as part of the contract deliverables under the "Thermal Management Research" contract F33615-91-C-2104. This contract was sponsored and administered by the Aero Propulsion and Power Directorate (APPD) of Wright Laboratory (WL) at Wright-Patterson Air Force Base (WPAFB). Dr. J.E. Leland was the Air Force Project Engineer/Technical Monitor at various stages of the program.

The present volume (Volume 2) outlines the design, analysis and fabrication research efforts performed under Task 004: Rotating Heat Pipe (RHP) Study including the high speed RHP test facility development at APPD's Thermal Laboratory and steady state performance tests conducted on four different test articles of RHPs. The other volumes of the final report are:

Volume 1: Electronics Cooling (Task 001)

Volume 3: Heat Pipe in High-G Environment: Analysis, Design and Testing (Task 002)

The work described here was performed entirely on-site at the Thermal Laboratory (WL/POOS) by UES, Inc., Dayton, Ohio with Dr. R. Ponnappan as the Program Manager and Principal Investigator. Messrs. M. Streby (UES), J. Tennant (UES), M.D. Ryan (UES) and D. Reinmuller (WL) provided the technical support. UES' Materials and Processes Division, together with the corporate publication group, provided the administrative and documentation support. The author sincerely appreciates the services by Ms. Dee Dee Donley, UES, Inc., in preparing this document.

The other contributors and participants whose services were valuable to this research effort are as follows:

1. Dr. R.W. Stephenson (Consultant) Section 2.2.3; Appendix A.3; Appendix A.4
2. Dr. Qun He (UES, Inc.) Section 2.5 and 4.3
3. Dr. M. Pais (Consultant) Section 2.5.2 and 3.2.4
4. M. Streby (UES, Inc.) Section 3.2 and 4.2

1.0 INTRODUCTION

Electrical machine designers are beginning to realize the severity of the thermal problems in advanced rotating electrical machines. Efficient, light-weight and fault-tolerant high speed electrical machines such as alternators, generators, actuator-motors, integral starter/generators, etc., are required for advanced military and commercial aircraft and machine tool applications. These machines are built using state-of-the-art and developing technologies which focus on shrinking the size and increasing the power-to-weight ratio. Of particular interest here is the permanent magnet rotor technology and the switched reluctance rotor technology which are improvements over the wound-rotor technology of the past. Because of the dual-use (commercial as well as military) potential of these machines, the Air Force and NASA are promoting increased attention in perfecting the enabling technologies through their more-electric aircraft (MEA) initiatives [1-3].

Thermal management of the rotors in these machines has been a challenging problem for the heat transfer experts. There are a variety of parameters - high speed, windage loss, high-g loadings, difficulty in measuring temperature in rotation, lack of a proper thermal coupling between the rotor and stator, etc. - that influence the thermal condition/control of the rotor in an electrical machine. In this report, a qualitative analysis is provided to illustrate the thermal issues relating to the rotor followed by some experimental results. A literature survey was done to review the relevant background research material. Among other possibilities, a rotating heat pipe (RHP) solution technique has been proposed and the test results of laboratory RHP hardware are presented. It is predicted that the future designs of advanced electrical machinery rotors will incorporate advanced built-in thermal solutions rather than using the inefficient conventional solution techniques.

1.1 LITERATURE REVIEW

A computer search of the relevant literature was done to obtain references on the “thermal management or cooling of rotating electrical machinery” including the key words such as high rotational speed, core-losses, induction machine, permanent magnet rotor, switched reluctance, more-electric aircraft, and rotating heat pipe. The selected references are divided into four

categories and discussed here. It is generally observed that there are very few published literature about thermal problems on commercial machines indicating a sensitivity about publishing the field problems. On the other hand, several papers are published on research and developmental machines sponsored by the government and corporate R&D organizations.

Category 1. Advanced electrical machine design and development: Richter [4] provides a review of the SRM technology development and strongly emphasizes the need for proper rotor heat transfer design in view of the SRM's high rotor iron losses. MacMinn and Jones [5] project the possibility of SRM designs with rotors capable of operation up to 400°C. Their 50,000 rpm SRM starter-generator for aircraft engine application uses engine lubricating oil as rotor and stator coolant. They observed that lower temperature annealing of the rotor laminations resulted in somewhat higher core losses than if higher temperature annealing was used. Goldberg [6] lists a variety of permanent magnet generators built for small engine applications. He notes that wound-rotors have limits of speed (24,000 rpm) and maximum temperature (100°C) limited by insulation materials, while the permanent magnet rotors have very high speed range and are good up to 260°C. Goldberg recommends air or oil cooling depending on the size and type of the generator. Magnetic circuit configurations suitable for aerospace permanent-magnet generators operating in the 0.25-10 kW-power and 10,000-100,000 rpm-speed ranges are studied by Amaratunga [7]. Based on the design optimization studies, Amaratunga concluded that the flux squeezing rotor configuration has the highest power density at small generator sizes while the conventional rotor is good at large sizes. A detailed thermal analysis for a 250 kW SRM generator with elaborate oil cooling arrangement is provided by Ferreira and Richter [8]. They used SINDA thermal model using a 2-D nodal-resistance network and mapped the rotor and stator temperatures. Initial test results of this 22,000 rpm, 270 VDC, 2.4 kW/lb machine with 6.6 kW rotor iron losses are given by Richter, Lyons, Ruckstader, et al. [9,10]. Faiz and Dadgari [11] provide a detailed network method of heat distribution and temperature calculation for a 12/10 pole SRM motor.

Category 2. Cooling of electrical machines using heat pipe technology: A total of 17 publications have been cited for this category and the earliest work was done in 1971. Corman and McLaughlin [12] used a multiple number of conventional heat pipes to cool a 10 hp, 12,000 rpm ac motor. The rotor heat pipes were mounted in off-axis mode and all the condenser

sections were cooled by air. Kukharskii and Noskov [13] showed how the rotor of an electric motor could be cooled by making the shaft of the rotor as a centrifugal-axial heat pipe (now known as a rotating heat pipe) and obtained a 20% increase in performance. Corman, Edgar, et al. [14] concluded that the use of heat pipes offered significant advantages over conventional cooling techniques. Oslejsek and Polasek [15] built several steel-water rotating coaxial heat pipes for cooling ac motors of different power ratings. They cooled an 80 kW, 1500 rpm motor that dissipated 1.6 kW of heat to 130°C from 200°C using a water cooled condenser. Chalmers and Herman [16] tested an unlaminated mildsteel rotor of an induction motor fan drive with a rotating water heat pipe and demonstrated the cooling of an 800 W load at 1030 rpm. The maximum temperature of the rotor without the heat pipe was 220°C and with the heat pipe the temperature dropped to 110°C.

By using an alcohol thermosyphon in the stator winding of a 90 kW enclosed motor, Tubis and Fanar [17] reduced the temperature rise by 23%. Groll, Krahling and Munzel [18] used copper-water heat pipes for cooling the stator and rotor of an asynchronous motor developed for locomotive drives. The off-axis rotating heat pipes were tested up to 5000 rpm in a simulated rotor but no actual motor testing is reported. Furuya, Wake, et al. [19] claim to have developed a reliable, low-cost heat pipe shaft which would reduce the size of a totally enclosed motor. A global review of heat pipe cooled motor manufacturers is given by Kukharskii and Ivannikov [20] who have noted that motor manufacturers have achieved a continuous torque increase by a factor of 1.35-2.0 for the heat pipe cooled machines. Sattler and Thoren [21] built a centrifugal heat pipe shaft for a 75 kW induction motor and compared the performances of the rotor shaft with and without the fluid. The rotor temperature of the filled and unfilled shaft was 60°C to 170°C, respectively. Thoren [22] presented additional results of a 150 kW motor testing and recommended heat pipe cooling for totally enclosed machines used in railways.

Koziej [23] noted that heat pipes were expensive and not easily adaptable to the production line and hence recommended solid-liquid phase change material (PCM) to cool the stator windings of an induction motor. He used paraffin to soak the heat of the stator-end winding loops and nearly isothermalized the stator. He also showed that by using PCM, the motor ventilator could be eliminated thereby reducing the noise level and increasing the time for windings to heat up to 80°C in case of motor overload. Hakim and Aziz [24] modeled the heat

flow in the stator of induction machine cooled by heat pipes using thermal resistive network method. They suggested the importance of using high thermal conductivity electrical insulating material for mounting the heat pipes in the stator. Bradford [25] enumerated seven different ways of installing heat pipes in rotating type electrical machines and recommended heat pipe cooling for future high energy density machines such as permanent magnet motors and generators.

Category 3. Related heat transfer simulation and analysis: A wealth of references were found in this category. Only a limited number of very appropriate research publications discussing the rotating heat pipe technology with direct bearing on rotor cooling are referenced here [26-35]. These references are important in understanding the existing level of RHP technology and to review and improve heat transfer modeling required for the high speed regime whereto the present research is focussed.

Category 4. Patents: Four important US patents were found appropriate for electrical machinery cooling applications [36-39]. The oldest patent was in 1974 and the most recent being in 1994. These patents essentially show that RHP technology could be used for rotor cooling in electric machines where the generated heat is trapped and cause overheating and performance deterioration.

1.2 CURRENT PROBLEMS

As we have seen in the previous section, heat pipe technology has been conceived and developed in the seventies and eighties for cooling mainly the induction motors used in terrestrial applications. Current requirements in aerospace and military applications involve advanced machinery such as permanent magnet rotor and SRM types which run at very high rotational speeds, up to 60,000 rpm. Even though high speeds provide advantages such as the ability to direct couple a generator to the gas turbine engine, thus eliminating the gear box, there are major concerns of high windage losses and shaft seals and bearing problems. In aerospace applications, use of conventional wick heat pipes is precluded as the wick may deprime during take off, landing and high-g maneuvers. The other major problem is poor thermal conduction through the shaft. The rotor mounting method may make the rotor thermally floating as illustrated in

Figure 1. The rotor shaft is in very poor thermal contact with the rotor and, hence, even oil jet cooling of the hollow shaft interior cannot cool the rotor adequately. The rotor to stator heat exchange is by convection and radiation which is inefficient at moderate temperatures (25-300°C). The typical safe operating temperature for the permanent magnet (PM) rotor is under 300°C.

Finally, the completely enclosed nature of these aerospace generators pose integration challenges such as ducting to the turbine bleed air and onboard stored coolant circulation loop.

1.3 ELECTRICAL MACHINE TYPES AND THERMAL LOADS

The general types of brushless rotating machine configurations and their characteristics are given in Table 1. Because of high speed capabilities and high power densities SRM and PM type machines have gained much popularity. Typical cross-sectional views of the SRM and PM machines are shown in Figure 2.

Thermal Loads: Heat is generated within the rotor due to one or all of the following causes:

- i) I^2R heating in the windings.
- ii) Eddy current and hysteresis effects in the laminations.
- iii) Windage - frictional heating of air or medium near the rotating surface.

All these factors cause the machine not only to lose power but also to overheat if uncooled. Because of the high speeds and high power densities of the advanced machines, the thermal loads are higher than those in conventional machines.

1.4 COOLING TECHNIQUES AND PROBLEMS

The traditional method of cooling used in electrical machines is the blowing of ambient air over exposed surfaces of the machine. Usually a ventilating fan is directly mounted on the machine shaft to force air through the air-gap between the rotor and stator and over the finned

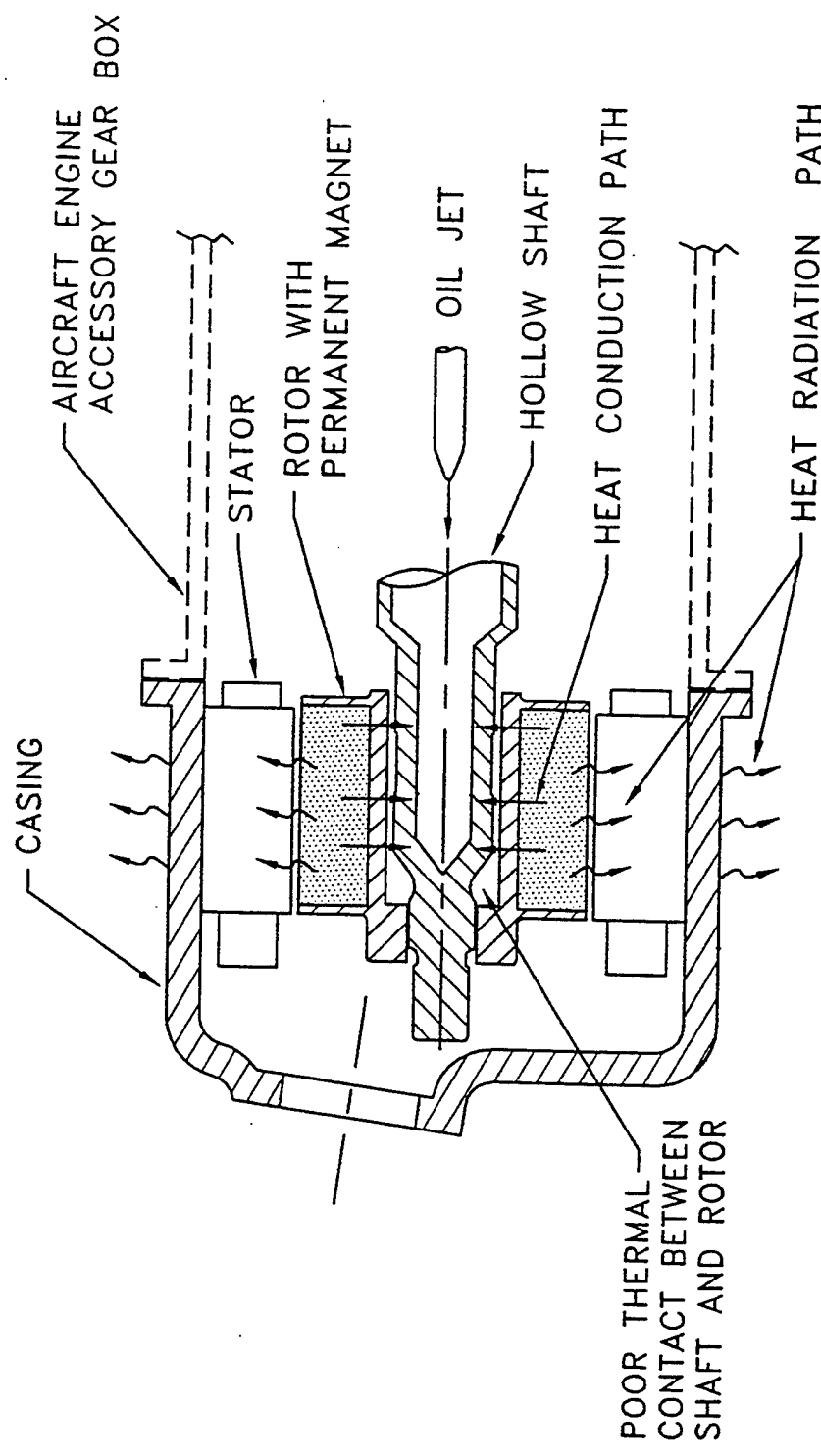


Figure 1. A Typical Permanent Magnet Machine Used in Aircraft Engine.

Table 1. Brushless Rotating Electrical Machine Types and Their Characteristics

TYPE	CHARACTERISTICS
1. Wound Rotor	<p>Example: ac Induction Motor Speed Capability†: Average; up to 24,000 rpm. Limited due to mechanical stress in winding assembly. Usually lower than SRM and PM.</p> <ul style="list-style-type: none"> • Highest rotor losses, I^2R loss, eddy and hysteresis losses. • Laminated rotor structure with slots and windings. • Temperature sensitive winding insulation ~100°C limit.
2. Switched Reluctance Machine (SRM)	<p>Example: Integral Starter/Generator MEA Application Speed Capability†: Very high; up to 60,000 rpm. Usually higher than WR and PM.</p> <ul style="list-style-type: none"> • Moderate rotor losses. • No winding or conductor in rotor. • Laminated rotor structure with magnetic losses (eddy current and hysteresis). • Windage losses due to high speeds and salient poles. • 400°C limit due to rotor mechanical shafts.
3. Permanent Magnet	<p>Example: PM generators for FADEC, etc. uses Alnico, Samarium-Cobalt, Neodymium magnets. Speed Capability†: High; up to 40,000 rpm.</p> <ul style="list-style-type: none"> • Least rotor losses; windage loss due to high speeds. • Light weight. • PM sensitive to temperature ~260°C limit. • No winding.

†Speed capability is mainly dependent upon the size, material and type of the rotor. Other factors include ratings of support bearings and prime-mover. SRM type rotors are designed to reach tip velocities up to 1030 ft./s. See Ref. [40].

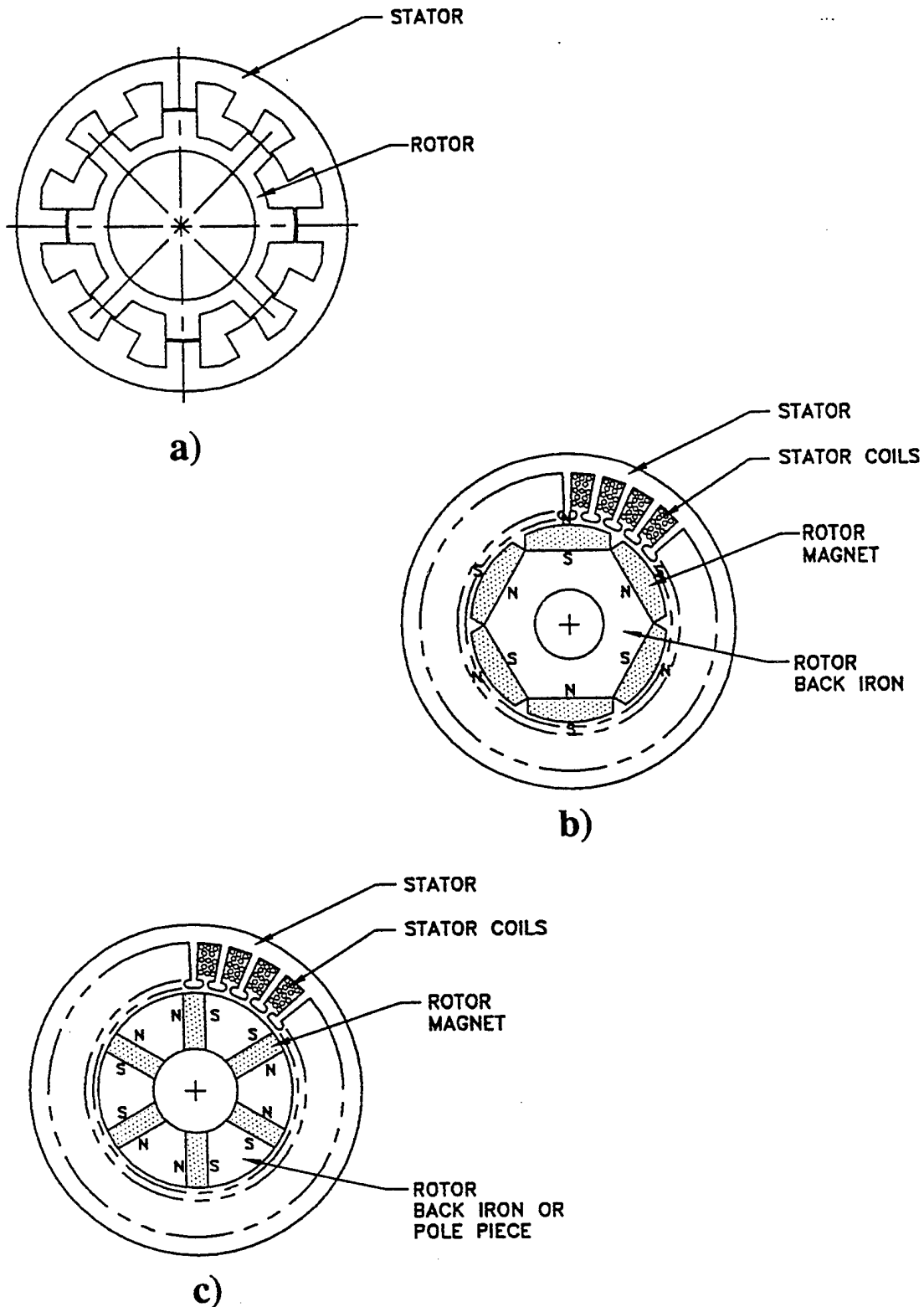


Figure 2. Cross-sectional Views (Typical) of SRM and PM Machines.

- 12/8 Pole Configuration SRM [Ref. 10]
- Radially magnetized PM machine [Ref. 7]
- Tangentially magnetized PM machine [Ref. 7]

outer frame of the stator. The next level of improvement in cooling is by circulating coolants through stator slots. Water or oils are used as coolants. Dielectric fluids are also used in some cases if a leakage of fluid into the air-gap is to be tolerated.

When the above mentioned methods are inadequate, more advanced techniques are explored for the high speed advanced SRM and PM type machines. The new cooling techniques are:

- 1) Active fluid circulation through the rotor and stator with advanced heat transfer enhancement techniques.
- 2) Spray cooling with liquid-air mixtures (single-phase over rotor and stator).
- 3) Spray cooling with evaporation of fluid (two phase).
- 4) Heat pipe and rotating heat pipe devices for stator and rotor respectively with air or liquid or spray cooling.

Each of the above cooling techniques has its merits and demerits. They all are at some stage of research and development in the industry. For instance, the Air Force program on Internal Starter/Generator (IS/G) SRM by GE and Sundstrand uses oil circulation through the rotor and stator hardware. Some of the limitations of these methods are listed below:

- 1) Single phase fluid circulation is limited in heat flux and heat transfer coefficient capabilities (under 10 W/cm^2 and $60\text{-}1800 \text{ W/m}^2\text{K}$ for oil forced convection) and requires a pump to circulate fluid through narrow openings. Also, this requires seals which create leakage and maintenance problems.
- 2) Spray cooling (single and two-phase) requires precision atomizer and pump; difficult to attain uniformity of spray over stator and rotor surfaces and positioning of nozzles pose physical constraints. In addition, at speeds higher than 15,000 rpm spray cooling of the rotor would cause excessive windage loss.
- 3) Heat pipe installation in combination with spray cooling sounds attractive as the rotor or stator isothermalization would be taken care of by the heat pipe while the

external heat removal would be easily handled by spray cooling. However, techniques are still in development and invasive placement of heat pipes is the prime negative factor because it would affect the magnetics of the stator or rotor as the case may be. If this aspect is included from the design stage itself, placement of the heat pipe within the stator or rotor or shaft structure may not be a problem.

- 4) For aircraft applications, storage and handling of coolant for the external condenser of the heat pipe or spray system is an additional burden.
- 5) Active cooling methods certainly require additional operational safety and fail-safes such as sensors and electronics.

1.5 ROTATING HEAT PIPE SOLUTION

In spite of the USA's pioneer research efforts [12] on rotating heat pipe technology for its intended applications in machine tools and motor cooling, there is no evidence that this technology has been incorporated in any commercial product manufactured in this country. There are reports [19,20] that Japan and Germany have exploited this technology in commercial motors. The statistics on the percentage of machines built globally with heat pipe cooling may not be important. However, it is important that the technology is cost-effective, reliable, and adaptable to the state-of-the-art machine (SRM and PM types) cooling.

The time is ripe to perfect the rotating heat pipe technology for directly supporting the development of a novel thermal management concept for emerging more-electric aircraft high power components. The targeted high power components of this effort are switched reluctance type high speed integral starter/generator (IS/G) and integrated power unit (IPU) and wire-wound type auxiliary power unit (APU) rotors. The goal of high power density requirement for these machines push the designer to the limits of existing technologies. Thermally, the precision rotor of a generator if cooled by air, will undergo higher differential temperatures because the volume to surface ratio is significantly poorer than for conventional distributed windings. For high performance machines, the thermal solution is to use rotating heat pipe with extended condenser section cooled by spray cooling. A possible arrangement is shown in Figure 3.

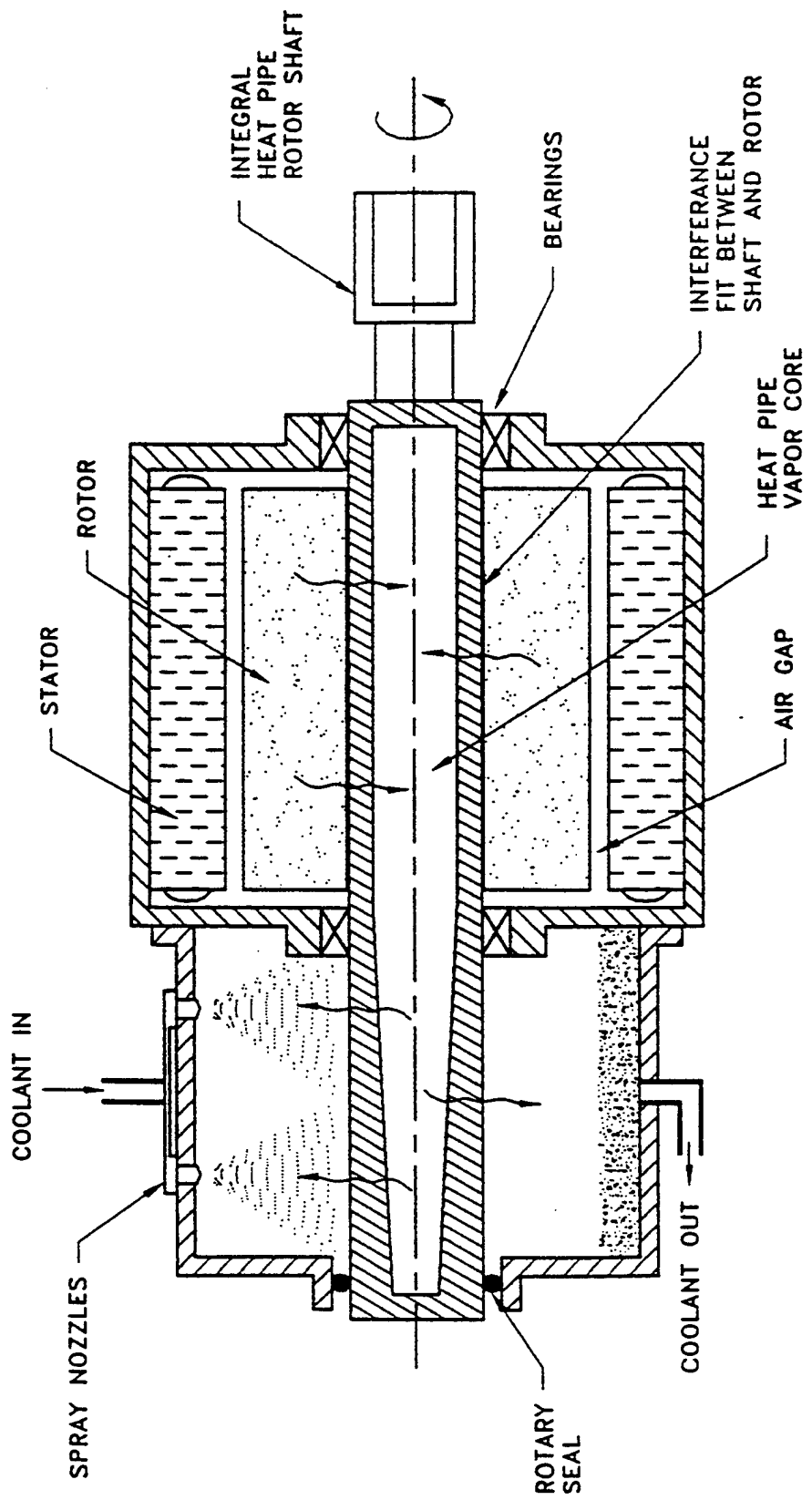


Figure 3. Rotating Heat Pipe Cooling Concept for Electric Motor or Generator.

Conceptually, the rotating heat pipe working principle is simple. The hollow shaft of the rotor itself is made as the rotating heat pipe which would be filled with a suitable working fluid and sealed. In rotation, the fluid is uniformly distributed over the inner wall of the shaft. Heat is transferred from the rotor through the wall thereby vaporizing the fluid. Due to higher vapor pressure, the vapor flows to the colder condenser section and condenses on the wall. The centrifugal force causes the condensate to flow along the tapered condenser inner wall back to the evaporator and evaporates, thus completing the heat transport cycle. The condenser is cooled externally by suitable spray medium for high heat flux and heat transfer coefficient advantages.

However, because of the fact that spray cooling requires fluid medium and high speed rotating seals, it is a concern that the RHP solution may not be acceptable for MEA. The alternative solution is air-cooling which can be provided easily onboard an aircraft and does not involve life-limiting seals. A further discussion on this issue is included in Section 4.4

The key technological challenges are:

- 1) Matching the heat load of the rotor to a compact and viable RHP shaft and coming up with a design which will be compatible with electromagnets and strength requirements of the rotor;
- 2) Providing the rotary seals at the shaft ends for the spray chamber;
- 3) Ensuring very good conductive (thermal) coupling between the rotor and the shaft, and;
- 4) Management of the fluid for spray and heat exchanging appropriate for the application in question.

1.6 SCOPE OF THE PRESENT RESEARCH

The major objectives of the present effort were, in general,

- 1) To explore the feasibility of using the rotating heat pipe technology for the cooling of rotors in advanced generators and motors currently being developed by the Air Force for the MEA program;

- 2) To design and analyze a high-speed (up to 60,000 rpm) RHP for a typical application requiring 0-3 kW of thermal transport;
- 3) To develop a high speed RHP test rig comprising comprehensive instrumentation and safety systems; and
- 4) To conduct elaborate on-axis, horizontal mode performance tests on the RHP hardware at varying power input and speed settings.

More specifically, the objectives were further narrowed down to two stages of design and development. In the first stage, a low-to-moderate speed (0-7,500 rpm) RHP, involving water and methanol as working fluids and stainless steel 316 as the container material, was to be designed, fabricated and tested as a learning experience. Parallelly, a computational modeling effort and test rig development effort were to be undertaken. In the second stage, high-speed (at least 30,000 rpm) RHPs, involving water and methanol as working fluids in stainless steel 316 containers, were to be designed, fabricated and tested.

An important related goal was to analyze the RHP test results, corroborate with the theoretical predictions and suggest future directions and recommendations for this research effort.

This research is restricted to on-axis mode of rotation in horizontal orientation only. Consideration of other aspects such as off-axis rotation (revolving heat pipes), inclined mode operation, straight cylinder and stepped cylinder RHPs, etc., are beyond the scope of the study.

2.0 DESIGN AND ANALYSIS OF RHP

2.1 DESIGN REQUIREMENT

Basically the RHP concept of cooling can be applied to all rotating electrical machinery using wound rotor, permanent magnet and switched reluctance type of rotors. The present design is based on a developmental switched reluctance rotor of an advanced IPU being developed by the Air Force [40]. The design input data are summarized in Table 2.

Table 2. RHP Design Preliminary Input Data

1. Application	To cool the rotor of an IPU of SRM type with 4 pole rotor, 6 pole stator and 125 kW generating capacity
2. Rotational speed	60,000 rpm
3. Rotor shaft dia.	2.54 cm (O.D.)
4. Rotor stack length	18.3 cm (represents RHP evaporator length)
5. Rotor thermal loss to be cooled by RHP	3.5 kW
6. Safe operating temperature range for IPU rotor	<388°C

A maximum thermal load of 3.5 kW generated within the laminated stack of the rotor is to be dissipated through the RHP evaporator. A mechanically comparable hollow shaft forming the RHP can retrofit in place of the rotor solid shaft. Assuming uniform heat generation and neglecting the heat losses by radiation and convection through the air gap of the IPU, the evaporator heat flux is calculated to be $Q/\pi dL_e = 24 \text{ W/cm}^2$. The rotor is required to be operating at temperatures under 660 K. This establishes the temperature range of the working fluid for RHP. Several fluids such as methanol, water, mercury and potassium could be used in 300-700 K range with varying choices of liquid transport factor. Water has been chosen here for convenience and ease of handling.

From the static water heat pipe research experience [41,42], a condenser heat flux of 24 W/cm^2 can be assumed for external water-evaporative cooling of the condenser. Hence, a minimum of 18.3 cm condenser length would be necessary. Adding 4.5 cm for each bearing support, the total length required for the RHP is 45.6 cm.

2.2 DESIGN THEORY AND PRINCIPLES

2.2.1 Working Principle

Figure 4 illustrates a typical geometry of the RHP designed to transport thermal energy in the axial direction. It consists of a hollow cylindrical shaft evacuated and filled with a small quantity (usually about 20% of the volume) of a pure working fluid and hermetically sealed. Heat is applied over the evaporator section which causes the working fluid to vaporize. The vapor flows to the low pressure region, namely, the condenser section where the latent heat of vaporization is removed causing the vapor to condense and form a liquid layer. The rotation about the axis of the RHP makes the condensate film to stick to the wall and distribute into an annular film layer. Usually, the condenser inner wall is shaped into an axial taper of about 2 arc degrees. This taper creates an axial component of the centrifugal acceleration on the fluid layer which makes it flow toward the broader end of the taper (evaporator end). Thus, the fluid is returned to the evaporator and the continuous circulation in a closed loop begins within the RHP. These processes of heat addition, evaporation of the liquid, vapor flow, heat removal and condensation, rotation motion in parting the centrifugal force on the condensate film, and return of the fluid to the evaporator complete the cycle, thereby establishing the RHP's heat transport action. A stable operation will be achieved if the rates of the various processes are balanced with respect to the physical design of the RHP.

The design parameters of an RHP are:

- 1) Length
- 2) Rotational speed

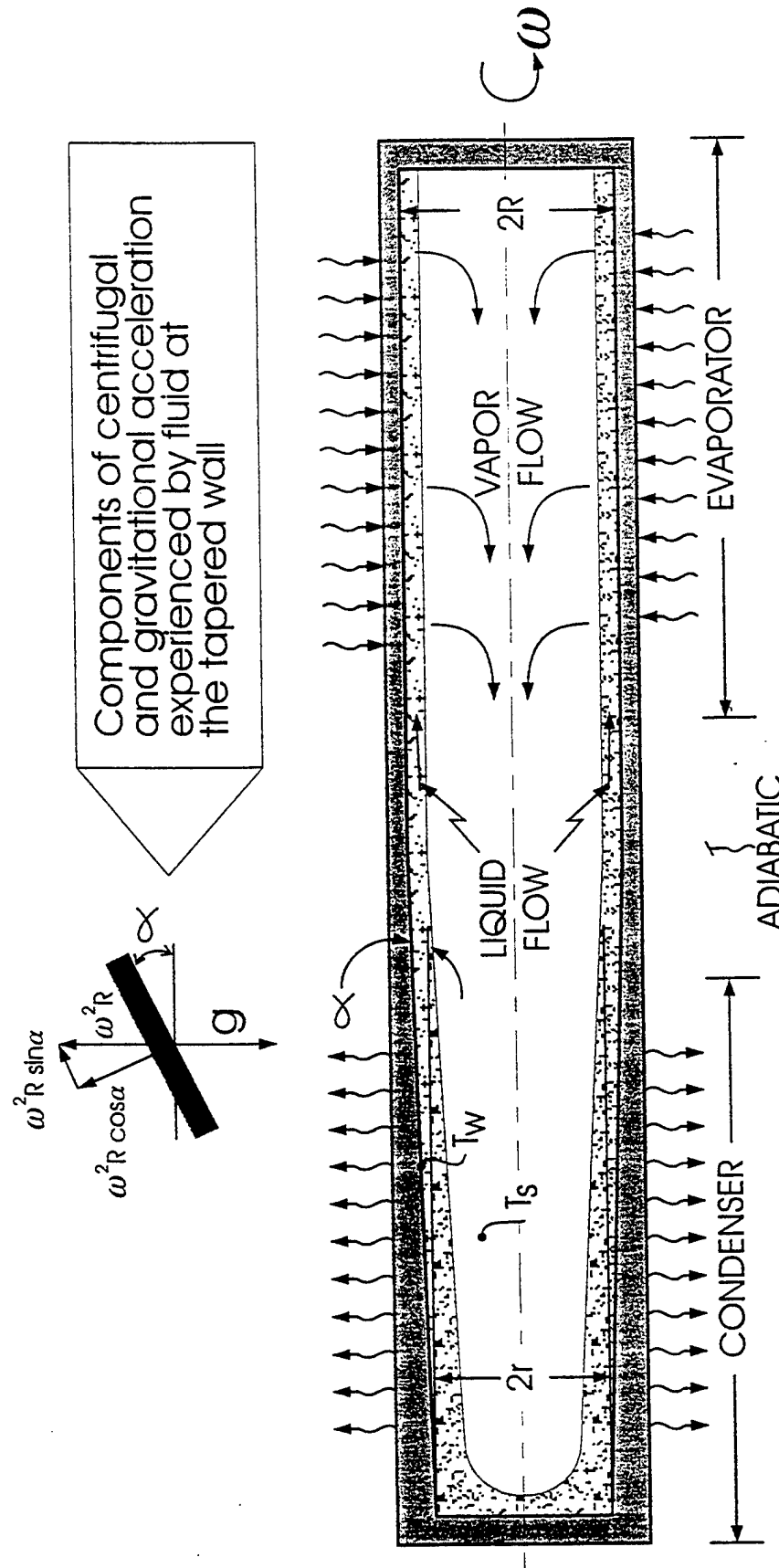


Figure 4. Geometry of the Rotating Heat Pipe (RHP).

- 3) Internal diameter of the pipe
- 4) Taper angle
- 5) Heat input rate
- 6) Heat removal rate, and
- 7) Working fluid thermophysical properties

In addition, other considerations such as the critical speed of the RHP and the support system, dynamic balancing, working fluid and containment material compatibility, liquid transport or merit number of the working fluid, etc., play a major role in the design of RHP. A descriptive compilation of RHP fundamental aspects can be found in ref. 31.

2.2.2 Condenser Taper

Fluid pumping action is created within the RHP due to a small taper on the inner wall. The axial component of the centrifugal acceleration during rotation pumps the condensate from condenser to evaporator. The magnitude of this acceleration is given by Eq. (1).

$$a_a = \omega^2 r_m \sin \alpha \quad (1)$$

The taper angle α is usually in the order of 1 degree. As an example, for a 2.54 cm dia. and 45.6 cm long stainless steel 316 shaft, a minimum wall thickness of 6 mm is required to provide the mechanical strength. This allows a taper angle of 0.8 degree for the condenser inner bore whose ID varies from 1.27 cm to 1.91 cm over its length of 18.3 cm. Substituting the values in Eq. (1), it can be seen that a_a varies from 0.03 G's to 446 G's for on-axis rotational speed variation from 500 to 60,000 rpm. Figure 4 shows the geometry of the RHP with tapered condenser inner wall.

2.2.3 Critical Speed

A study of the rotor dynamics involved in the design of a high speed shaft was necessary to determine the critical speeds of the present low and high speed RHP designs and methods to

move critical speeds outside of the operating range of the developmental IPU. Appendixes A.1 and A.2 show the preliminary calculations. Later, a rigorous rotor dynamic analysis was performed on both long (47.94 cm) and short (26.67 cm) versions of the RHP designs. Results of the analysis of the long version confirmed the first critical speed of 15,200 rpm at which the RHP went into resonance and was damaged during testing. The frequency of the first critical speed is determined mainly by the bending characteristics of the rotor. Appendixes A.3 and A.4 present the details of the rigorous rotor-dynamics analysis. The first three undamped critical speeds were computed at several support stiffnesses. The support stiffness of the rotor is defined as the effective stiffness of the bearing and bearing mount in series at both bearing locations.

Figure 5 illustrates the critical speed versus support stiffness of the 47.94 and 26.67 cm long RHPs for the first three modes. Also, superimposed in this figure are the curves, S_1 and S_2 corresponding to the radial bearing stiffnesses for bearings at axial-preloads of 25 and 40 lbs, respectively. The intersections of these curves with the critical speed lines define the first three critical speeds. It is observed that the first mode critical speed is increased from 15,200 rpm to 37,000 rpm by shortening the length. The axial preload variation did not affect the critical speeds significantly. Changes in bearings and bearing mounts have little effect on the first critical speed, due to their locations being on nodal points. Our interest was to move the first critical speed above the 40,000 rpm which is well above the operating speed of most AF applications.

Modifications considered to raise the first critical speed included: 1) increasing rotor diameter, 2) reducing bearing span, 3) increasing shaft wall thickness and 4) addition of a third center-bearing. Of these options an additional third bearing was ruled out due to the high temperatures at the middle of the shaft, which would quickly destroy a bearing in that location. In addition, mechanical assembly and alignment procedures would be very hard. Increasing the RHP wall thickness would severely decrease the heat transport capability of the RHP. An approximate equation, Eq. (2), to determine the first critical speed was derived from the fundamental principle of conservation of potential and strain energy applicable to a round, simply supported beam with two degrees of freedom. The center part and the end supports of the beam are allowed to deflect. Also, the bending stiffness of the beam is taken into account in this

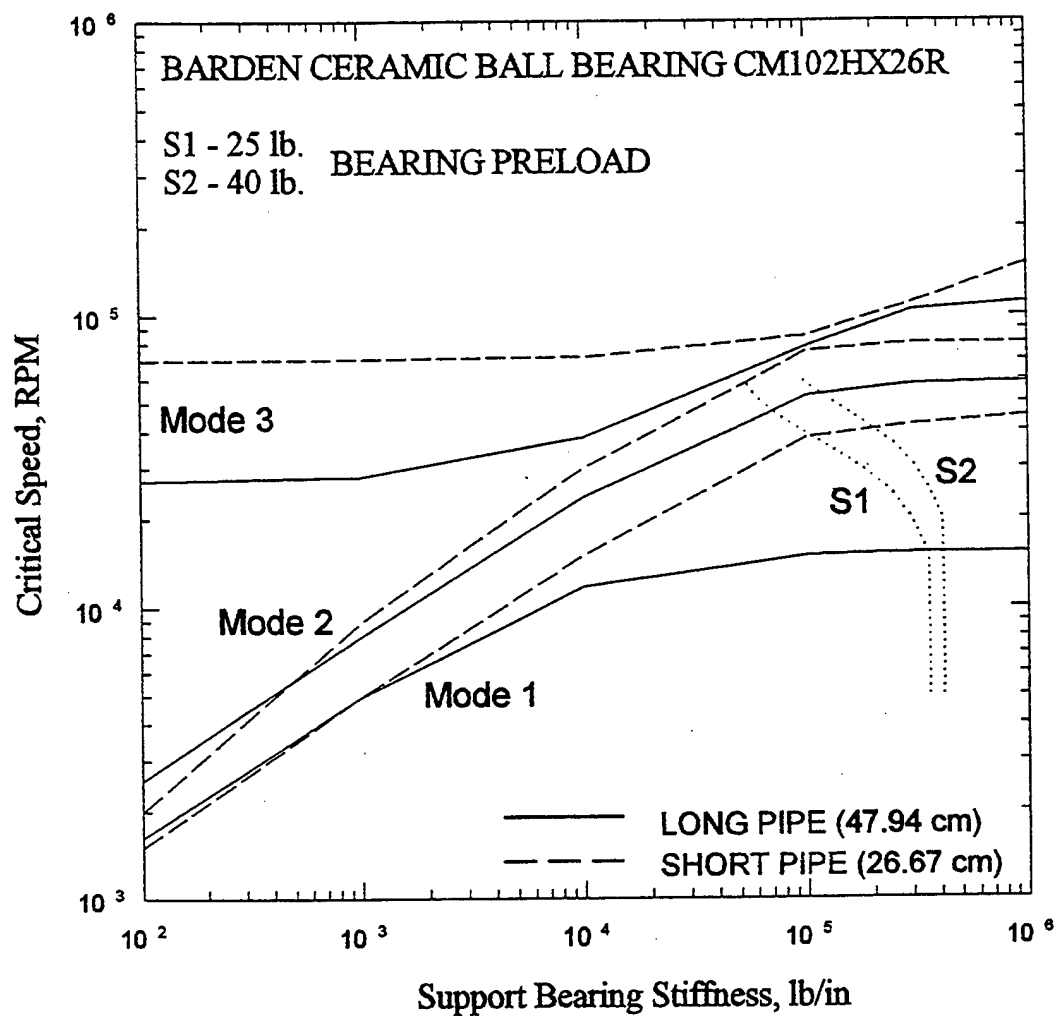


Figure 5. RHP Critical Speed vs. Bearing Support Stiffness.

equation [45]. To find the first critical frequency for a particular RHP design, this equation is solved for frequency, ω .

$$(2K - \omega^2 \rho A L) \left(\frac{EI\pi^4}{2L^3} - \omega^2 \rho A \frac{L}{2} \right) - \omega^4 \left(2\rho A \frac{L}{\pi} \right)^2 = 0 \quad (2)$$

The first critical speed in rpm, N , is found from Eq. (3)

$$N = \frac{30\omega}{\pi} \quad (3)$$

The results of the rigorous analysis and the approximate equation method are listed in Table 3.

Table 3. Critical Speed Analysis Data

RHP Design	Critical speed, rpm Rotor Analysis [45]		Approximate	
	Mode 1	Mode 2	Equation	Error
	Mode 3		Mode 1	
Original	15,200			
18.87" (47.94 cm)	48,000	63,000	15,800	(3.9% high)
Revised	37,500			
10.5" (26.67 cm)	High	High	39,400	(5.1% high)

2.2.4 Choice of Materials

Stainless steel 316 is chosen for the envelope, fill tube and end cap material for its strength, weldability, and high temperature properties. Also, it is preferred for its compatibility with fluids such as mercury, potassium, alcohol and water which are candidate working fluids for the RHP. Noncondensable gas generation problem is known to exist for stainless steel water heat

pipes. However, proper cleaning procedures including several hours of heating at 400°C in electric furnace are recommended for longer useful life of the water/stainless steel heat pipes.

2.2.5 Fluid Inventory

The quantity of fluid charge for continuous operation without evaporator dryout is calculated based on a uniform liquid film thickness (δ) on the inner surface. An expression given for smooth-wall cylinder by Vasiliev [30] is modified for a tapered RHP as given in Eq. (4).

$$\delta = \left[\frac{Q^2}{4\pi^2(\omega^2 r_m - g) \sin \alpha r_m \rho_f^2 h_{fg}} \right]^{0.25} \quad (4)$$

Substituting water property data at 200°C and mean taper radius value in Eq. (4) for maximum heat input load of 3500 W, the required film thickness at 500 rpm is 0.95 mm and 0.075 mm at 60,000 rpm. A nominal 1 mm film thickness is recommended to cover the entire speed range. It should be noted that excess fluid would decrease condenser heat transfer and insufficient fluid would decrease transport capacity. Table 4 compares the fluid inventory data of the present LSRHP design with those from the literature. There are minor differences in calculated and actual inventory data.

2.2.6 Heat Transport Capacity

Nusselt type condenser heat transfer analysis described by Daniels and Al Jumaily [27] is followed here. The condenser heat flux (q_c) of the RHP is given as

$$q_c^4 = \frac{(\omega^2 r_m - g) \sin \alpha \Delta T_{f,c}^3}{1.2656 L_c} \left[\frac{\rho_f^2 h_{fg} k_f^3}{\mu_f} \right] \text{W/m}^2 \quad (5)$$

Table 4. LSRHP Inventory of Fluid - Comparison of Three Designs

WATER RHP SYSTEM	INTERNAL SURFACE AREA (cm ²)			INTERNAL VOLUME (cm ³)			INVEN- TORY (cm ³)	FILM THICK (mm)
	EVAP.	COND.	TOTAL	EVAP.	COND.	TOTAL		
1. MARTO [43,44] (5.4 kW 2800 RPM)	374	331	705	741	344	1085	WATER 150 (13.8% of Int. Vol.)	2.12
2. VASILIEV [30] (3.5 kW 2000 RPM)	254	225.5	479.5	348.5	197.2	545.6	50 (9.2% of Int. Vol.)	1.04
3. WL/UES (LSRHP DESIGN)	124.5	114	239.4	59.7	45.3	105	23.9 (22.8% of Int. Vol.)	1.00

where

$$\bar{h}_{fg} = h_{fg} + 0.35 c_p \Delta T_{f,c}; \Delta T_{f,c} = T_s - T_w$$

$$\omega = \frac{2\pi N}{60} ; N_L = \frac{\rho_f^2 \bar{h}_{fg} k_f^3}{\mu_f}$$

$$Q = q_c A_c ; A_c = 2\pi r_m L_c \quad (6)$$

Liquid transport factor, N_L , for potential working fluids are plotted as a function of temperature as shown in Figure 6. Even though mercury and potassium have superior transport factor compared to water, the latter is chosen for convenience of handling and safety. The peak temperature range (313-563 K) is also attractive for most rotors. Heat transport capacities as calculated from Eq. (5) for methanol, water and mercury at selected operating temperatures for the present LSRHP design are given under Section 2.3.2 and those of HSRHP for water and methanol are given under Section 2.4.2. Mercury shows phenomenal transport capabilities at all rotational speeds. Water has moderate capacities and methanol has the least of the three fluids. Although the internal heat transfer advantages due to the spinning action are great, the overall heat transport performance is reduced by factors such as wall resistance, external heat transfer coefficients coupling the RHP to source and sink.

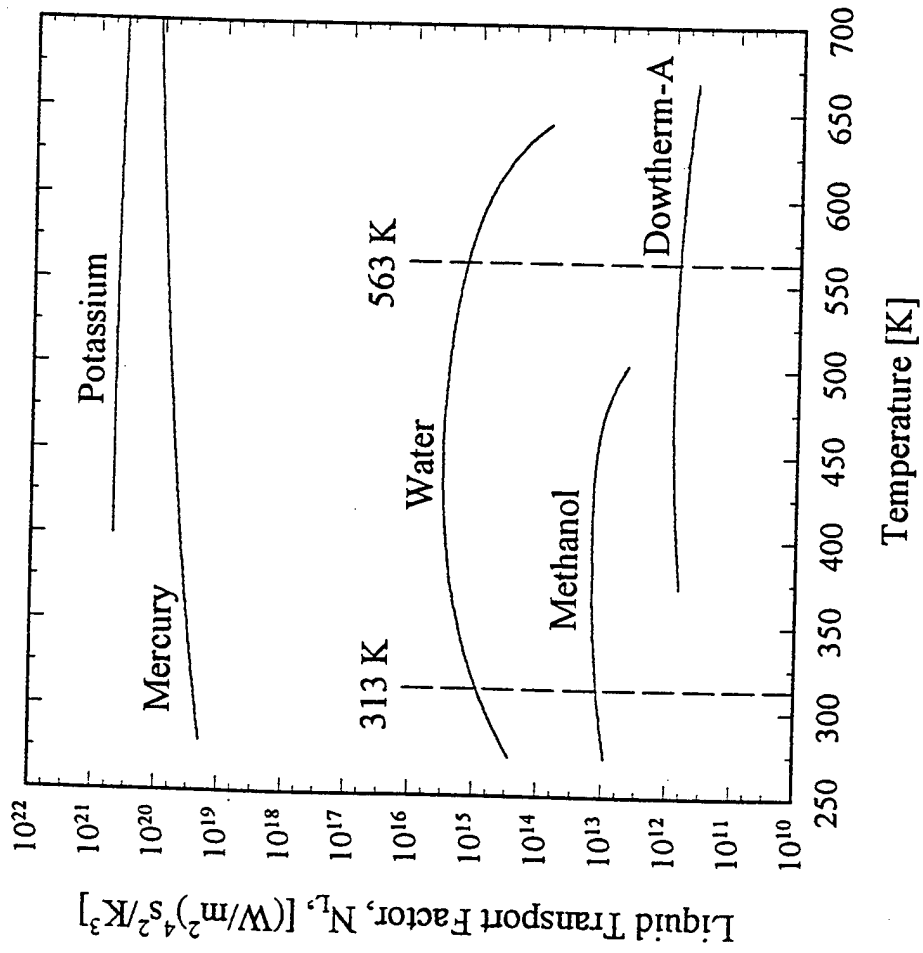


Figure 6. Liquid Transport Factor for Various Fluids.

2.2.7 Wall ΔT and Thermal Expansion

Simple radial heat conduction through cylindrical wall is calculated for stainless steel 316 with $k_{ss} = 16.27 \text{ W/m}^\circ\text{C}$. The ΔT for evaporator and condenser are 0.016°C/W and 0.038°C/W based on the average wall thicknesses of 3.2 and 4.8 mm, respectively. Linear expansion of the 47.94 cm long RHP calculated for a temperature rise of 275°C is 2.35 mm and the corresponding diametrical expansion is 0.111 mm.

2.3 LSRHP DESIGN

2.3.1 Physical Dimensions

The overall design details of the low to moderate speed RHP are given in a schematic diagram shown in Figure 7. The condenser end-plug was designed to be directly coupled to the drive-motor. The active length, that is, the vapor-core length of the RHP was equally divided into evaporated and condenser lengths with a short adiabatic section in the middle. Three short sections, 1.27 cm each at the ends and middle, were designated for infrared temperature sensor target spots. The actual LSRHP had 250.83 cm^3 of internal surface area and 105 cm^3 of internal volume and was filled with 19.7 g of fluid charge which accounts for 18.9% by volume and an average film thickness of 0.83 mm at 25°C for water. Table 5 provides the complete details of the LSRHP design and test parameters.

2.3.2 Design Heat Transport Capacity

Theoretical heat transport capacities of the LSRHP design were computed as functions of condenser film ΔT for different fluids and rotational speeds. The results are shown in Figure 8 for an average working temperature of 140°C . It may be noted that, even though the capacities are plotted for speeds up to 60,000 rpm, it is not practical to run this LSRHP design at high speeds due to the critical speed and bearing limitations.

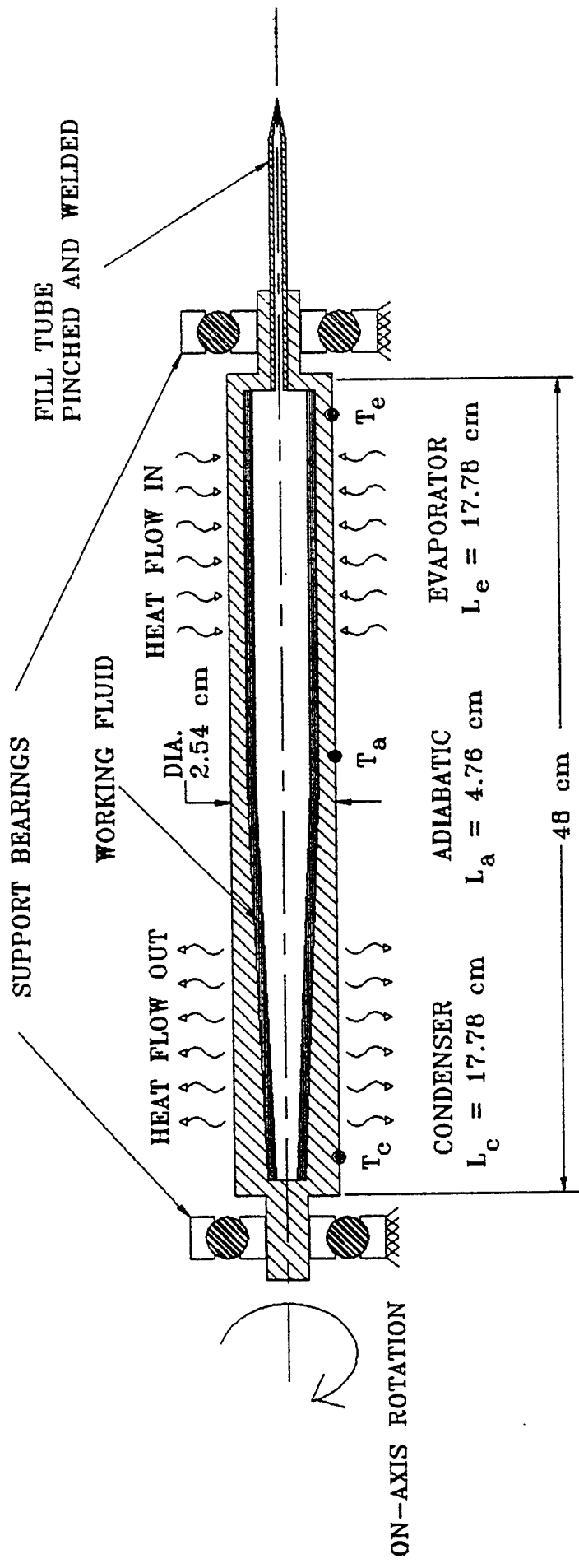


Figure 7. LSRHP - Schematic Diagram of Overall Details.

Table 5. LSRHP Test Hardware Design and Test Parameters

<u>Details</u>	<u>Water RHP</u>	<u>Methanol RHP</u>
Mechanical:		
Material	Stainless steel 316	
Active length (total)	47.94 cm	
Outer diameter	2.54 cm	
Inner diameter - condenser	1.27 / 1.91 cm	
Inner diameter - evaporator	1.91 cm	
Internal surface area	250.83 cm ²	
Active evaporator/condenser length	17.78 / 17.78 cm	
Condenser taper (half cone)	0.8°	
Evaporator internal surface	V-threads, 40/cm	
External surface finish	Black painted; $\epsilon=0.9$	
Weight of filled RHP	1.255 kg	1.247 kg
Working Fluid:		
Type/Quality	Degassed deionized water; 18 MΩ-cm	Analytical grade methanol; 99.99% pure
Quantity filled	0.0197 kg	0.019 kg
Design heat transport capacity:		
At 7000 rpm, 140°C and $\Delta T_{fc} = 25^\circ\text{C}$	~3000 W	~850 W
Testing:		
Heat Transport	250-2250 W	250-1200 W
Operating Temperature Range	25-220°C	25-190°C
Orientation / Rotation	Horizontal / on-axis	
Speed	3000-7000 rpm	
Heating	RF Heating Coil	
	Calibrated with water calorimetry	
Cooling i) Air Only	6.7-20 psig; 35-50 SCFH	
ii) Air-water mist using single fan spray with air-atomizer nozzle	Air: 20 psig; 35 SCFH Water: 0.5-0.29 l/min	

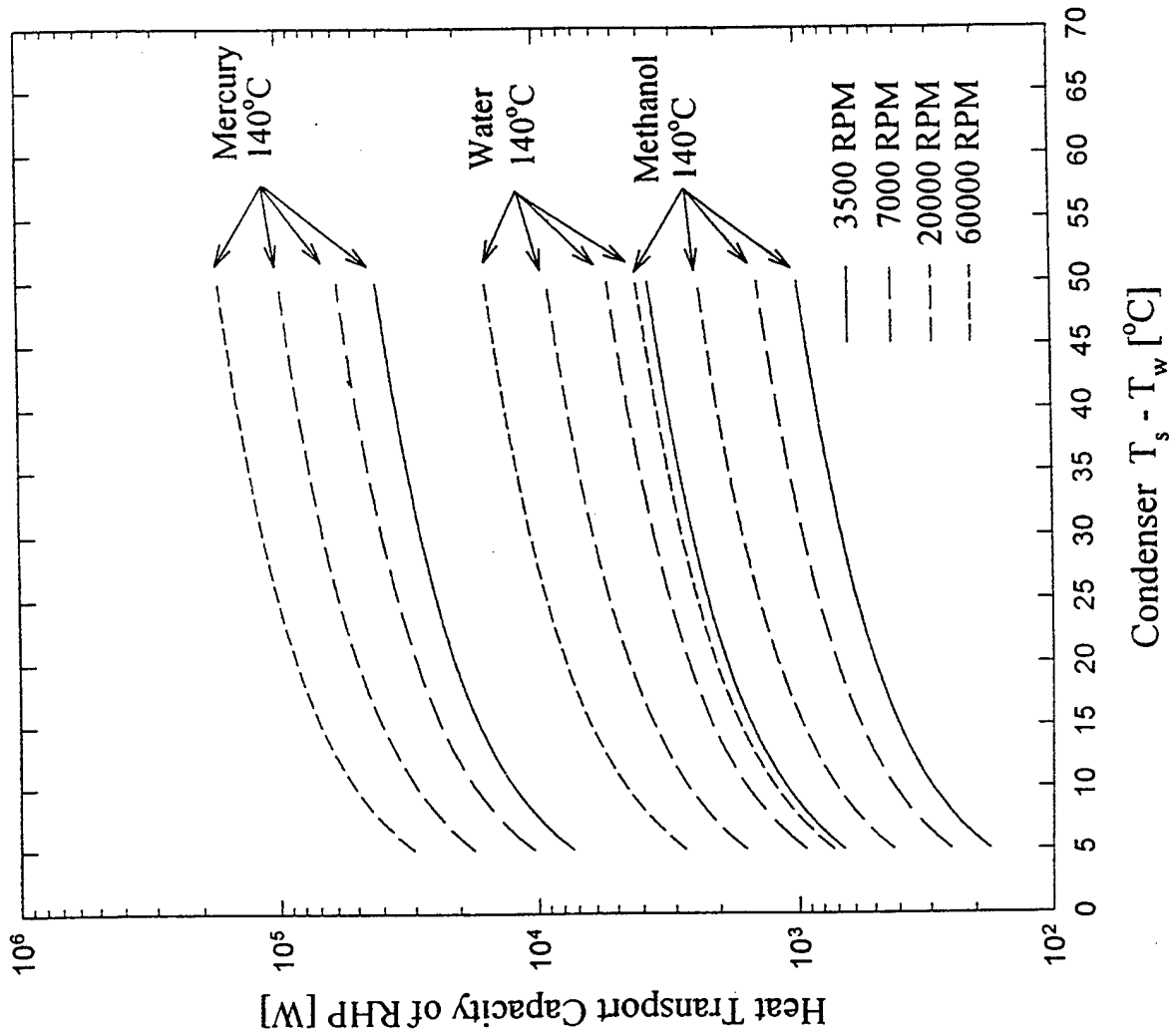


Figure 8. Theoretical Heat Transport Capacities of LSRHP.

2.4 HSRHP DESIGN

The requirements of the HSRHP design based on the revised developmental switched reluctance generator are listed in Table 6.

Table 6. HSRHP Design: Revised Input Data

1. Application	:	To cool the rotor of an IPU of SRM type with 4 pole rotor, 6 pole stator and 125 kW generating capacity
2. Rotational speed	:	40,000 rpm
3. Rotor shaft diameter	:	2.54 cm (O.D.)
4. Rotor stack length	:	12.3 cm (represents RHP evaporator length)
5. Rotor thermal loss to be cooled by RHP	:	1924 W (rotor poles and yoke losses)
6. Safe operating temperature range for IPU rotor	:	<388°C

2.4.1 Physical Dimension

Based on the knowledge gained from low and medium speed tests and using the design criteria of critical speed and rotor dynamics, a revised version of the RHP was designed.

Figure 9 shows the high speed modified short version RHP that is 37.2 cm long (26.67 cm between bearing centers) and good for tests up to a speed of 40,000 rpm. At this speed, the water filled unit is capable of transporting 2088 W and the methanol unit is capable of 600 W as seen in Figure 10.

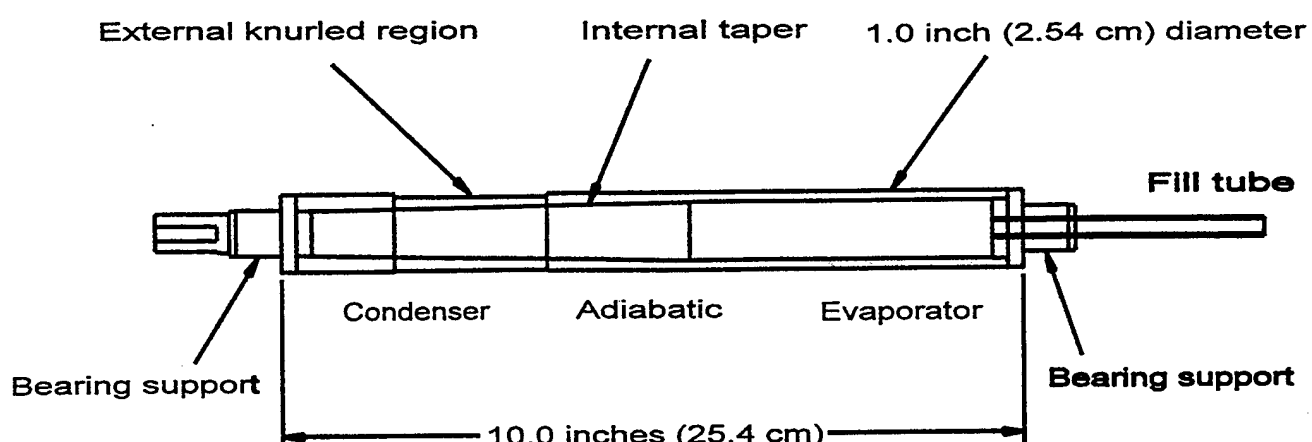


Figure 9. HSRHP - Modified Short Version RHP.

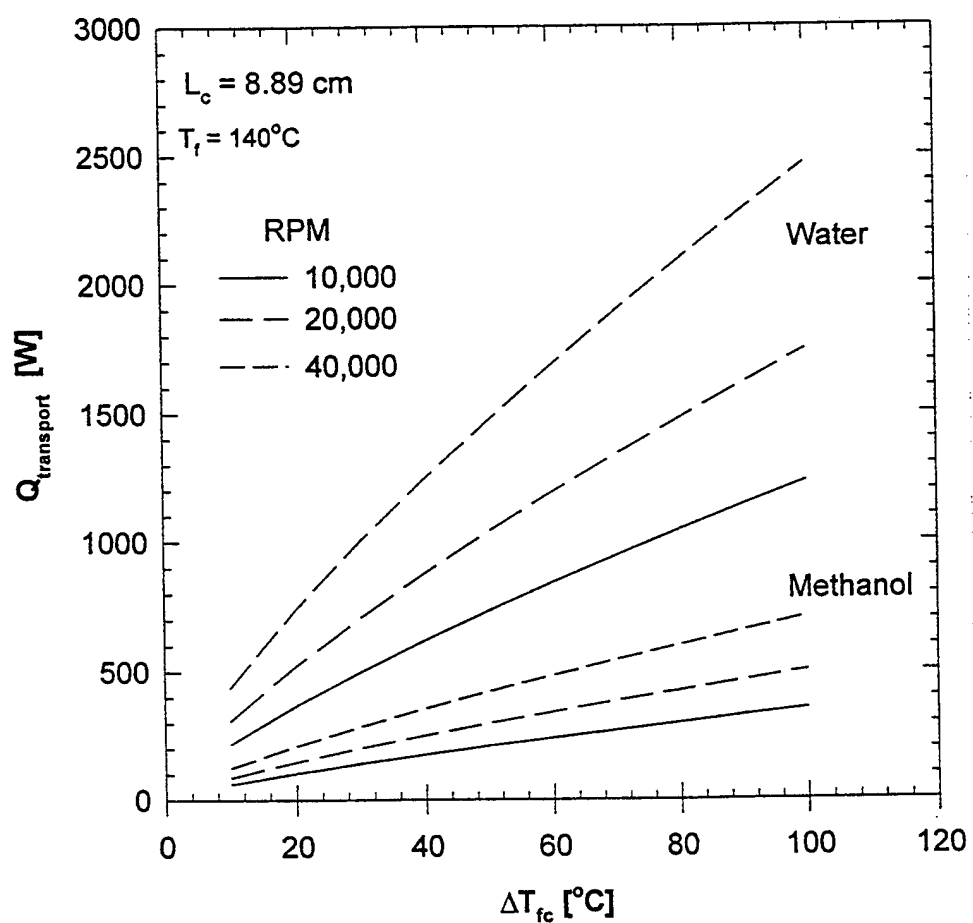


Figure 10. Theoretical Heat Transport Capacities of HSRHP.

The reduced length is necessary to keep the first critical speed higher than the required operating speed for the chosen 2.54 cm diameter design. This design was expected to simulate all the IPU rotor thermal requirements. The extension of the condenser length outside the IPU rotor is an application issue to be handled separately. For the convenience of laboratory testing, a design with approximately equal lengths of condenser and evaporator was selected. The new RHP design and testing parameters are listed in Table 7.

2.4.2 Design Heat Transport Capacity

Similar to the graphs shown in Figure 8, the heat transport capacity results are presented in Figure 10 for the case of the HSRHP design.

2.5 NUMERICAL ANALYSIS AND MODELING

An effort to numerically model the combined heat transfer processes accurately was initiated under this project as a result of the observation that the available RHP literature (Daniels and Al-Jumaily, 1975 [27], Harley and Faghri 1995 [46], Vasiliev and Khrolenok 1983, etc. [30]) did not cover the modeling aspects at high speed operations of the RHP. In addition, the internal heat transfer behavior was investigated by these authors via a Nusselt type analysis which focused attention on liquid phase only and had limited applicability. Hence, it was decided to critically evaluate the modeling approaches and assumptions of the existing literature and make an effort to revise the analysis to address the high speed and coriolis effects as well. The following paragraphs present the details of this attempt.

2.5.1 Critical Evaluation of Selected Literature

A. Daniels and Al-Jumaily (1975) studied theoretically and experimentally the heat transfer of tapered rotating heat pipes in steady state, basically the condensation rate in the condenser. Their theoretical approach assumed that the limit of the heat transfer of a rotating heat pipe was the condenser. He utilized Nusselt type laminar flow theory to the condensate film. Vapor friction drag and momentum drag on vapor-liquid interface were taken into account. Their assumptions were:

Table 7. HSRHP Test Hardware Design and Test Parameters

Mechanical:	
Material	Stainless steel 316
Length - overall/bearing centers	37.2 / 26.67 cm
Active length - vapor space	22.89 cm
Outer diameter	2.54 cm
Inner diameter - condenser	1.46 / 1.91 cm
Inner diameter - evaporator	1.91 cm
Internal surface area	132.63 cm ²
Internal volume	57.44 cm ³
Effective evaporator/adiabatic/ condenser length	7.6 / 3×1.9 / 8.9 cm
Condenser taper (half cone)	1.0°
Evaporator internal surface	V-threads, 40/cm
External surface finish	Black paint; $\epsilon=0.9$
Working fluid:	
	<u>Water RHP</u>
Type/Quality	Degassed deionized water; 18 MΩ-cm
	<u>Methanol RHP</u>
Type/Quality	Analytical grade methanol; 99.99% pure
Quantity filled	0.0105 kg
Weight of filled RHP	0.627 kg
Temperature range	20-200°C
Design heat transport capacity: Refer to Fig. 10 at 40,000 rpm, 140°C and $\Delta T_{fc} = 80^\circ\text{C}$	2088 W
	600 W

- 1) filmwise condensation;
- 2) laminar condensate film flow;
- 3) temperature distribution within the film is linear;
- 4) the vapor space is at constant pressure;
- 5) fluid properties are assumed constant;
- 6) the density of the fluid is much higher than that of the vapor;
- 7) velocity gradients in the circumferential directions are negligible;
- 8) the analysis refers to the upper half of the heat pipe relative to the center line;
- 9) due to the small taper angle, a mean radius is taken for the condenser;
- 10) the condenser wall temperature is assumed uniform over its length;
- 11) the slope of the condensate film is much less than the taper angle;
- 12) film thickness is zero at the end of the condenser.

From the force balance of the condensate film in x and y directions (x is along the tapered wall of the heat pipe or the flow direction of the condensate involving the viscous stress, pressure gradient, centrifuging force and gravity; y is perpendicular to the wall involving pressure gradient, centrifuging force and gravity, see Figure 4.), with the boundary conditions of non-slip at the wall and force balance at the liquid-vapor interface (liquid viscous stress, vapor friction drag and vapor momentum drag), Daniels and Al-Jumaily came up with expressions for film thickness distribution, film velocity, and local heat flux along the condenser section as functions of rotational speed, temperature difference between the saturation temperature and the condenser wall temperature, working fluid properties, as well as the geometry of the heat pipe. Neglecting vapor drag, an average heat transfer rate was found to be as in Eq. (7) which is reproduced from Eq. (5).

$$Q^4 = [(\omega^2 r - g) \sin\alpha \Delta T^3 / (1.26 L_c)] * [\rho^2 h_{fg} k^3 / \mu] \quad (7)$$

where Q is the heat transfer rate, ω is heat pipe rotation speed, r is the average condenser radius, α is the taper angle, ΔT is the difference between the saturation temperature and the condenser wall temperature, L_c is the condenser length, ρ is the liquid density, h_{fg} is the average enthalpy

change of the vapor to subcooled liquid, k is the liquid thermal conductivity, and μ is the liquid dynamic viscosity.

Theoretically, Daniels and Al-Jumaily showed that the vapor drag forces increase with heat transfer rate, but they are significant only at high heat transfer rate. Also at higher rotational speeds, the effects decrease because the body force increases rapidly with increasing ω thus canceling out the effects of the vapor drag terms. The gravitational effects become significant only at lower speeds. *It can be concluded that at high rotational speed, the gravitational and vapor drag effects can be neglected.*

Experiments were conducted with a heat pipe of: $L_c = 152$ mm (critical liquid film Reynolds number is 240 for Arcton 113 at 2000 rpm), $r = 16.9$ mm, $\alpha = 2$ degree, $L_{\text{total}} = 325$ mm, $L_a = 123$ mm, $L_e = 50$ mm, $\omega = 600, 800, 1000, 1200$ rpm, $Q_{\max} = 1600$ W (~ 20 W/cm 2), and with fluids - Arcton 113, Arcton 21 and water. $P_{\text{vapor at evaporator}} = P_{\text{saturation}}(T_{\text{vapor at evaporator}})$, $P_{\text{vapor at condenser}}$ was measured (not quite precisely). It was found that higher α , ω and r yield higher heat transfer. There is an optimal unique working fluid charge for a particular set of conditions (i.e., heat transfer rate Q and rotating speed ω). The experiments showed that there might be an upper limit on the speed (i.e., beyond this limit, increasing ω will not increase the heat transfer rate). Their experimental results for water did not agree with their theoretical prediction due to, according to the authors, the small fluid charge.

B. Harley and Faghri (1995) carried out a transient two dimensional numerical analysis on tapered rotational heat pipes coupling both liquid and vapor phases. For the vapor, it was assumed that,

- 1) gravity effects are negligible in comparison to those of the centrifugal force;
- 2) vapor space radius is taken constant.

For liquid film, the Nusselt-type thin film analysis was used with the following assumptions:

- 1) filmwise condensation;

- 2) inertia and convection in liquid are negligible;
- 3) liquid film thickness is much less than the vapor space radius;
- 4) vapor density is much less than that of liquid;
- 5) the slope of the condensate film is much less than the taper angle;
- 6) circumferential velocity and temperature gradients are negligible;
- 7) non-slip boundary conditions at both wall and liquid vapor interface;
- 8) at liquid vapor interface, vapor friction is accounted but not momentum drag as done by Daniels and Al-Jumaily;
- 9) vapor gradient along the axis is accounted while Daniels and Al-Jumaily set it zero. (A numerical simulation by the present author has verified Daniels and Al-Jumaily's assumption);
- 10) linear temperature profile across the film;
- 11) The whole analysis is valid for only the "critical" liquid filling ratio, which is defined as the amount of liquid that produces a liquid film with a zero film thickness at both ends of the heat pipe.

The numerical simulation parameters were: $Q = 800 \text{ W}$, $\omega = 600 \text{ rpm}$, $L_{\text{total}} = 325 \text{ mm}$, $L_{\text{evaporator}} = 50 \text{ mm}$, $L_{\text{adiabatic}} = 123 \text{ mm}$, $L_{\text{condenser}} = 152 \text{ mm}$, $R_{\text{vapor}} = 21.25 \text{ mm}$, $R_o = 26.5 \text{ mm}$, $\alpha = 2 \text{ degree}$, copper and Freon-113.

The numerical results presented by Harley and Faghri are:

- 1) The vapor core was nearly isothermal, with temperature variations of less than 6 degree;
- 2) The centerline vapor temperature was nearly constant along the length of the rotating heat pipe. The saturated vapor assumption by Daniels and Al-Jumaily was valid ($P_{\text{vapor}} = \text{constant}$) .
- 3) A rotating heat pipe did not undergo solid-body rotation, i.e., the radial variation of the tangential vapor velocity was not linear.

C. Vasiliev and Khrolenok (1983), in studying the heat transfer enhancement of a longitudinally grooved rotating heat pipe, used an approach of minimum total specific energy to obtain a boundary condition instead of assumed zero film thickness boundaries as utilized by Daniels, et al. and Harley, et al. The heat pipe Vasiliev, et al., studied was a step cylinder with a radius increase at the end of condenser and adiabatic sections. The film thickness at the intersection of two regions was determined by treating the film as falling down the edge of the inner surface of a long rotating cylinder. Vasiliev, et al. experimental results agreed very well with their theoretical prediction.

2.5.2 Verification of Daniels and Al-Jumaily Analysis

Some numerical calculations were carried out by Pais 1996 [47] to check the validation of some of Daniels, et al. assumptions based on the condensate film thickness and film velocity.

Pais took Daniels, et al. approach to the condensate film in a rotational heat pipe and obtained numerically the film thickness and velocity profile. He stated that the working fluid for reasons of convenience assumed to be water; the physical conditions were taken to be temperature $T_{sat} = 100^{\circ}\text{C}$, pressure = 1 bar and the heat transfer rate $Q = 800 \text{ W}$. The dimensions of the RTS were the same as studied by Harley, et al. (1995) and Daniels, et al. (1975), respectively. Since, only the liquid film was modeled here, some assumptions were made with respect to the parameters of the vapor flow domain, namely, the pressure derivative was being neglected and the axial velocity derivative was set to 80 s^{-1} , according to the numerical experiment of Harley, et al. (1995). Figure 11 shows the film thickness in the condenser section as calculated by Pais.

Based upon Pais's film thickness profile, it was found that taking the radius of the condenser as constant, yielded negligible effects on the heat transfer rate. The maximum change was less than 0.05%. The next check was the assumption that the film slope is much less than the taper angle. It was obvious from Figure 11 that this assumption was not valid based on the film thickness by Pais, at least near the condenser boundary. This assumption was closely related to

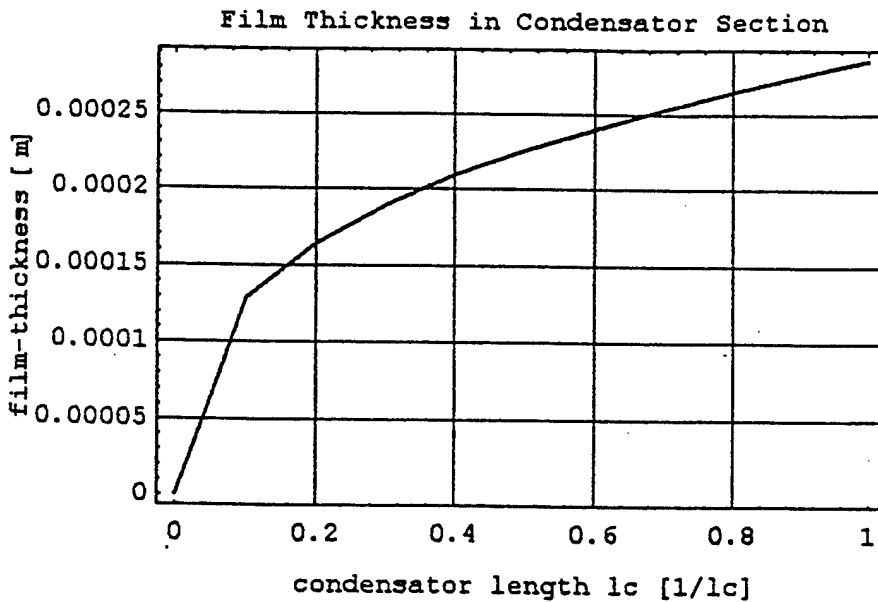


Figure 11. Condensate Film Thickness.

the assumed film thickness boundary condition. If a non-zero boundary condition was used, then the film slope was much less than the taper angle. The difference in the condensation rate between zero film thickness boundary and non-zero film thickness boundary varies from 0% to 33%, depending on the initial film thickness from zero to maximum. By using the zero boundary condition, Daniels et al overestimated the heat transfer rate.

In order to study the liquid film shape, especially the boundary conditions, a theoretical analysis was carried out to a rotating cylindrical pipe filled with certain amount of fluid without heat input. A force balance between centrifuging force and surface tension was used. It was found that for wet fluid, the liquid film is concave toward the rotation axis. The film thickness at the boundary is always higher. The higher the rotation speed, the flatter the liquid film's free surface became.

Figure 12 shows the liquid free surface inside a cylinder under rotation. The parameters used for this calculation are: pipe length 325 mm, rotational speed 1000 rpm, pipe inner radius 16.9 mm, liquid filling volume 20 percent of total internal volume, contact angle 45 degree.

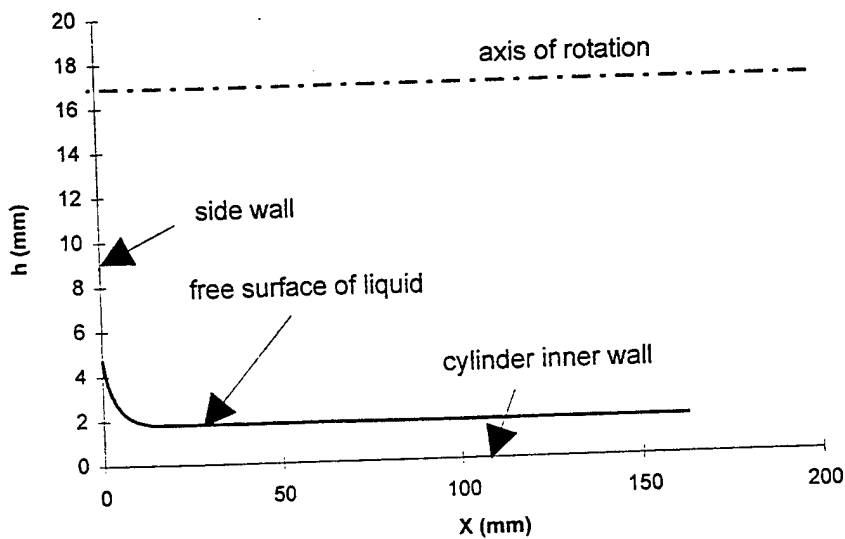


Figure 12. Free Surface Profile of Liquid Film Inside a Cylinder under Rotation.

2.5.3 Summary of Findings and Suggested Future Course

Based on the preliminary analysis mentioned above, it was suggested that the zero film thickness boundary conditions adapted by Daniels, et al. and Harley, et al. need to be reconsidered. Vasiliev, et al. minimum free energy approach may be the right direction. That is, find the boundary liquid film thickness by minimizing the total specific energy of the condensate film. For low rotation speed, the Nusselt type approach to the condensate film is quite satisfactory according to Daniels, et al. and Vasiliev, et al. study results. Still, the Coriolis effects on the performance of the RHP were not addressed. With high rotation speed, the Coriolis force may play an important role. Harley, et al. numerical simulation showed that the vapor undergoes a non-solid body rotation. It may be worthwhile to investigate the role of the Coriolis force on the heat transfer of the tapered rotational heat pipe.

Daniels, et al. suggested that there is an upper limit of heat transfer when rotation speed is increasing. Wu and Peterson (1991) [48] presented the effect of rotational speed on the evaporation and condensation coefficient in horizontal rotating heat pipes. It showed that beyond certain rotational acceleration, the heat transfer would drop and approach a minimum constant when the acceleration is increasing. But all the available data were in the range of less than 40 g acceleration. No RHP literature was found at much higher rotational acceleration. For the

rotational heat pipe used to cool the rotor of a high speed, the rotational acceleration would reach 15000 g.

To model the heat transfer and performance of a high speed RHP, a computational model capable of simulating the heat and momentum transfer characteristics of rotating heat pipe should be developed. The approach for this future research effort should be as follows:

1) *Literature review*

To investigate current literature to determine the most appropriate method for modeling the interface between the vapor and liquid phases, i.e., finite difference, finite volume, or finite element. This objective will also entail the decision on the exact methods to be used for the adaptive grid and the appropriate form of the boundary conditions. Surveys will also be undertaken to assist in the development of the conjugate heat transfer model and in the ground -work studies related to boiling, turbulence, etc.

2) *Vapor phase computational model*

To develop an axisymmetric computational model of the vapor phase. Initially, it will be assumed that the vapor phase domain covers the entire interior of the rotating heat pipe.

3) *Liquid phase computational model*

To develop an axisymmetric computational model of the liquid phase. This model will be coupled with the computational model developed in approach 2.

4) *Conjugate heat transfer model*

To develop an axisymmetric computational model of the heat transfer within the RHP wall. This model will be coupled with the model developed in approach 3.

5) *Experimental validation of computation results*

To compare the results of numerical analysis with the available experimental results for mutual refinement of analytical and experimental tools.

6) *Three-dimensional rotating heat pipe model*

Initial work on extension of the axisymmetric model developed in approach 4 to three-dimensions and on including geometric alterations such as helical grooves or internal fins.

7) *Ground-work studies*

Preliminary studies regarding the importance of the induced swirl and coriolis force effects should be undertaken, Ground-work regarding the introduction of the boiling phenomena and turbulence into the computational model should also be undertaken.

3.0 EXPERIMENTAL WORK

3.1 HARDWARE FABRICATION

3.1.1 LSRHP

A prototype test hardware of the LSRHP, 68.58 cm long (including the fill tube) and 2.54 cm diameter consisted of a main tube, two end-caps and a fill tube was fabricated out of stainless steel 316 bar stock and SS304 tubing. One end-cap had a 7.94 cm long extension for coupling to the drive-motor and the other end-cap had a 12.7 cm long fill tube to connect to the working fluid process station. The fabrication drawing is shown in Figure 13(a-b). The machined parts were vapor degreased and chemically cleaned before joining by welding. The fill tube and end-caps were welded to the main tube by TIG welding process inside a glove box filled with argon gas. The condenser section taper (cone angle of 1.6°) was machined by a specially made taper drill and reamer with long shank lengths. The evaporator section was finely grooved on the inside wall with 38 threads per cm V-shaped grooves for enhancing evaporative heat transfer. The empty pipe was weighed (1235.2 grams) and internally rinsed with pure alcohol before connecting to the fill-station. A schematic diagram of this fill station apparatus is shown in Figure 14. While being pumped down (evacuated), the pipe was vacuum-baked at 340°C and 3×10^{-7} torr for 72 hours using wrap-around heater tapes. This process was necessary to make sure that the holding vacuum (with the vacuum pump valved off from the pipe) was better than 5×10^{-4} torr. Initially, the LSRHP unit was filled with 19.7 grams of distilled water and the fill tube was sealed by crimping and welding. The crimp tool was clamped onto the fill tube with sufficient torque until the flattened portion was cut and TIG welded. This process ensured crimp leak-tightness against atmospheric air leaking into the RHP. The filled pipe weighed 1254.9 grams.

Fill process details for water-RHP: The original uncrimped fill tube had a length of 5 inches to allow an extra 2 inches length for crimping and cutting in case the same RHP unit was reprocessed for a different fluid. Deionized water was degassed insitu by boiling at 100°C for

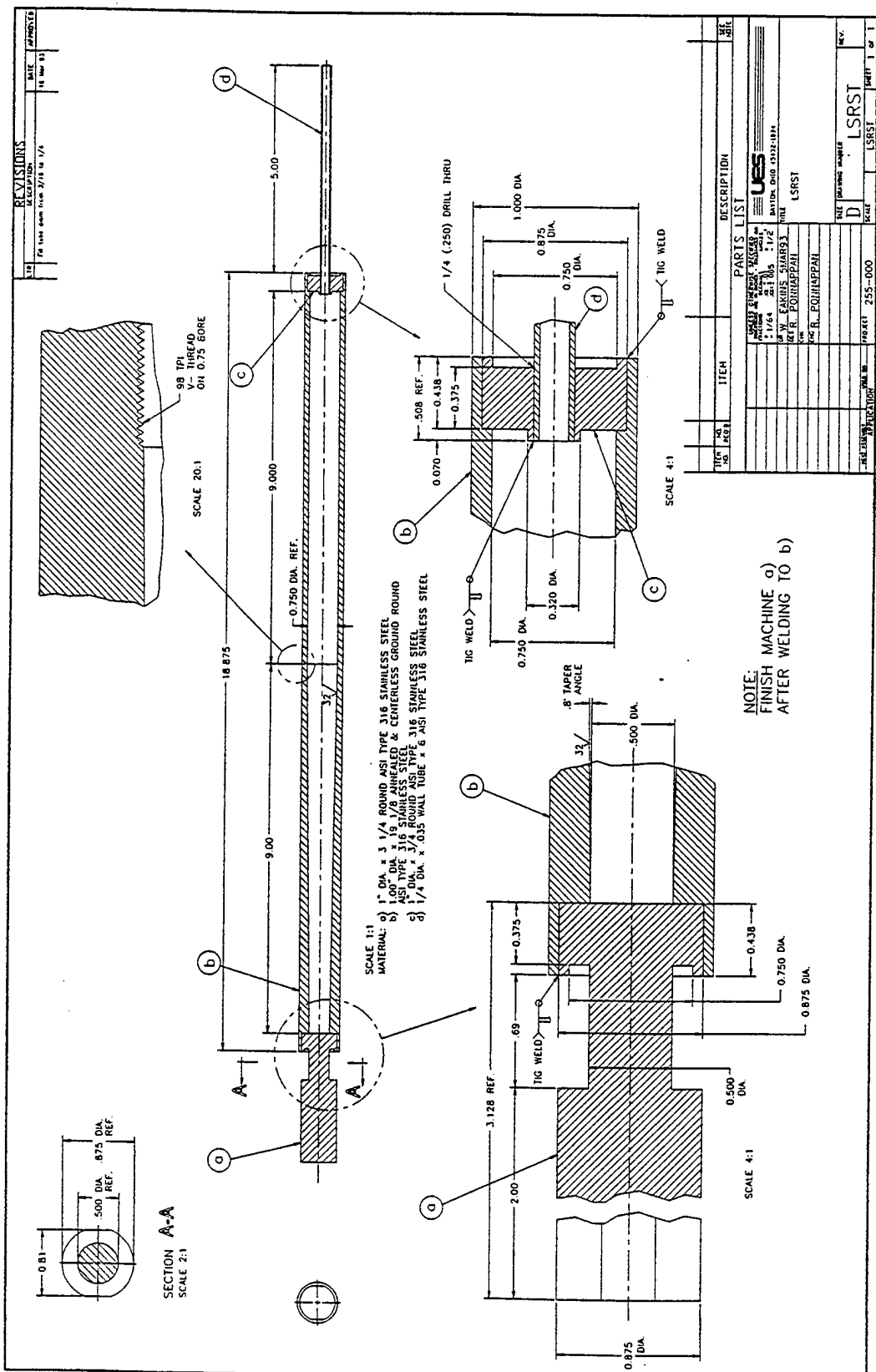


Figure 13a. Fabrication Drawing of the LSRHP Unit.

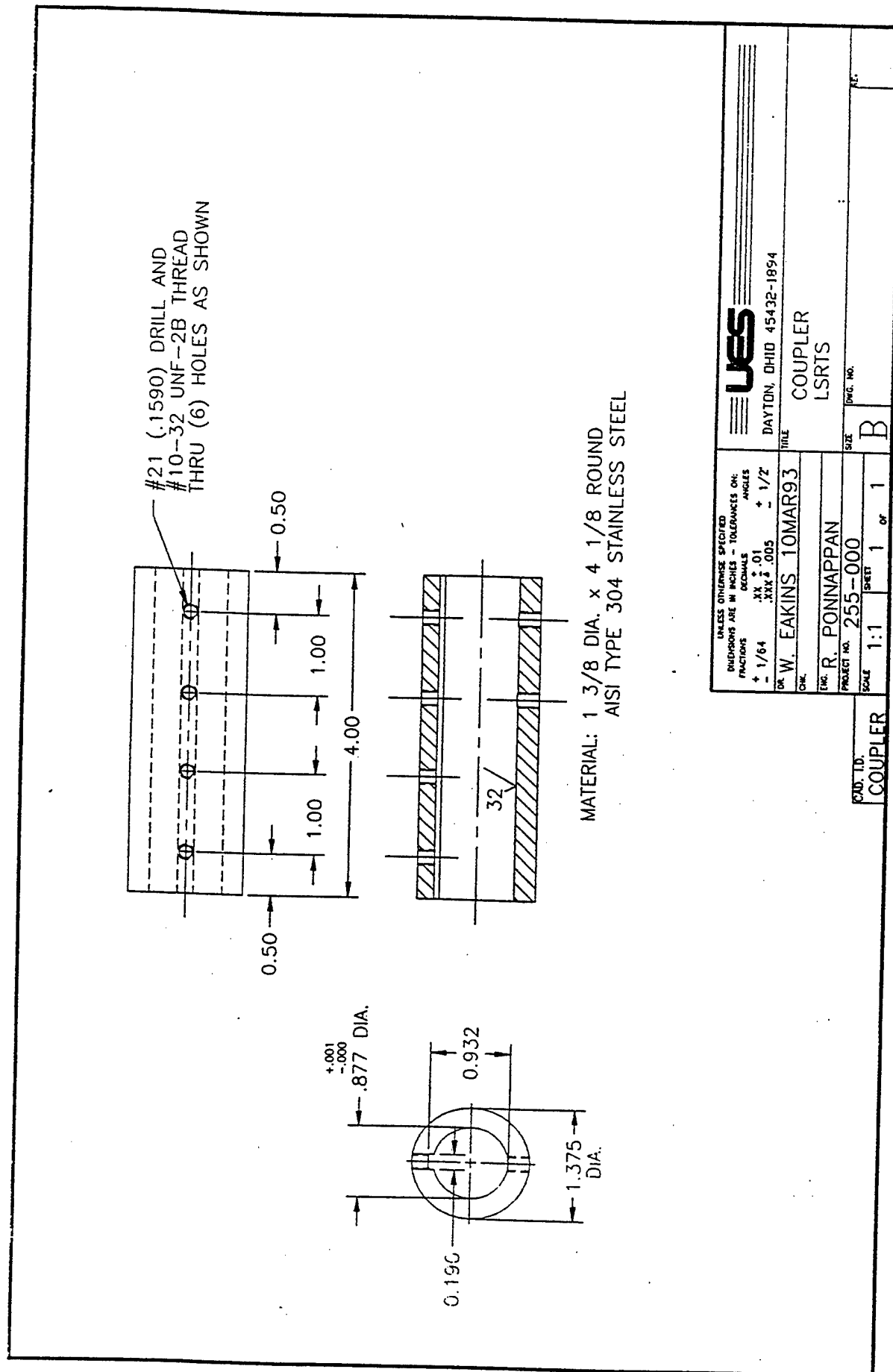


Figure 13b. Fabrication Drawing of the LSRHP Unit.

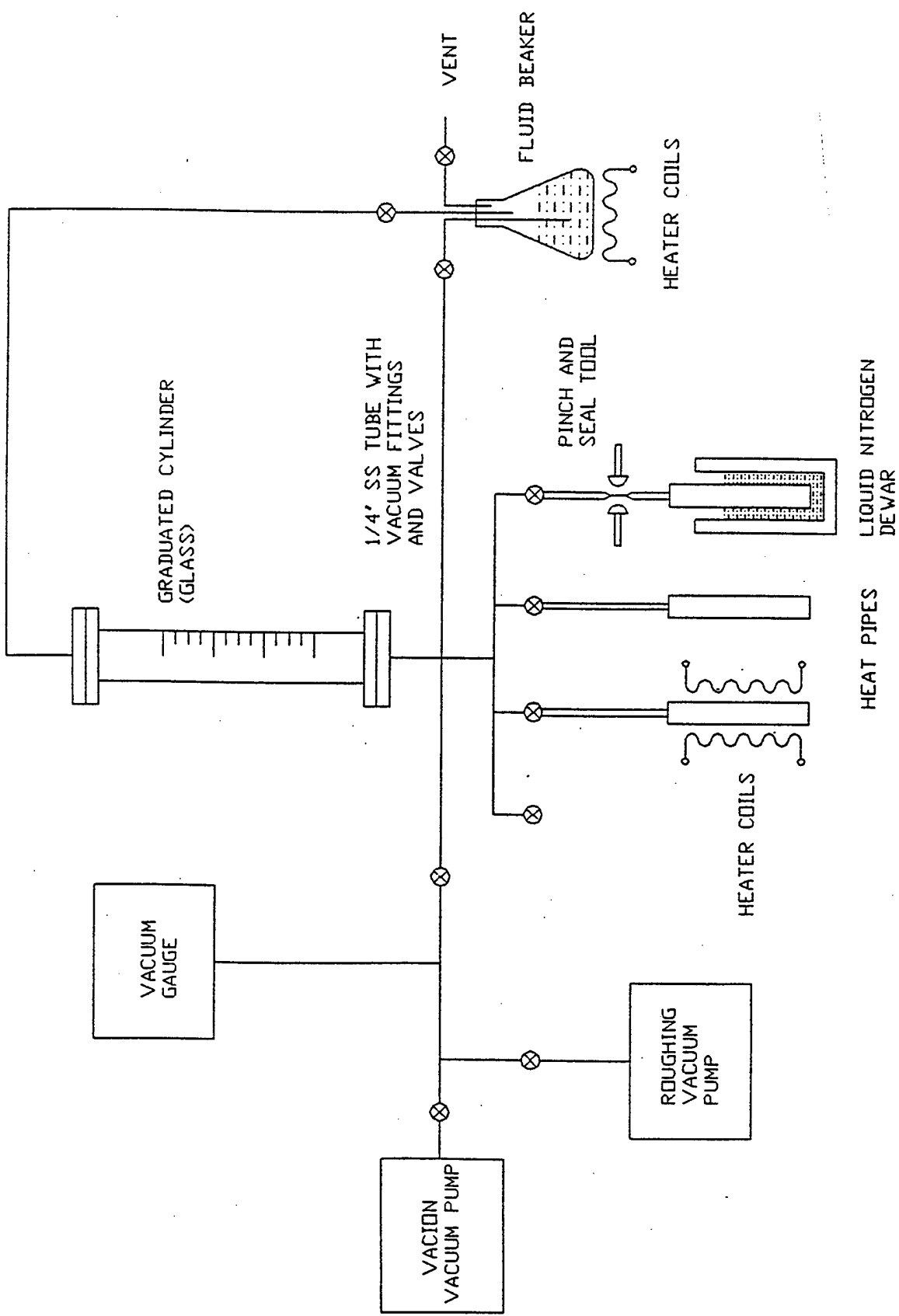


Figure 14. Working Fluid Fill-Station - A Schematic Diagram.

5 minutes and cooling to room temperature (with vent valve closed while cooling) and filled into the RHP. A graduated cylinder in the fill station and the vacuum-suction process were used to transfer a required volume of the fluid into the RHP. The LSRHP unit was first filled with 24 ml of water at room temperature and this was later verified by the difference in weights of the unit before and after filling. An important precaution taken during the crimping process was to raise the internal pressure of the RHP to above atmospheric pressure so that any leakage in the unit would be from the RHP to the ambient and not vice versa. This was accomplished by heating the RHP hardware unit to 117°C just minutes before the crimping operation was started.

External surface finish: Three short segments, 3.81 cm long each at the ends and the middle, were painted with diffuse-black ($\epsilon=0.98$) over the smooth machined surface for infrared temperature sensing. The 17.78 cm long condenser segment was cross-knurled with fine knurl pattern for enhancing heat removal by air-water mist cooling. The 17.78 cm long evaporator segment was fine-cross-knurled and black-painted for good heat reception during non-contact heating by radiation from nichrome heater.

Fill re-process for methanol-RHP: After completion of the tests on water-RHP, the LSRHP unit was reprocessed for methanol-RHP. The crimp-seal was opened by cutting the end of the fill tube. Enough length of the fill tube (3 in.) was still available to process the unit as before. Water was drained and the inside was rinsed thoroughly with alcohol. After drying with clean air, the unit was installed in the process station for vacuum-baking and filling. Essentially the same procedure used earlier for water-RHP was followed now. Analytically pure methanol was used for this filling. The inventory of methanol filled was 25 ml at 25°C which accounted for 19.0 grams of working fluid with the final weight of the methanol-RHP measuring 1247.0 grams.

3.1.2 HSRHP

History on initial version: Initially an 18 in. long (nominal length between bearing support centers), 1 in. O.D., 0.75 in. I.D. hardware with 5 in. fill-tube was fabricated out of

SS316 bar stock. The parts fabrication drawings are shown in Figures 15-17. This version was merely an extension of the LSRHP in thermal design point of view and was not rigorously analyzed for its dynamic stiffness. Support bearing stiffness details, balancing criticality, machining run-out tolerances in terms of the internal taper and external diameter, etc., were not clearly understood at that time of the development. A practical way of experiencing the overall picture of the dynamics, vibration and critical speed was to test a hardware. Hence, this initial long version was fabricated and spin-tested without any heating or cooling loads on the high speed test rig assembled for that purpose. The axial pre-load on the bearings was 35 lbs. This testing turned out to be an important learning experience and eye-opener on several issues. The speed was incremented in steps of 500 rpm and everything appeared normal up to 13,500 rpm. The next step increase brought disaster. The fill-tube simply curled up due to a whipping action and damaged the mist-lube nozzle to the bearing. The fill tube was shortened to 2.5 in. and the spin-test was resumed later with 100 rpm step increase. The increase from 14,400 to 14,500 rpm generated a loud resonant noise and within fractions of a second, the test crashed. Inspection revealed that the main tube got bent like a bow and the fill tube end bearing broke apart. Luckily, there was no major equipment damage or any personnel injury as the test was remotely controlled for safety.

Subsequently, a rigorous analysis of the rotor dynamics was initiated and a conservative design approach incorporating adequate factor-of-safety was followed in all aspects. The original ambitious goal of 60,000 rpm was dropped to a conservative 30,000 rpm and the high heat transport capacity of 3.5 kW requirement was scaled down to 2 kW and less. The following 10 in. nominal length, short and modified HSRHP unit evolved.

Short modified version: Two identical sets of the HSRHP hardware were fabricated - one for water and the other for methanol filling. As before, SS316 bar stock and SS304 fill tube were used. The end-caps, and the fill-tube were of similar design as the LSRHP. The fabrication drawings in Figure 18 (a-d) show the dimensions, weld and finish details. The cleaning of RHP parts after machining was done as described here.

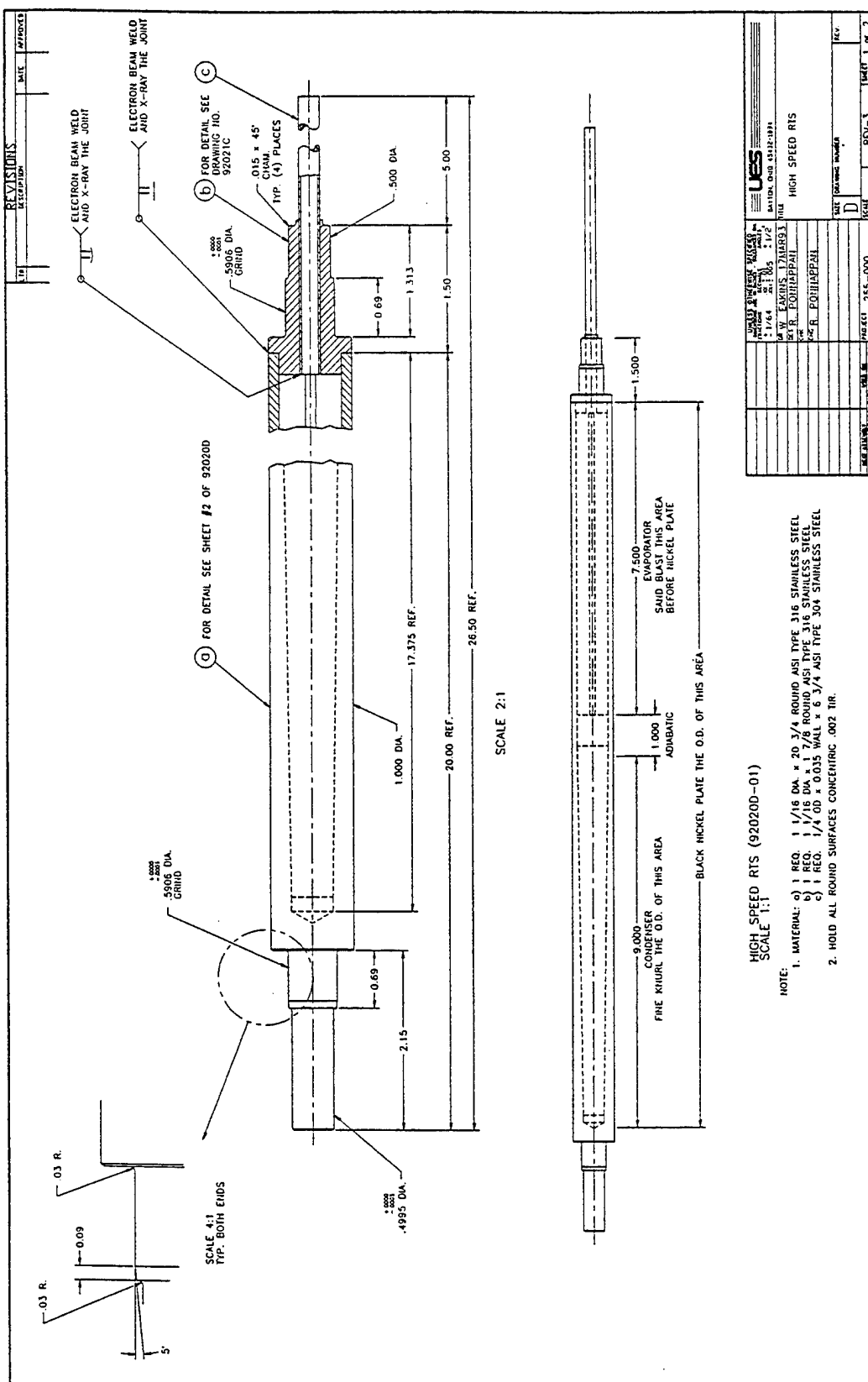


Figure 15. Fabrication Drawing of the First HSRHP Unit - Assembly.

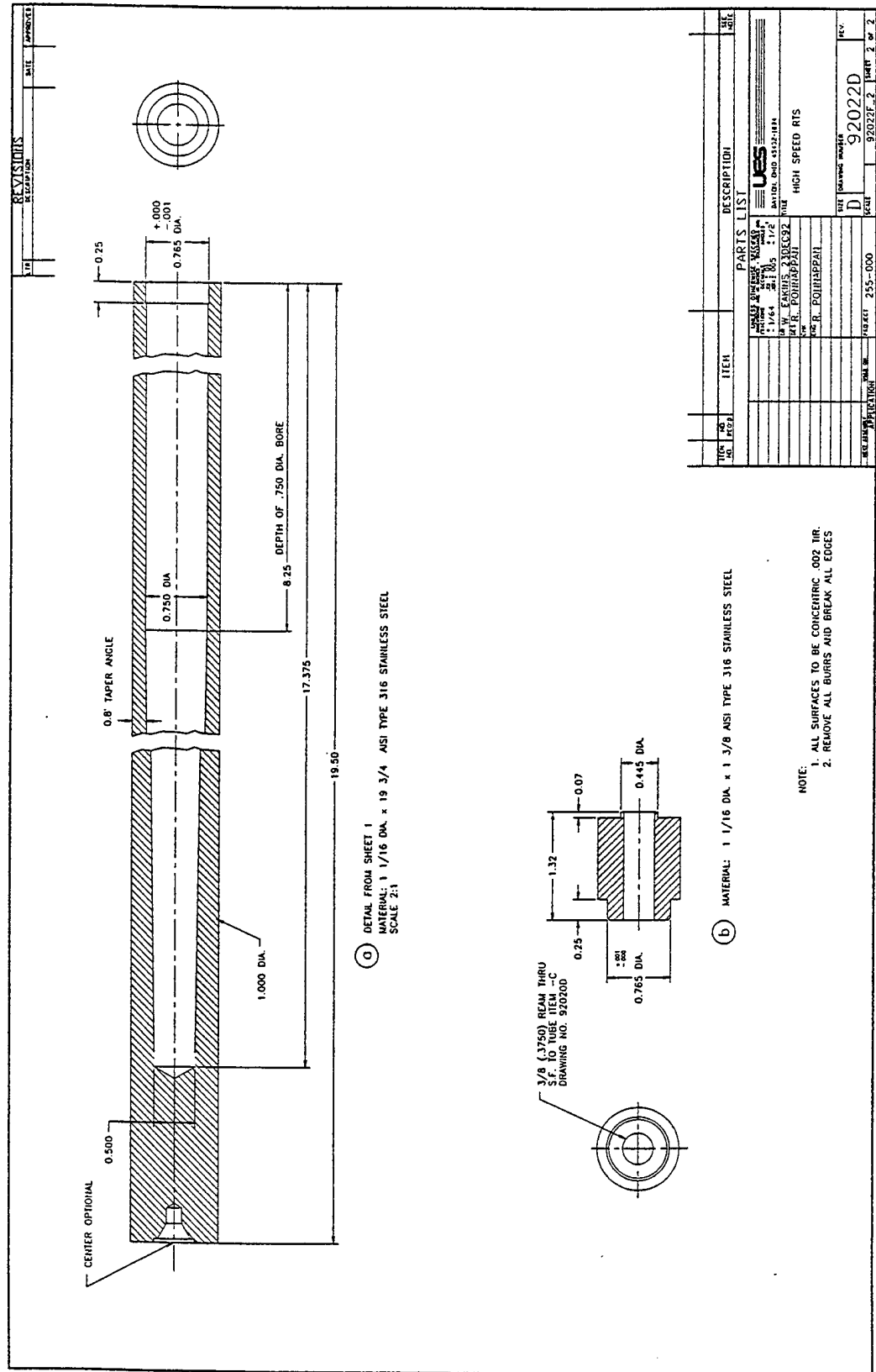


Figure 16. Fabrication Drawing of the First HSRHP Unit - Taper Tube.

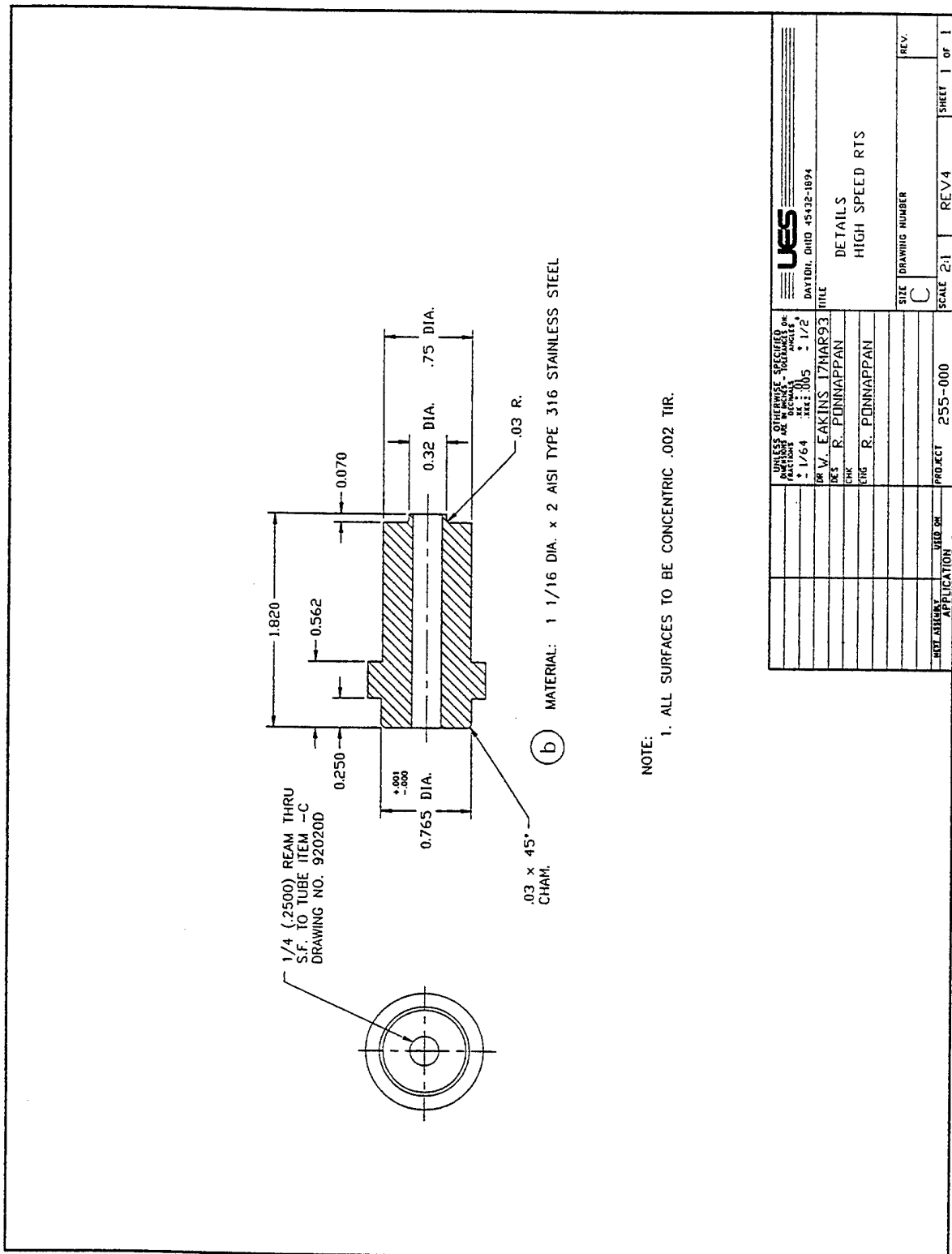


Figure 17. Fabrication Drawing of the First HSRHP Unit - End-caps.

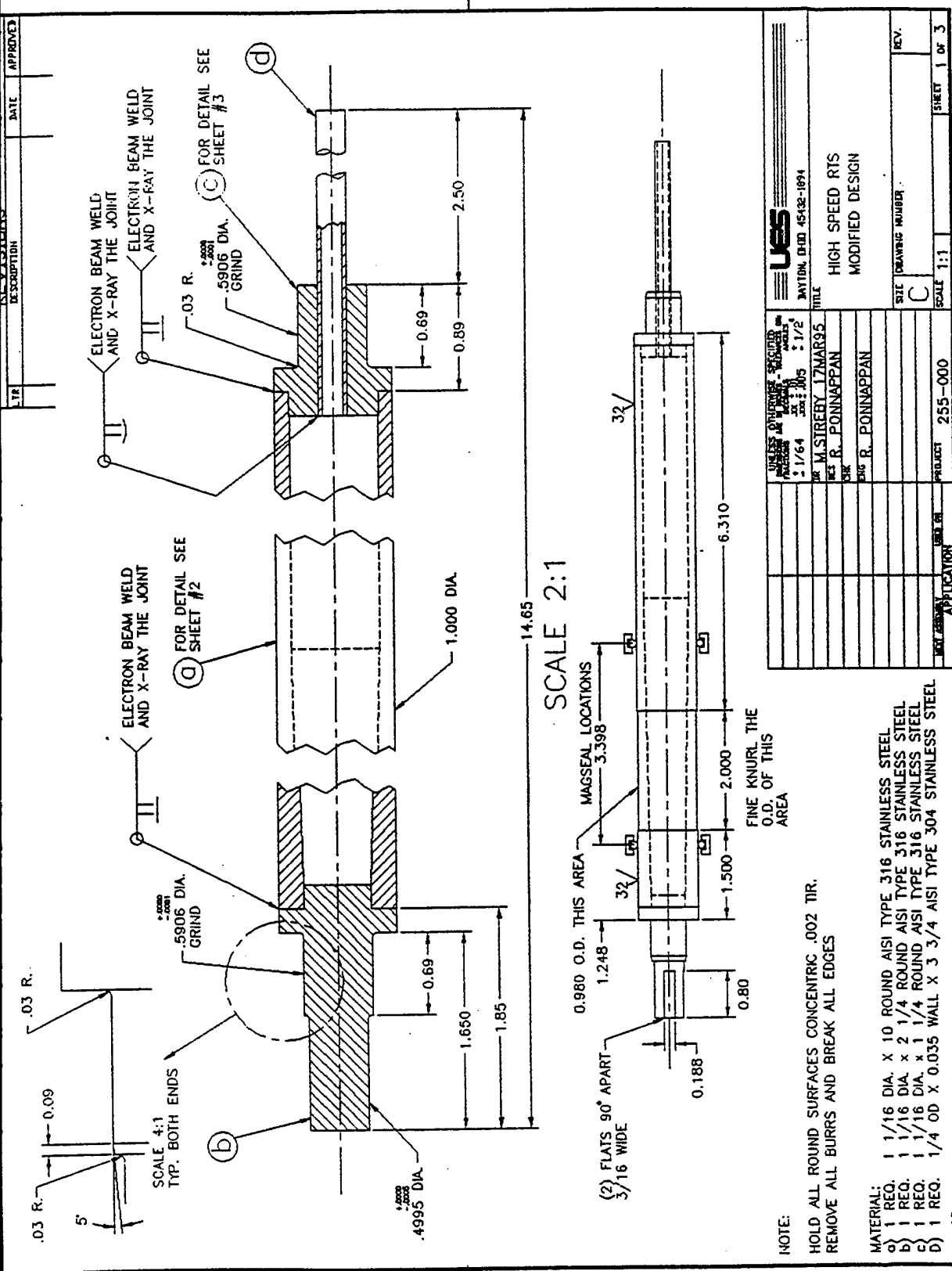


Figure 18a. Fabrication Drawing of the Modified HSRHP - Overall Details.

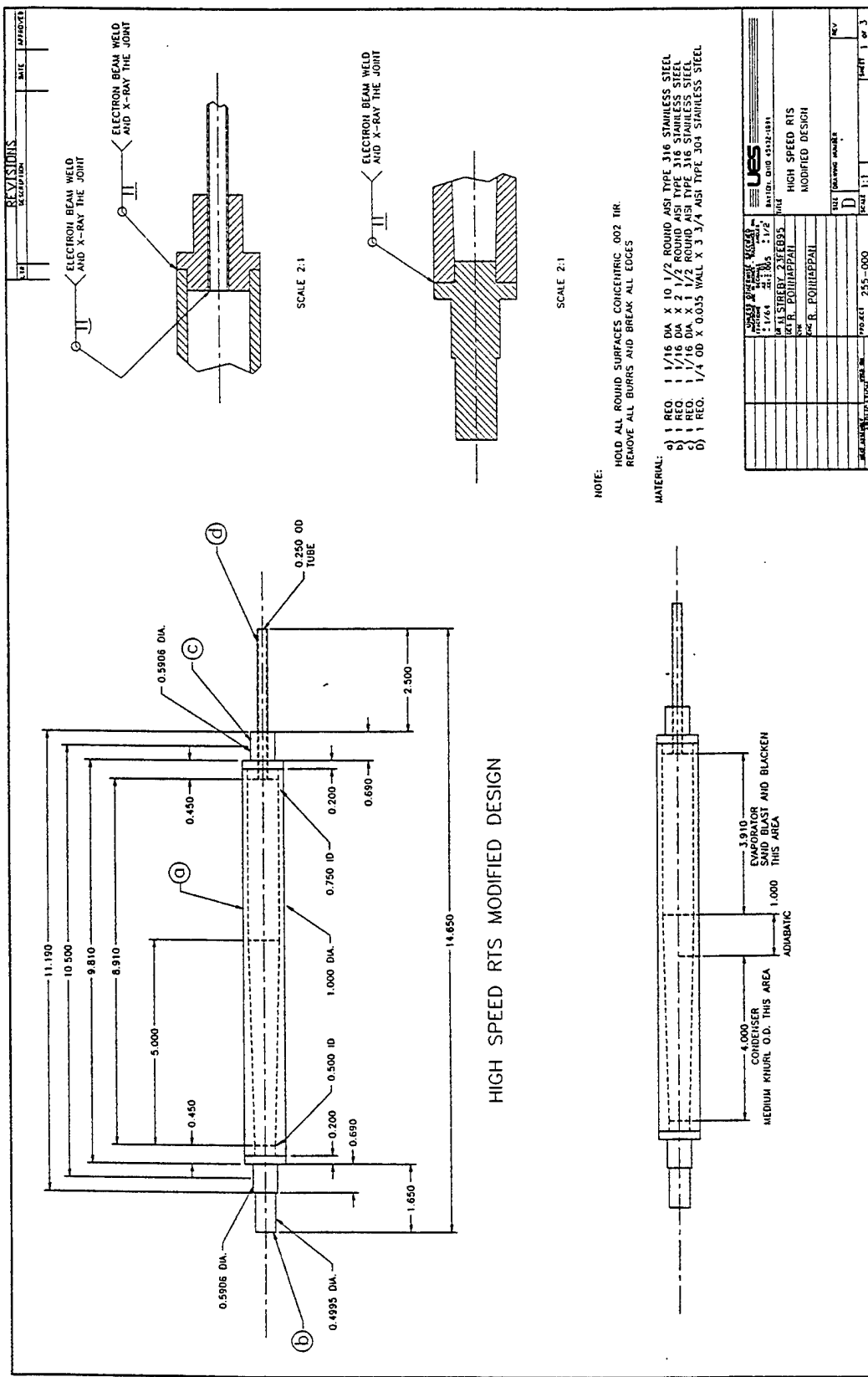


Figure 18b. Fabrication Drawing of the Modified HSRHP - Assembly.

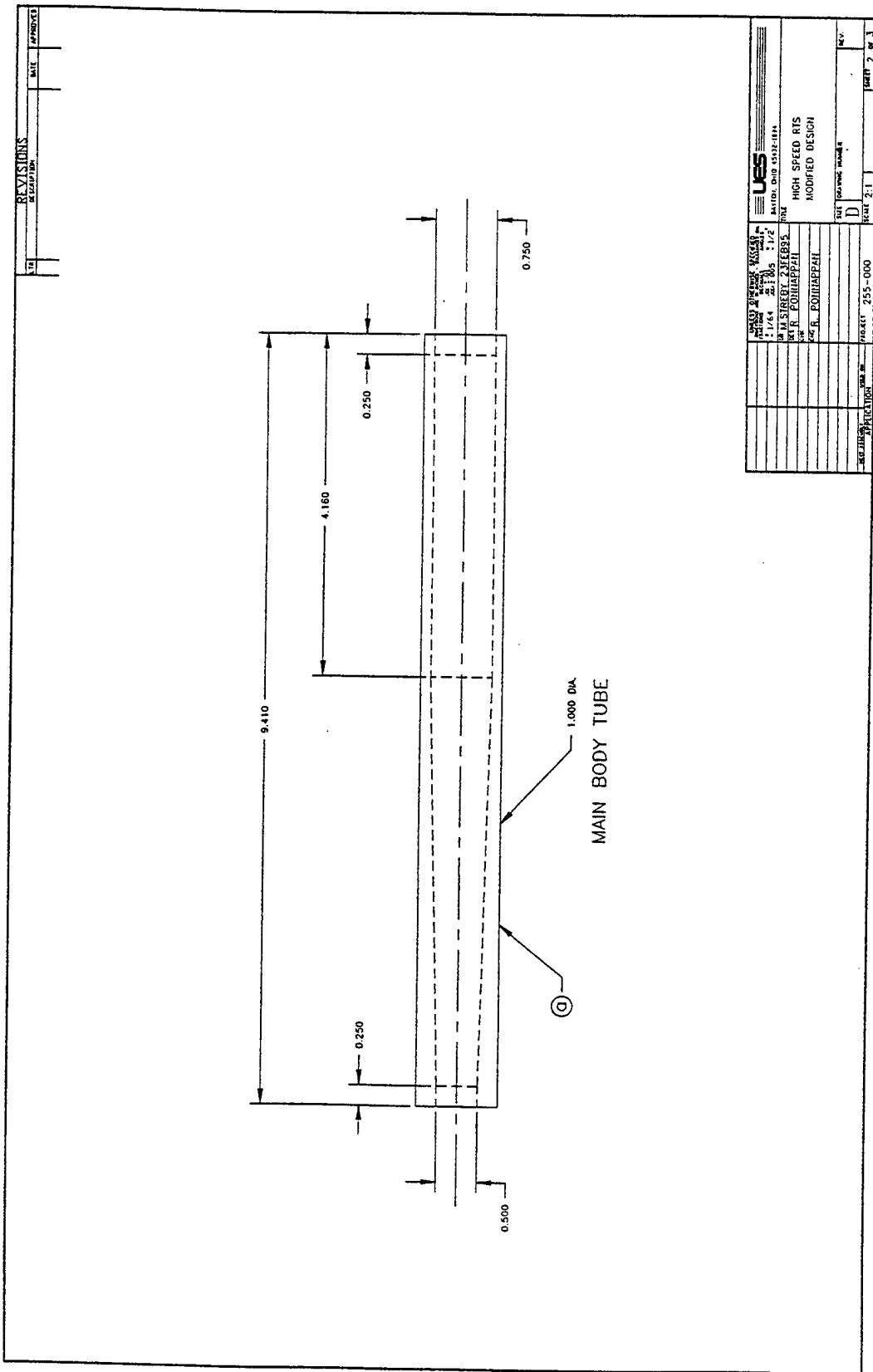


Figure 18c. Fabrication Drawing of the Modified HSRHP - Taper Tube.

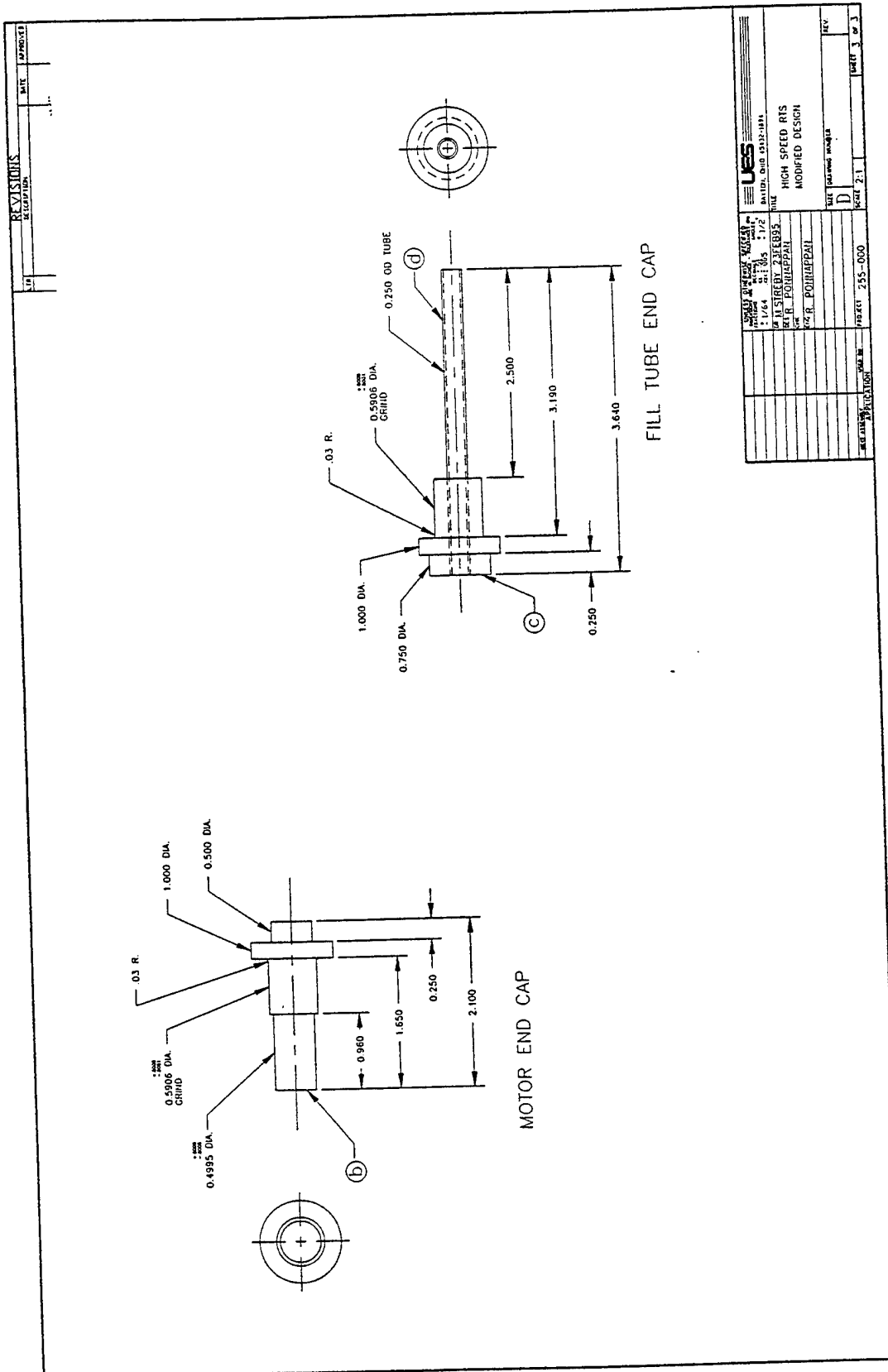


Figure 18d. Fabrication Drawing of the Modified HSRHP - End-caps.

Cleaning Procedure for Heat Pipe Parts made of Stainless Steel

1. Rough-clean machined parts by vapor degreasing in trichloroethylene or equivalent degreasing agent to remove oil, grease and scales.
2. Scrub with metal wire brush, if necessary, to clean tough stains.
3. Thorough clean using the following procedure:
 - a) Immerse in OAKITE Deoxidizer SS solution (50% dilute) for 20 minutes.
This solution contains:

Nitric Acid	20-30% by weight
Hydrofluoric Acid	10% by weight
 - b) Rinse in demineralized or deionized water.
 - c) Dry with clean filtered air.
 - d) Rinse with anhydrous isopropyl alcohol.
 - e) Force dry with clean filtered dry nitrogen heated to 160°F (70°C)
or
If unit is to be used in conjunction with water, place in electric furnace and heat in air to 400°C for one hour.
4. Cap pipe ends and place in clean plastic bags.
5. Use powder-free clean gloves to handle cleaned parts.

The joining process used this time was EB-welding as opposed to TIG welding used before. This was to ensure good weld-penetration to provide strength. End-cap welding to the main tube was done with slightly larger (about 1/8 in.) diameter parts and after welding, the whole assembly was machined to final size taking the reference from previous stage machining operation. This ensured the axis of the tube to be the same as those of the bearing journals. A total indicated reading (TIR) tolerance of 0.002 in. was imposed to accomplish concentricity of round surfaces. Figure 19 shows the photograph of one of the two finished HSRHP units.

Filling and sealing: The working fluid filling process was the same as that of the LSRHP described earlier except one improvement made for the crimp-seal process. A trial dry-crimping process was practiced using simulated test piece of plumbing, vacuum gauge and fittings. The

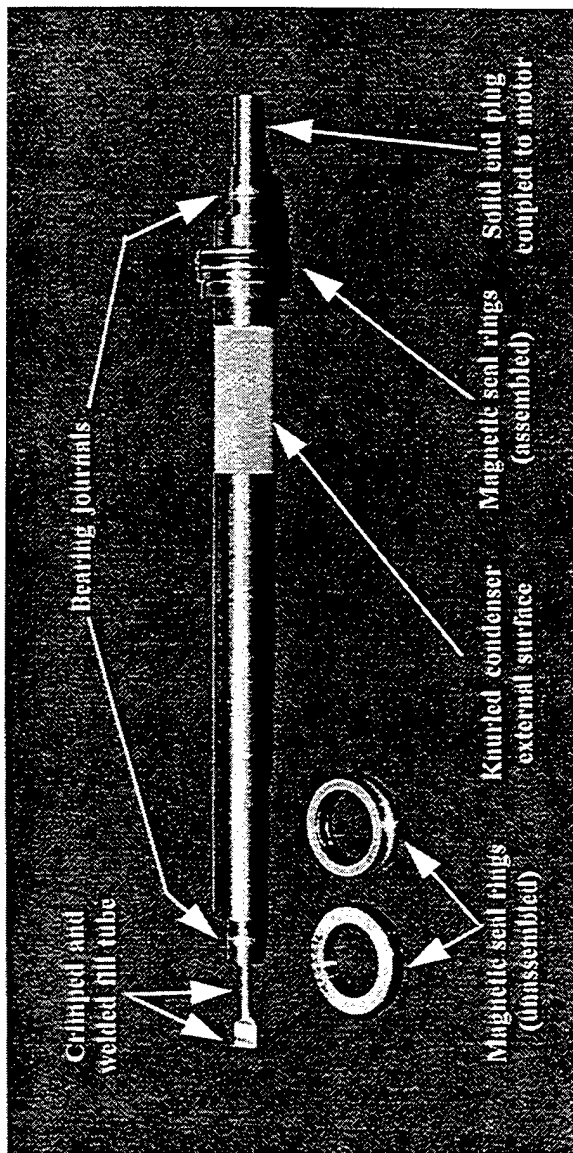


Figure 19. Photographic View of the HSRHP with Mage Seal Ring.

exact amount of tightening torque needed to completely press the 1/4 in dia. × 0.035 in. wall SS304 tube over 1/2 in. length was measured with a torque-wrench. The leak-tightness and vacuum holding-pressure were checked with air bubble test in water and with vacuum gauge, respectively. Two pairs of 1/2 in. wide crimp-bars were used side-by-side. Both crimps were applied right after the required amount of fluid had been transferred to the RHP and before the RHP was removed from the fill station and taken to the welding station. The inner crimp tool was held in place while the outer tool was removed in order to saw-cut the flattened fill tube and TIG weld the exposed tip to seal permanently. Then the inner crimp tool was removed.

The two HSRHP units were filled one after the other and the details of the process-log are summarized for reference in Table 8.

3.1.3 Dynamic Balancing

The balancing requirement for the RHPs was set to limit the CG shift to less than 20 micro-inch which translated to limiting the dynamic unbalance to within 0.0002 ounce inch. After final machining, the RHPs were balanced in a horizontal balancing machine up to 3500 rpm at the Dayton Balancing Co., Inc. Corrections were done by removing material from the wall of the RHP by grinding. Balancing at higher speeds could not be done as there are no facilities available. The RHPs were checked for balance again after filling the working fluids. The results of the balancing measurement and corrections are provided in Table 9. The balance readings below 1500 rpm were unstable, possible due to the fluid sloshing inside the pipe.

3.1.4 External Surface Finish

Unique surface finish requirements were necessary for various operational functions. The bearing journals were ground to -0.0001/+ 0.0000 in. tolerance for perfect assembly with the precision high speed ceramic ball bearings. The magnetic seal o-rings required a sand-blasted surface with average roughness range between 32 and 63 μ in. This was critical to fit the viton o-rings on the RHP in order to maintain the leak tightness and to overcome the frictional torque

Table 8. HSRHP - Filling Process-log Summary

Process Details	Methanol HSRHP	Water HSRHP
Measurements before filling:		
Fill tube length, inch	2-5/8	2-5/8
Internal volume of main tube, cm ³	57.5	57.5
Fill tube volume, cm ³	1.6	1.6
Empty RHP weight, g	616.2	617.3
Empty pipe after dynamic balancing, g	614.5	616.4
Vacuum baking duration, dates	9/13/95 - 9/19/95	9/19/95 - 9/26/95
Baking temperature, °C	340	340
Vacuum level, torr	2.6×10^{-7}	4.2×10^{-7}
Fill volume at 25 °C, cm ³	7.2	12
Weight after filling, g	620.2	626.9
Actual inventory, g	5.7	10.5
Estimated uniform film thickness at 25 °C, mm	0.56	0.81
Fill volume at 25 °C, %	12.6	18.32
Crimp torque, ft. lb.	40	40
Temp. of RHP while crimping, °C	80	100
Fill tube length after crimping and welding, in.	1-1/4	1-1/4

Table 9. Balancing Data of the RHPs at 3500 rpm

Description	RHP ID	Unbalance, Ounce Inch	
		Solid End	Fill Tube End
<u>Before Filling:</u>			
a) Initial unbalance	water	0.015	0.007
	methanol	0.004	0.006
b) Final residual unbalance after correction	water	0.00007	0.0002
	methanol	0.0002	0.0001
<u>After Filling:</u>			
Residual unbalance uncorrected	water	0.0002	0.002
	methanol	0.0018	0.0009

of the rubbing contact between the face-seal rings. The heat transfer surface in the condenser section was knurled for enhancing heat transfer during spray cooling. The infrared temperature sensing target spots were supposed to have high emissivity value ($\epsilon > 0.9$). The LSRHP was black painted for this purpose. But, the paint got scratched easily or application of the paint in the assembled set up was difficult and caused contamination of other equipment. Hence, it was decided to black-oxide coat the HSRHP units. This was accomplished by a proprietary blackening process done at Rite-Way Black & Deburr, Inc., Dayton. This process involved acid etch and caustic dipping at 250°F followed by water and oil rinses. It produced a thin (~10 μm) layer of black oxide on the surface.

3.2 TEST SET UP

3.2.1 Overall System Description

A schematic diagram of the test-setup used in testing the LSRHPs is given in Figure 20(a) and that of the HSRHPs is given in Figure 20(b). This is comprised of several subsystems, namely, induction heating coil and RF source, mist cooling chamber, high-speed drive-motor system, infrared sensor and actuator, computer-based data acquisition system,

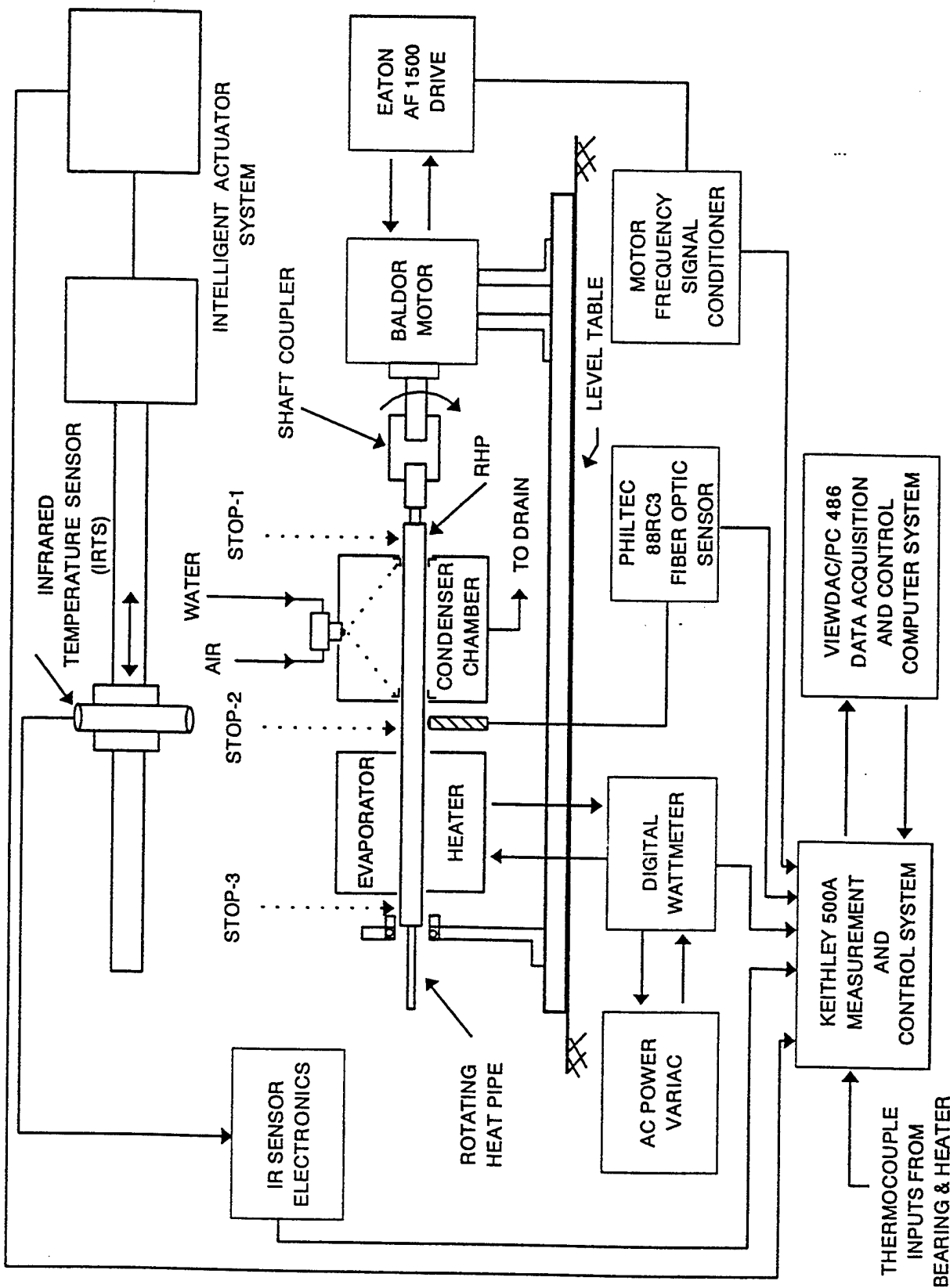


Figure 20(a). Schematic Diagram of the Experimental Setup - LSRHP.

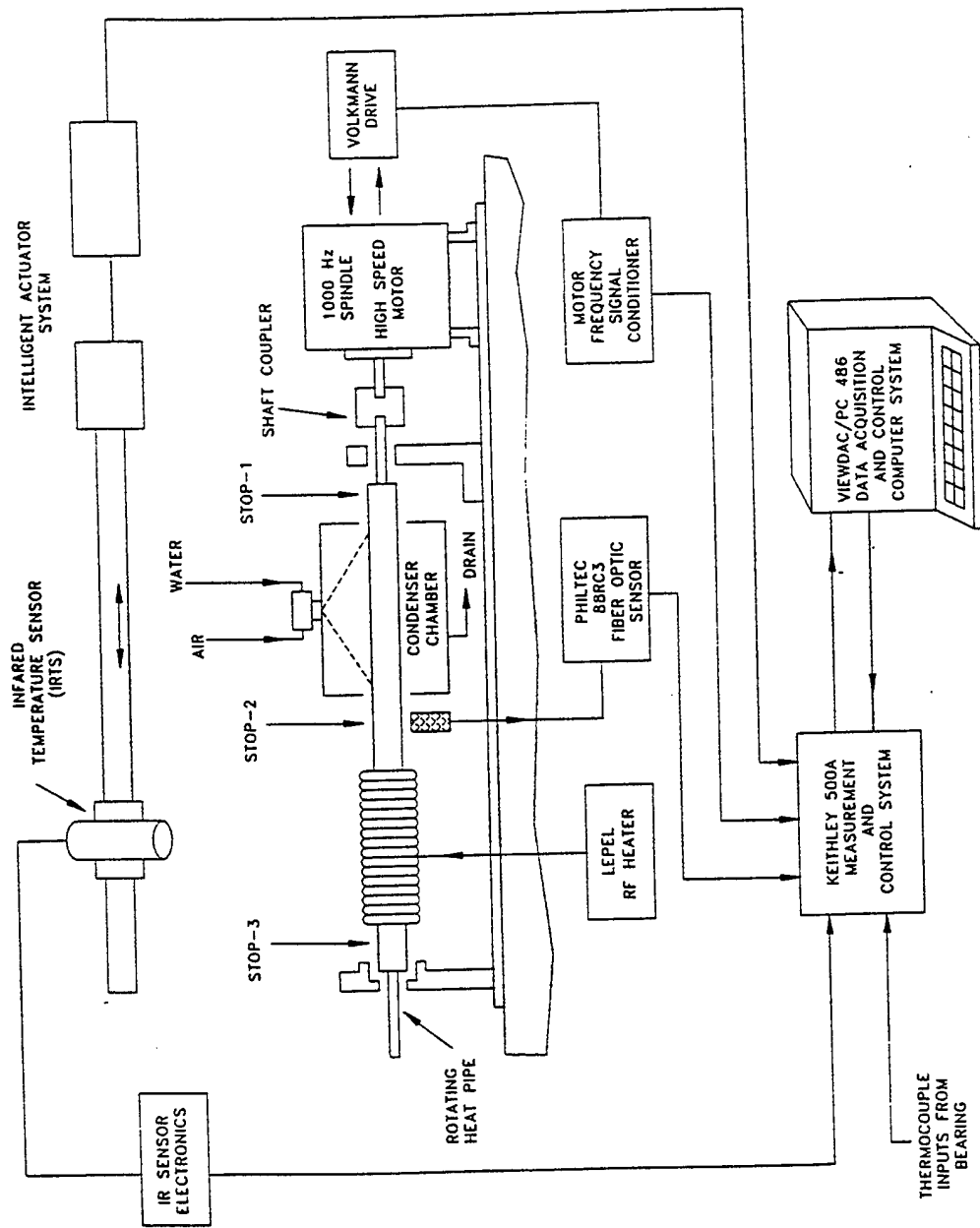


Figure 20(b). Schematic Diagram of the Experimental Setup - HSRHP.

vibration sensor and safety interlocks. The RHP can be spun about its longitudinal axis at any speed up to 60,000 rpm by controlling the variable frequency input of the motor-drive. A calibrated setting of the RF heater power can generate the desired heat load on the RHP evaporator. The condenser section can be set up, to be cooled by either air-water mist or air-jet only or oil-spray cooling mode. The external wall temperature of the RHP can be measured at three exposed sections as indicated by the IR sensor stop-position marked in Figure 20. The IR sensor has a target spot size of 3.8 mm diameter circle and $\pm 0.5^{\circ}\text{C}$ accuracy in 0-400°C and it was calibrated using a stationary black-body type source. A computer-controlled intelligent actuator traverses this sensor along the RHP within a distance of 15 cm. The data acquisition software used is VIEWDAC. A fiber-optic displacement sensor is positioned at the midpoint of the RHP to monitor and safeguard against excessive vibration. The RF and high speed equipment are located in a separate room away from operating personnel and control instrumentation for safety reasons and closed-circuit TV is used for viewing the tests while operating.

Photographic views of the set up in the LSRHP testing configuration are shown in Figures 21 and 22. Figure 23 shows the photograph of the new and additional hardware (including the cooling chamber, RF coil, spray nozzles, magseals, etc.) procured for the HSRHP testing. Appendix B shows the drawings of the test rig comprising 48 items such as the motor mount, base-plate, bearing supports, shaft coupler, etc.

All the performance tests on both water and methanol RHPs were conducted on horizontal orientation and on-axis rotation mode under steady state conditions of the test parameters (Tables 5 and 7). The tests were started typically by spinning the RHP initially at 3000 rpm, followed by the applications of the desired heat input to the evaporator and subsequently increasing the speed in steps to the maximum level possible. At every step, steady state readings of temperature, flow rate and power input were recorded. It took approximately 30 minutes for every step. The condenser cooling rate was controlled by regulating the air or water flow rate to the single fan-spray air-atomizer nozzle for the case of LSRHP testing and a calorimetric measurement of the condenser heat transfer was impossible in the present setup.

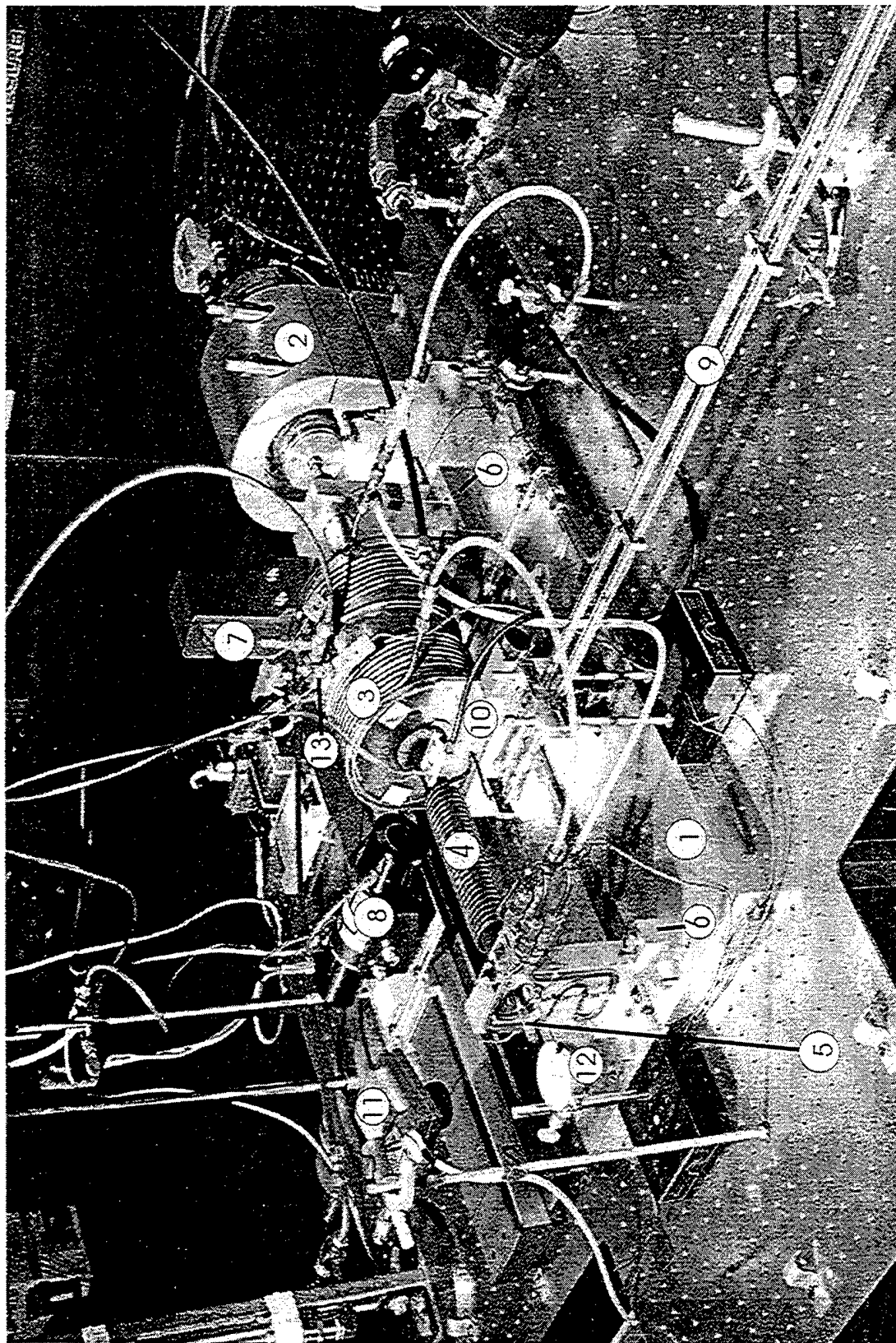


Figure 21. Photograph of the RHP Test Setup.

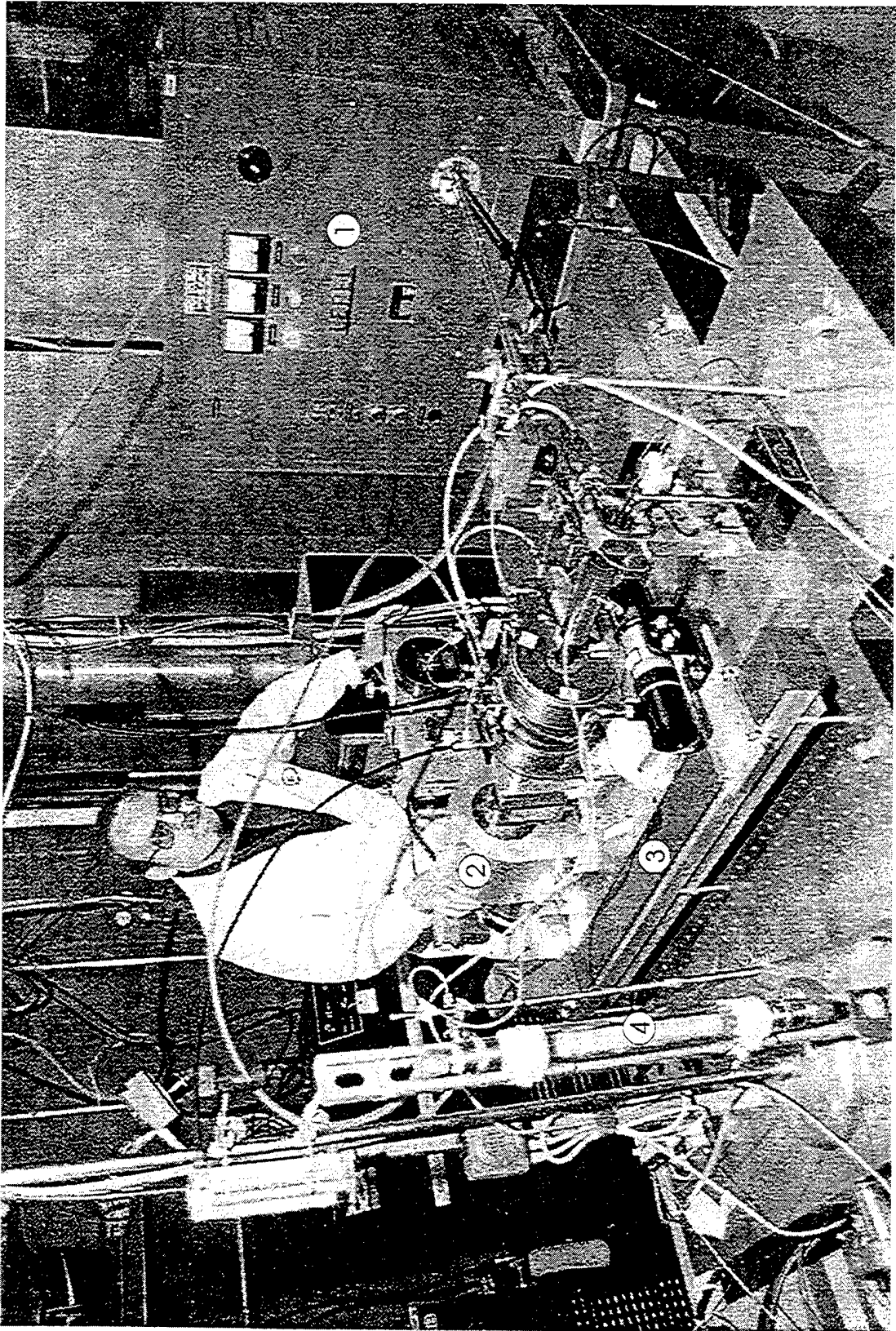


Figure 22. Photograph of the Setup with Induction Heater in the Background.

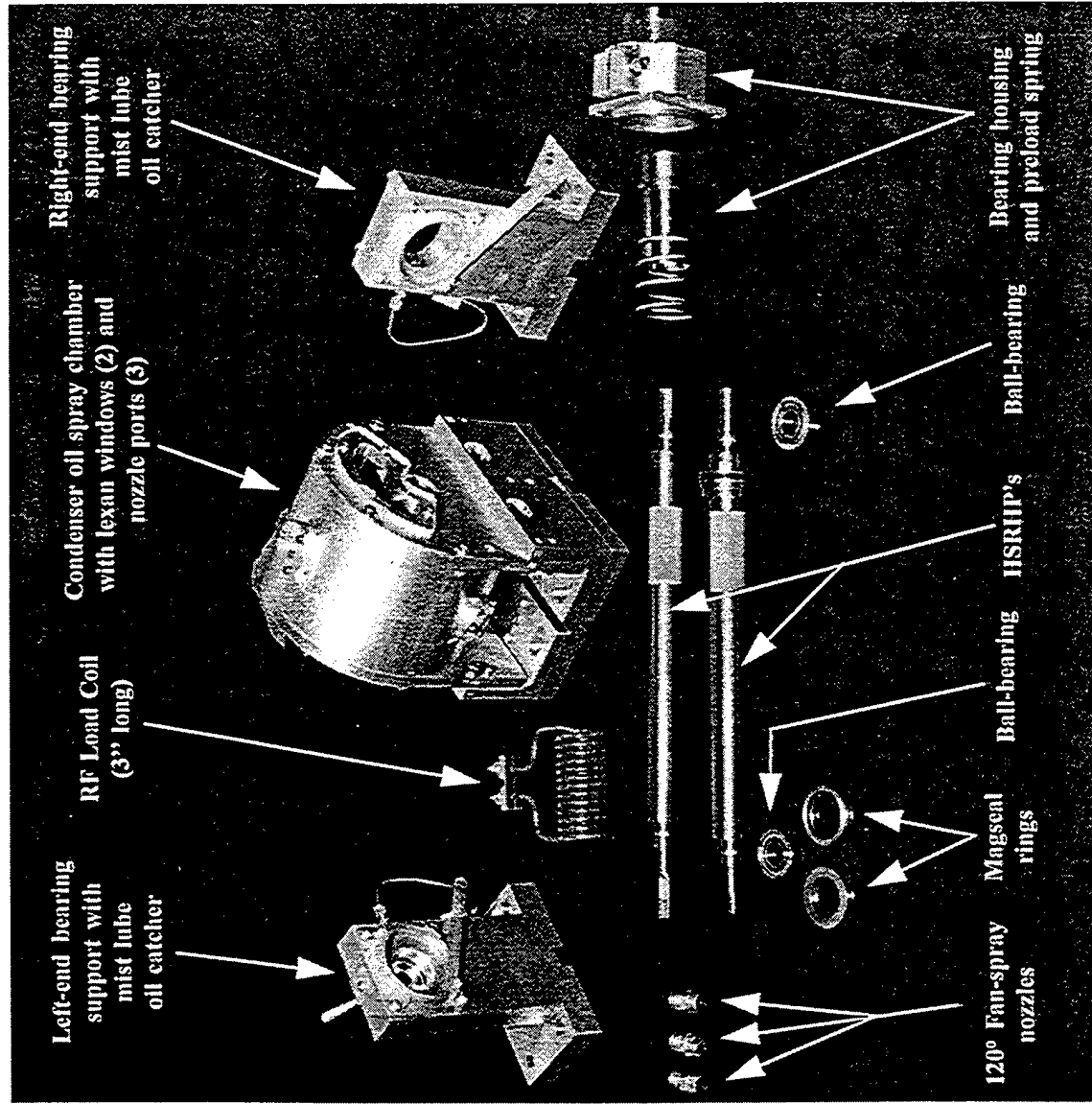


Figure 23. Photograph of the HSRHP Units and Parts of the Setup.

In the case of HSRHP testing, the condenser cooling was controlled by regulating the oil flow rate to the three nozzles mounted on the chamber and a calorimetric measurement was possible in this setup. However, the heat input to the evaporator in terms of the power transported through the evaporator stainless steel wall was precisely calibrated using a calorimetric measurement on the RF load coil as described in Section 3.2.3.

3.2.2 Drive and Mechanical Support System

The torque requirement for the motor was calculated based on the inertia of the RHP. Appendix C shows this detail.

Motor: The high speed spindle (motor-drive) specifications are as follows:

Manufacturer	:	FAG, Germany
Supplier	:	Pope Corporation, Haverhill, MA, USA
Style No.	:	M17-60/5
Serial No.	:	161844/099
Horsepower	:	6.71; kW: 5.0; kVA: 8.0
Current	:	13.2 amp
Voltage	:	350
Frequency	:	0-1000 Hz
Enclosure	:	TELC
Cooling/Lube	:	Oil-mist for bearing lubrication; circulating water coolant for stator winding 3-5 lpm; thermistor controlled high temperature cut-out. Oil-mist: 7808 oil - 22 centistoke; 60-80 drops/minute - 22 psig
Overall Unit Length	:	24.3 cm
Overall Diameter	:	12.0 cm
Shaft Extension	:	1/2 in. dia. × 2 in. long; right-hand thread assembly to rotor shaft

An input frequency controlled electronic-drive control system is used to control the motor. The specifications are as follows:

Model	:	Volkman 9000-94010 series digital adjustable speed AC drive
Input Volts	:	460 VAC; 60 Hz
Rated Power	:	13.5 kVA

Output : 0-460 V; 0-1000 Hz 3 phase
Option : 66% dynamic braking using resistor bank
Installed

High Speed Bearing:

Barden ceramic ball bearing type CM102HX26R; angular contact; axial preloading necessary; DN=10⁶. SS compression spring with k=63.4 lb/in. is used for preloading.

Flexible Coupling:

Thomas miniature flexible disc

Style : CB
Size : 37
Speed : 55,000 rpm
Weight : 2.11 oz.
Bore : 0.5005 in.
Torque : 19 in./lb
Material : Aluminum body, brass pins, SS discs

Mist-lube system:

Manufacturer : Norgren
Model No. : 10-015-004
1 quart 19 oz. reservoir
8-132 bearing inches
79°C; 250 psig inlet air pressure

3.2.3 Heating System

Nichrome Heater: In the beginning of this research effort, nichrome heater was used to heat the evaporator by radiation mode. An Inconel sheathed heater with 1000°C maximum operating temperature was chosen. The heat flux and possible heat reception calculation for a concentric geometry are given here.

$$\begin{aligned}\text{Required heating load} &= 3500 \text{ W} \\ \text{Evaporator area} &= \pi dl = \pi \times 2.54 \times 18.3 = 145.9 \text{ cm}^2\end{aligned}$$

$$\text{Heat flux required} = 3500/145.9 = 24 \text{ W/cm}^2$$

Radiation power reception for a concentric geometry,

$$\begin{aligned} Q_R &= F_{SC} A \alpha \sigma (T_s^4 - T_c^4) \\ &\approx 1 \times 145.9 \times 0.9 \times 5.67 \times 10^{-12} (1273^4 - 473^4) \\ &\approx 1918 \text{ W} \end{aligned}$$

$$\text{Heat flux possible} = 1918/145.9 = 13.1 \text{ W/cm}^2$$

For full load testing, alternate heating methods may be employed.

For the LSRHP initial round of tests, a heater with the following design was fabricated and used.

Nichrome Heater Design for LSRHP:

Heater wire type	:	Inconel sheathed; ARI supplied single core Nichrome
		1/8" sheath diameter
		0.8 ohm/ft.; 982°C max. temp. (1255 K)
Wrap dia. (mean dia.)	:	1-1/2 + 1/8 = 1-5/8"
Length per turn	:	$\pi \times 1-5/8$
Length of heater coil		
(helical close coiled)	:	7"
Diameter of coil	:	1.5" I.D.; 1.75" O.D.
Total cable length	:	$\pi \times 1-5/8 \times 56 = 285.9" = 23.8 \text{ ft.}$
Resistance at room temp.	:	$23.8 \times 0.8 = 19.06 \text{ ohms}$
Power supply	:	240 VAC
Max. power possible	:	$\frac{V^2}{R} = \frac{240^2}{19.06} = 3022 \text{ W}$
Max. current	:	$\frac{V}{R} = \frac{240}{19.06} = 12.6 \text{ amp}$

RF Heating System: Because of the poor heat transfer coupling between the nichrome heater and the RHP evaporator, it was decided to use an induction heating system. This

necessitated the manufacture of load-coils and calibrating them in conjunction with the RF heater unit for use in RHP testing.

The specifications of the RF heater unit are:

Model	:	LEPEL T-5-3-KC-BW
Serial No.	:	8710-J
Type	:	T-504-346-2
Output	:	5 kW (max.); 200-400 kHz RF tube oscillator with solid state rectifier
Input	:	12.7 kVA; 460 VAC; 3 phase; 60 Hz

Two copper load coils were fabricated - one was 6 in. long and the other was 3 in. long - in order to be used for the longer version LSRHP and the short version HSRHP, respectively.

The physical dimensions of the coils are as follows:

	<u>6" Coil</u>	<u>3" Coil</u>
Coil diameter (I.D.)	1-1/2 in.	1-1/4 in.
Coil length	6 in.	3 in.
Number of turns	16	13
Copper tube dia.	1/4 in.	3/16 in.
Pitch of coil	3/8 in.	1/4 in.
Length of tube	8 ft.	5 ft.

The coils were painted with glyptal for electrical insulation between turns. A 4 ft. long extension conductor-pair made of 1/4 in. diameter copper tube connected the load-coil to the RF unit. Figure 24 shows the drawing of the 6 in. coil design and the 3 in. coil is similar to this design except the dimensions.

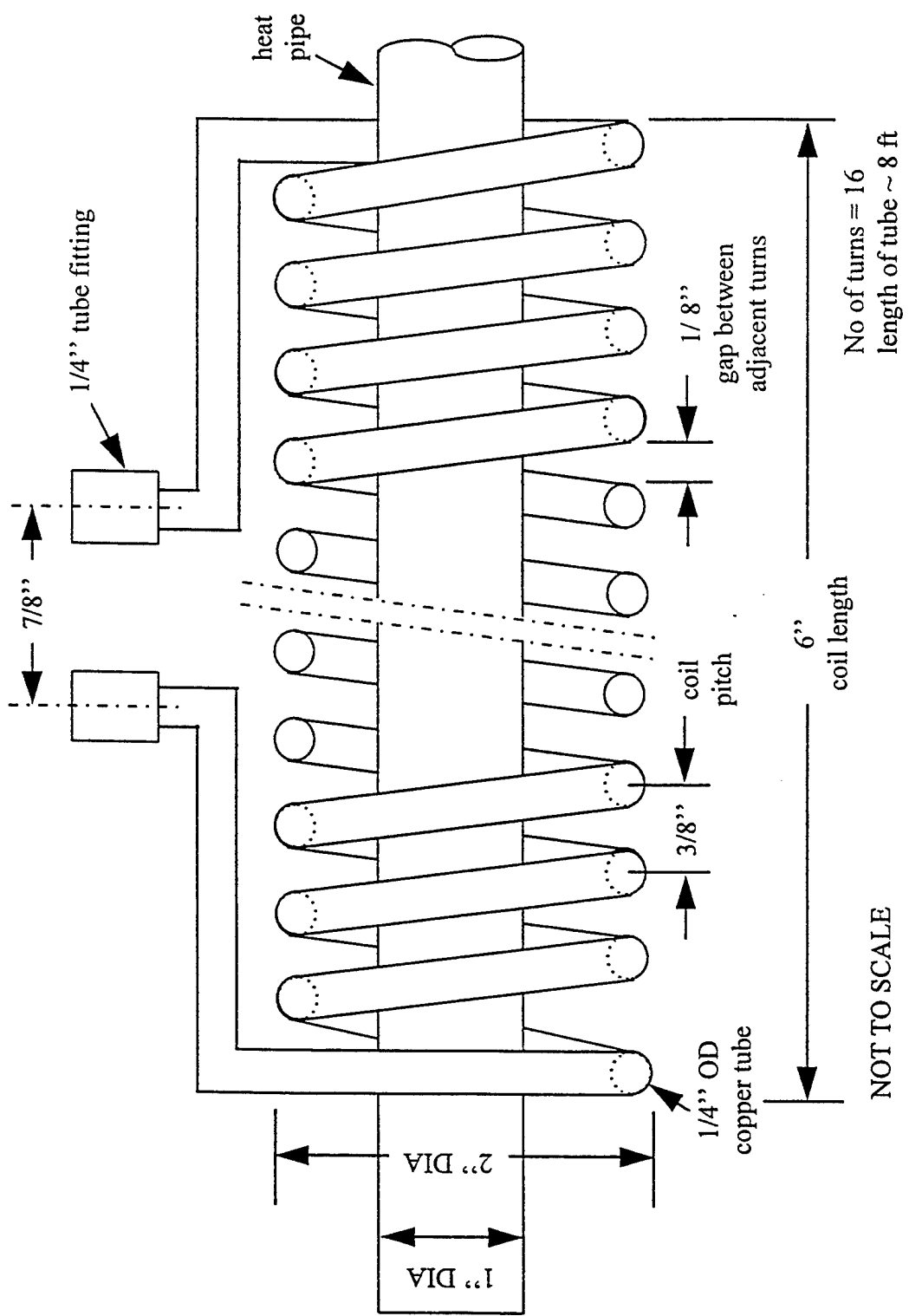


Figure 24. RF Load-Coil Design (6 in. Coil).

Evaporator Heat Input Calibration: The property of self-heating of steel materials by eddy currents when placed in the core of an RF load coil was effectively used here. A 15 cm long, 3.8 cm ID helical coil with 16 turns made of 0.6 cm diameter copper tube was fabricated. A stainless steel-316 tube, machined to the same dimension as the RHP was kept inside the RF coil as the load. A non-inductive flow-swirler was kept inside the pipe for improved flow mixing. Circulating water from a temperature controlled bath was pumped through the load-tube. The RF unit along with the load coil was tuned at 395 kHz and power was applied through the coil by setting the signal current in the potentiometer to the desired level. By measuring the water flow rate and rise in temperature precisely, heat generation rate in the wall of the load-tube was determined. Heat loss from the outer surface of the load-tube would not affect the calorimetry because we are interested only in the amount of heat carried by the water. Hence, the heat input measurement in RHP tests directly represents the transported heat from the evaporator down to the condenser. A schematic diagram of this calibration setup is shown in Figure 25(a) and the calibration curve in terms of the heat generation on RHP vs. the power control voltage of the Lepel unit is given in Figure 25(b).

Uncertainty Analysis for RF Power Calibration: Based on the combined type K thermocouple and Fluke 2280 datalogger temperature measurement accuracy of $\pm 0.3^\circ\text{C}$, the RF power calibration is accurate to ± 5 to 24% in the range of operation 2500 to 250 W, respectively. The uncertainty increased as the power level decreased. Appendix E provides the details of the uncertainty analysis.

3.2.4 Cooling System

One of the most important pieces of data needed from a RHP is its ability to transport heat. To accurately measure the heat removed from the condenser, several methods have been investigated and tried. Three major problems to calorimetry are:

- 1) Temperature measurements on a high speed rotating surface that is obscured by coolant mist and a fluid film proved difficult.

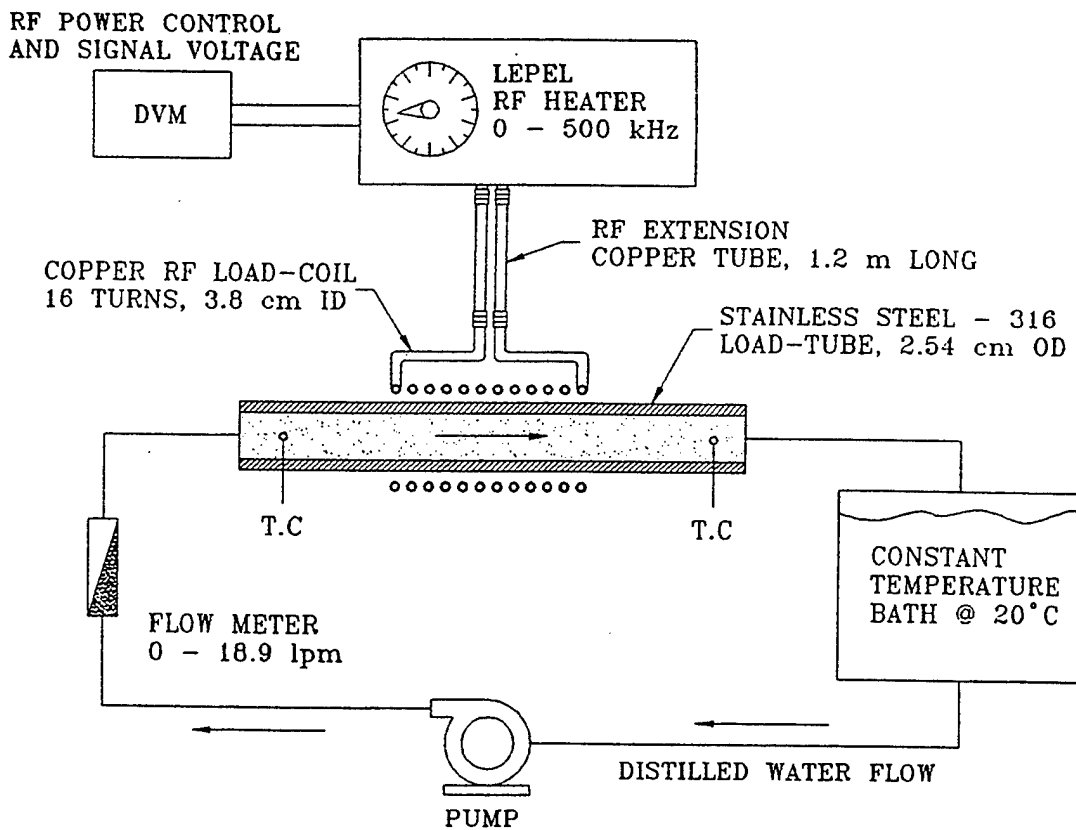


Figure 25(a). RF Load-coil Calibration Equipment Layout.

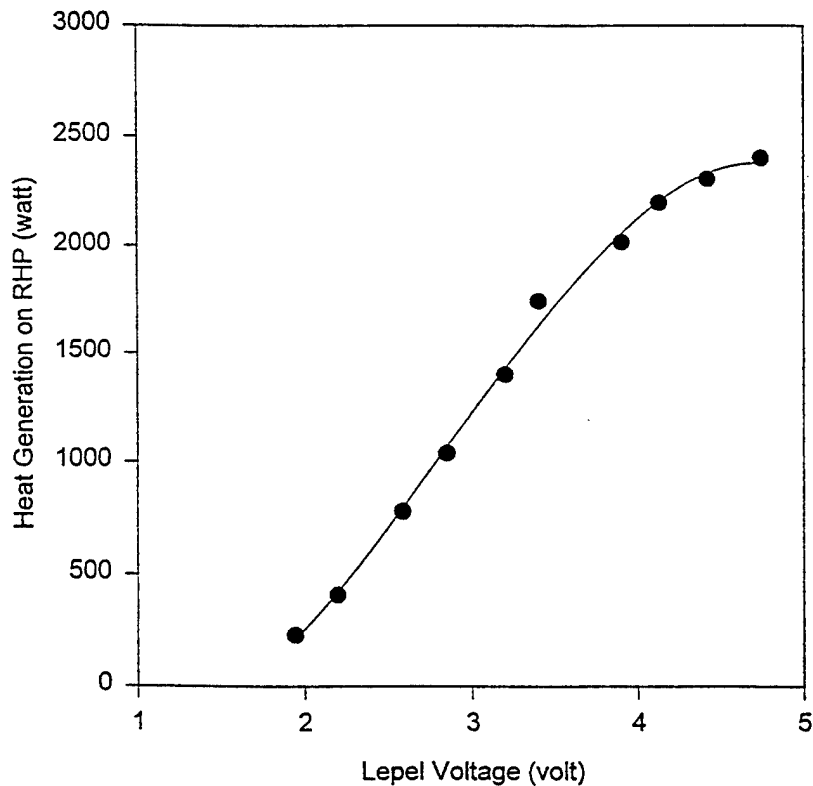


Figure 25(b). Heat Generation on RHP vs. RF Power Control Voltage.

- 2) Phase change of liquid to vapor can efficiently remove heat but vapor leaks through poor shaft seals.
- 3) Gas and liquid-tight rotating seals have high friction which can add unaccounted heat to the RHP. Our criteria for good calorimetry were to use a single fluid with no interaction with outside environment, low friction magnetic shaft seals and an insulated cooling chamber.

Oil-spray Cooling: To minimize weight and simplify integration to aircraft systems, cooling of electrical machines is best achieved by using existing aircraft fluids. To examine the cooling performance of actual aircraft fluids, such as turbine fuel (JP-8) and oils (MIL-7808), the condenser section of the high speed RHP may be spray-cooled with these fluids. In the present setup, 7808 oil is used and the cooling is accomplished by three spray jets impinging on the knurled condenser surface. Measurements of coolant flow, inlet and outlet temperatures provide heat transport data. Figure 26 illustrates the layout of the oil-spray cooling system used in HSRHP testing.

The fabrication drawings of the cooling chamber are included in Appendix D.

Magnetic Seal: The above cooling arrangement involves dynamic rotary shaft seals for providing leak-tight sealing around the RHP at the end-plates of the chamber. The magseal unit consists of a pair of rings attached to each other at the carbon face seal by magnetic force. One ring is stationary and made of magnetic material. It mounts into the end of the chamber. The other ring is the rotating part and it fits on the RHP. Both rings have stationary O-ring type seal. The O-ring on the rotating ring of the seal also acts as the torque transmitter to the rubbing contact of the face-seal which is a very low friction (23 micro inch flatness) contact. The seals were supplied by Magnetic Seal Corp., Warren, RI. These types of seals are in use presently in several aircraft, helicopters and missile applications (such as accessory drive, turbine engine main shaft, gear box input shaft, transmission input quill, and pneumatic starter) for lube oil sealing at speeds ranging from 6,180 rpm to 41,000 rpm. The supplier claims that magseals last up to four times longer than spring-loaded seals and up to ten times longer than lip seals. The operating conditions of these seals are:

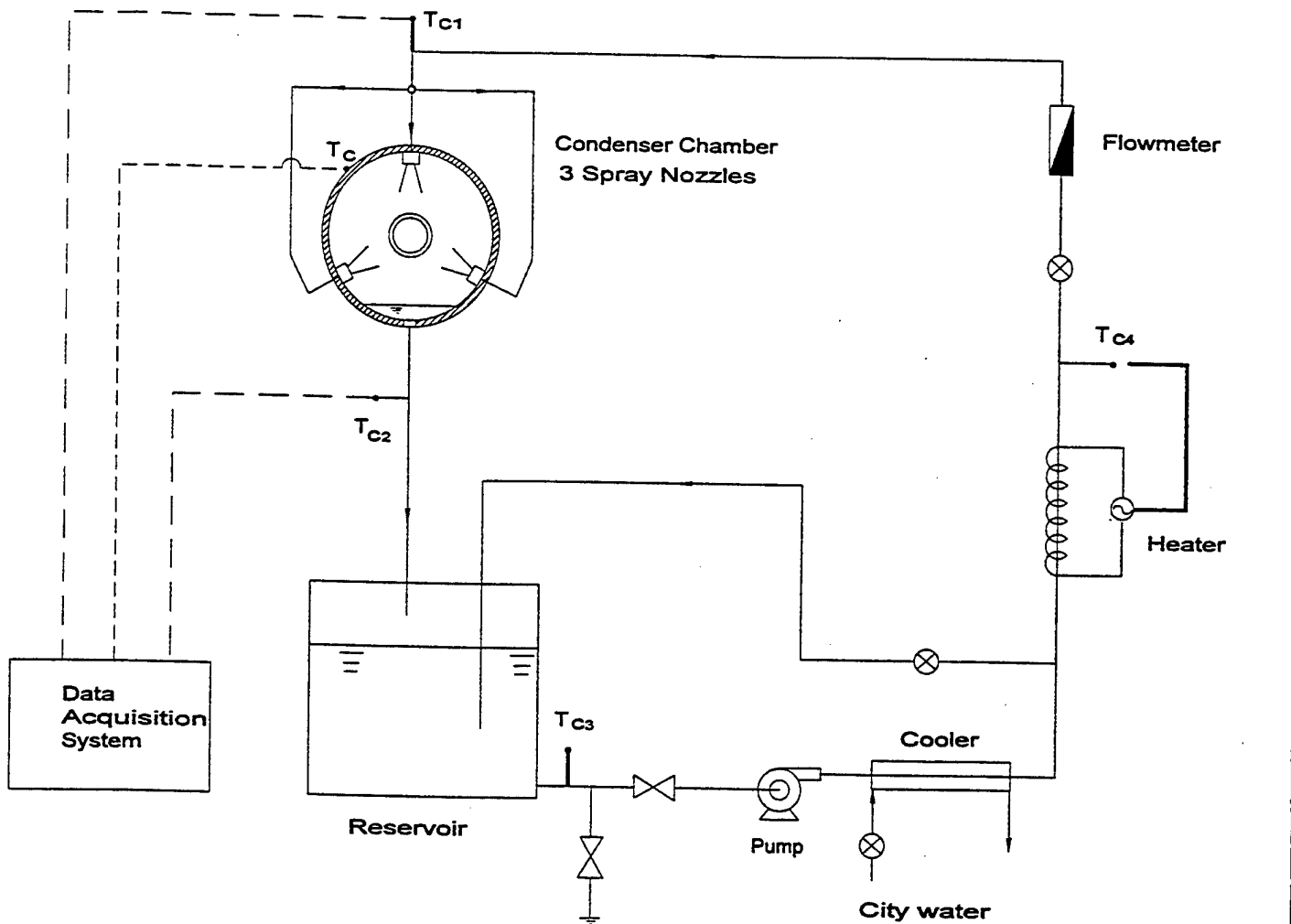


Figure 26. Schematic Diagram of the Oil-Spray Cooling System.

Chamber Side:

Fluid medium in chamber : Jet fuel, MIL-L-7808 oil, or antifreeze-water mixture
Temperature : 5 to 30°C
Pressure : 0 to 50 psig (-4 psig with reverse-taper ring mounting on housing)

Outside the Chamber:

Medium : Air
Temperature : Ambient
Pressure : Ambient

Other Details

Shaft speed : 40,000 rpm max.
Axial shaft movement : 0.040 in. max.
O-ring material : Viton; good up to 230°C
Magnet ring : ALNICO-5 (chrome coated)
Seal cage : SS416
Seal ring : Carbon graphite (GS-122)
Surface rubbing speed : Up to 17,000 feet per minute

Heat Generation:

<u>Shaft Speed</u>	<u>ΔP, psi (Pressure differential across the seal)</u>	<u>Lubricated</u>	<u>Dry</u>
5,000	2	6.15	30.41
10,000	2	12.13	60.83
15,000	2	18.28	91.24
20,000	2	24.26	121.48
25,000	2	30.41	151.89
30,000	2	36.39	182.30

Spray Nozzle: Three identical fan-nozzles are mounted at 120° apart on the cooling chamber. The nozzles are fan type with sheet-like spray and are Model 1/4 NF10120 supplied by BETE Fog Nozzle, Inc.

Other Cooling Methods:

- 1) Air-water mist: Early tests on the LSRHP employed this cooling arrangement. A single air-atomizer nozzle (Model DELAVAN ALX 60-04-A-ENPB) was mounted on the top of the cooling chamber (earlier version without magseals; see Appendix B) and the flat-spray jet was targeted on the RHP condenser. Shop air at 50 psig and chilled water from recirculating bath were used. Steam generated during powered tests was confined by felt-type gland seals at the chamber end-plates. This seal and cooling arrangement were not favored since the glands always leaked and calorimetry of heat output was impossible.
- 2) Air cooling: This method is the most preferred cooling technique for practical convenience. The BETE nozzles used for the oil spray cooling were used in the same setting except the chamber was removed, thereby avoiding the use of the magnetic seals. Though this is a convenient method, it is limited in the heat removal capacity.

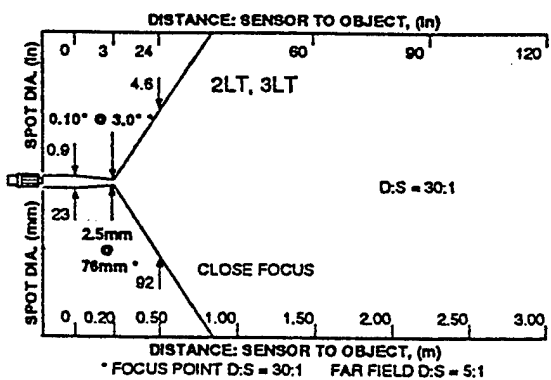
Trade-off Between Various Cooling Methods: In the present research, all three condenser-cooling methods (air-jet, air-water mist and oil-spray) have been employed at various stages of testing of different hardware. In the interest of comparing and contrasting for selecting the right choice, all three cooling methods have been explored for a final evaluation. These methods posed different levels of difficulties from hardware design to reliability and service life issues related to the MEA applications. For example, in the case of air-jet cooling, calorimetric measurement of heat removal rate is difficult; in the case of air-water mist, use of water onboard the aircraft would be objectionable; and in the case of oil-spray cooling, dynamic seal around the rotating shaft is a problem. From the ensuing test results, a comparative picture of these cooling methods will be given and discussed further in Section 4.4.

3.2.5 Instrumentation

Instrumentation: The schematic drawings of the instrumentation along with the test setup have been shown in Figures 20(a-b). The motor-drive system with a variable speed controller drive, the evaporator heating and the condenser cooling systems were described in previous sections. The external wall temperature of the RHP is monitored at three exposed positions as indicated in the sketch by an IR temperature sensor traversing alongside the RHP. The IR sensor has a target spot size of 3.8 mm dia. circle and $\pm 0.5^{\circ}\text{C}$ accuracy in $0\text{-}400^{\circ}\text{C}$. Other sensors and measurements include accelerometers on the bearing support, a fiber optic displacement sensor to monitor the deflection of the RHP at the midsection, thermocouple sensors for bearing, heater and insulation temperatures, frequency sensor for motor speed and input power to the heater. The IR sensor is calibrated to measure surfaces with black oxide or coated with flat black paint (emissivity = 0.98) good up to 815°C . A data acquisition system comprising VIEWDAC software and a personal computer are used. The base plate supporting the RHP is mounted on a table which can be tilted for providing favorable or adverse tilt orientation for the RHP.

IR Temperature Sensor: The specifications of the IR temperature sensor are given below:

Manufacturer/Model	:	Raytek Thermalert ET Series Model No. B1TET3LTCF Sl. No. 34077
Specifications	:	Close focus mode with D:S = 30:1
1) Optical	:	Optical resolutions at minimum 90% energy. See sketch below Target spot size of 0.15 in. at 4.6 in.



2) Thermal : Current output (switch selectable)
 LT model ranges:
 1 0 to 100°C
 2 0 to 200°C
 3 0 to 400°C
 4 0 to 800°C

Spectral response of thermopile detecting element:
 LT Version: 8 to 14 microns
 Accuracy: $\pm 1\%$ of reading
 Repeatability: $\pm 0.5\%$ of reading

3) Operational : Response time of 300 msec.
 Emissivity 0.1 to 0.99 in 0.01 increments
 Averaging:
 1) With no averaging: 0.3 sec response time
 2) With maximum averaging: 5 sec.

Failsafe: Full scale (20.3 mA)

4) Electrical : Power: 12 VAC; 100 mA; 50 to 60 Hz
 Current version 4-20 mA
 5 pin DIN connector, 15 ft. cable

5) Physical : NEMA 4
 Ambient operating temperature 0 to 50°C without active cooling
 Dimensions: 7.02 in. long \times 2.24 in. dia.
 Weight: 1.2 lbs.

IR Sensor Calibration: The IR temperature sensor was calibrated using a temperature controlled reference surface which was also cooled with the black paint used on the RHP. The calibration source and the instrumentation details are shown in Figure 27. The calibration data: temperature vs. IR sensor voltage are plotted as seen in Figure 28 and also programmed in the computer for VIEWDAC to record the measured temperatures directly in degrees C.

3.3 TEST PROCEDURE

3.3.1 Test Configuration

All the performance tests conducted on all models of the LSRHP and HSRHP units were steady state tests and the mounting orientation was horizontal on-axis rotation. During the heat loss tests of the nichrome heater arrangement, the LSRHP was adversely tilted (evaporator above condenser) to 45° and kept non-rotating.

All steady state performance tests were conducted typically by applying a desired heat input to the heater and spinning the RHP at the desired speed and condenser cooling. Temperature and power input data were recorded for each setting. Experimental parameters varied were heater power input, rotational speed, and air-water flow rates of the mist cooling or oil flow rate of the oil-spray. The test matrix consisted of $Q_1 = 250 \text{ W}, 500 \text{ W}, 750 \text{ W}, 1000 \text{ W}, 1250 \text{ W}, \text{ and } 1500 \text{ W}$; $N = 500 \text{ to } 7000 \text{ rpm}$ in steps of 500 rpm for LSRHP and $N = 5000 \text{ to } 30,000 \text{ rpm}$ in steps of 5000 rpm for HSRHP in both accelerating and decelerating modes. Condenser cooling methods included spin in air, air jet cooling, water-air mist cooling and oil-spray cooling.

3.3.2 Heat Balance Analysis - LSRHP

Calorimetric measurement of heat removal from the RHP condenser section is very difficult. Hence, it is necessary to compute the heat transport through the RHP from the input heat by subtracting the losses. Figure 29 shows a model for heat flow to and out of the RHP. Under steady state conditions,

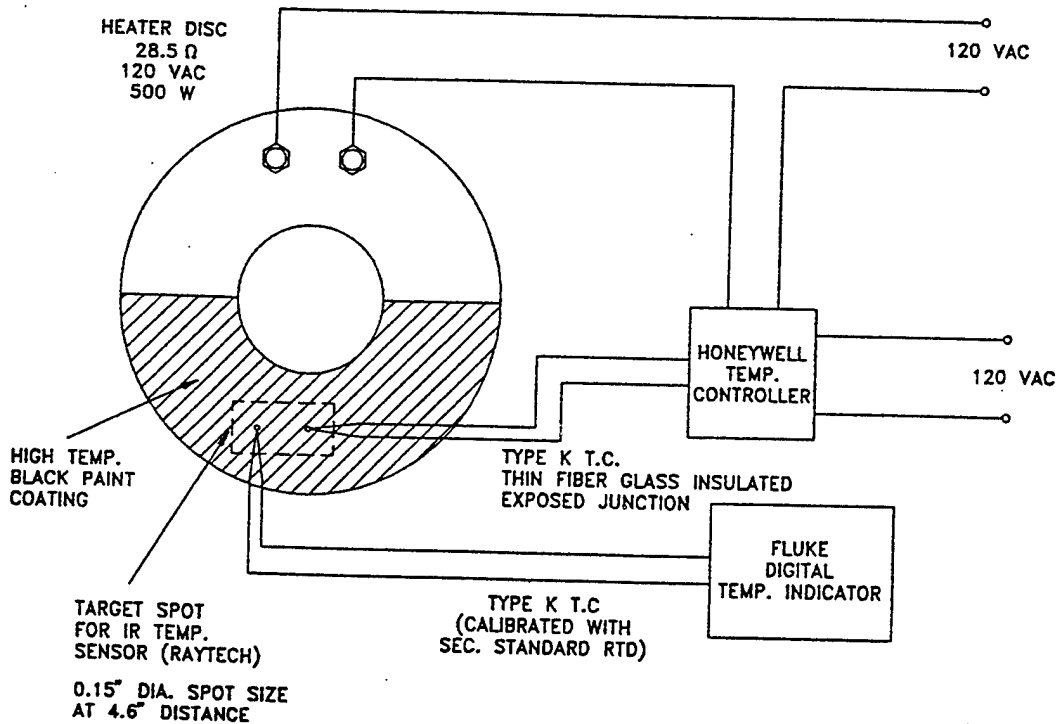


Figure 27. Calibration Source (0-300°C) for IR Sensor.

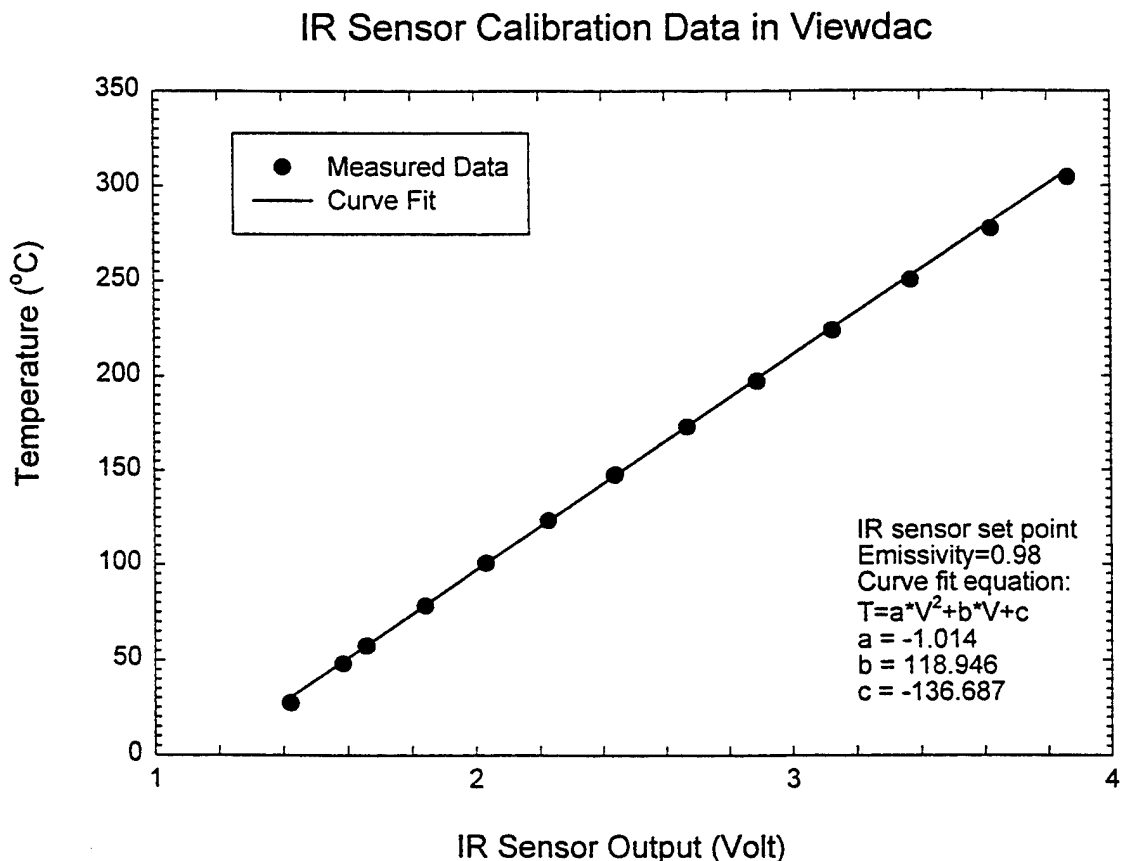


Figure 28. IR Sensor Calibration Data.

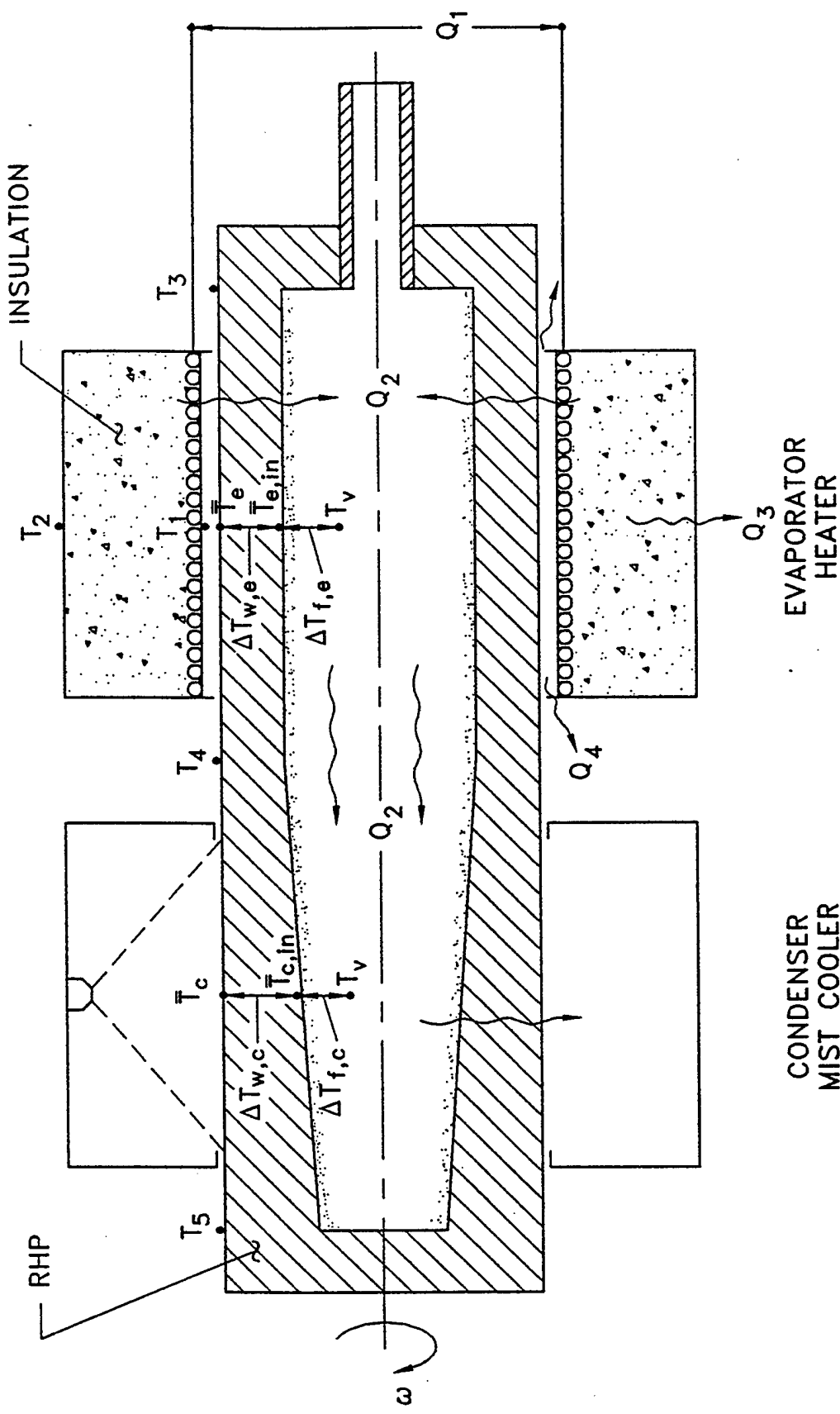


Figure 29. Heat Balance Representation.

$$Q_1 = Q_2 + Q_3 + Q_4 \quad (8)$$

where

- Q_1 = heater power input
- Q_2 = heat exchanged from heater to RHP by convection and radiation which is also the heat transported from evaporator to condenser
- Q_3 = heat loss through the heater insulation
- Q_4 = heat loss by radiation from heater ends

T_1 through T_5 are measured temperatures at RHP locations indicated in Figure 29

Case 1: Heat loss tests: Heat loss tests conducted up to the limiting temperature of the heater ($T_1 = 860^\circ\text{C}$) enable us to determine effective thermal conductivity of the insulation as a function of the insulation ΔT . During heat loss tests, $Q_2 = 0$ and all the heat supplied (Q_1) are lost. Heat loss by radiation from heater ends to the ambient (Q_4) is calculated by Eq. (9).

$$Q_4 = 2A_1\epsilon\sigma(T_1^4 - T_0^4) \quad (9)$$

Now, $Q_1 - Q_4 = Q_3 = \frac{2\pi k_{\text{insu}} L_e (T_1 - T_2)}{\ln(r_o/r_i)}$ (10)

From Eq. (10), k_{insu} is determined for all heat loss test runs and plotted as k_{insu} versus $(T_1 - T_2)$. This graph is used later to determine Q_3 in actual performance tests where the RHP is rotating and transporting heat.

Case 2: Performance tests: When the pipe is rotating, heat is transferred from the heater by radiation and convection such that

$$Q_2 = Q_{\text{rad}} + Q_{\text{conv}} \quad (11)$$

$$Q_{\text{rad}} = A_e F \alpha_w \sigma (T_1^4 - \bar{T}_{3-4}^4) \quad (12)$$

$$Q_{\text{conv}} = hA_e(T_1 - \bar{T}_{3-4}) \quad (13)$$

The convective heat transfer is determined using Eq. (14) which is Bjorklund and Kays [26] correlation involving Taylor number.

$$\text{Nu}/\text{Nu}_{\text{cond}} = 0.175 \text{ Ta}^{0.5} \quad (14)$$

Various terms here are defined as follows:

$$\begin{aligned} \text{Ta} &= \left(\frac{c}{R_1} \right)^{0.5} \left(\frac{R_1 \omega c}{v_{\text{air}}} \right) \\ \text{Nu}_{\text{cond}} &= \left(\frac{c}{R_1} \right) / \ln \left(1 + \frac{c}{R_1} \right) \\ \text{Nu} &= \frac{hc}{k_{\text{air}}} \end{aligned} \quad (15)$$

Also, Q_2 can be determined by subtracting the calculated heat losses Q_3 and Q_4 from Q_1 . That is,

$$Q_2 = Q_1 - (Q_3 + Q_4) \quad (16)$$

3.3.3 Reprocessing of the LSRHP

After concluding the performance tests on the water RHP, the 10 cm long fill tube pinched-end was cut off in order to reprocess the pipe. The pipe was emptied and thoroughly rinsed with alcohol before installing in the fill-station for vacuum baking and filling. Analytical grade methanol was filled and the fill tube was crimped and welded.

4.0 RESULTS AND DISCUSSIONS

During this research study, four different RHP test articles were manufactured and tested with varying degrees of complications and test parameters. Table 10 lists the progressive evolution of these test articles and the test conditions. The following sub-sections describe the results of all the test articles investigated in the order they were done.

Table 10. Evolution of RHP Test Articles and Tests

RHP Test Article	Working Fluid	Tests	Remarks
1. LSRHP #1 0-3500 rpm	Water	<ul style="list-style-type: none">● Heat loss● Spin in air● Air-jet cooling● Air-water mist cooling	Nichrome heater Baldor low speed motor/drive 0-1250 W (max.)
0 - 7000 rpm	Water	<ul style="list-style-type: none">● Air-jet cooling● Air-water mist	RF heating Pope High speed spindle/drive 0-2250 W (max.)
2. LSRHP #2 0-7000 rpm	Methanol (Reprocessed LSRHP #1)	<ul style="list-style-type: none">● All modes as above	RF heating Pope spindle 0-1200 W (max.)
3. HSRHP #1 5000-30,000 rpm	Methanol	<ul style="list-style-type: none">● Air-jet cooling● Oil-spray cooling	RF heating Pope spindle 0-922 W (max.)
4. HSRHP #2 5000-30,000 rpm	Water	<ul style="list-style-type: none">● Air-jet cooling	RF heating Pope spindle 0-750 W (max.)

4.1 LSRHP - EARLY TESTS

4.1.1 Heat Loss in Resistive Heater

Heat loss data obtained from the heat loss experiments for both heaters are plotted as functions of ΔT_{insu} in Figure 30. ΔT_{insu} is the difference between the heater side and the ambient side measured temperatures. Heater 2 has lower loss compared to heater 1 due to its

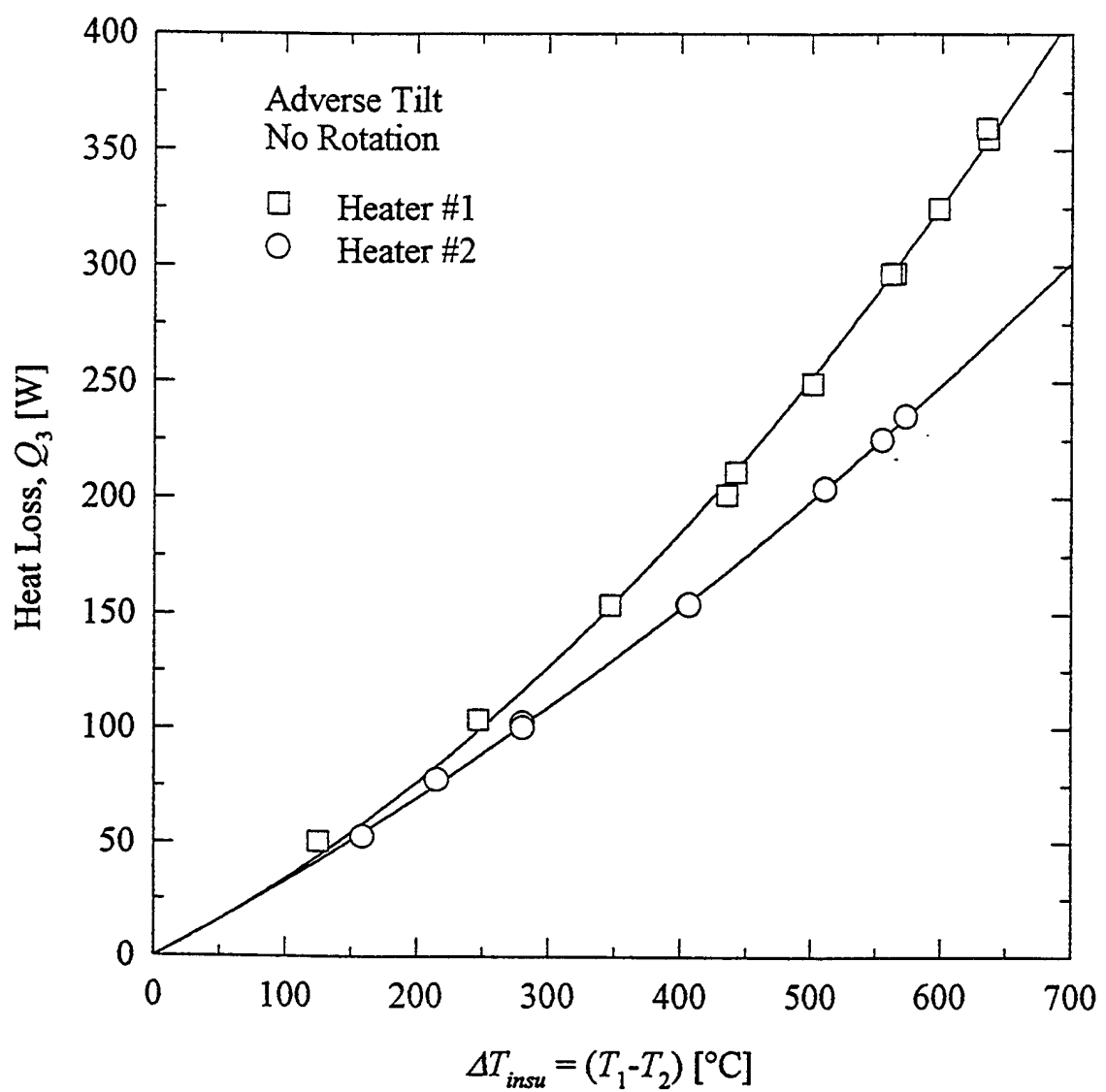


Figure 30. Heat Loss Data for Nicrome Heater.

larger size and construction. These results are used to estimate the heat losses for high power input test runs.

4.1.2 Effect of Cooling Rate on Temperature Profile

Three different cooling methods (spin-in-air, air jet and mist cooling) were used during the tests. In order to illustrate the effect of cooling rate variation on the RHP, data for $Q_1 = 250$ W and 2000 rpm were compiled and plotted on temperature versus length graph as shown in Figure 31. It is clearly seen that the pipe temperatures are the highest for spin-in-air case and the lowest for mist cooling case. The pipe was nearly isothermal end-to-end during spin-in-air test at certain conditions indicating that there was no noncondensable gas in the pipe. As the data points indicate, four extra stops for the condenser were programmed for the IR sensor and the condenser mist chamber was removed to enable this. Mist cooling quenched the condenser more than the other cooling methods and hence the operating temperature was lower. Also, it is noted that the overall ΔT of the RHP was the highest for mist cooling. Progressive increase or decrease of rotational speed made significant changes in condenser temperature profiles for air-jet and spin-in-air cooling modes while the same did not have any effect on mist cooling mode.

A comparison of results for air-jet cooling and mist cooling is done at slightly elevated power input of $Q_1 = 750$ W as shown in Figure 32. The pipe operated about 50°C lower for mist cooling. Changes in rpm had greater effect in air-jet cooling and it is interesting to observe that at 2000 rpm, the pipe is nearly isothermal. The slightly anomalous data (lower temperatures) at the condenser near midsection of the pipe are due to uneven distribution of air-jet stream at that location.

Figure 33 illustrates the temperature profile for mist cooling at constant rotational speed (1800 rpm) for power inputs of 250, 500, 750, 1000, and 1250W. The cooling rate was kept constant for all power input levels. Power input was incremented by 250 W at 15 minute intervals after recording the temperature data corresponding to the previous power setting.

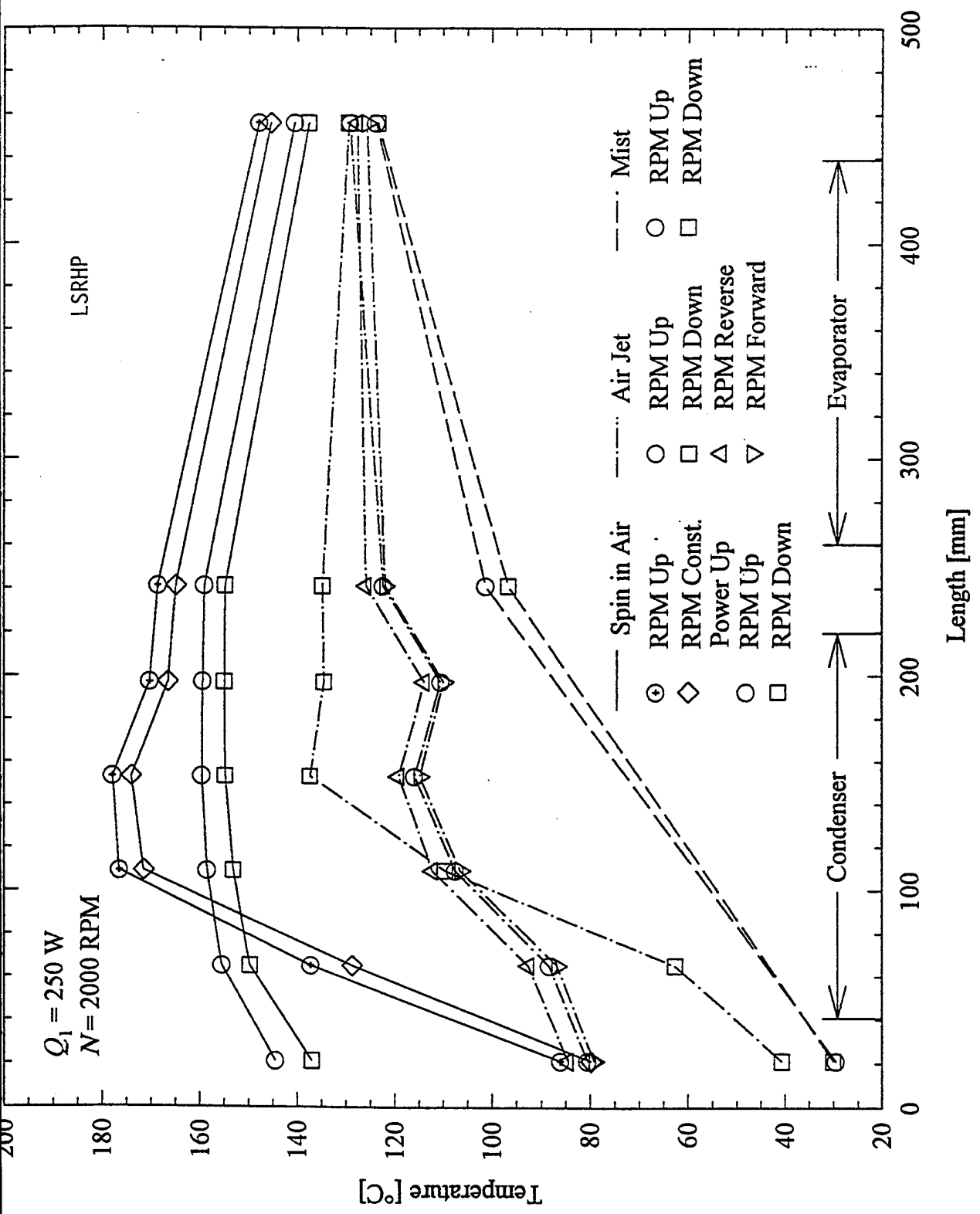


Figure 31. Effect of Cooling Rate on Temperature Profile (250 W).

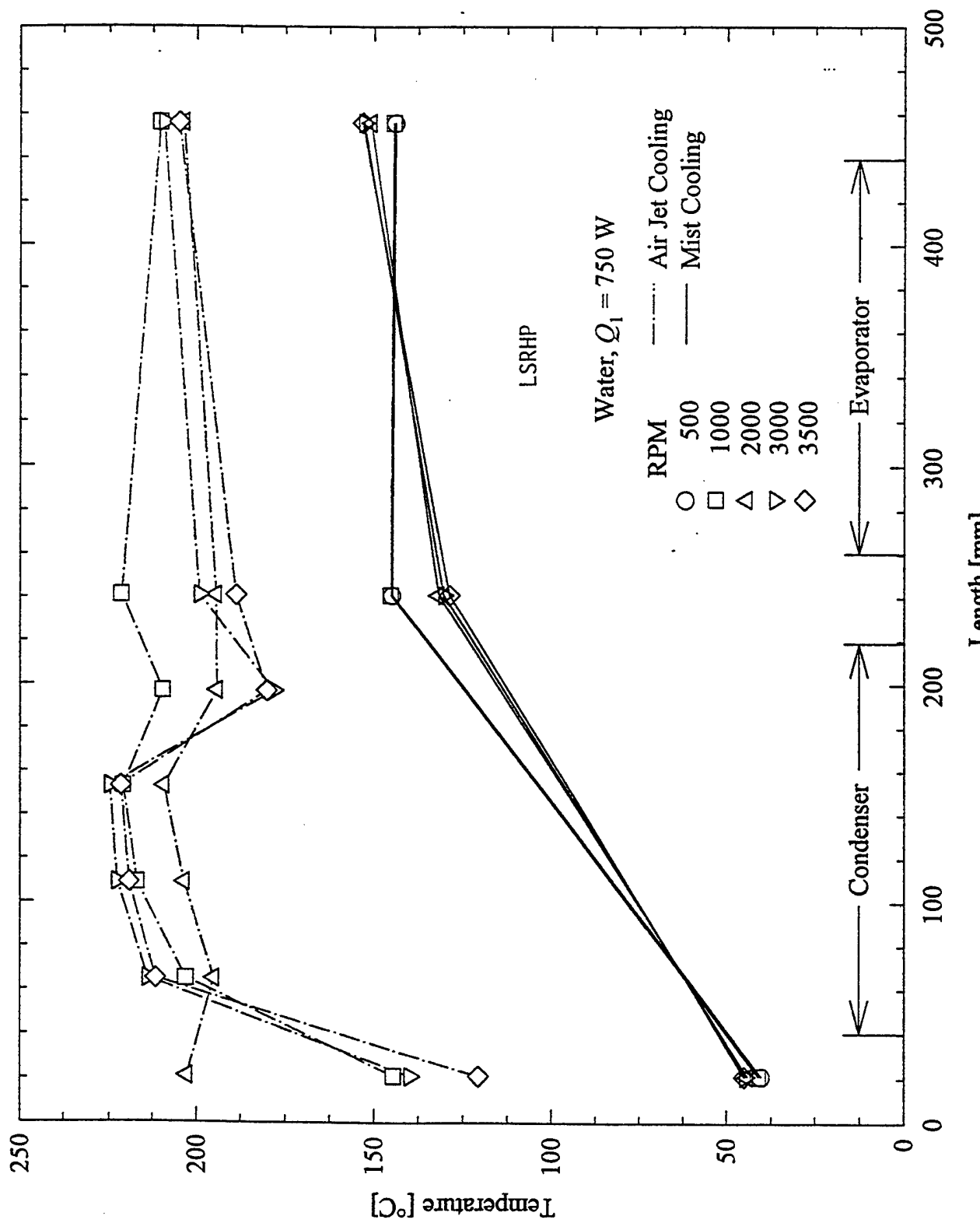


Figure 32. Effect of Cooling Rate on Temperature Profile (750 W).

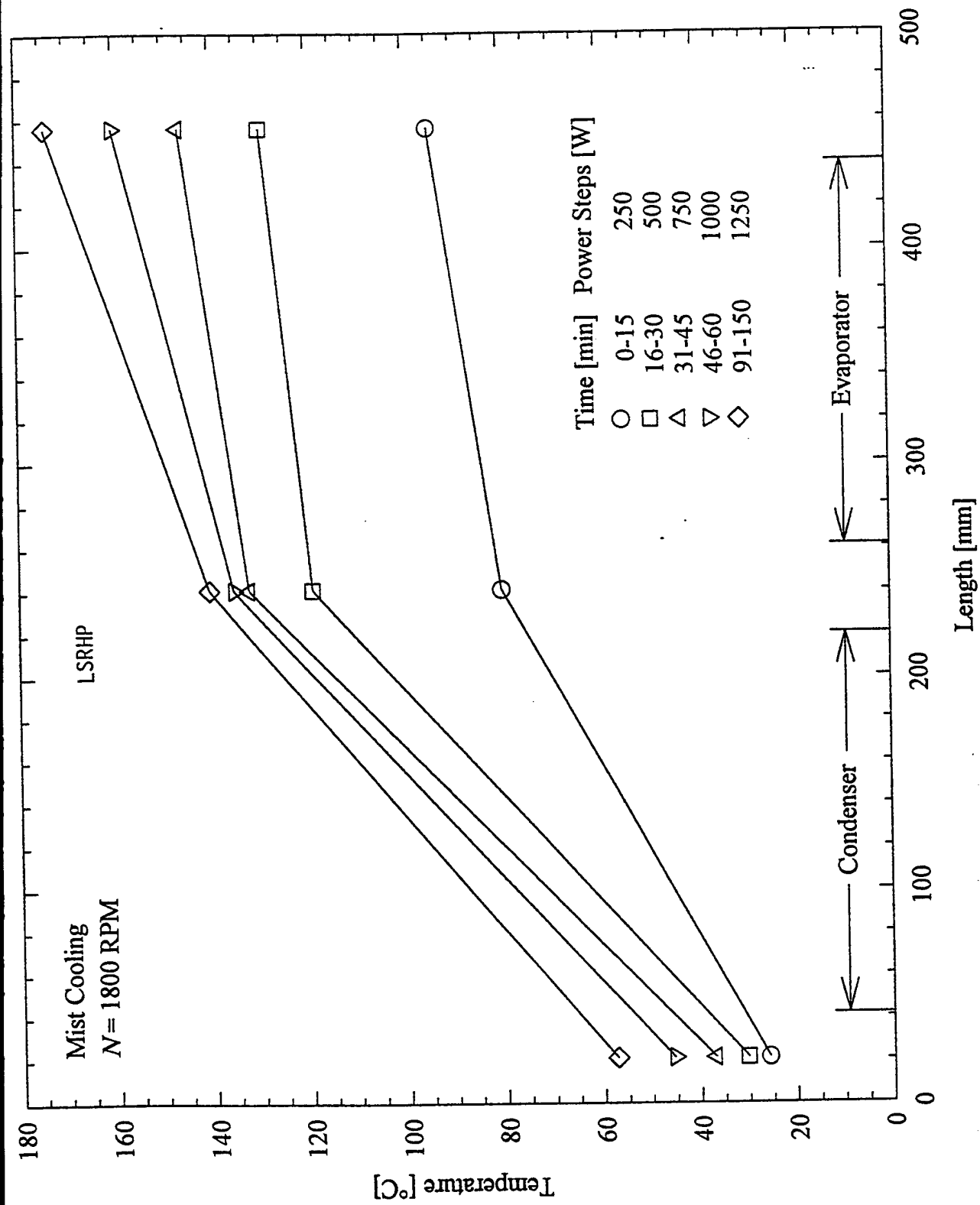


Figure 33. Temperature Profile at Constant Speed (1900 rpm) and Different Power Inputs for Mist Cooling.

Because of the powerful cooling nature of mist cooling, the condenser temperature is very low compared to that of evaporator. This is a condition called quenched condenser, which is not observed with air-jet cooling.

4.1.3 Effect of Rotational Speed

Low power input and spin-in-air cooling test data are considered for illustrating the effect of speed on the temperature profile. The condenser section temperature was monitored at five locations. Figures 34 and 35 show the 3D plots for increasing and decreasing speeds, respectively. The speed was changed in steps of 200 rpm and sufficient time was allowed between steady state readings. It can be seen from the figures that the evaporator and midsection temperatures increased or decreased in tune with the speed. However, the condenser section temperature variation was not consistent. This is attributed to the type of condensate film formation. At low speeds, the condensate may form a puddle at the bottom due to gravity effect. Hence, as the speed is increased progressively, the puddle may also rotate without uniformly distributing to an annular ring. On the other hand, as the speed is decreased from high speed, the already formed annular film continues to rotate undisturbed to lower speeds.

4.1.4 Heat Transport Capacity

Quantitative estimates of heat transport from evaporator to condenser of the RHP for all the experimental data sets were obtained in two ways using Eqs. (11) and (16). These results were plotted as Q versus ΔT_{He} and one such plot is shown in Fig. 36. It was generally observed from this figure that Eq. (11) overpredicted and Eq. (16) underpredicted the heat transport. Due to the difference in c/R_1 ratios (present value of 0.33 versus 0.05-0.25, the valid range for Eq. (14)), in using the Taylor number correlation [26] for the present situation, it was decided not to use the results of Eq. (11). On the other hand, the results of Eq. (16) being conservatively measured data, were accepted. Figure 37 shows these results for 3500 rpm tests in the form of percent

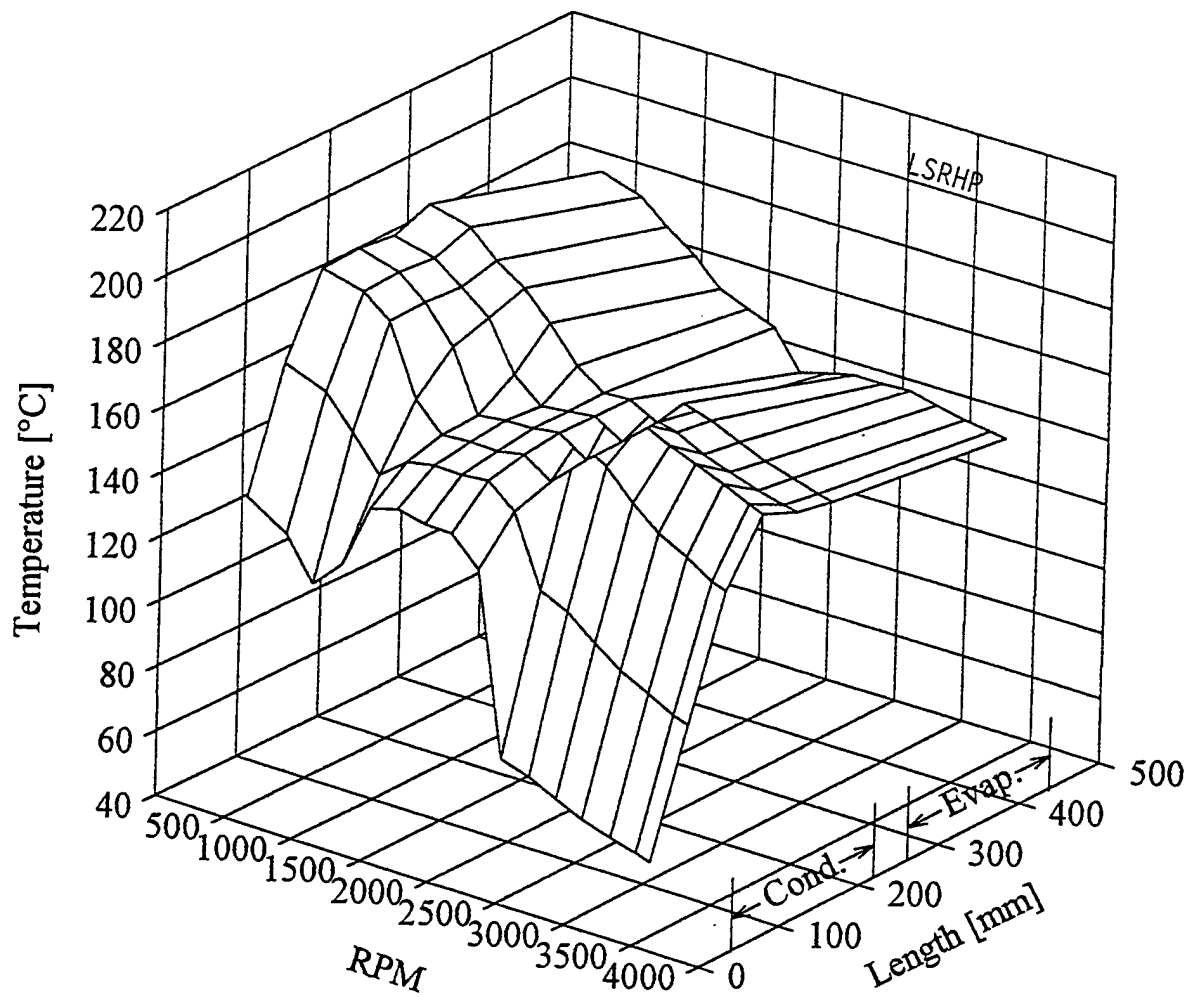


Figure 34. Effect of Rotational Speed on Temperture-Profile (Increasing Speed).

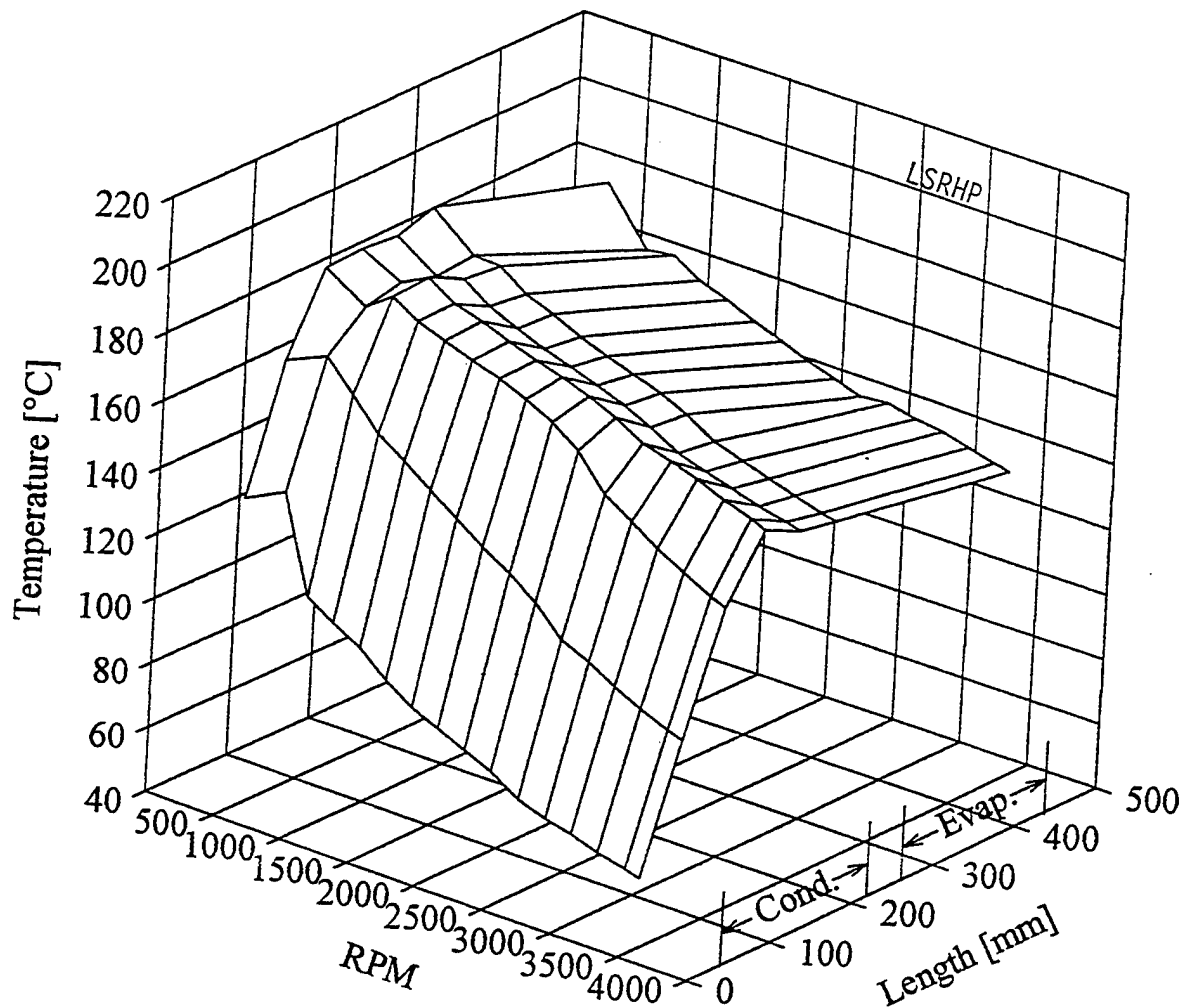


Figure 35. Effect of Rotational Speed on Temperature-Profile (Decreasing Speed).

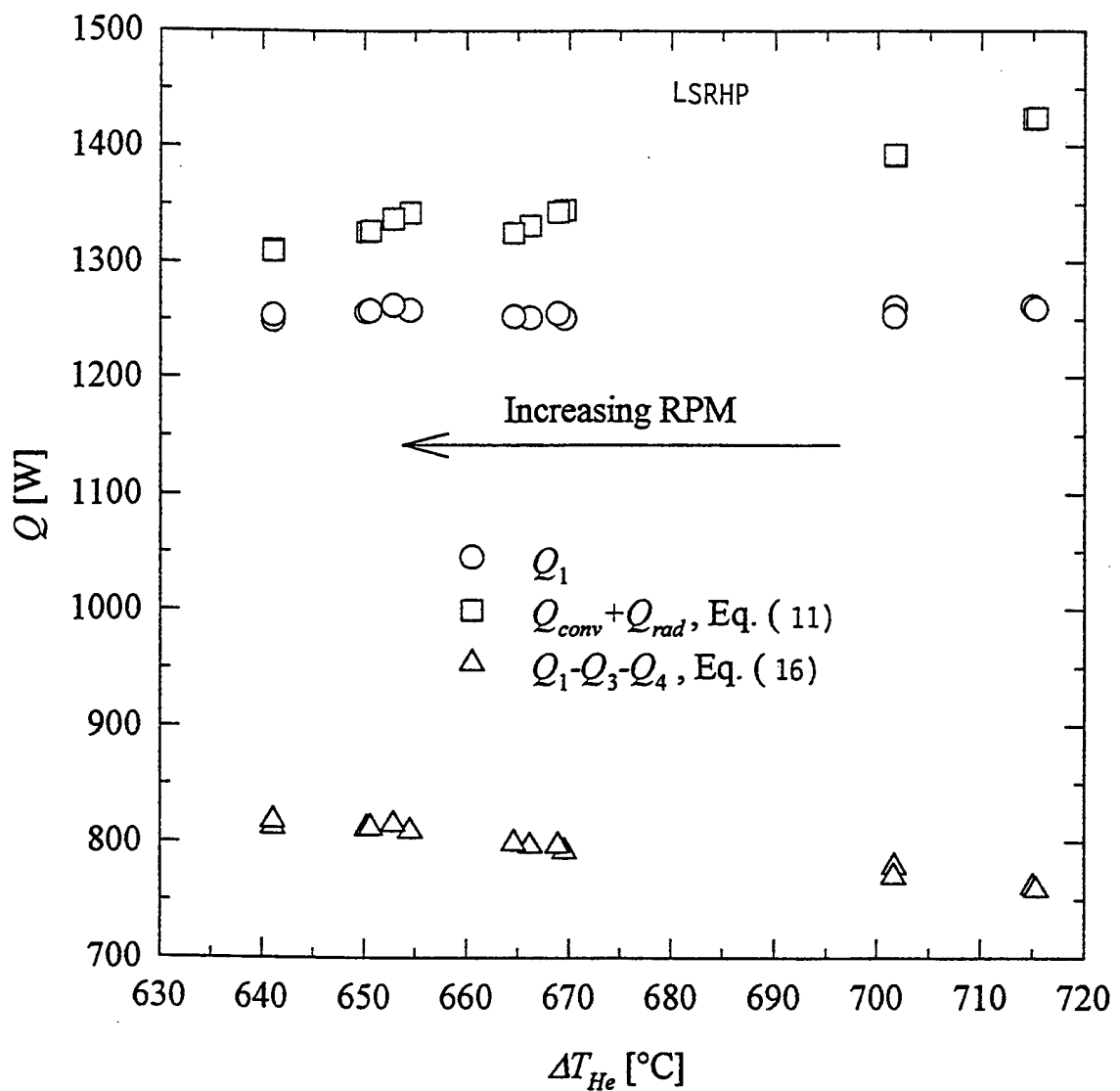


Figure 36. Heat Transport Capacity Estimates and Losses ($Q \propto V_s \Delta T_{He}$).

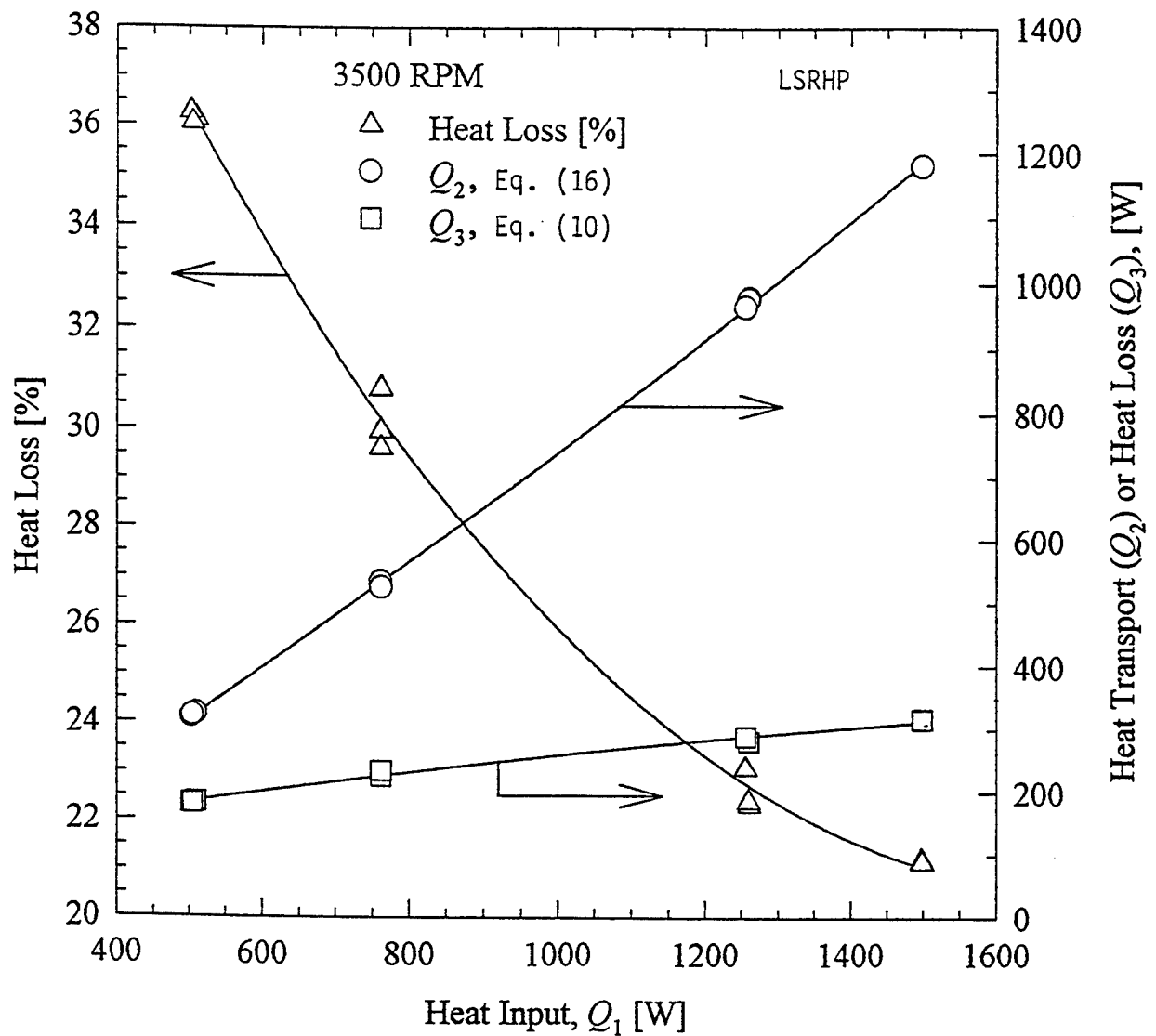


Figure 37. Heat Transport Capacity Estimates and Losses (Q_1 vs. Q_{loss} and Q_2).

heat loss and heat transport (Q_2) as functions of heat input (Q_1). The heat loss varied from 21 to 36% while the transported heat increased with increase in input power.

Theoretically calculated heat transport capacity is compared with experimental values corresponding to 3500 rpm test runs as seen in Figure 38. As the vapor core temperature is not measured in these tests, an approximation is made by assuming the adiabatic temperature (T_4) to be the saturation temperature (T_s) which is also equal to the vapor temperature (T_v).

Experimental value for ($T_s - T_w$) corresponds to $\Delta T_{f,c}$ in Eq. (17)

$$\Delta T_{f,c} = T_v - \Delta T_{w,c} - \bar{T}_c = T_4 - 0.038 Q_2 - \frac{(T_4 + T_5)}{2} \quad (17)$$

where T_4 , T_5 and Q_2 are measured data. Only a few selected data are plotted in this graph to illustrate the validity of theoretical prediction. Depending upon the cooling rate (air or mist cooled), the saturation temperature of the fluid varied inside the RHP. Experimental operating temperature of each steady state point is marked in the plot for comparing with the theoretical limit curves. Most of the experimental data fall within the theoretical limit curves. This simply means that our experimental operating conditions were not exactly in tune with the fringes of the theoretical curves. Also, it is practically difficult to set the test conditions to track the limit.

Even though the heater was designed for 3.5 kW, test runs were limited to 1500 W in order to protect the heater from burning out. Highest heater temperature reached at this power level was 825°C.

4.1.5 Overall Temperature Difference (ΔT_{ec})

Average temperatures of the evaporator and condenser \bar{T}_e and \bar{T}_c were calculated from the measured temperatures, T_3 , T_4 and T_5 , see Figure 29 , for a few selected test runs wherein the rotational speed was increased from low to high and back to low. The overall temperature difference of the pipe,

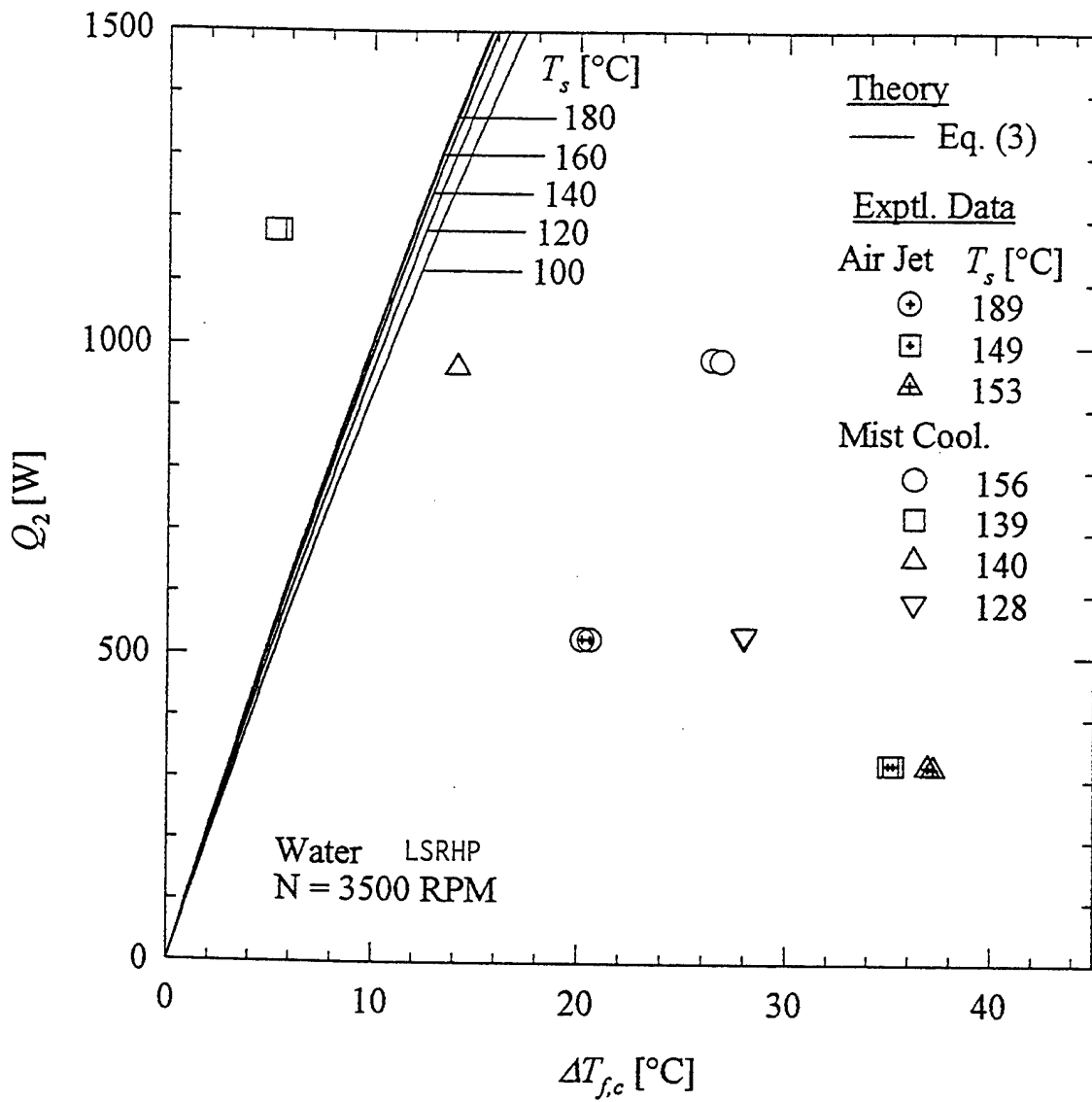


Figure 38. Comparison of Theoretical and Experimental Values of Q for Various T_s at 3500 rpm.

$$\Delta T_{ec} = \bar{T}_e - \bar{T}_c \quad (18)$$

was plotted for these cases as a function of speed as seen in Figure 39. ΔT_{ec} variation with speed is random and depends on increasing or decreasing of speed. At certain speeds, the pipe exhibits sudden drop or increase of ΔT which is characteristic of nonuniform condensate film formation and/or film instability. It is suspected that at certain conditions (speed up or down, rpm magnitude, condenser cooling rate, etc.), the condensate film may form a wavy or rivulet pattern and thus influence ΔT_{ec} . Also, see Section 4.2.2 on fluid distribution model.

4.1.6 Summary of Early Tests on LSRHP

The following is a summary of the LSRHP research results and findings:

- 1) A low speed version of the 2.54 cm dia 45.6 cm long stainless steel RHP was designed, fabricated and tested up to 3500 rpm with water as the working fluid.
- 2) Traversing infrared temperature sensor system was successfully used which precluded the use of troublesome slip ring assembly needed for thermocouple sensors.
- 3) The radiatively coupled nichrome heater and the air-water mist cooling condenser worked satisfactorily as heat source and sink, respectively.
- 4) Air-jet cooling was inefficient and the pipe operating temperature reached its safe limit (225°C) at $Q_1 = 750 \text{ W}$. However, temperature measurements over condenser length were feasible. With mist cooling, Q_1 could be increased to 1500 W and the highest evaporator temperature was 183°C .
- 5) The overall temperature difference of the pipe is very sensitive to condenser cooling method and rotational speed. Between 1000 and 2000 rpm, drastic changes in ΔT_{ec} are indicative of condensate flow pattern changes and instability.
- 6) Heat transport capacity of the RHP for all the test conditions was determined by heat input and loss measurements and plotted with the theoretical capillary limit

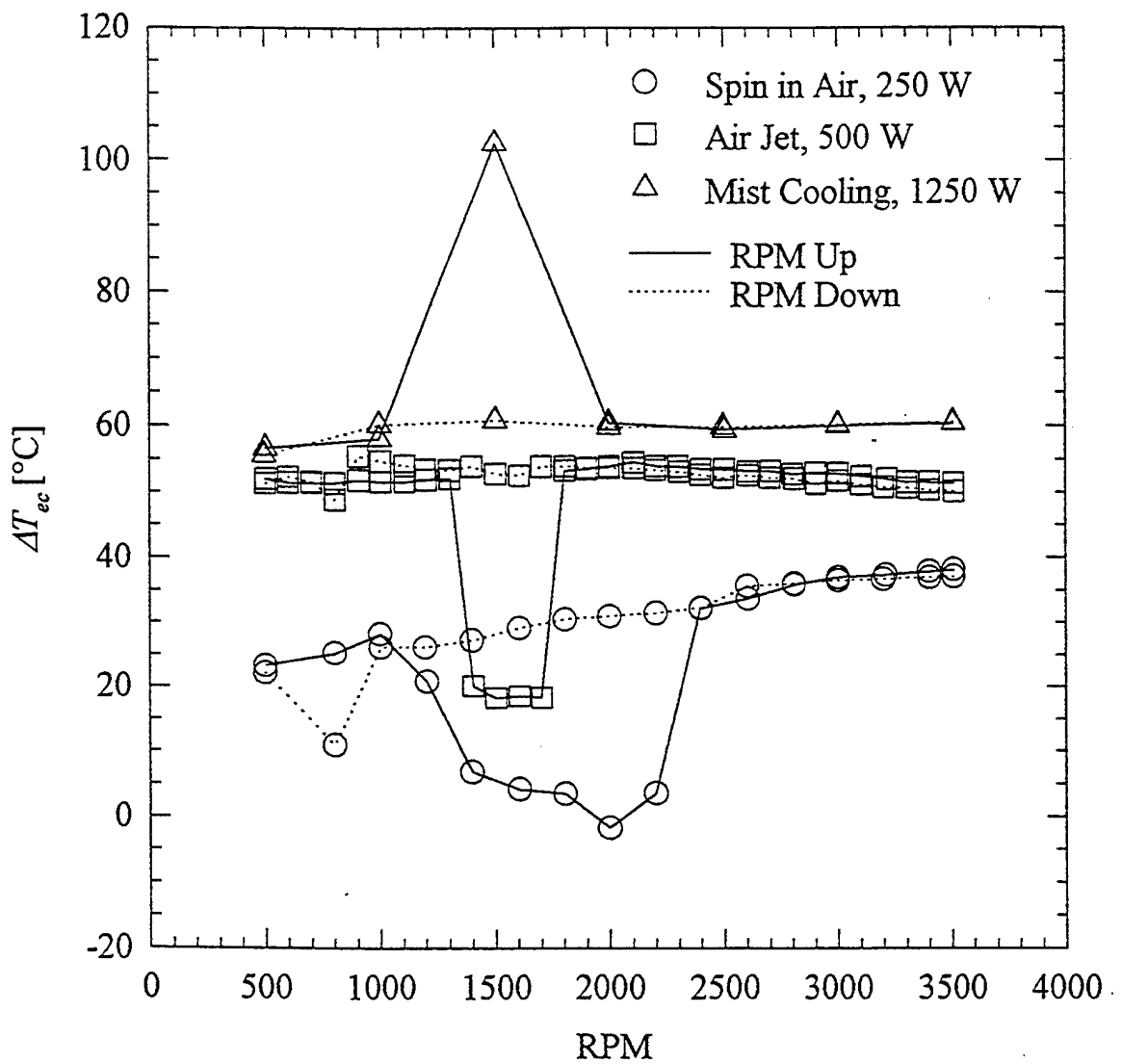


Figure 39. Overall Temperature Difference as a Function of Speed for Different Cooling and Heat Inputs.

curves. Except the 1200 W test data, all other experimental data fall within the theoretical limit envelope.

- 7) No sign of noncondensable gas generation was noticed in this steel-water system up to 500 hours of cumulative testing.
- 8) Because of the inability to measure the vapor core and internal wall temperatures, heat transfer coefficients could not be calculated.
- 9) The instrumentation and test setup together with the data collection system were verified for their future use in high speed RHP testing.
- 10) Other working fluids (methanol and mercury) can be loaded into this RHP and tested easily.

4.2 LSRHP - ADDITIONAL TESTS

The experimental results presented are steady state data for horizontal test orientation of the RHP. The heat transport measurement is based on the RF heater calibration using a water flow calorimetry of identical configuration and is reliable within $\pm 5\%$ of reported values. The IR sensor was precalibrated against a black body surface and is accurate to $\pm 0.5^{\circ}\text{C}$ in $0 - 400^{\circ}\text{C}$. The parameters varied are speed, input power and condenser cooling rate/method. The data points of the three axial temperatures are joined by straight lines as there are no data for intermediate locations. The input power to the evaporator was increased in steps of 250W every 15 minutes in order to avoid sudden thermal shock to the system until the desired power level was reached in all the test runs.

4.2.1 Axial Temperature Profile

Figure 40 shows the axial temperature profiles for air jet cooling and air - water mist cooling at various power inputs. The 2000 rpm data for air-jet cooling do not follow the trend as at other speeds because of possible film instability explained in Section 4.1.5. With air cooling, the heat transport is only 225W for a nominal operating temperature of 210°C whereas for mist cooling the transport capacity is increased by an order of magnitude (2250W) while keeping the

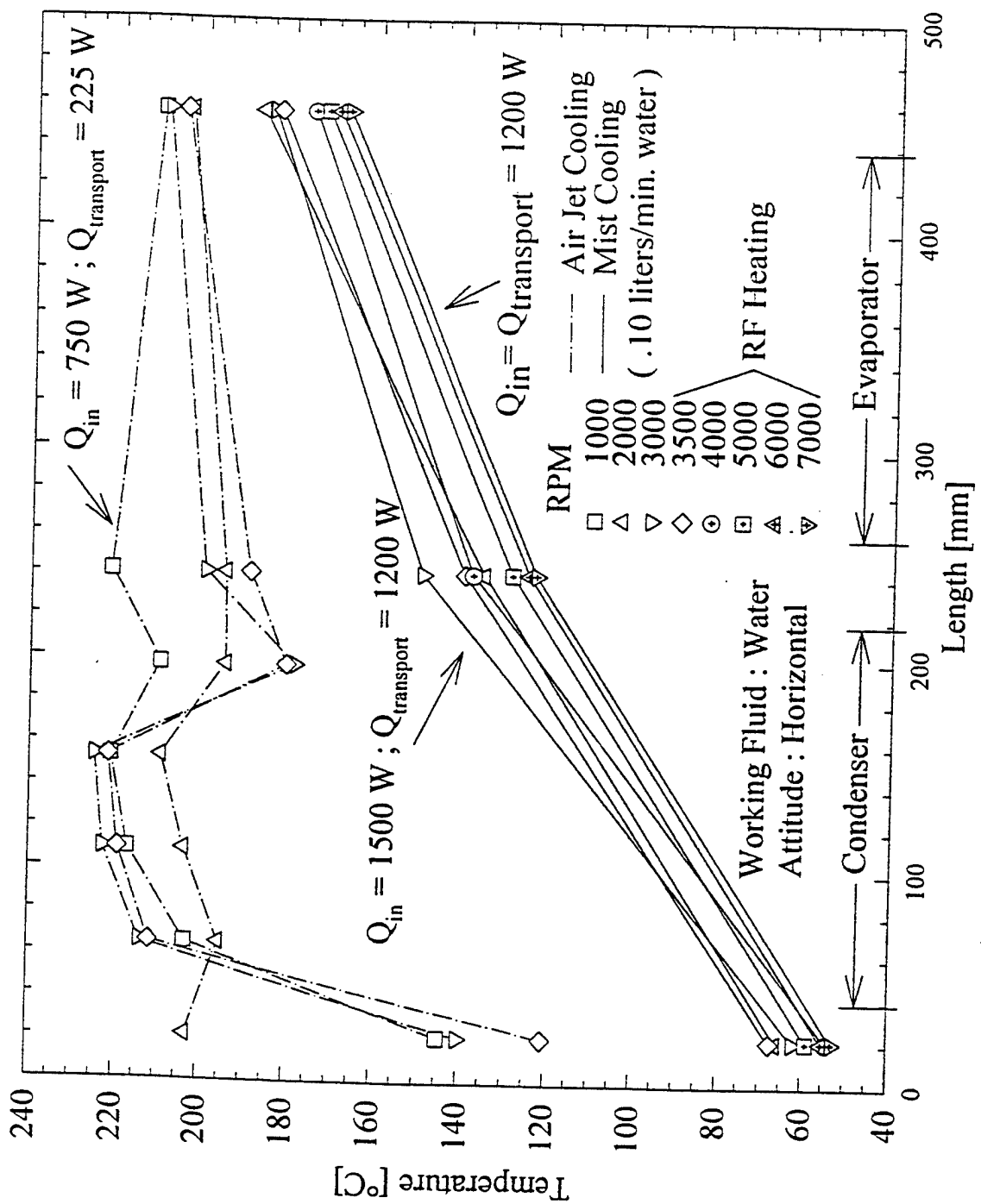


Figure 40. Temperature Profiles at Various Cooling Methods and Power Inputs.

temperature under 210°C (Figure 43). In the case of RF heating $Q_{in} = Q_{transport}$ as per calibration of the RF heater. The nichrome heater previously used had about 20% heat loss. The plots of 1200W transport verify that change of heating method does not affect the temperature profiles. Figure 41 shows the profiles for 1750W at four different speeds. The condenser end temperatures are significantly influenced by spin rate. This indicates that at higher speeds the condensate removal from the condenser is more effective as expected and determined by Eq. (1). Figures 42 and 43 show similar plots for 2000W and 2250W, respectively. The reason why a significant drop in condenser temperature occurs for 5000 to 6000 rpm, is because of an increase in transport capacity at higher speeds. Different water flow rates of the mist cooling were tried and found that as the heat transport was increased, the minimum speed and mist level required to keep the condenser end temperature level with the midsection temperature also had to be increased. If this balance was not maintained, in other words, while increasing the power, if the speed or mist flow rate is not increased, the condenser end temperature rose higher and higher and subsequently increasing the evaporator temperature beyond the safe limit of 225°C. If this trend were to continue, the evaporator would dry-out and eventually burn-out.

4.2.2 Fluid Distribution Model

Based on the axial temperature profiles, two internal operating characteristics dependent on speed can be modeled for a fixed Q_{in} and external cooling rate.

- 1) Flooded condenser with partially dried evaporator refer to Figure 44(a): At a certain threshold speed, the RHP does not generate sufficient axial acceleration to uniformly distribute the condensate film throughout the evaporator length. Consequently, the condenser is flooded while the evaporator is deprived of fluid. Increased film thickness in condenser increases the film ΔT and reduces the heat transfer. Also, partially dried out evaporator increases the operating temperature. T_c tends to equal or exceed T_a . Any further drop in speed can cause evaporator to fully deprime leading to a burn out.
- 2) Efficient condenser with fully primed evaporator refer to Figure 44(b): Speeds higher than the threshold speed, distributes the fluid more uniformly throughout

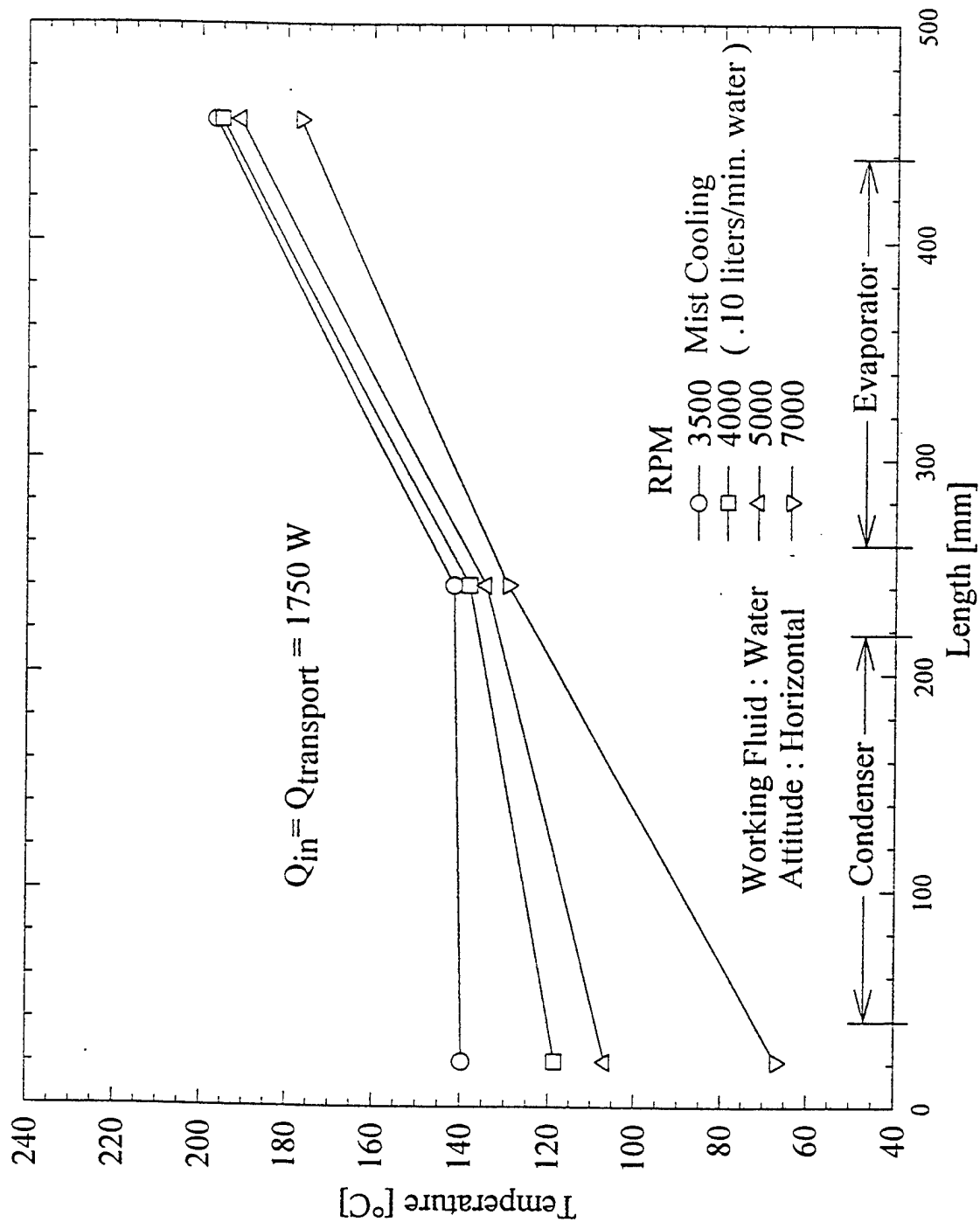


Figure 41. Temperature Profile for 1700 W at Various Speeds.

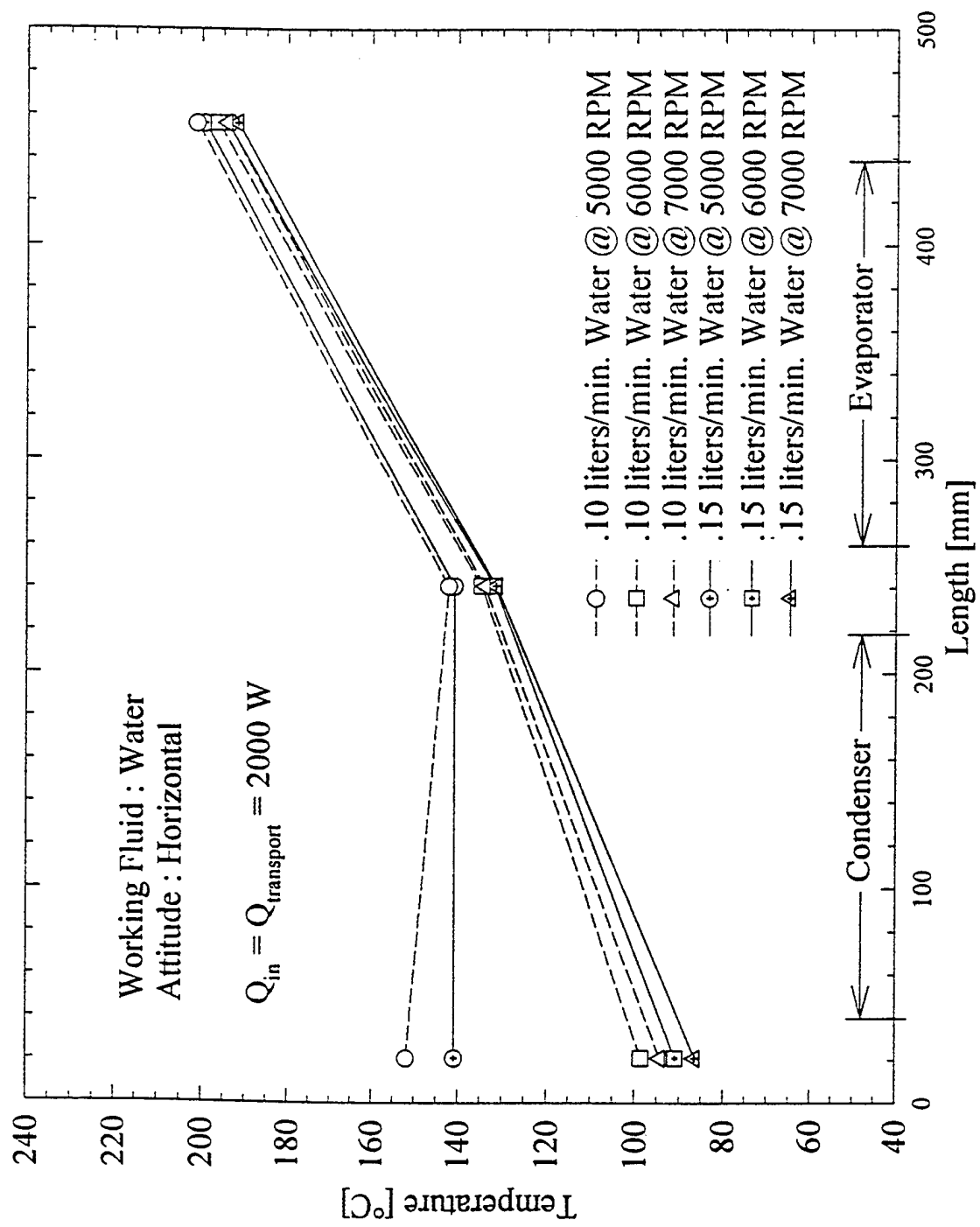


Figure 42. Temperature Profile for 2000 W at Various Cooling Rates and Speeds.

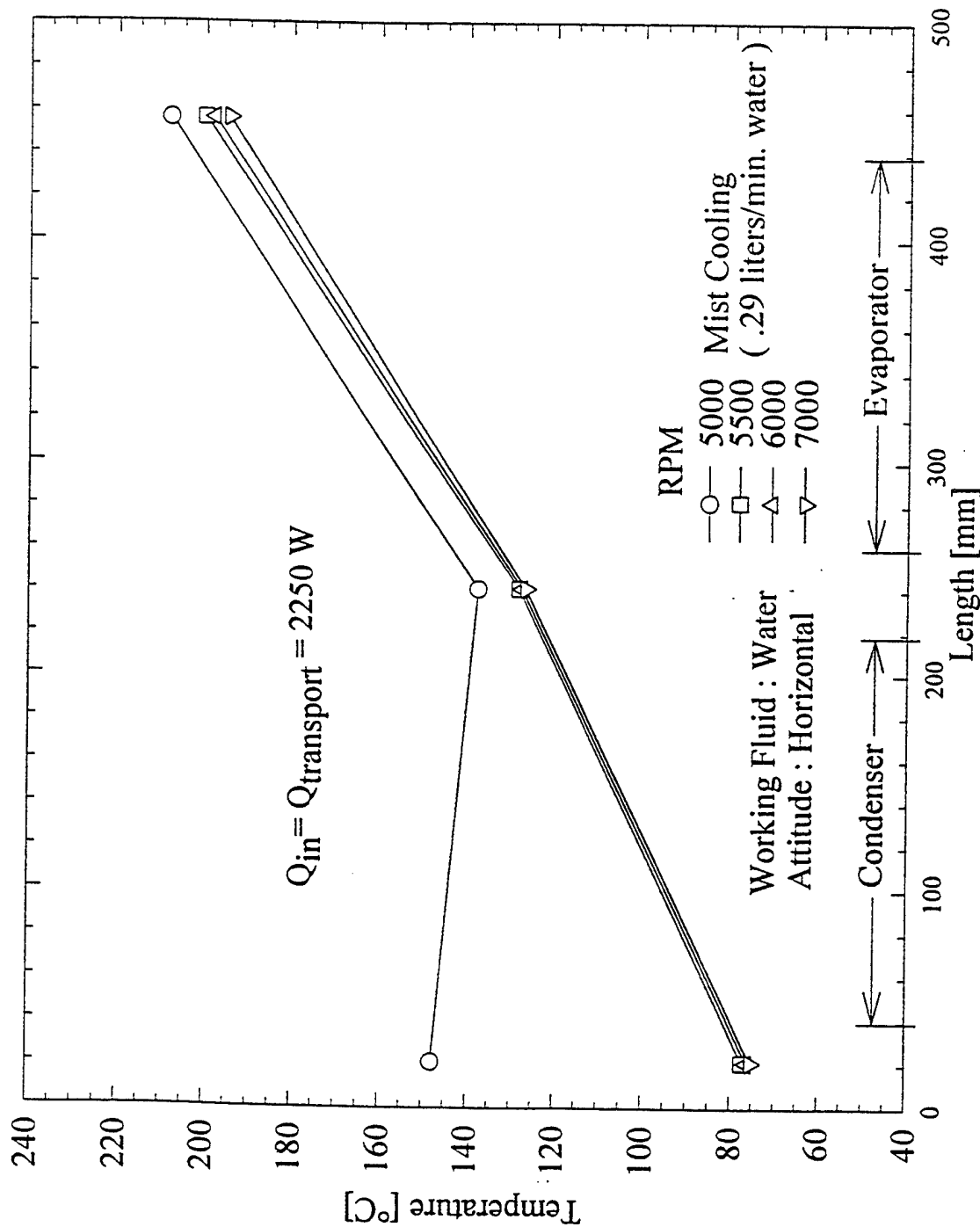
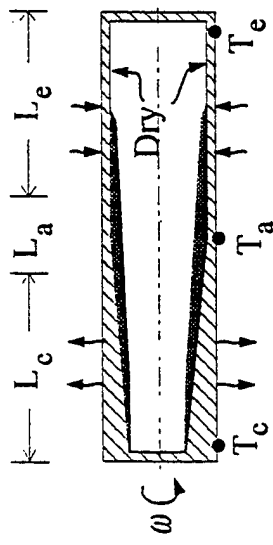


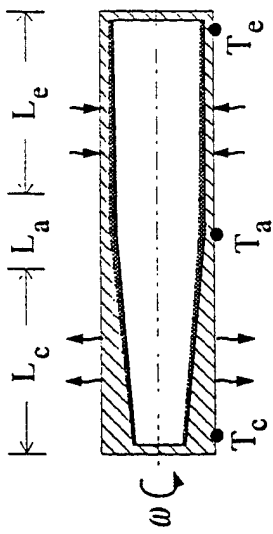
Figure 43. Temperature Profile for 2250 W at Various Speeds.

a)



- Flooded condenser
- Partially dry evaporator
- Low speeds
- Thick liquid film in L_c
- Low ΔT_{ac} ; $T_c \rightarrow T_a$
- High ΔT_{fc} ; Poor heat transfer
- Higher operating temp.

b)



- Efficient condenser
- Fully primed evaporator
- High speed
- Thin liquid film in L_c
- High ΔT_{ac} ; $T_c \rightarrow T_{coolant}$
- Low ΔT_{fc} ; Enhanced heat transfer
- Lower operating temp.

Figure 44. Fluid Distribution Model for RHP.

the entire length. Condenser film thickness decreases and heat transfer increases. Full length of the evaporator participates in heat transfer which reduces the operating temperature. T_c approaches the external coolant temperature. Any further increase in speed will reduce the operating temperature to the design limit. In the present experiment, 7000 rpm was a system limitation. It may be noted that any higher speed capability will certainly enhance the heat transport up to a theoretical limit determined by Eq. (5).

4.2.3 Heat Transport Capacity

The heat transport capacity of the RHP was calculated based on the Nusselt theory of condenser heat transfer analysis described by Daniels and Al Jumaily [7]. According to this analysis, the heat transfer rate at the inner wall of the RHP condenser, as given in Eq. (1), depends on a group of thermophysical properties of the working fluid and some mechanical parameters associated with the design and rotation. The fluid properties group is called the liquid transport factor which comprises the density, thermal conductivity, viscosity and latent heat. The mechanical parameters are condenser length, radius, and taper angle. The other parameters involved are rotational speed, gravity and condensate film thickness/temperature difference. For the chosen fluids and hardware design, the theoretical transport values were calculated and plotted as shown in Figure 45 for 3500 and 7000 rpm at an operating temperature of 140°C. It was separately found that the capacity does not vary significantly within the useful temperature range of operation (300-500K) compared to the effects of ΔT_{fc} and speed for both water and methanol RHPs.

4.2.4 Comparison With Theory

Experimental data points based on the approximate ΔT_{fc} estimation from actual temperature measurements are plotted in Figure 45 along with the theoretical transport curves for comparison. The average operating temperature values calculated as

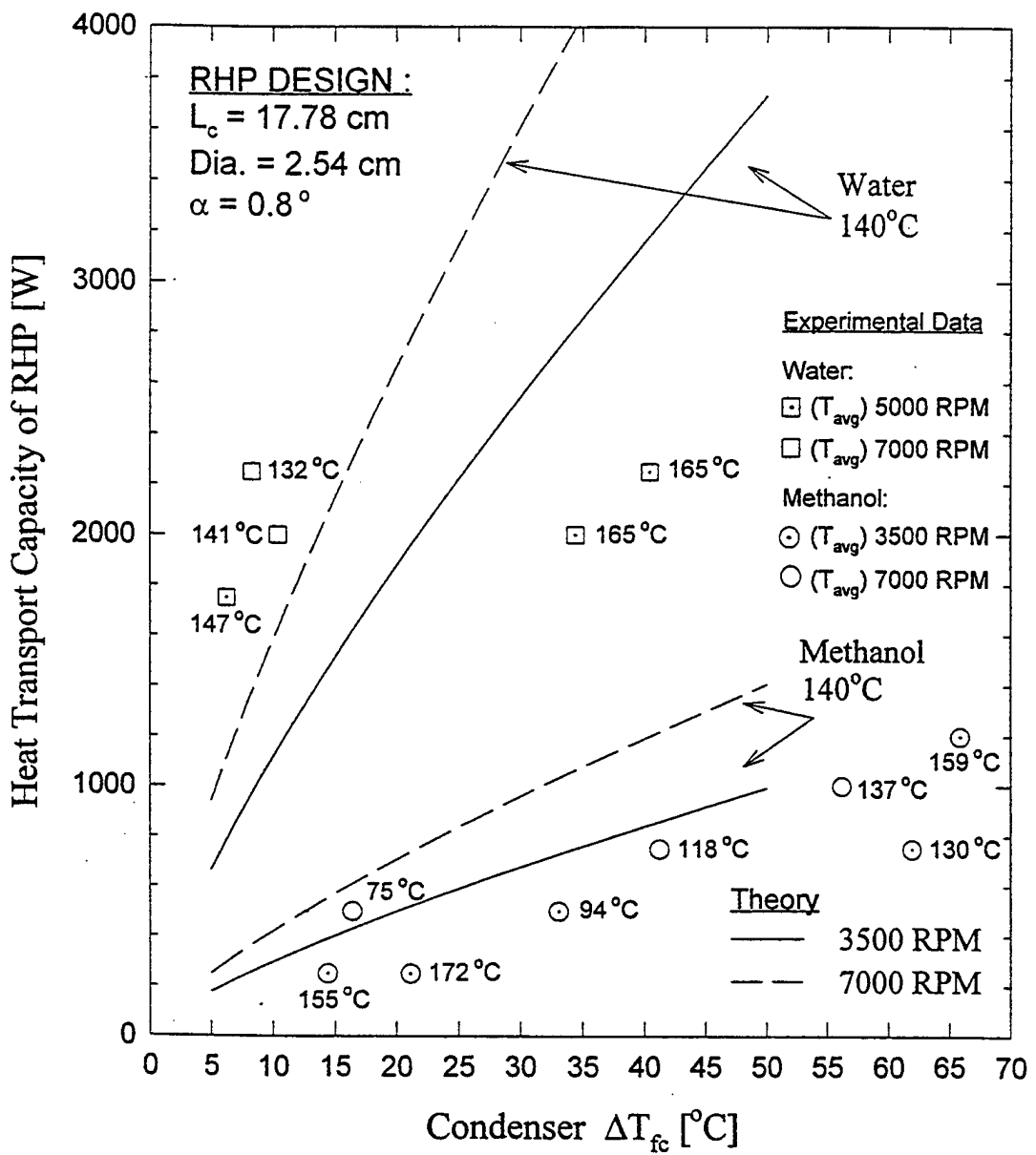


Figure 45. Comparison of Theoretical and Experimental Heat Transport Capacity of the LSRHP Test Articles No. 1 and No. 2.

$$T_{avg} = \frac{1}{3}(T_e + T_a + T_c) \quad (19)$$

from each experimental point is also shown on the graph. Only those data sets which showed the highest condenser-end temperature were used in this plot. In this way, the data corresponding to a quenched-condenser mode of operation were excluded. For normal or near-saturation condition of operation, $T_v = T_s$ and T_v can be obtained by assuming $T_v \approx (T_e + T_c)/2$ and $\Delta T_{fc} \approx 0.5(T_e + T_c) - T_a$ where T_e , T_a and T_c are experimentally measured data at the external locations marked in Figure 7 and Figure 20(a-b). In the absence of internally measured data, this is the closest approximation possible for comparing with the theory. It may be noted that the wall- ΔT s at these points are very small because of the near-adiabatic conditions. Calculations of radiation and convective heat losses from the exposed segments of the RHP to the ambient show that the losses are less than 2.5% of $Q_{transport}$ and hence the above approximation is reasonable.

4.2.5 Comparison of Performances of Water and Methanol RHPs

Maximum Transport: The maximum heat transport attained in laboratory experiments conducted within the safe operating temperature limits is 2250 W for the water RHP and 1200W for the methanol RHP. Figures 46 and 47 show the corresponding temperature profiles of these test runs. It is interesting to note the marked differences between them. The water RHP has nearly twice the transport capacity as that of methanol RHP. The condenser-end temperature is very low in the water RHP compared to the near-isothermal behavior of the methanol RHP. Noncondensable gas blockage in the water RHP is suspected and this aspect is explained elsewhere in this report. The evaporator-to-midsection ΔT is very steep in both RHPs and this is due to the insulating effect of the return-condensate internal-flow which forms a thick layer of liquid-film at the adiabatic section inner wall.

Axial Temperature Profile: External surface temperatures at three or seven spots depending upon the condenser cooling arrangement of the RHP were measured during the performance tests. These temperatures depended on 1) the condenser cooling rate and method,

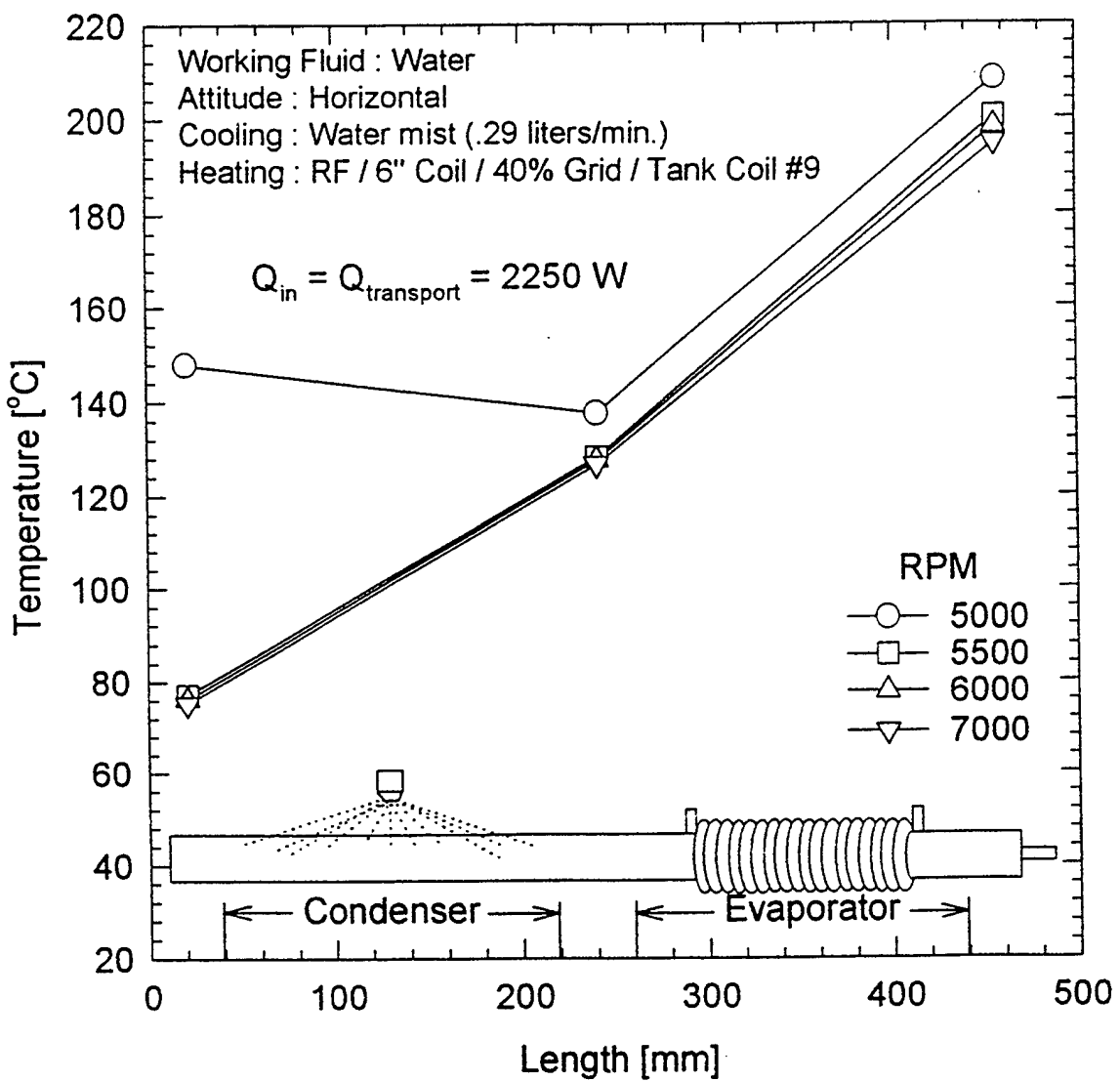


Figure 46. Performance of Water-RHP ($Q_{transport} = 2250 \text{ W}$).

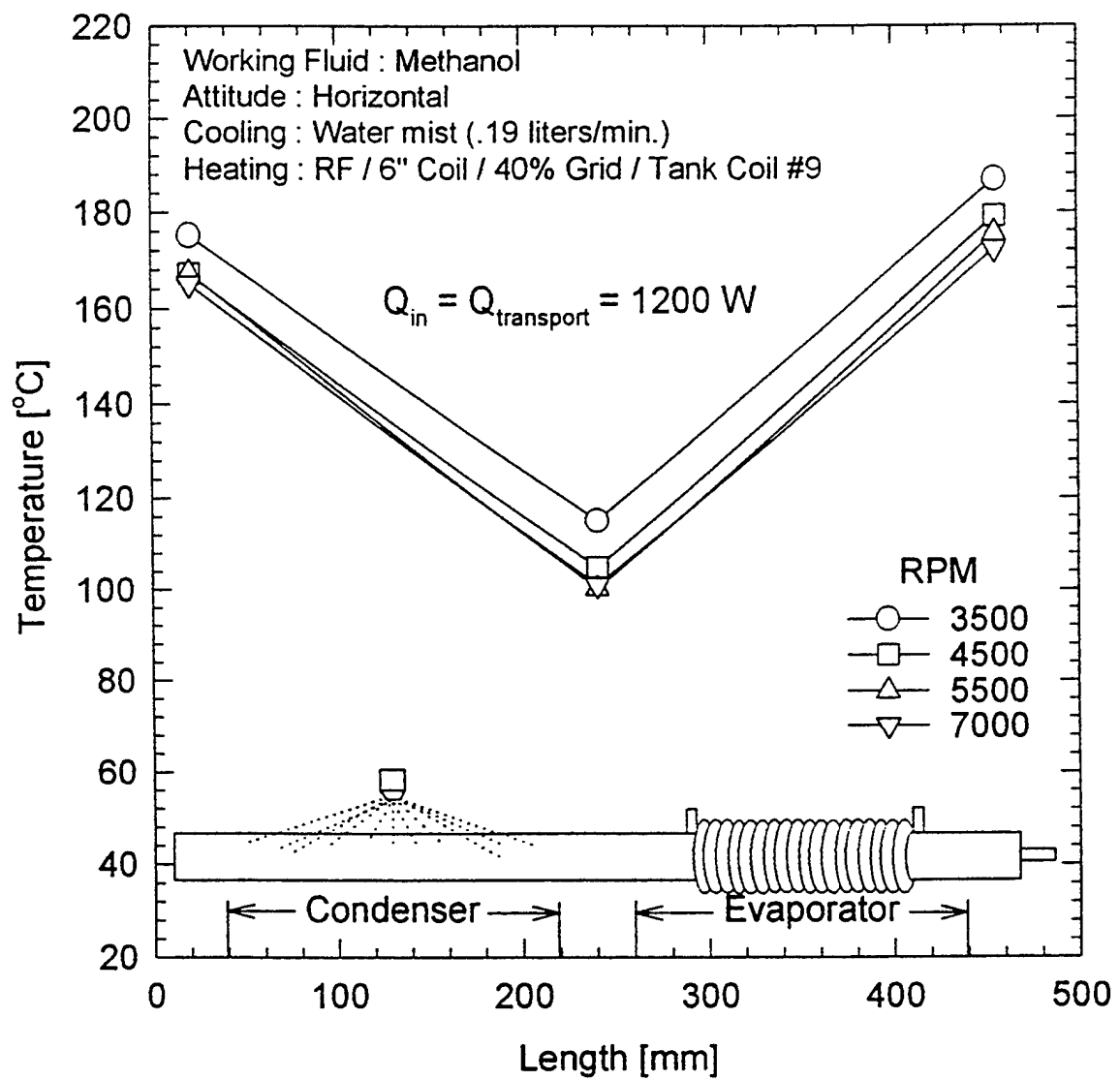


Figure 47. Peak Performance of Methanol-RHP ($Q_{transport} = 1200 \text{ W}$).

2) the evaporator power input, and 3) the rotational speed as illustrated in the axial temperature plots presented here. Figure 48 shows the changes in temperature of the methanol RHP due to the rotational speed variation from 3000 to 7000 rpm and cooling method variation for $Q_{\text{transport}} = 250 \text{ W}$. Obviously, water-mist-cooling provided the best cooling of the condenser compared to the air-cooling. The temperature spread in air-cooling is three times that in the mist-cooling for the same speed variation. Removal of the spray chamber from the condenser section aided the measurement of condenser temperatures at four more locations.

NCG-Free Profiles: It is interesting to note in Figure 48 that the condenser temperatures are higher than the mid-section temperatures. This portrays two facts about the condition of this methanol RHP. Number one fact is that there is no noncondensable gas inside this RHP and the other fact is that the condenser is not flooded with the working fluid. In the case of mist-cooling, condenser-flooding due to external quenching is evident as the condenser-end temperature is much lower than the mid-section temperature. The set of solid symbols represents the air-cooled test run with the cold spray-chamber over the condenser. The difference in the RHP performance between these two air-cooling methods is minimal.

NCG Effect: Figure 49 shows the axial temperature profiles of the water RHP with air-cooling at 250 W, 500 W and 750 W evaporator input power levels. A nichrome wire radiant heater was used and the maximum speed was only 3500 rpm in this earlier batch tests. However, an important comparison of the axial temperature profiles between the methanol and water RHPs can be made. That is, the presence of NCG in the water RHP is evident from the profiles shown in Figure 49. A nearly 100°C drop in the condenser-end temperature is an obvious symptom of gas blockage. The approximate location of the NCG front is marked by the vertical lines "GG" in Figure 49 and it is very clear how the NCG slug gets compressed to the condenser-end with increase in heat transport. Even though a small quantity of NCG may be tolerable, any incompatibility between the working fluid and the container may continuously generate NCG which could shut out the condenser completely. Hence, the useful life of the RHP itself might be shortened. In the present research, stainless steel-316 and water (a combination generally known to generate hydrogen) were selected for strength and weldability reasons. Now that NCG

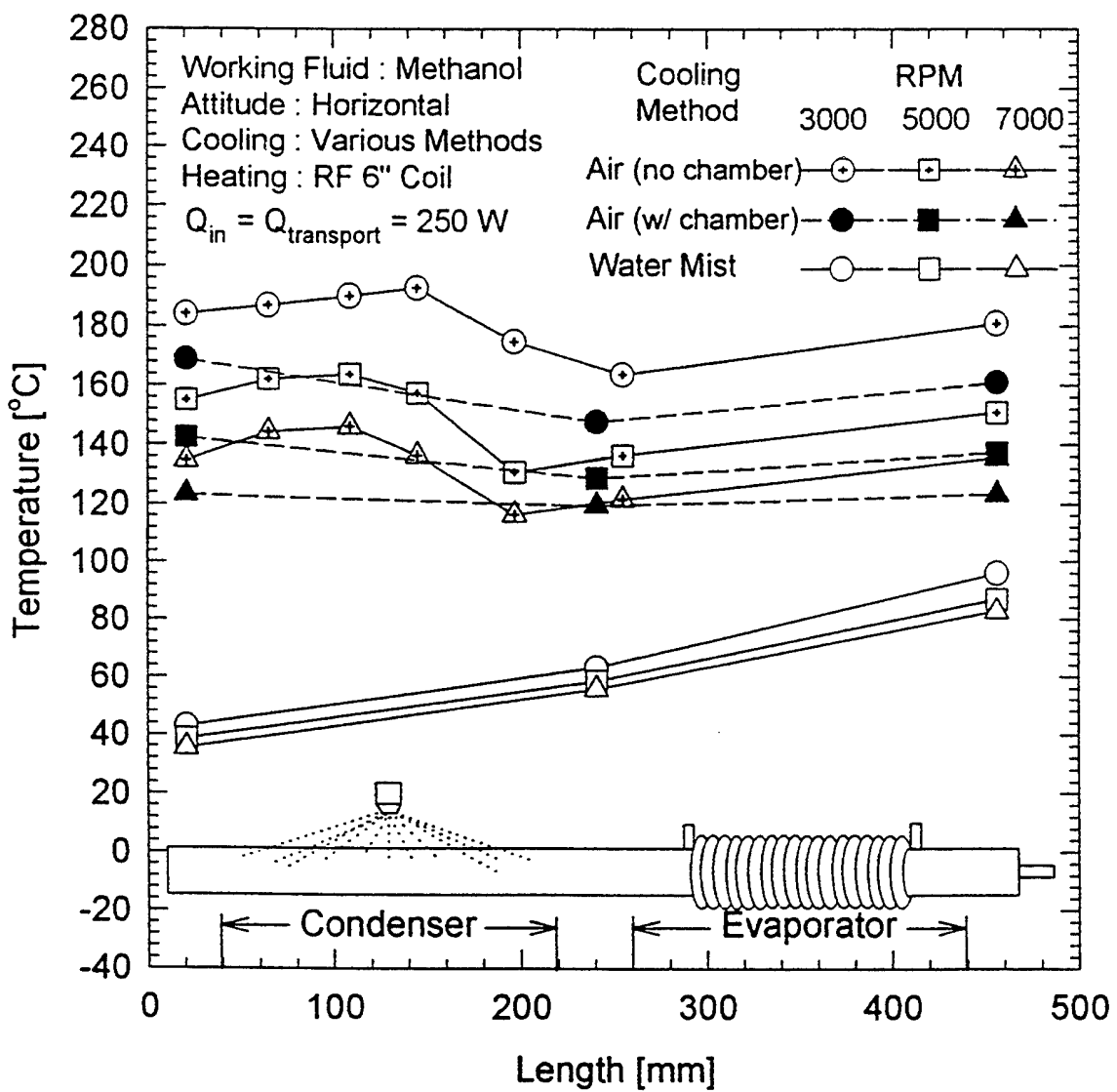


Figure 48. Axial Temperature Profiles - Methanol-RHP (Various Cooling).

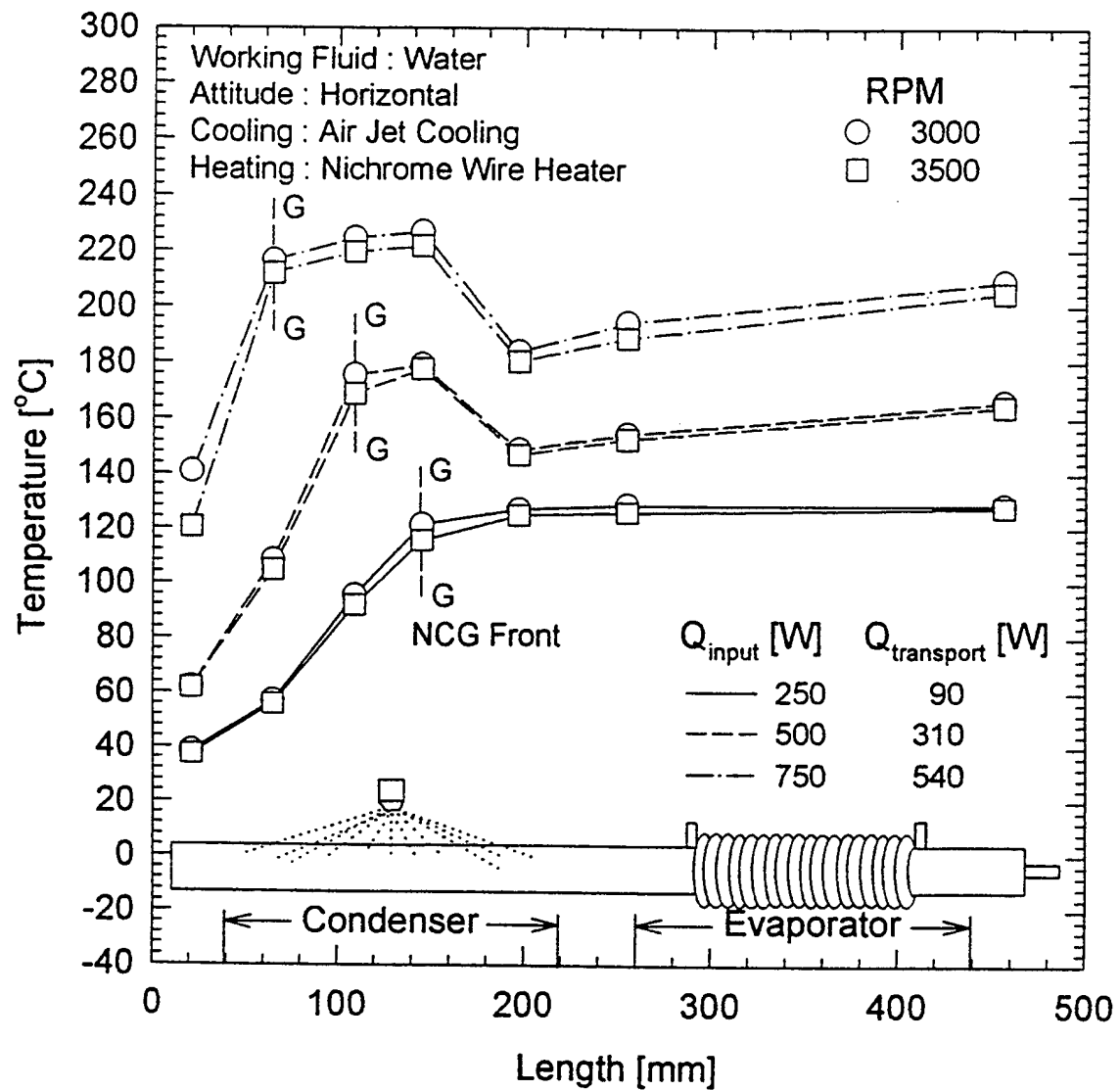


Figure 49. Axial Temperature Profiles - Water-RHP (Air Cooling).

generation is evident in the water RHP, methods to solve this must be sought. Copper-plating and water treatment to inhibit hydrogen generation are possible solutions. At higher power input tests with mist-cooling, the condenser temperatures could not be measured and hence the NCG front cannot be clearly located on the profiles shown in Figure 46.

Effect of Cooling Rate and Speed: The higher the condenser cooling rate and the faster the rotational speed, the cooler the RHP runs for a fixed power input as evident from the foregoing plots (Figures 46-49) and Figure 50. Figure 50 shows the temperature profiles of the methanol RHP for 750 W at 4000 and 7000 rpm with three different settings of the mist-cooling. The temperature spread due to the rpm change is more pronounced than that due to the mist-cooling rate. Similar performance characteristics were observed for the water RHP also (See Ref. 6).

Temperature Leveling Effect: Another interesting observation was made with respect to the low (500 W) and high (1000 W) power input test runs of the methanol RHP shown in Figure 51. This observation is the temperature leveling effect of the RHP for the 1000 W test. In addition to the overall drop in temperature due to increase in speed, the RHP tries to attain isothermality. The 500 W test does not show this effect. The inference is that, at a certain balanced or optimum condition (a balance of speed, heat input and output), the pipe exhibits such a behavior. For 750 W test (not shown here) also this leveling effect was observed. Such characteristics were never observed in the case of the water RHP. The reason may be the presence of NCG in the water RHP.

Summary of Additional Tests on LSRHPs: Identical design stainless steel-water and stainless steel-methanol rotating heat pipes were successfully tested for performance at rotational speeds up to 7000 rpm in horizontal orientation and on-axis mode. The steady state heat transport capacity of the water-RHP was nearly twice (2250 W) that of the methanol-RHP (1200 W) when tested with water mist-cooling and RF heating within the temperature limit of 200°C. A fairly good agreement was seen between the theoretically obtained transport capacity and the experimental results. Contrary to the earlier findings and understanding of the water-

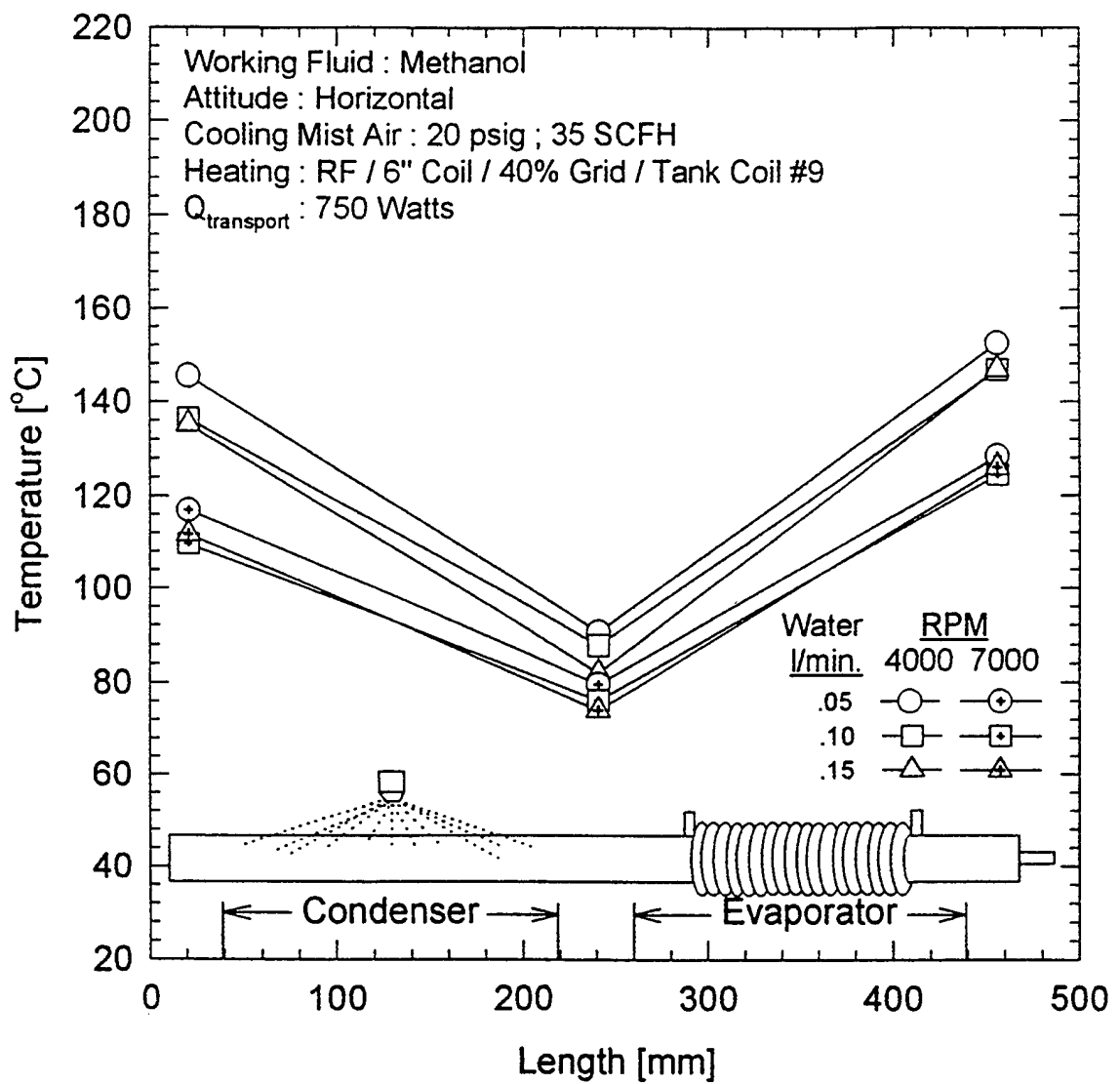


Figure 50. Effect of Mist-Cooling Rate - Methanol-RHP; 750W; 4000 and 7000 rpm.

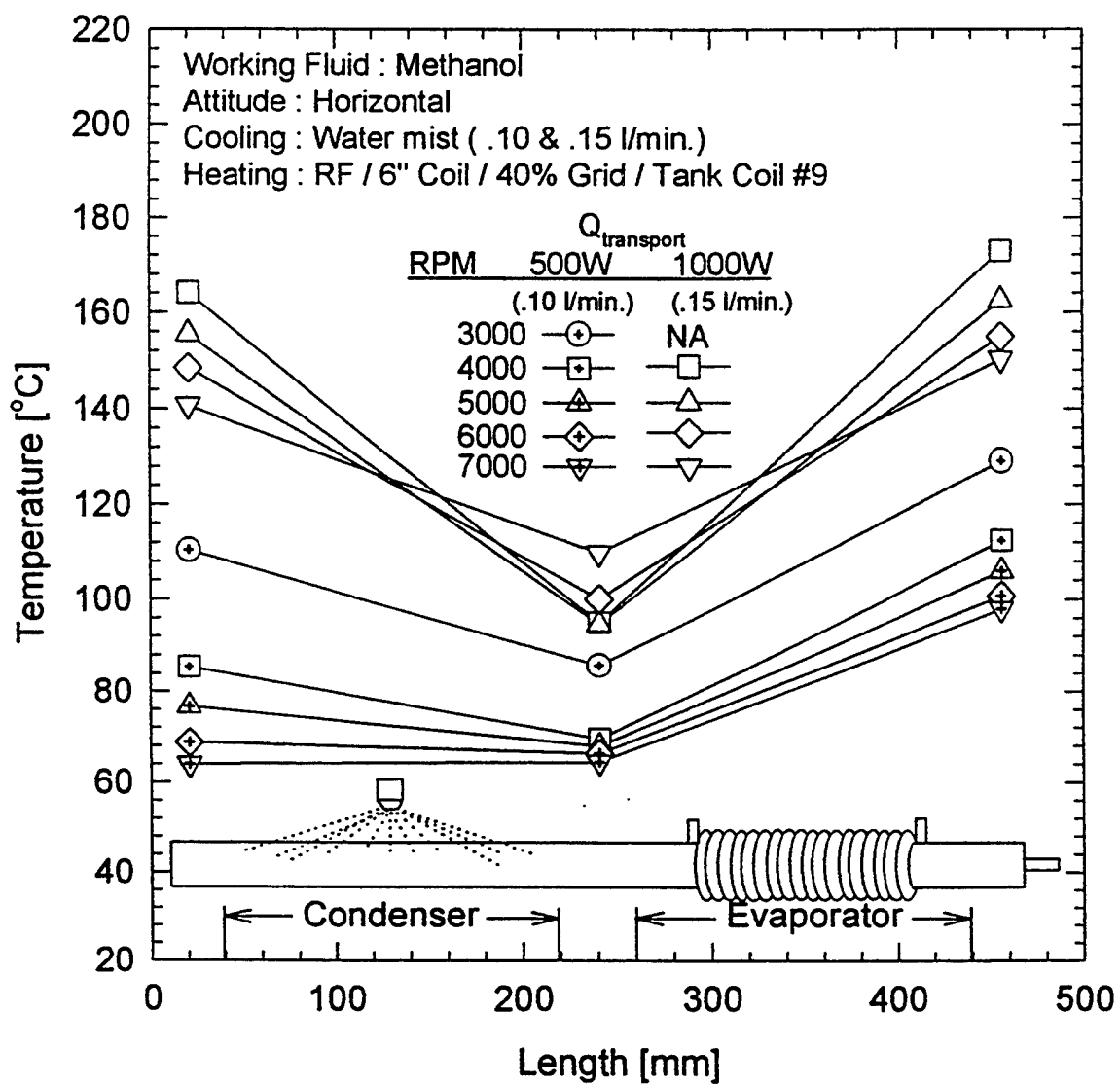


Figure 51. Temperature Leveling Effect - Methanol-RHP; 500 and 1000 W; 3000-7000 rpm.

RHP, it has been determined that an unknown quantity of some non-condensable gas (possibly hydrogen) was present at the time of testing. This fact was further confirmed by the contrasting temperature profiles of the methanol RHP.

A temperature leveling effect from end-to-end for the methanol-RHP was observed at certain balanced or optimum speed and cooling rate settings. This effect was not observed in the testing of the water-RHP.

It has been concluded that the use of a water-in-stainless steel system may be avoided if the application of the RHP is intended for long periods of operation and unless a special gas-inhibiting process is incorporated in the fabrication of the RHP. On the other hand, methanol-in-stainless steel is an excellent system if the capacity limitation is acceptable.

4.3 HSRHP - TESTS

4.3.1 Air Cooling Tests - Water and Methanol RHPs

Both HSRHP test articles no. 1 and no. 2 were tested at speeds up to 30,000 rpm and power inputs up to 750 W in the air cooling mode. The magnetic seals and chamber were not necessary since the cooling air was exhausted into the room. This configuration allowed four additional temperature monitoring spots on the condenser section. In order to get a feel for no load (heat load) performance, the RHPs were run with no heat input to the evaporator at all speeds. In all cases of the tests, temperatures as measured on the outside wall were plotted as functions of the axial length. Figures 52 through 55 show these plots for methanol-HSRHP for 0, 250, 500 and 750 W, respectively. Compressed air at room temperature was blown at the rate of 525 SCFH. The ends of the RHP warmed up by 8°C due to the frictional heating effect of the support bearings at 30,000 rpm for the 0 W input case (Figure 52). Enhanced cooling effect due to increased speed is evident from these plots. The dip in the midsection temperatures (500 W and 750 W cases) is due to the insulating effect of the condensate return liquid film.

10" Methanol Pipe

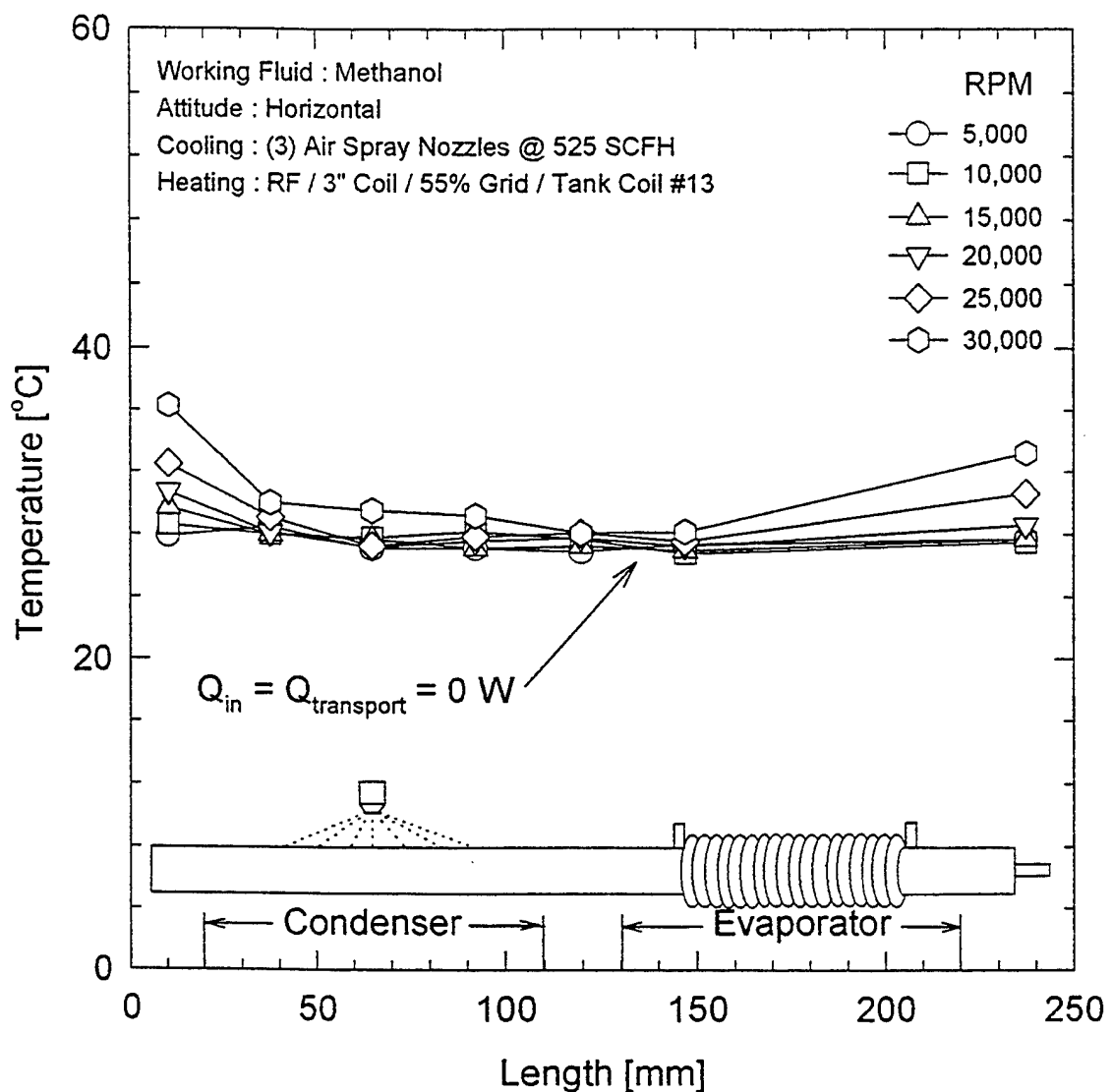


Figure 52. Axial Temperature Profile of Methanol-HSRHP: Air Cooling; 0 W.

10" Methanol Pipe

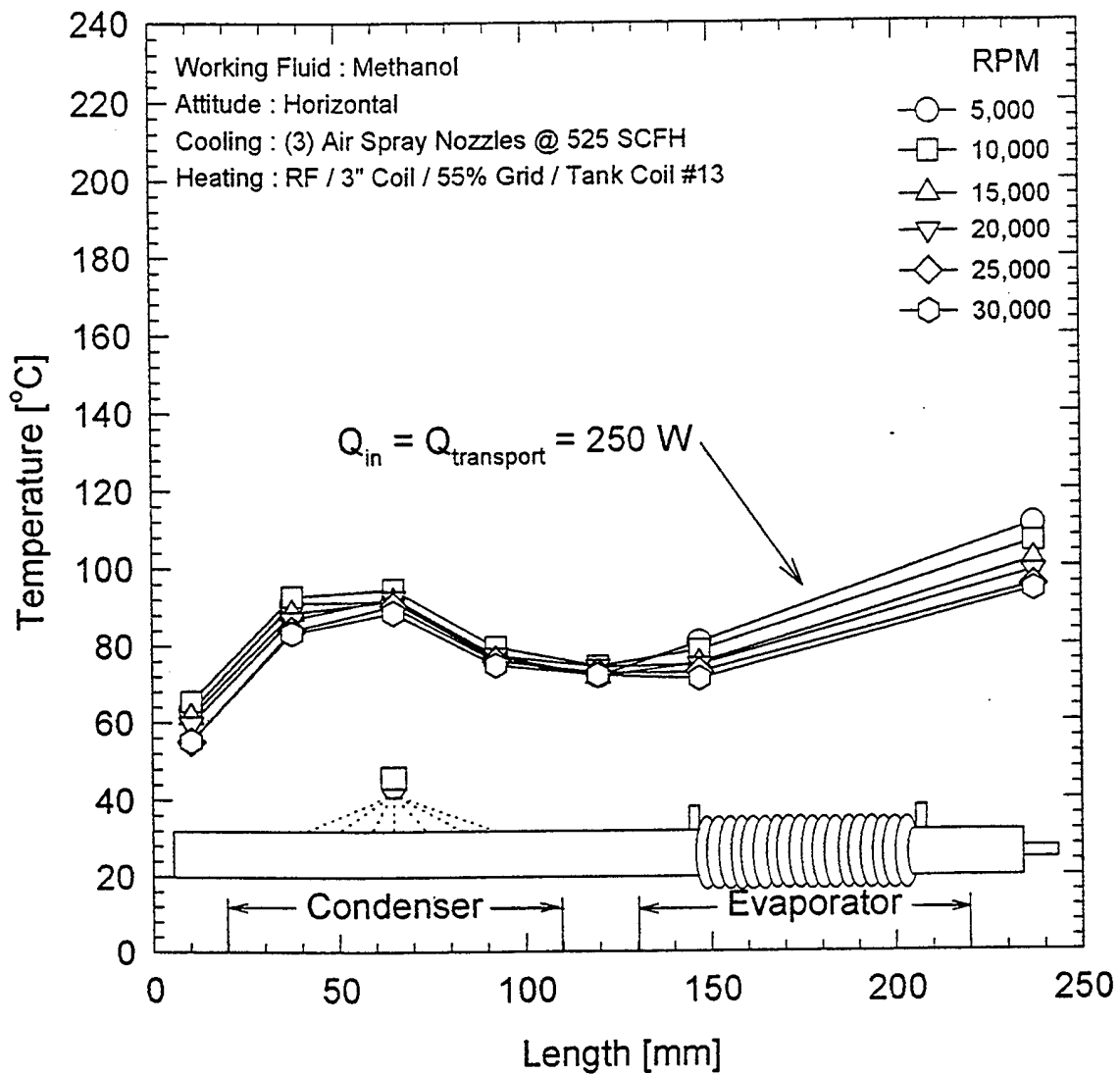


Figure 53. Axial Temperature Profile of Methanol-HSRHP: Air Cooling; 250 W.

10" Methanol Pipe

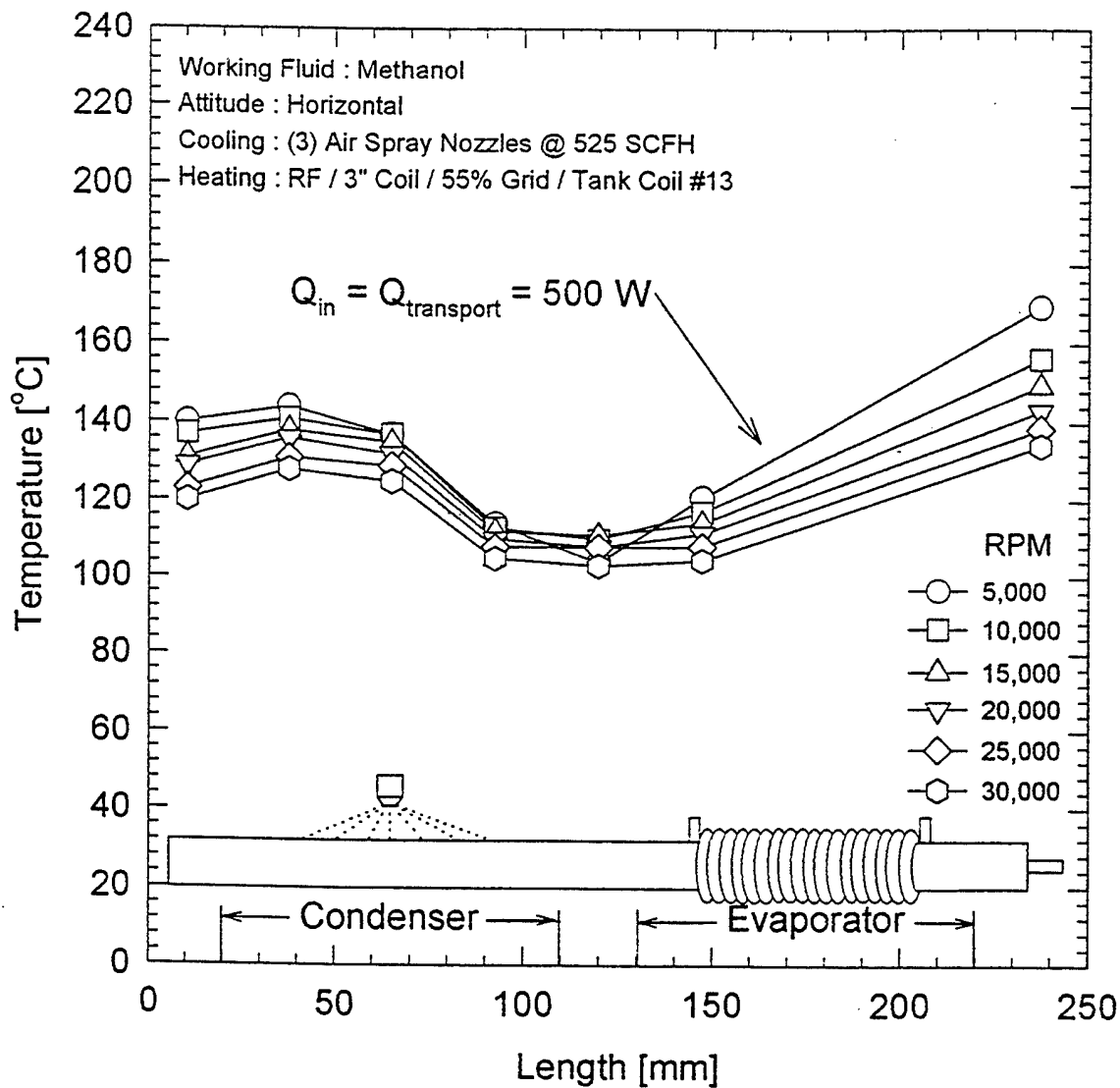


Figure 54. Axial Temperature Profile of Methanol-HSRHP: Air Cooling; 500 W.

10" Methanol Pipe

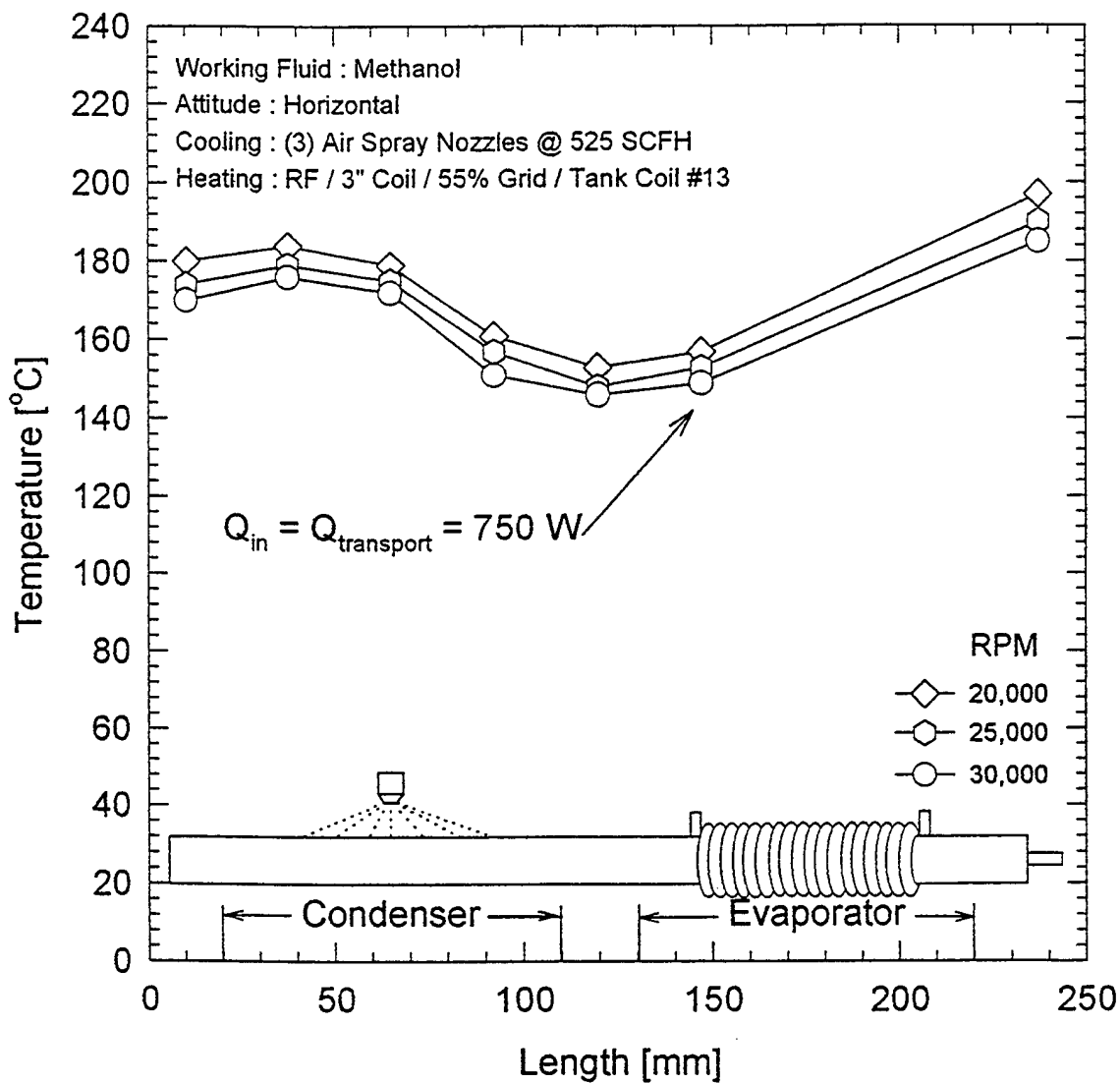


Figure 55. Axial Temperature Profile of Methanol-HSRHP: Air Cooling; 750 W.

Figures 56 through 59 show the plots for water-HSRHP for 0, 250, 500 and 750 W cases, respectively. The conditions of tests are identical to those of the methanol unit. The water unit operates at slightly lower temperatures compared to the methanol unit for identical test conditions. This may be attributed to the difference in their liquid transport factor explained in Section 2.0.

4.3.2 Oil-Spray Cooling Tests - Methanol RHP

Temperature Profile: The axial temperature profiles for the oil-spray cooled mode are presented for 0, 250, 500, 750, and 922 W cases, respectively in Figures 60 through 64. As in air-cooled mode, the three nozzle system inside the condenser chamber was used. The magnetic seals were in place to contain the oil and the oil flow rate was 0.75 gpm. The 0 W input case plotted in Figure 60 shows that the condenser-end of the HSRHP was approximately 15°C warmer than the evaporator-end. This is attributed to the heat generated by the magseals. Because of this added heat input in the condenser region, the temperature profiles for all levels of heat input at the evaporator appear to show a negative trend with respect to the speed. Without the heating effect of the seals, the temperature profiles should follow the correct trend.

Calorimetry: By measuring the temperature rise of the spray-oil at the condenser chamber, the heat removed by the oil was calculated. As seen included in Figure 64, the values of Q_{out} at various speeds averaged 656 ± 20 W for an input of 922 W which means that there was about 29% of unaccounted losses. The measurement accuracy of various parameters and the un-insulated condenser chamber contribute to this discrepancy. An uncertainty analysis is provided in Appendix E.2.

4.4 DISCUSSION ON THE CHOICE OF CONDENSER COOLING

It is evident from the foregoing test results that the external condenser cooling method is one of the most important factors in determining the maximum heat transport capacity of any RHP. For a given condenser length, the external heat removal depends on the convective heat

10" Water Pipe

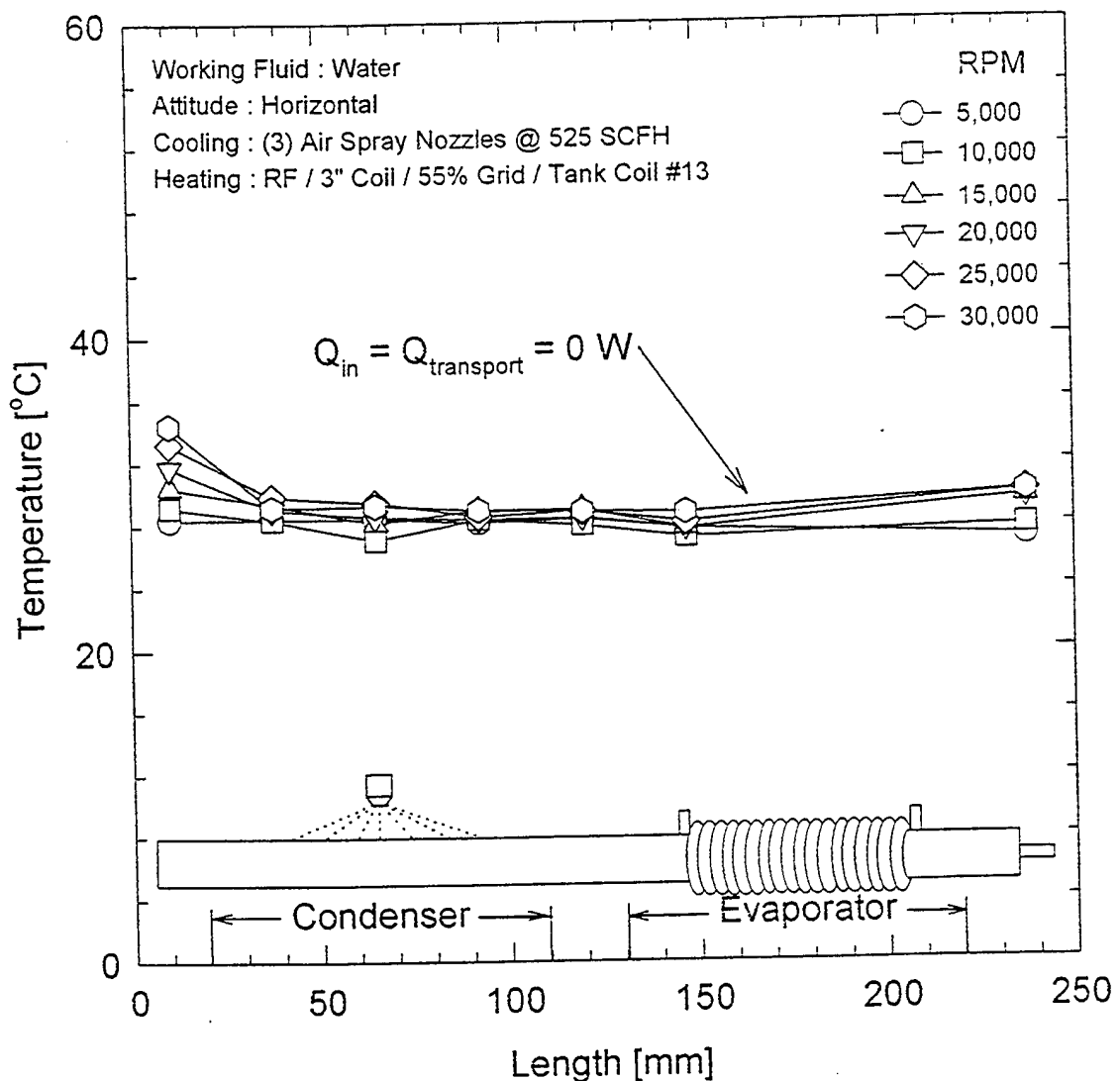


Figure 56. Axial Temperature Profile of Water-HSRHP: Air Cooling; 0 W.

10" Water Pipe

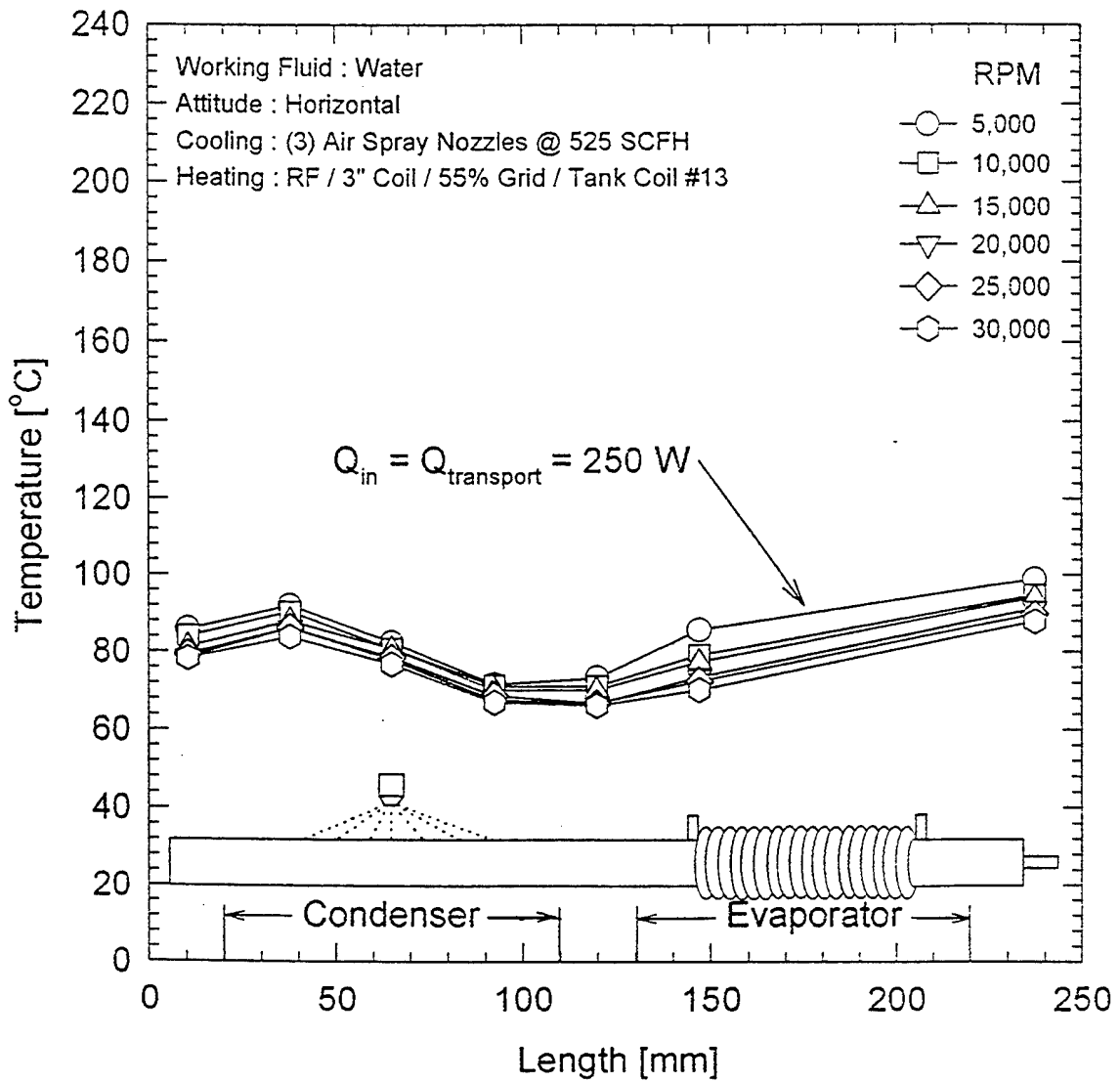


Figure 57. Axial Temperature Profile of Water-HSRHP: Air Cooling; 250 W.

10" Water Pipe

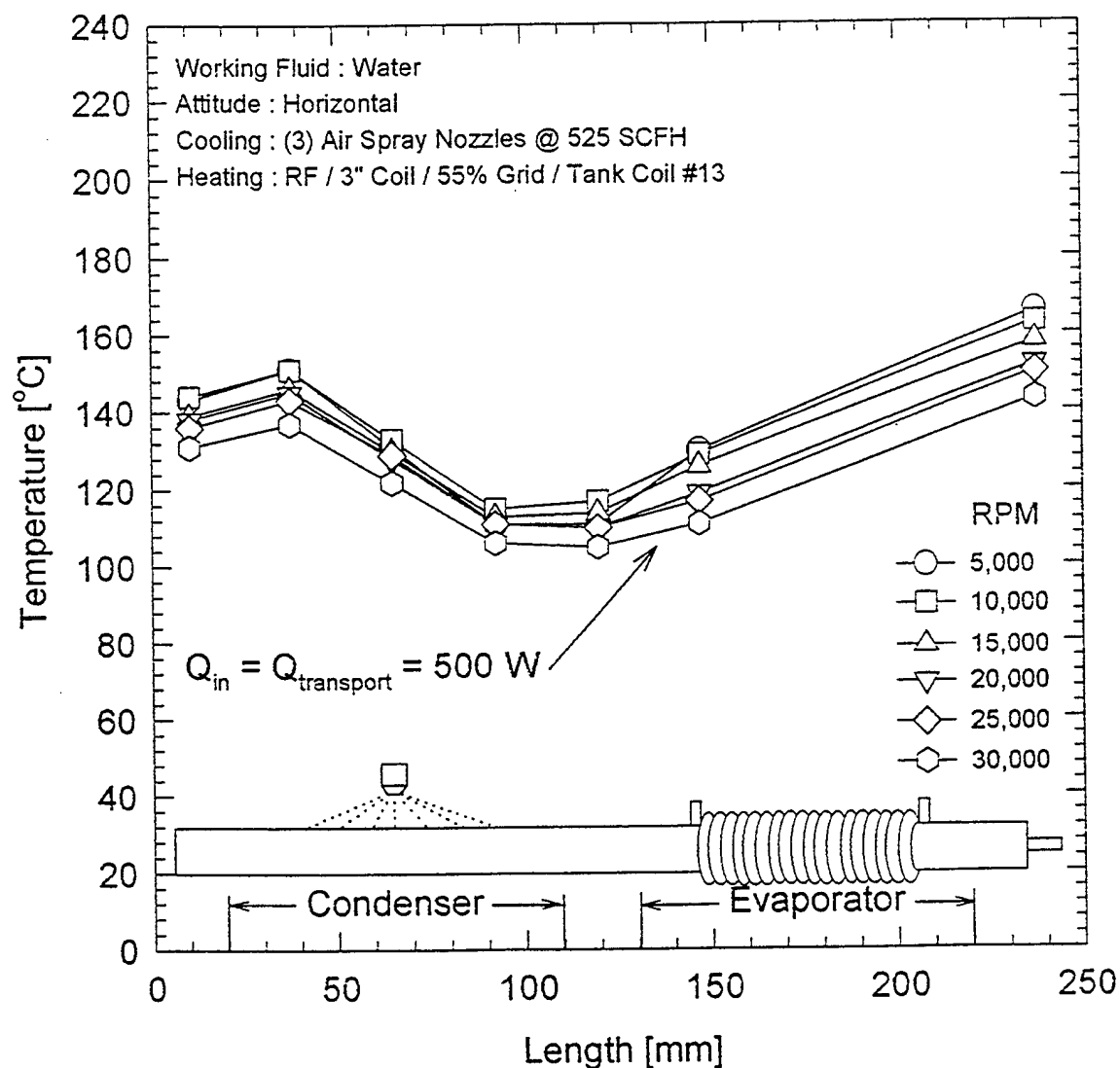


Figure 58. Axial Temperature Profile of Water-HSRHP: Air Cooling; 500 W.

10" Water Pipe

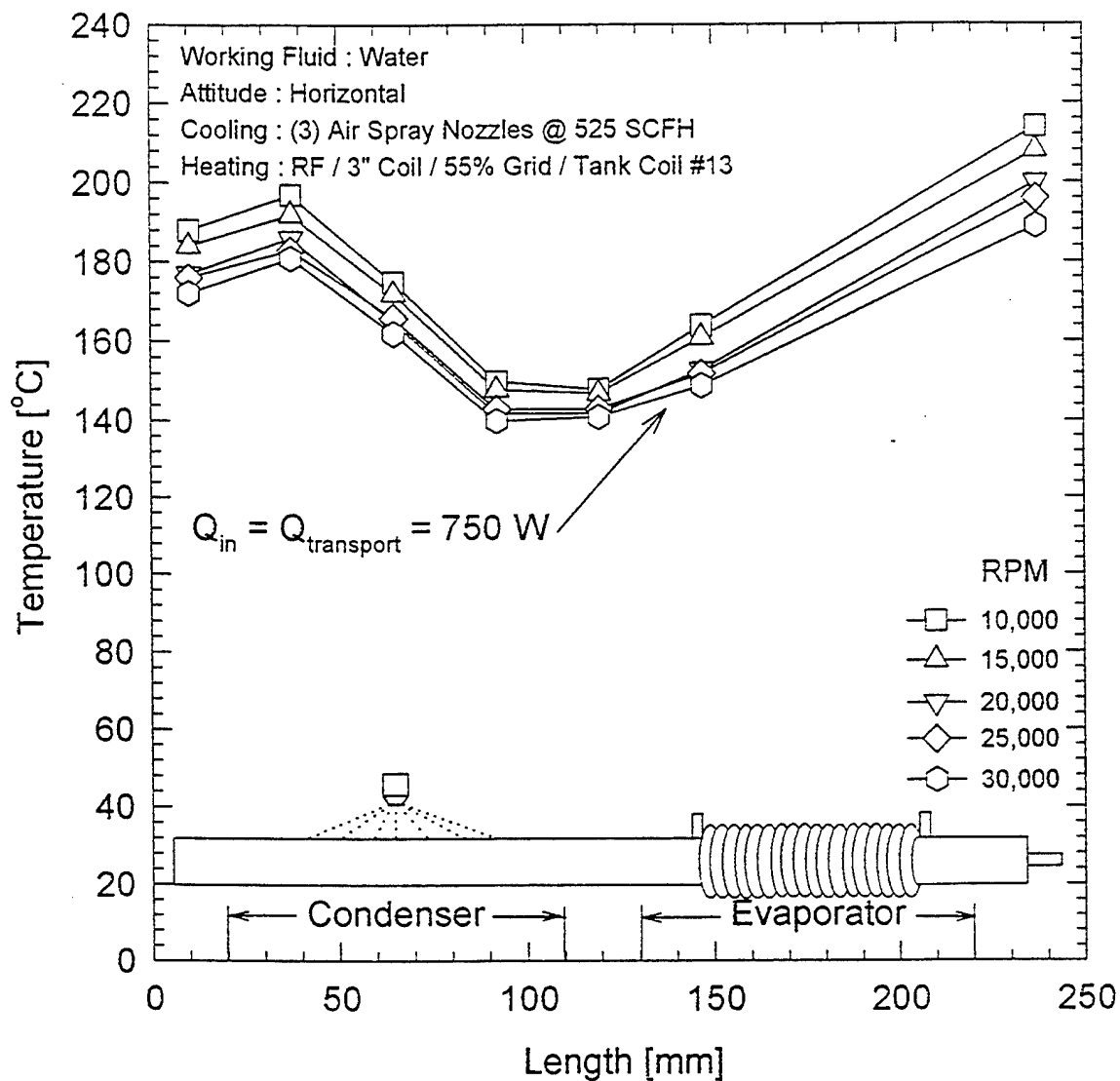


Figure 59. Axial Temperature Profile of Water-HSRHP: Air Cooling; 750 W.

10" Methanol Pipe

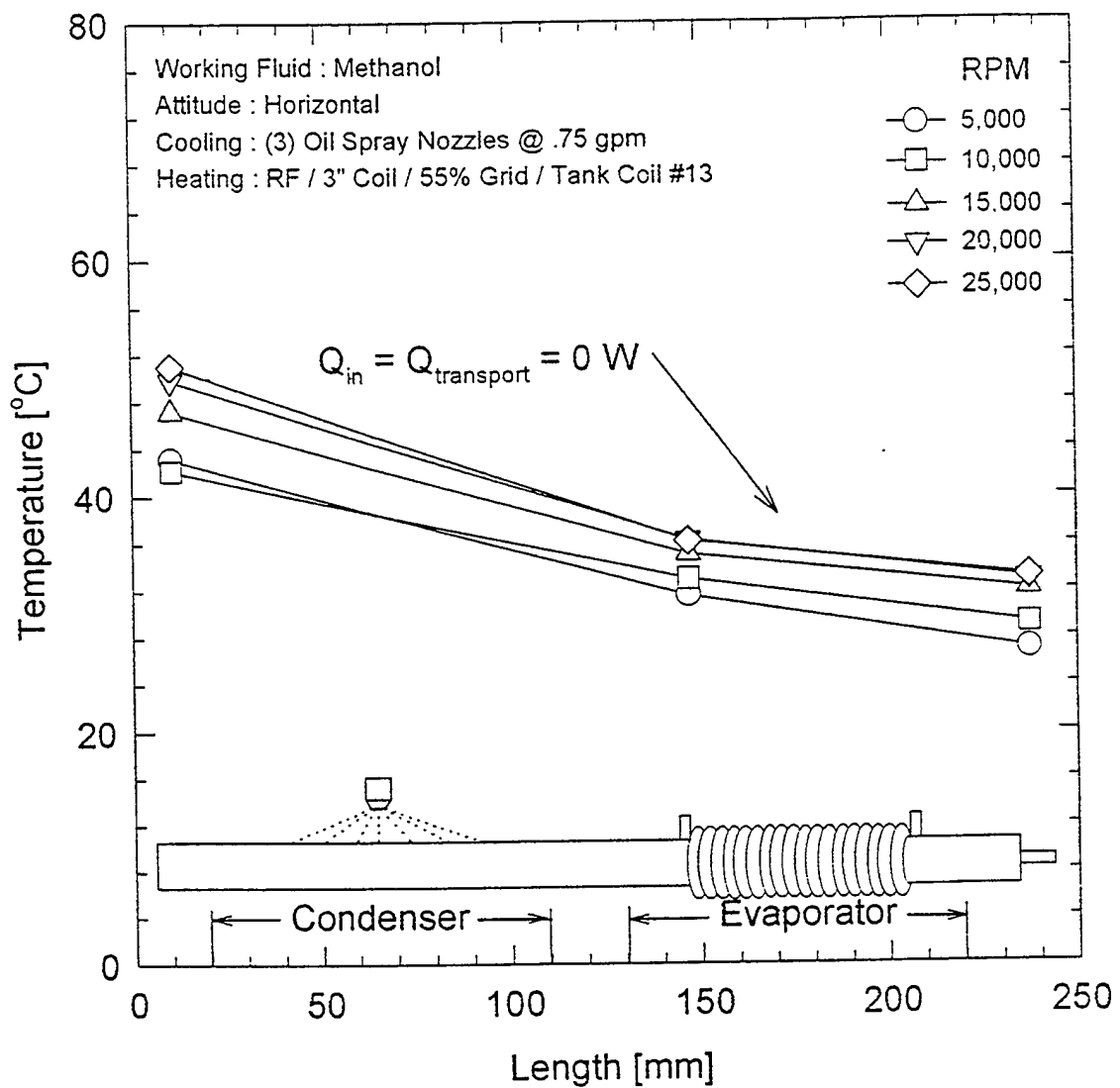


Figure 60. Axial Temperature Profile of Methanol-HSRHP: Oil-Spray Cooling; 0 W.

10" Methanol Pipe

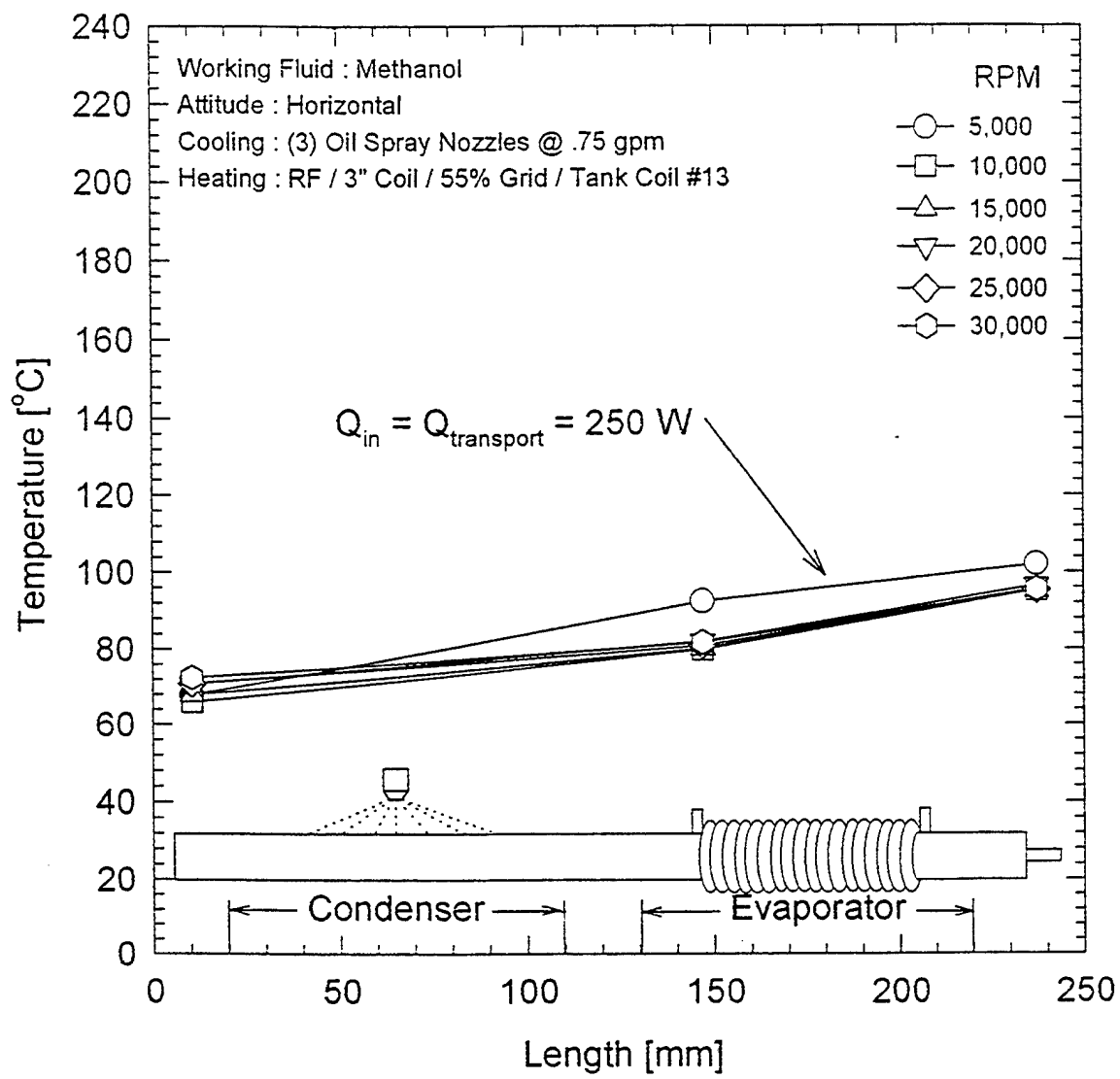


Figure 61. Axial Temperature Profile of Methanol-HSRHP: Oil-Spray Cooling; 250 W.

10" Methanol Pipe

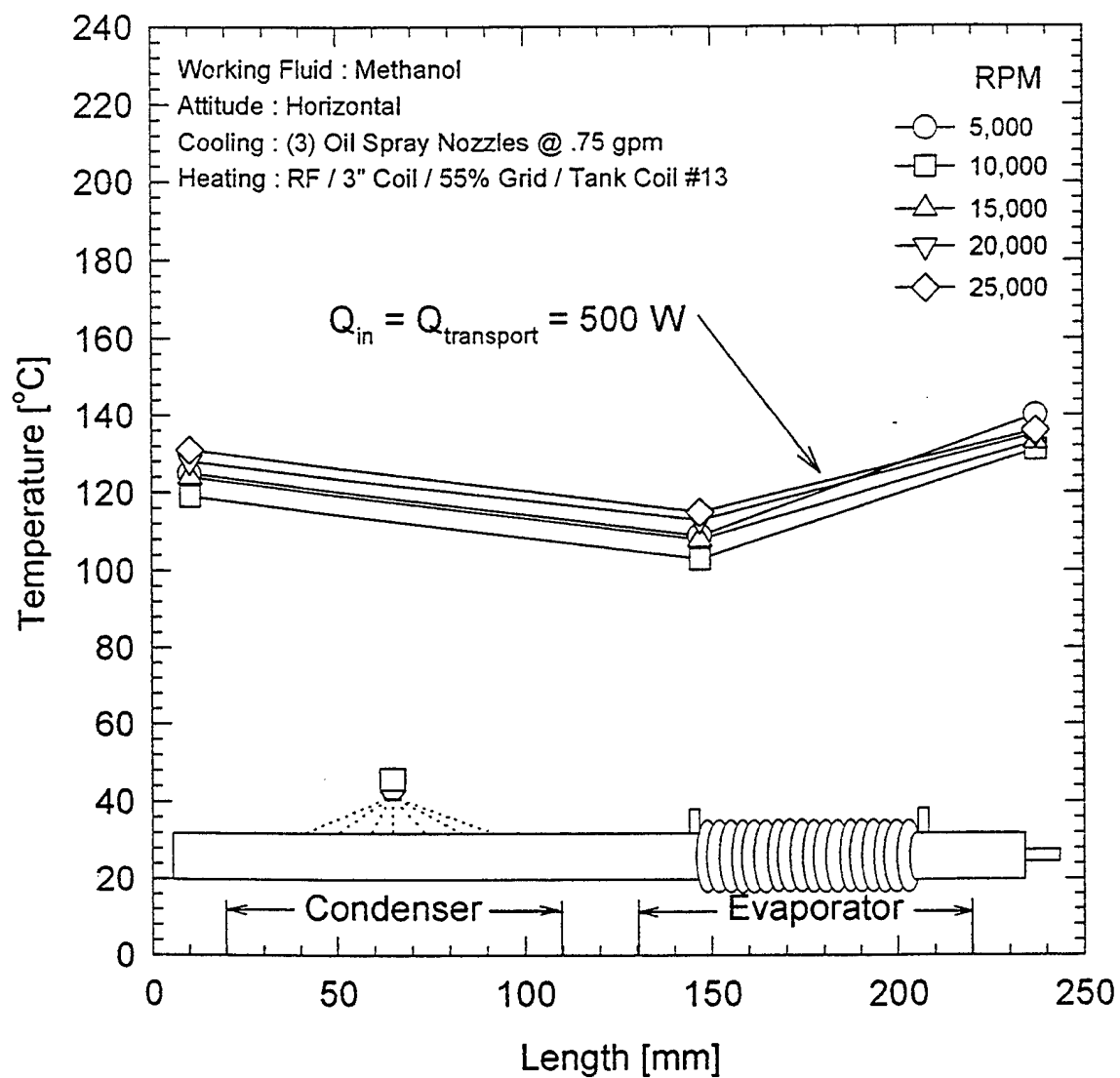


Figure 62. Axial Temperature Profile of Methanol-HSRHP: Oil-Spray Cooling; 500 W.

10" Methanol Pipe

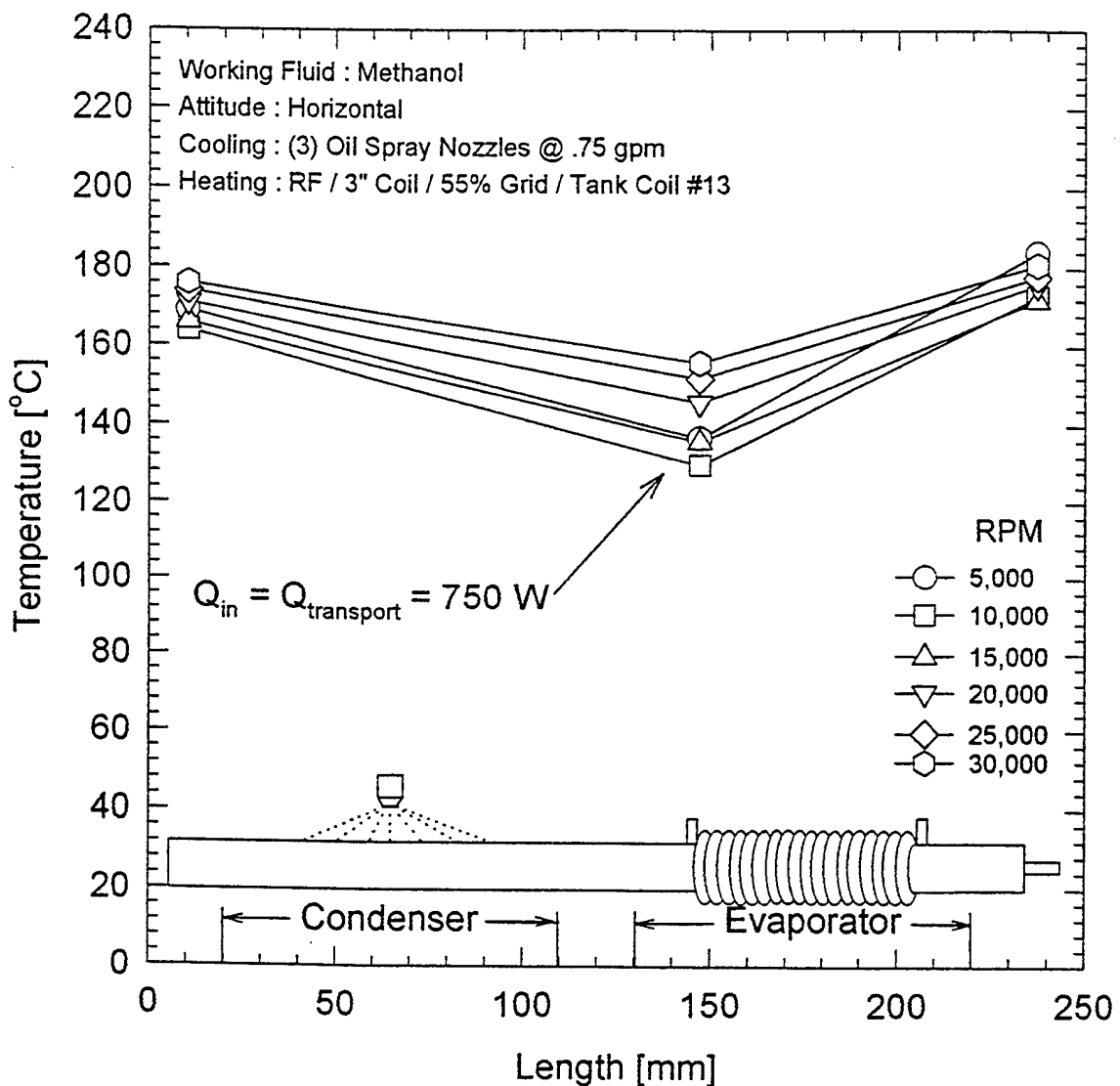


Figure 63. Axial Temperature Profile of Methanol-HSRHP: Oil-Spray Cooling; 750 W.

10" Methanol Pipe

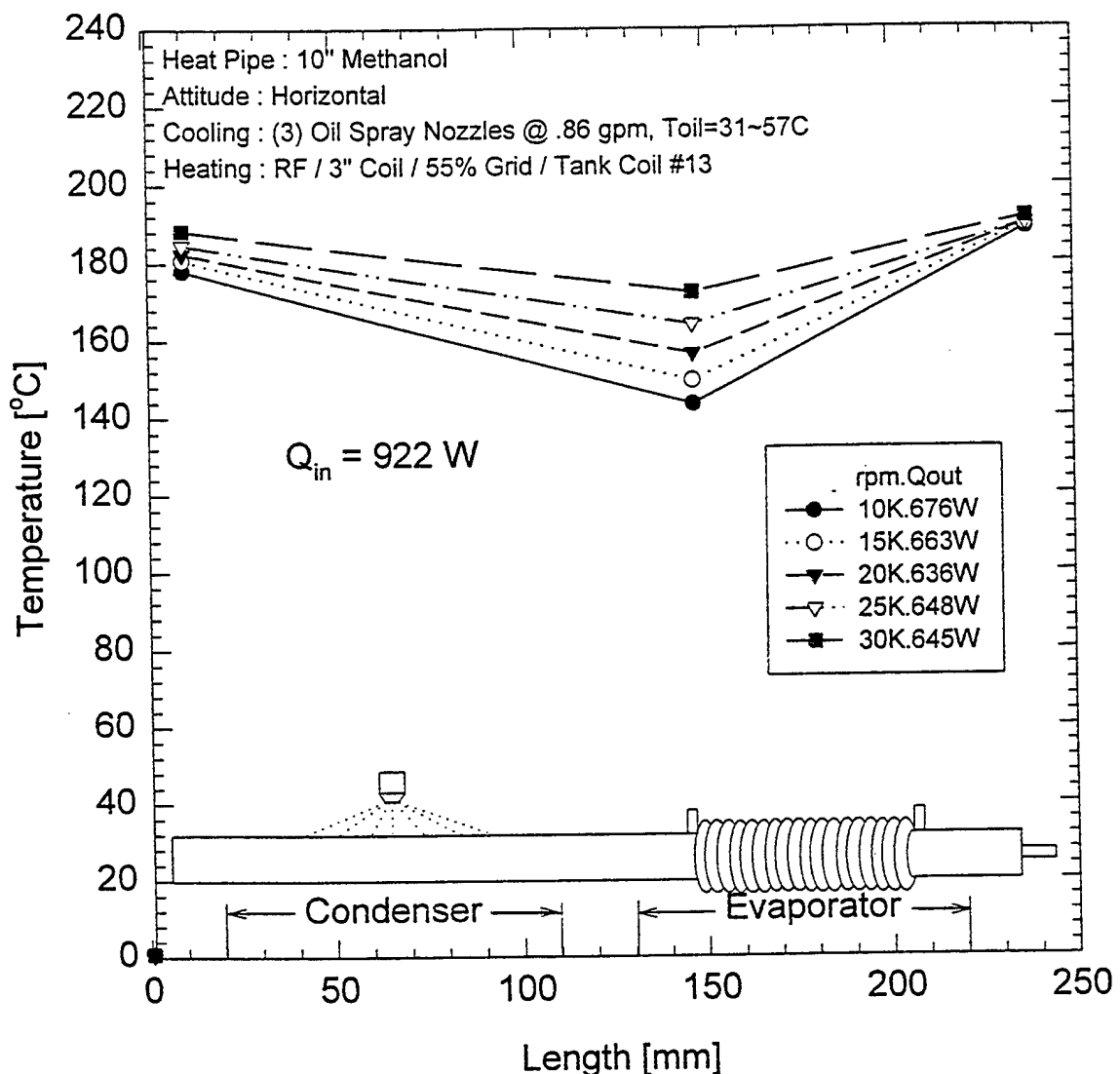


Figure 64. Axial Temperature Profile of Methanol-HSRHP: Oil-Spray Cooling; 922 W.

transfer coefficient (h_c) of the cooling process. Obviously, h_c will be the highest for the air-water mist because of the very high phase-change (liquid-to-vapor) energy potential. This is verified to be true in the LSRHP tests wherein a 2250 W transport capacity has been attained (Figure 43). The corresponding performance limit with air-jet cooling is only 225 W (Figure 40). It should also be noted that the air-jet cooling arrangement in these tests was not optimized for maximizing the transport capacity and, hence, we cannot discard this method of cooling for its poor performance. From an MEA standpoint, use of stored water coolant may not be acceptable.

In the later tests on the HSRHP units, only air-jet and oil-spray cooling were employed. Both techniques may be feasible according to the MEA design philosophy. However, the least complicated process or system may appeal better than those involving rotary seals, life-limiting factors and service downtimes. In the HSRHP units, only half the length of the condenser size used in LSRHP was employed because of the size reduction brought about by critical speed consideration. Due to the powerful fan-jets (3) with an air flow rate of 525 SCFH at 80 psig, transport capacity as high as 750 W was attained for both HSRHPs (Figures 55 and 59). This result is a welcome feature for MEA. With suitable RHP design modifications, including condenser length and diameter, air flow rate and pressure, IPU rotor interface, etc., one can easily meet the IPU cooling requirements by employing an air-cooled condenser design. The limit on cooling capacity may be more than compensated for due to the avoidance of problematic seals.

It may be noted that the oil-cooling experiments were performed (in spite of the difficulties) in the present research effort, simply to compare and contrast the results for better understanding. It should not be construed that oil cooling with magseal arrangement is recommended for advanced IPU or MEA applications. However, for the intermediate needs where a retrofit to an existing system is possible in medium speed ranges (5,000-15,000 rpm), the oil-cooling mode of RHP rotor may be the most advantageous.

5.0 SUMMARY OF CONCLUSIONS AND RECOMMENDATIONS

5.1 CONCLUSIONS

The following is the summary of major findings of the present research effort.

- 1) The rotating heat pipe (RHP technology has been fairly well researched in the low to medium speed ranges up to 12,000 rpm. Electrical machine rotor cooling has been the major application area of this technology. There are no published research literature dealing with RHP at rotational speeds in the range of 12,000-60,000 rpm.
- 2) The present work is the first ever effort to plan and demonstrate the performance of the RHP at speeds up to 30,000 rpm. This design is potentially paving the way for addressing the thermal management issues of the advanced permanent magnet and switched reluctance type, high power density electrical machines, IPU, IS/G, etc., which are currently in development under the Air Force's more-electric aircraft initiative.
- 3) Rotor dynamics aspects including the critical speed phenomena, balancing, thermal expansion, vibration monitoring and control, high speed bearings and lubrication, etc., are overwhelming complexities which need special attention at all times of the RHP development.
- 4) Methanol and water in stainless steel RHPs were processed and tested in the temperature regime 25-200°C and heat transport capacity range of 100-2250 W. Air-cooling, air-water mist cooling and oil-spray cooling methods were devised and successfully employed in laboratory testing. Also, RF induction heating and infra-red temperature sensing techniques were favorably used in these tests.
- 5) The existing models of theoretical analysis for predicting RHP performance were reviewed and the areas of improvement and modifications which include separate vapor and liquid phase numerical modeling, Corolis force effects at high speeds,

and conjugate heat transfer modeling to couple the external and internal heat transfer mechanisms were identified.

- 6) It was found that single phase cooling methods are less efficient for condenser heat removal. On the other hand, the more efficient methods (air-water mist and oil-spray) are cumbersome and involve problematic seals. A compromise could be to optimize the design for efficient air-cooling which would be preferable for an aircraft application.
- 7) The thin oxide coating formed inside the RHP container by baking it at 450°C for 2 hours in air atmosphere was supposed to inhibit gas generation in the water-RHPs. There are mixed results on this aspect. The LSHRP unit showed NCG effects and the HSRHP tests are inconclusive.
- 8) Two general operating conditions of internal heat transfer processes are observed and characterized based on the fluid distribution model. For a given heat load, flooded condenser with partially dry evaporator condition exists at low speeds and an efficient condenser with fully primed evaporator condition results at high speeds (>5000 rpm).
- 9) The results are very encouraging and there is a great potential for this technology to mature and find application in the thermal management of the advanced high power electrical generators.

5.2 RECOMMENDATIONS

The following recommendations are suggested for future work in this research.

- 1) The non-contact external surface temperature measurement is the only viable technique known and being used. In order to obtain detailed mapping of the axial temperature profile, additional target spots within the evaporator and condenser zones should be obtained.
- 2) An RF load-coil with sufficient opening (for IR target spots on the RHP evaporator wall) at close intervals (at least 1 inch pitch) may be made and calibrated.

- 3) The present RF heater cannot be precisely controlled for output power to ± 25 W. A better RF heater unit will improve the overall accuracy of the experimental results.
- 4) Tests with adverse and favorable tilt of the RHP axis may be carried out for evaluating the limits of performance.
- 5) A calorimetric measurement of the condenser heat removal may be performed for the case of air-cooled tests.
- 6) The heat addition due to the magseals and bearings influence the axial temperature profile. Numerical analysis should be performed to decouple these effects from the temperature profile due to the normal mode of heat transport.
- 7) The comparison of experimental data and the theoretical results reveal poor match due to the uncertainties in the theoretical model and the inability to measure the internal temperature of the RHP. A numerical model which would predict the RHP performance in terms of the evaporator heat input and external surface temperatures must be developed.
- 8) In order to simplify the fabrication of the internal taper, stepped or straight cylinder designs without taper may be tried. These designs would be as efficient as the taper designs because of the high speeds.
- 9) Internal fins or sinter wick designs may be considered for enhancing the evaporative and condensing heat transfer within the RHP.
- 10) The suspected NCG effect in water-stainless steel system may be further explored.

6.0 REFERENCES

1. Quigley, R.E. Jr., "More Electric Aircraft," 8th Annual Applied Power Electronic Conference and Exposition - APEC '93 San Diego, CA. Conference Proceedings IEEE APEC-93 1993, pp. 906-911.
2. Cronin, M.J., "Advanced Power Generation Systems for More Electric Aircraft," SAE Technical Paper Series 912186, SAE Aerotech Conf., Long Beach, CA, Sept. 1991.
3. Colegrove, P.G., "Integrated Power Unit for a More Electric Airplane," AIAA Paper 93-1188 Aerospace Design Conference, Irvine, CA, Feb. 1993.
4. Eike Richter, "Switched Reluctance Machines for High Performance Operation in a Harsh Environment - A Review Paper" Int. Conference on Electrical Machines, MIT Cambridge, MA, 13-15 August 1990, Vol. 1, pp. 18-24.
5. MacMinn, S.R. and Jones W.D., "A Very High Speed Switched-Reluctance Starter-Generator for Aircraft Engine Applications," NAECON 89, Dayton, OH, 1989, pp. 1758-1764.
6. Norman Goldberg, "Generators Inside Small Engines," AIAA Paper 92-3755, 28th Joint Propulsion Conference and Exhibit, Nashville, TN, July 6-8, 1992.
7. Amaratunga, G.A.J., "Comparison of Magnetic Circuit Configurations for Small Aerospace Generators," Ph.D. Thesis Wolfson College, Cambridge University, December 1982.
8. Ferreira, C.A. and Richter E., "Detailed Design of a 250-kW Switched Reluctance Starter/Generator for an Aircraft Engine," SAE Technical Paper Series 931389, SAE Aerospace Atlantic Conf. & Exposition, Dayton, OH, April 20-23, 1993.
9. Richter, E., Lyons, J.P., et al., "Initial Testing of a 250 KW Starter/Generator for Aircraft Applications," SAE Technical Paper Series 941160, SAE Aerospace Atlantic Conf. & Exposition, Dayton, OH, April 18-22, 1994.
10. Richter, E., Radun, A.V., et al., "An Integrated Electrical Starter/Generator System for Gas Turbine Application, Design and Test Results," Proceedings of the ICEM, Sept. 7-9, 1994, France.

11. Faiz, J. and Dadgari, A., "Heat Distribution and Thermal Calculations for a Switched Reluctance Motor", *Journal of Electrical and Electronics Engineering*, Australia, Dec. 1992, vol. 12, no. 4, pp. 349-61.
12. Corman, J.C. and McLaughlin, M.H., "Thermal Design of Heat-Pipe Cooled A-C Motor," *ASME Paper #71-WA/HT-14*, pp. 1-9, 1971.
13. Kukharskii, M.P., Noskov, V.A., "Closed Evaporation Cooling of the Rotor of an Electric Machine," *Elektrotehnika*, n2, Feb. 1974, pp. 41-44.
14. Corman, J.C., Edgar, R.F., McLaughlin, M.H., Merchant, B.W., and Tompkins, R.E., "Heat Pipe Cooled Induction Motor", *IEEE Trans. on Power Apparatus and Systems* v PAS-93 n4, Jul - Aug 1974, pp. 1069 - 1075.
15. Oslejsek, O., Polasek, F., "Cooling of Electrical Machines by Heat Pipes", 2 IHPC, Bologna, Italy, Mar - Apr 1976, ESA SP112 Vol. 1 pp. 503-514, 1976.
16. Chalmers, B.J. and Herman, J., "Induction-Motor Fan Drive with Unlaminated Rotor and Heat Pipe Cooling," *Proc. IEE*, May 1977, Vol. 124, No. 5, pp. 449-453.
17. Tubis, Y.B., Fanar, M.S., "Intensification of Cooling for Low-Voltage Enclosed Induction Motors," *Elektrotehnika*, 1976, Vol. 47, No. 10, pp. 96-101.
18. Groll, M., Krahling, H., Munzel, W.D., "Heat Pipes for Cooling of an Electric Motor," *J. Energy*, Dec 1978, Vol. 2, No. 6, pp. 363-367.
19. Furuya, S., Wake, A., Matsumoto, K., Koizumi, T., "Development of Heat Pipe Shaft for Motor Cooling," Furukawa Denko Jiho/Furukawa Electric Review n71, Mar. 1981, pp. 29-34.
20. Kukharskii, M.P., Ivannikov, V.A., "Effectiveness and Applications of Centrifugal Heat Pipes in Electric Machines," *Elektrotehnika*, 1982, Vol. 53, No. 9, pp. 47-49.
21. Sattler, K., Thoren, F., "Totally Enclosed Heat Pipe Cooled Induction Motor,: Theoretical and Experimental Results," *Proc. ICEM*, pp. 683-6 Vol. 2, 1984.
22. Thoren, F., "Heat Pipe Cooled Induction Motors," *5IHPC Proceedings*, Part 1, May 14-18, 1984, pp. 365-371.
23. Koziej, E., "New Cooling Methods of Electrical Machines," *Rozprawy Elektrotechniczne*, Vol. 31 n 3-4, 1985, pp. 687-692.

24. Abdel-Hakim, M., Abdel-Aziz, M.M., "Thermal Model for Electrical Machines Cooled by Heat Pipes," *Modeling, Simulation & Control, B, AMSE Press*, 1986, Vol. 6, No. 2, pp. 47-55.
25. Bradford, M., "The Application of Heat Pipes to Cooling Rotating Electrical Machines," 4th IEE Conf. Publ. n 310, Sep 13 - 15, 1989, pp. 145-149.
26. Bjorklund, I.S., Kays, W.M., "Heat Transfer Between Concentric Rotating Cylinders," *Journal of Heat Transfer*, Vol. 81, No. 3, August 1959, pp. 175-186.
27. Daniels, T.C., Al-Jumaily, F.K., "Investigations of the Factors Affecting the Performance of a Rotating Heat Pipe," *International Journal of Heat and Mass Transfer*, Vol. 18, No. 7/8, July/August 1975, pp. 961-973.
28. Ruschak, K.J., Scriven, L.E., "Rimming Flow of Liquid in a Rotating Horizontal Cylinder," *J. Fluid Mech.*, Vol. 76, part 1, 1976, pp. 113-125.
29. Daniels, T.C., Williams, R.J., "Experimental Temperature Distribution and Heat Load Characteristics of Rotating Heat Pipes," *International Journal of Heat and Mass Transfer*, Vol. 21, 1978, pp. 193-201.
30. Vasiliev, L.L., Khrolenok, V.V., "Study of a Heat Transfer Process in the Condensation Zone of Rotating Heat Pipes," *Heat Recovery Systems*, Vol. 3, No. 4, 1983, pp. 281-290.
31. Metzger, D. E., Afgan, N. H., (Editors) "Rotating Heat Pipes and Thermosyphons : Heat and Mass Transfer in Rotating Machinery," Hemisphere Publishing; Washington DC. 1984, pp. 608-700.
32. Marto, P.J., Wanniarachchi, A.S., "Influence of Internal Axial Fins on Condensation Heat Transfer in Co-Axial Rotating Heat Pipes," First International Symposium on Transport Phenomena, Honolulu, HI, Apr - May, 1987, pp. 235-244.
33. Yerkes, K.L., "Technology Review: Utilizing Rotating Thermosyphon Technology in Aircraft Thermal Management and Control," SAE Tech Series 901961, Aerospace Tech. Conf., Long Beach, CA, Oct, 1990.
34. Hayase, T., Humphrey, J.A.C., Greif, R., "Numerical Calculation of Convective Heat Transfer Between Rotating Coaxial Cylinders with Periodically Embedded Cavities," *Journal of Heat Transfer*, Vol. 114, August 1992, pp 589-597.

35. Ponnappan, R., Leland, J.E., "Rotating Heat Pipe for Cooling of Rotors in Advanced Generators," AIAA 94-2033, *6th AIAA/ASME Joint Thermophysics and Heat Transfer Conference*, Colorado Springs, CO, June, 1994.
36. Gray, Vernon, H., "Methods and Apparatus for Heat Transfer in Rotating Bodies," U.S. Patent 3,842,596, Oct. 22, 1974.
37. Lloyd, Wayne, B., Logan, Dale R., and Tang, Yu-Sun, "Heat Removal Apparatus for Dynamoelectric Machines," U.S. Patent 3,914,630, Oct. 21, 1975; Assignee: Westinghouse Electric, Pittsburgh, PA.
38. Harano, Keiichi and Oyama, Shigeaki, "Rotary Electric Machine with a Heat Pipe for Cooling," U.S. Patent 4,240,000, Dec. 16, 1980; Assignee: Fujitsu Fanue Ltd., Tokyo, Japan.
39. Ponnappan, Rengasamy and Beam, Jerry E., "Rotor Cooling Structure," U.S. Patent 5,283,488, Feb. 1, 1994; Assignee: U.S. Air Force, Washington DC.
40. Klass, R.M. and McFadden, B., "More-Electric Aircraft Integrated Power Unit Designed for Dual-Use," SAE Paper No. 94-1159.
41. Ponnappan, R., "Task 1: Heat Transport System Study Copper-Water and Steel-Sodium DWAHP - Thermal Energy Storage and Heat Transfer Support Program," Final Report June 87 - Sept. 90. WRDC-TR-90-2121, Volume 1, APPL, WL, WPAFB, March 1991.
42. Ponnappan, "Double Wall Artery Heat Pipe," Final Report Oct. 81 - Sept. 83, AFWAL-TR-83-2041, APL, AFWAL, WPAFB, June 1995.
43. Marto, Paul J., "An Analytical and Experimental Investigation of Rotating, Noncapillary Heat Pipes," NASA CR-130373, September 1973.
44. Marto, P. and Weigel, H., "The Development of Economical Rotating Heat Pipes," 3rd IHPC, Palo Alto, CA, May 1978, pp. 709-724.
45. Stephenson, R., Roush Anatrol, Inc., RHP Vibration Analysis Report, and personal communications, 13 December 1994.
46. Harley, C. and Faghin, A., "Two-dimensional Rotating Heat Pipe Analysis," Tran. of the ASME Vol. 117, Feb. 1995, pp. 202-208.

47. Pais, M., "Numerical Simulation of Heat Transfer in a High Speed Rotating Thermosyphon," Unpublished progress reports and private communications May-Aug 1996.
48. Wu, D. and Peterson, G.P., "A Review of Rotating and Revolving Heat Pipes," ASME National Heat Transfer Conference, Paper No. 91-HT-24, ASME, New York, 1991.

APPENDIX A

CRITICAL SPEED AND ROTOR DYNAMICS ANALYSIS

- A.1 Natural Frequency Calculations for Cantilever and Simple Support Beams of Representative Cross Sections
- A.2 Critical Speed Calculation for Simple Rigid Rotor in Flexible Supports
- A.3 High Speed RHP Rotor Dynamics Analysis
- A.4 Revised RHP Rotor Dynamics Analysis

A.1 NATURAL FREQUENCY CALCULATIONS FOR CANTILEVER AND SIMPLE SUPPORT BEAMS OF REPRESENTATIVE CROSS SECTIONS

A. CANTILEVER

The natural frequency of a cantilever beam shown in Figure A.1 (which represents the overhang of the fill tube in RHP) is given by Eq. (A.1) (Reference A.1).

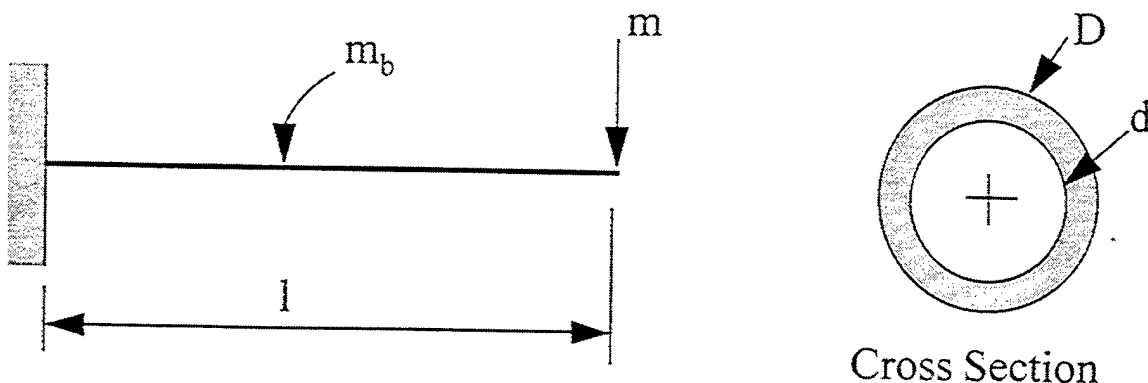


Figure A.1. Fill Tube as Cantilever Beam.

$$\omega_n = \sqrt{\frac{3EIg_c}{(m + 0.23m_b)l^3}} \quad (\text{A.1})$$

Material of the fill tube is SS304; 1/4" O.D., 0.035" wall, density, $\rho_{ss} = 489 \text{ lb}_m/\text{ft}^3$ ($0.283 \text{ lb}_m/\text{in}^3$)

Length of beam, $l = 6"$

$$\begin{aligned} \text{Mass of Beam, } m_b &= \frac{\pi}{4} (D^2 - d^2) l \rho_{ss} \\ &= \frac{\pi}{4} (0.25^2 - 0.18^2) \times 0.283 \\ &= 0.04014 \text{ lb}_m \end{aligned}$$

End load, $m = 0$

$$\text{Gravitational Constant, } g_c = 32.2 \frac{\text{lb}_m}{\text{lb}_f} \cdot \frac{\text{ft}}{\text{s}^2}$$

Modulus of Elasticity, $E = 28 \times 10^6 \text{ lb/in}^2$

$$\begin{aligned}\text{Moment of Inertia, } I &= \frac{\pi}{64} (D^4 - d^4) \\ &= \frac{\pi}{64} (0.25^4 - 0.18^4) = 0.1402 \times 10^{-3} \text{ in}^4\end{aligned}$$

Therefore,

$$\omega_n = \sqrt{\frac{3 \times 28 \times 10^6 \times 0.1402 \times 10^{-3} \times 32.2 \times 12}{0.23 \times 0.04014 \times 6^3}} = 1510.7$$

$$\text{units: } \left[\frac{\text{lb}_f}{\text{in}^2} \cdot \frac{\text{in}^4}{\text{lb}_m \cdot \text{in}^3} \cdot \frac{\text{lb}_m \cdot \text{in}}{\text{lb}_f \cdot \text{s}^2} \right]^{1/2} \equiv \left[\frac{1}{\text{s}} \right] \equiv \frac{\text{radians}}{\text{second}}$$

$$\text{That is, } \omega_n = \frac{1510.7}{2\pi} \text{ Hz or } \frac{1510.7}{2\pi} \times 60 \text{ rpm} = 14,419 \text{ rpm}$$

For other lengths, Eq. A.1 yields the following results:

Length (l), inches:	1.5	2.5	4.4	6.0
Natural frequency ω_n , rpm:	230,818	83,094	26,749	14,419

Figure A.2 shows the graph of this calculation and the design points for the LSRHP and HSRHP units.

B. SIMPLE SUPPORT

The natural frequency of a simple support beam shown in Figure A.3 (which represents the end-bearing support RHP) is given by Eq. (A.2)

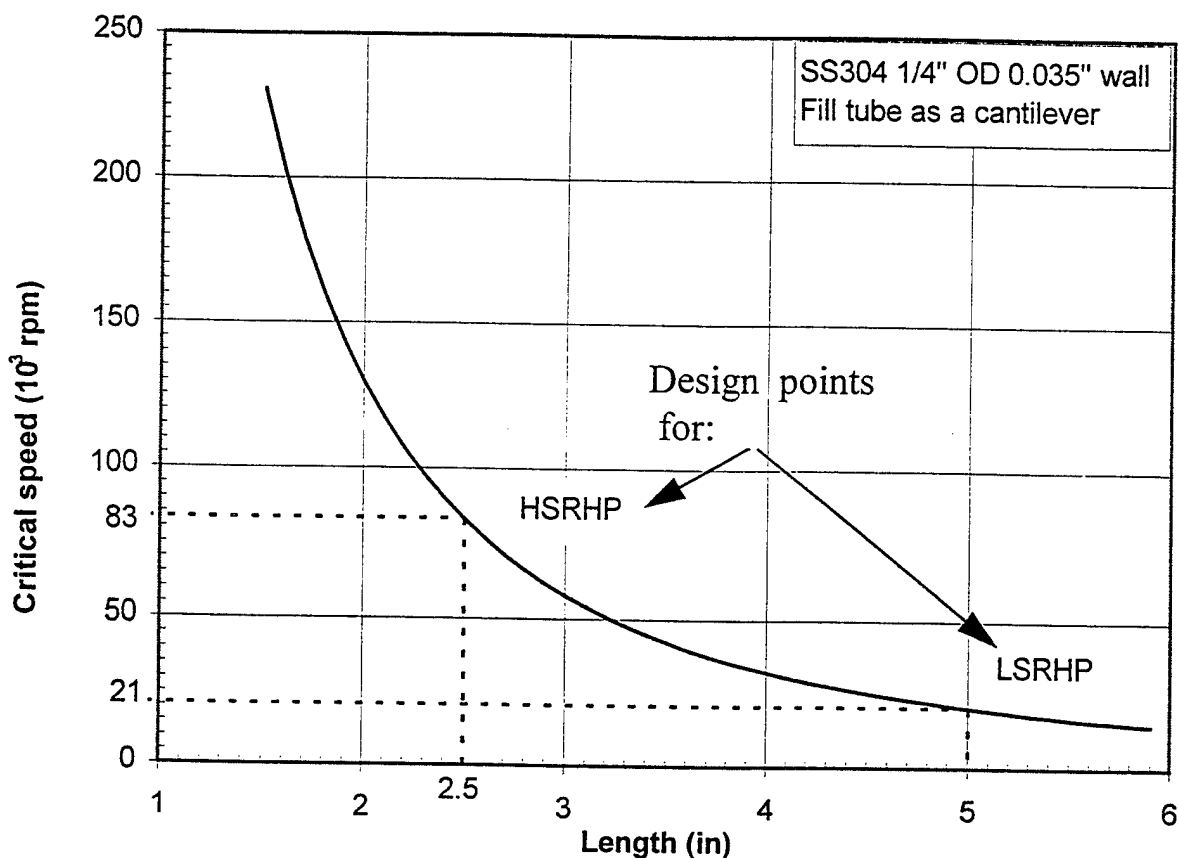


Figure A.2. Critical Speed Graph for Fill Tube.

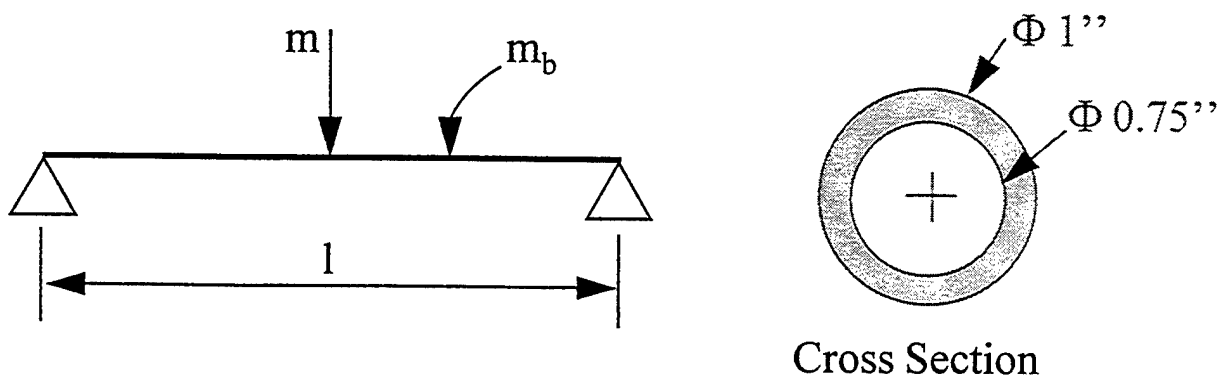


Figure A.3. RHP as Simple Support Beam.

$$\omega_n = \sqrt{\frac{48EIg_c}{(m + 0.5 m_b)l^3}} \quad \text{radians/s} \quad (\text{A.2})$$

Material of the RHP is SS316; 1" O.D., 0.75" I.D., $\rho = 0.283 \text{ lb}_m/\text{in}^3$.

Uniform cross section is assumed for simplicity as the 1.6° taper in the condenser I.D. is considered small.

Mass of the beam, $m_b = \frac{\pi}{4} (D^2 - d^2) \rho_{ss} l = 1.73 \text{ lb}_m$

Concentrated load, $m = 0$

Modulus of elasticity, $E = 28 \times 10^6 \text{ lb/in}^2$

Moment of inertial, $I = \frac{\pi}{64} (D^4 - d^4) = 0.0336 \text{ in}^4$

Length of beam, $l = 18 \text{ in.}$

Therefore,

$$\omega_n = \left(\frac{48 \times 28 \times 10^6 \times 0.0336 \times 32.2}{0.5 \times 1.73 \times 18^3} \right)^{0.5}$$

For $l = 15"$; $\omega_n = 293.5 \text{ Hz}$ or $17,609 \text{ rpm}$

For $l = 15"$; $\omega_n = 422.7 \text{ Hz}$ or $25,363 \text{ rpm}$

For $l = 10.5"$; $\omega_n = 865 \text{ Hz}$ or $51,900 \text{ rpm}$

Figure A.4 shows the graph of critical speed vs. length for the RHP as simple support beam and the design points for the LSRHP and HSRHP units.

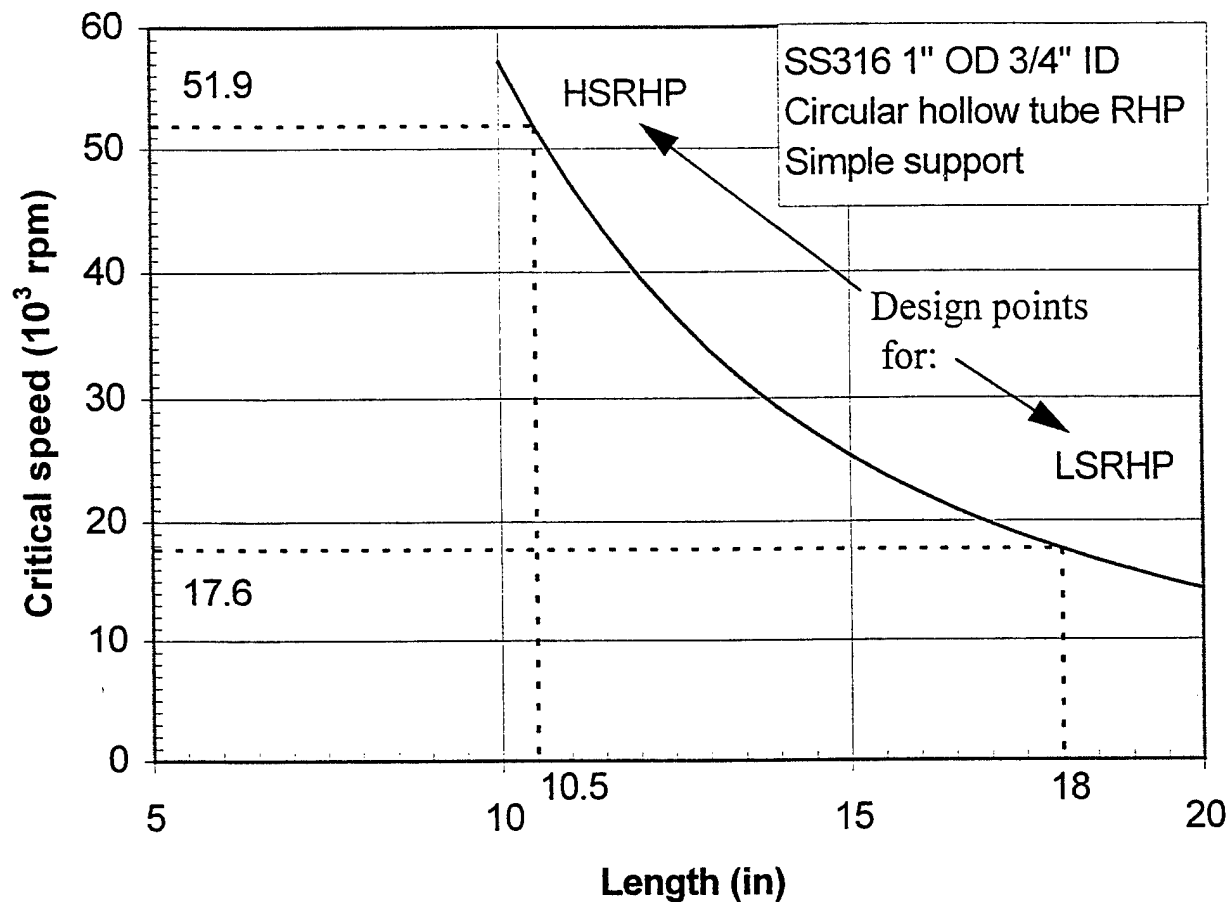


Figure A.4. Critical Speed Graph for RHP Tube.

A.2 CRITICAL SPEED CALCULATION FOR SIMPLE RIGID ROTOR IN FLEXIBLE SUPPORTS: (HOLLOW CYLINDER ROTOR IN BALL BEARING SUPPORTS) (Refer to Figure A.5)

Assumptions

- 1) The rotor C.G. is midway between the bearings.
- 2) The bearings have identical stiffness properties.
- 3) Damping effects are neglected.

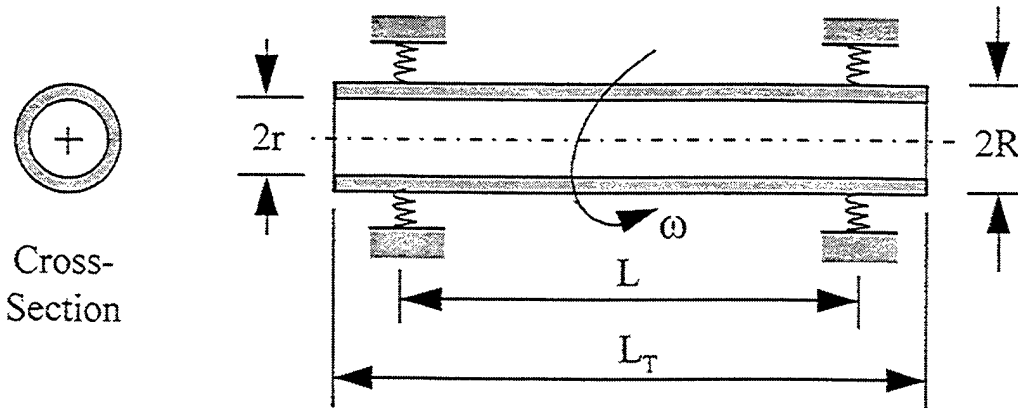


Figure A.5. RHP as a Simple Rigid Rotor in Flexible Supports.

- 4) The classification of HSRHP as a simple rigid rotor is questionable in the strict definition of such a rotor. However, this assumption is made to calculate typical numbers for critical speeds of the present design.
- 5) Condenser taper is ignored in this calculation.

Physical Dimensions and Bearing Data:

W = Actual weight of the HSRHP = 1158 g (2.55 lb.)

= Mg (mass \times gravity)

R = Outer radius = 0.5 in.

r = Inner radius = 0.375 in.

L = Length between bearing centers = 18-1/2 in.

L_T = Total length of HSRHP without fill tube = 22 in.

K = Stiffness of rotor end supports, (lb./in.)

The bearings used in this setup are Barden's CM102HX26R ceramic ball bearings rated for 70,900 rpm. The radial spring rates in lb./inch for various axial thrust (preloading) are given below.

RPM	Thrust, lb.				
	25	40	50	60	70
60,000	52,400 lb./in	95,400 lb./in	133,000 lb./in	175,500 lb./in	220,000 lb./in

Translatory critical speed, ω_T is calculated as

$$\begin{aligned}
 \omega_T &= \sqrt{\frac{2K}{M}} = \sqrt{\frac{2K}{W/g}} \\
 &= 6348.76 \text{ radians/s} \\
 &\div 2\pi = 1010.4 \text{ cps} \\
 &\times 60 = 60,626 \text{ rpm for } 50 \text{ lb. thrust case}
 \end{aligned} \tag{A.3}$$

Conical critical frequency, ω_C is calculated as

$$\begin{aligned}
 \omega_C &= \left(\frac{KL^2}{2I} \right)^{0.5} \\
 I &= \text{Moment of inertia} = I_T - I_p \\
 I_T &= \text{Translatory inertia} = \frac{M}{12} [3(R^2 + r^2) + L^2] \\
 I_p &= \text{Polar inertia} = \frac{M}{2}(R^2 + r^2)
 \end{aligned} \tag{A.4}$$

Therefore,

$$\begin{aligned}
 I &= \frac{M}{12} [L^2 - 3(R^2 + r^2)] \\
 &= \frac{2.55}{12 \times 386.4} [18.5^2 - 3(0.5^2 + 0.375^2)] \\
 &= 0.18757 \text{ lb. in. s}^2
 \end{aligned} \tag{A.5}$$

For 60,000 rpm and 50 lb. thrust,

$$\begin{aligned}\omega_c &= \left(\frac{133,000 \times 18.5^2}{2 \times 0.18757} \right)^{0.5} \\ &= 11,015 \text{ radian/S} \\ &\div 2\pi = 1753 \text{ cps} \\ &\times 60 = 105,188 \text{ rpm}\end{aligned}$$

These calculation results are summarized for various radial bearing stiffnesses supplied by the bearing manufacturer for 60,000 rpm as follows.

Bearing Data		Critical Speed, rpm	
Thrust (lb.)	Stiffness (lb./in.)	First Mode Translatory ω_T	Second Mode Conical ω_C
25	52,400	38,054	66,024
40	95,400	51,346	89,087
50	133,000	60,626	105,188
60	175,500	69,692	120,831
70	220,000	77,973	135,256

Inference: According to this result, the HSRHP in the present configuration, must be preloaded to a minimum of 50 lb. of axial thrust at all times when spinning up to 60,000 rpm.

A.3 HIGH SPEED RHP ROTOR DYNAMICS ANALYSIS

a. SUMMARY

A rotor dynamics analysis has been performed on the high speed RHP rotor to determine the critical speeds and the response of the rotor to unbalance. The first critical speed is calculated to be at approximately 15,200 rpm. This critical speed is very lightly damped and large vibration amplitudes of the rotor are predicted when operating at this speed. The second

and third critical speeds are calculated to be at approximately 48,000 and 63,000 rpm. Although the damping levels at these two critical speeds are relatively higher than that of the first 'mode, the amplification factors are still large and high vibration levels are expected at these speeds also.

Although operation of the rotor near the critical speeds is not recommended because of the low damping levels, it may be acceptable to accelerate the rotor through the critical speeds so that steady state operation between critical speeds is possible. A transient analysis of the rotor system would be required to evaluate the rotor behavior for transitioning the critical speeds.

The frequency of the first critical speed is determined mainly by the bending characteristics of the rotor. Any changes in the bearings and bearing mounts will have only a minimal effect since the bearing locations on the shaft are essentially node points for this mode. If it is desired to increase the first critical speed, modifications to the rotor bending stiffness are required. Possible modifications include a larger rotor diameter, a different bearing span, and adding a third bearing at the center of the rotor.

The second and third critical speeds show some sensitivity to the effective rotor support stiffness at the bearing locations and stiffer bearings will increase these critical speeds to some degree. In the limit, if the bearings and bearing mount structures are completely rigid, the highest frequencies attainable for these critical speeds for this rotor configuration are calculated to be at approximately 60,000 rpm and 110,00 rpm.

The mode shape for the third critical speed shows large deflections at the coupling location on the rotor. Therefore, the mass of the coupling and distance to the coupling from the drive end bearing should be minimized.

The second and third mode also show sensitivity to the distance that the 0.25 inch fill tube extends beyond the rotor. This distance should also be minimized.

b. ANALYSIS

b.1 Approach

A finite element based computer program developed specifically for the analysis of rotor systems was used in this analysis. In this program, the rotor is discretized as a number of beam elements with specified length and diameter properties. A formulation is used that allows for a consistent mass matrix and shear and rotary inertia effects are included. A two noded beam element is used that allows for a linear taper along both the inside and outside diameters. Details of the beam element implemented are given in Reference A.1. The individual beam elements are assembled by the finite element method to form the rotor mass, gyroscopic, and stiffness matrices. Lumped mass elements are also available that can be used to include mass and inertia effects at discrete points on the model. The rotor matrices are augmented to include the bearing and bearing mount mass, stiffness, and damping characteristics. The bearing properties may be speed dependent and any frequency dependent compliance effects of the bearing housing can also be included in the analysis.

For computational efficiency, a Guyan reduction procedure is performed on the rotor matrices that retains only the specified master degrees of freedom along the rotor. This matrix reduction approach can significantly reduce the size of the rotor matrices and therefore solution times without any significant effect on the solution results. The master degrees of freedom are chosen to characterize the deflection of the rotor for the modes within the frequency range of interest for the analysis. Details of the reduction algorithm and many features of the solution procedures used are discussed in Reference A.2.

After the system matrices are formed, a forced response or eigenvalue (damped or undamped) analysis may be performed using standard algorithms.

Material properties of the rotor are assumed to be isotropic. Damping of the rotor itself is normally not considered. However, damping effects in the bearing and bearing housing structure may be included.

b.2 Shaft Model

The RHP model used in this analysis consists of 26 beam elements to model the shaft and fill tube. A summary of the model is given in Table A.1 which tabulates the length and diameters of the elements. Note that the coupling and oil slingers are included using lumped mass elements at nodes 1,5, and 22. For the stainless steel, the material properties used are listed below.

Elastic modulus	28.OE6 lb/in ²
Shear modulus	10.8E6 lb/in ²
Density	0.290 lb/in ³

It should be noted that this analysis does not include any effects that the fluid inside the rotor may have on the dynamics of the system. The 0.25 inch stainless steel fill tube is assumed to extend 2.0 inches beyond the rotor.

b.3 Bearing and Bearing Mount

The radial stiffnesses of the bearings used to support the RHP are dependent on the axial preload and speed of the rotor. In this analysis, the bearing stiffnesses at a preload of 25 pounds are used. These values are summarized in Table A.2. Damping in the bearings is also included in the analysis. The damping values are calculated assuming 2% critical damping. The two roller element bearings are located in the model at nodes 4 and 23 as stiffness and damping elements between the rotor and bearing mount.

Each aluminum bearing mount is included in the model as a single degree of freedom mass, damping, and stiffness system that attaches to ground. The horizontal and vertical stiffness values assumed for both bearing mounts are 7.5E5 lb/in and 5.4E6 lb/in, respectively. The calculated effective masses at each bearing mount in the horizontal and vertical directions are 0.301 lb and 0. 534 lb. A 2% critical damping value is also included.

Table A.1. Summary of Rotor Model

Element Data :

Elem	Type	Mat	Nodes	Len	DK1	DM1	DK2	DM2	ID1	ID2	CumL
					Mass	It	Ip	CX	CY		
					KX	KY					
1	1	1	1	2	0.7300	0.5000	0.5000	0.5000	0.5000	0.0000	0.7300
2	2		1		0.6600E-01	0.0000E+00	0.0000E+00				
3	1	1	2	3	0.7300	0.5000	0.5000	0.5000	0.5000	0.0000	1.4600
4	1	1	3	4	0.2640	0.5906	0.5906	0.5906	0.5906	0.0000	1.7240
5	1	1	4	5	0.4260	0.5906	0.5906	0.5906	0.5906	0.0000	2.1500
6	2		5		0.9000E-02	0.0000E+00	0.0000E+00				
7	1	1	5	6	0.4750	1.0000	1.0000	1.0000	1.0000	0.0000	2.6250
8	1	1	6	7	1.0000	1.0000	1.0000	1.0000	1.0000	0.5000	3.6250
9	1	1	7	8	1.0000	1.0000	1.0000	1.0000	1.0000	0.5274	4.6250
10	1	1	8	9	1.0000	1.0000	1.0000	1.0000	1.0000	0.5548	5.6250
11	1	1	9	10	1.0000	1.0000	1.0000	1.0000	1.0000	0.5822	6.6250
12	1	1	10	11	1.0000	1.0000	1.0000	1.0000	1.0000	0.6096	7.6250
13	1	1	11	12	1.0000	1.0000	1.0000	1.0000	1.0000	0.6370	8.6250
14	1	1	12	13	1.0000	1.0000	1.0000	1.0000	1.0000	0.6643	9.6250
15	1	1	13	14	1.0000	1.0000	1.0000	1.0000	1.0000	0.6918	10.6250
16	1	1	14	15	1.1250	1.0000	1.0000	1.0000	1.0000	0.7192	11.7500
17	1	1	15	16	0.7500	1.0000	1.0000	1.0000	1.0000	0.7500	12.5000
18	1	1	16	17	1.4500	1.0000	1.0000	1.0000	1.0000	0.7500	13.9500
19	1	1	17	18	1.4500	1.0000	1.0000	1.0000	1.0000	0.7500	15.4000
20	1	1	18	19	1.4500	1.0000	1.0000	1.0000	1.0000	0.7500	16.8500
21	1	1	19	20	1.4500	1.0000	1.0000	1.0000	1.0000	0.7500	18.3000
22	1	1	20	21	1.4500	1.0000	1.0000	1.0000	1.0000	0.7500	19.7500
23	1	1	21	22	0.4370	1.0000	1.0000	1.0000	1.0000	0.1800	20.1870
24	2		22		0.9000E-02	0.0000E+00	0.0000E+00				
25	1	1	22	23	0.4260	0.5906	0.5906	0.5906	0.5906	0.1800	20.6130
26	1	1	23	24	0.2640	0.5906	0.5906	0.5906	0.5906	0.1800	20.8770
27	1	1	24	25	0.6230	0.5000	0.5000	0.5000	0.5000	0.1800	21.5000
28	1	1	25	26	1.0000	0.2500	0.2500	0.2500	0.2500	0.1800	22.5000
29	1	1	26	27	1.0000	0.2500	0.2500	0.2500	0.2500	0.1800	23.5000

ROTOR WEIGHT: lbs.

Material 1: 2.4896

Lumped Mass: .84000E-01

Total : 2.5736

Length Dimensions in inches

Table A.2. Bearing Stiffness vs. Speed at 25 lb. Axial Preload

<u>SPEED, RPM</u>	<u>STIFFNESS, LB/IN</u>
5000	357,000
10,000	355,000
15,000	353,000
20,000	295,000
25,000	237,000
30,000	177,000
35,000	128,000
40,000	95,800
45,000	75,550
50,000	63,400
55,000	56,280
60,000	52,400

Note that although the vertical stiffness of the bearing mount is significantly higher than the bearing stiffness values, the bearing mount horizontal stiffness is of the same magnitude of the bearing stiffness at slow speeds.

c. RESULTS

c.1 Free-Free Modes

It is sometimes useful to compute the free-free natural frequencies of a non-rotating rotor as a method of determining the accuracy of the rotor model used. In the free-free condition, the bearings and bearing mounts are not included in the model and therefore the frequencies are only a function of the dynamic characteristics of the shaft. These computed frequencies may be compared with the free-free frequencies determined from test by suspending the actual rotor to determine if any mass or stiffness adjustments should be made to provide improvement to the rotor model. Although this procedure is normally performed on rotors with complicated geometries, this information has been provided for the RHP rotor for reference.

The first three non-zero natural frequencies of the RHP rotor with free-free boundary conditions and corresponding modes shapes are shown in Figure A.6. In the figure, the drive end of the shaft is at axial location 0.0 and the two bearing locations are shown for reference. Note that except for the relatively high displacement of the fill tube, the mode shapes are typical for a free-free beam. For these results, the coupling mass and the oil stingers are not included in the model.

c.2 Critical Speeds

The first three undamped critical speeds have been computed at several support stiffnesses, where the support stiffness of the rotor is defined as the effective stiffness of the bearing and bearing mount in series at both bearing locations. This information is shown in the form of a critical speed map in Figure A.7.

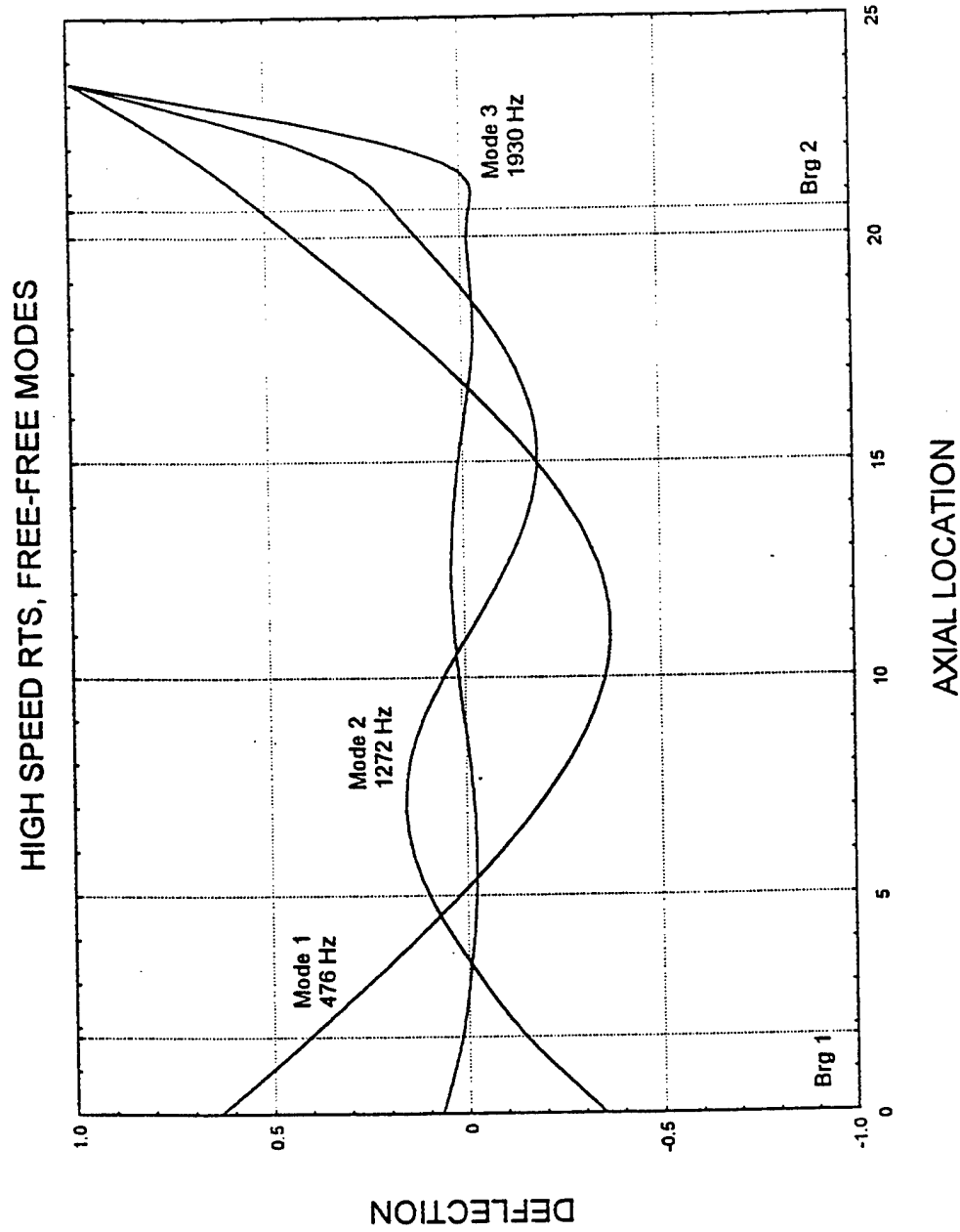


Figure A.6. HSRHP - Deflection in Free-Free Modes.

HIGH SPEED RTS CRITICAL SPEED MAP

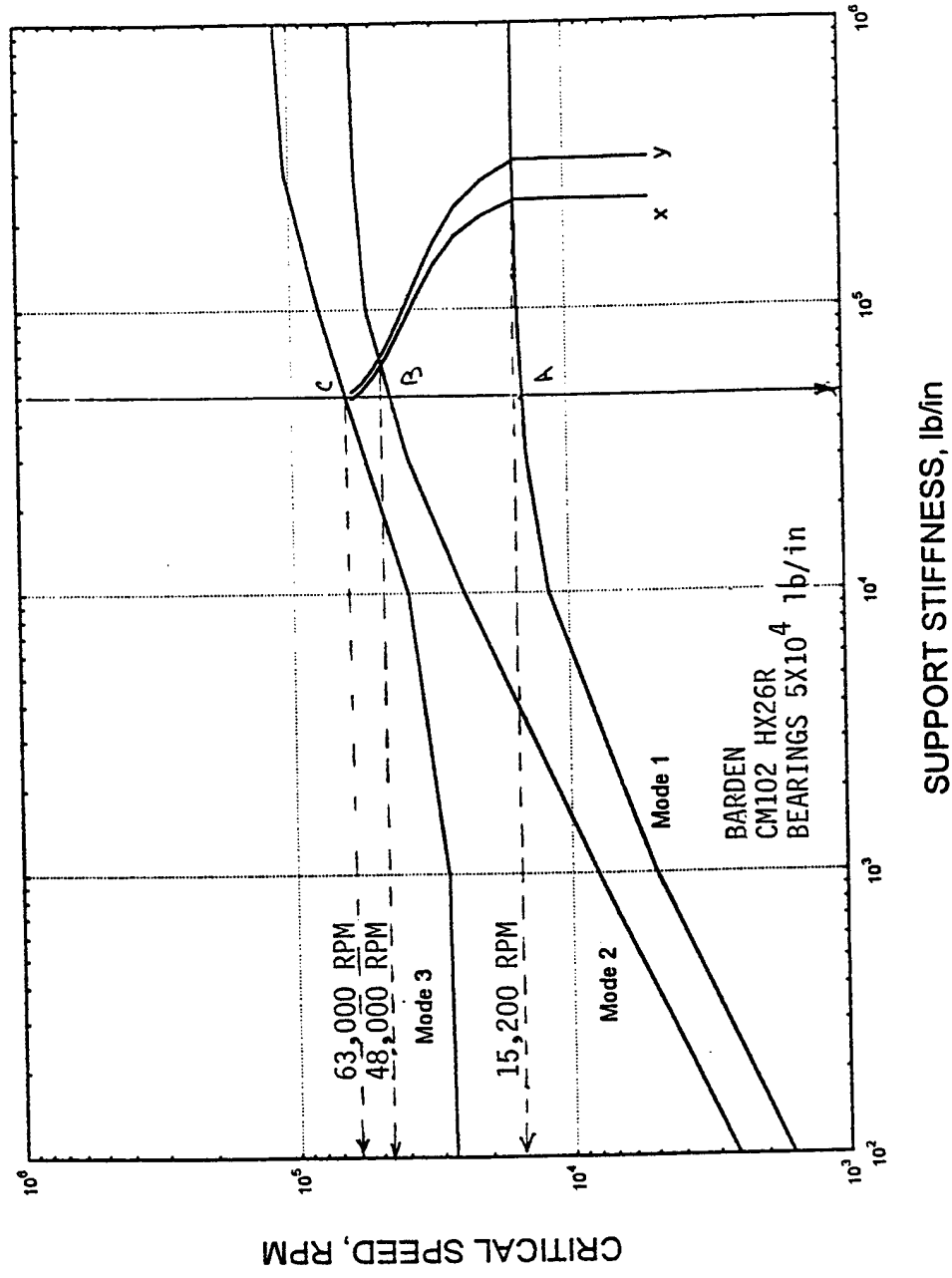


Figure A.7. HSRHP Critical Speed Map.

Also plotted in the figure are the horizontal (x) and vertical (y) support stiffnesses as a function of rotor speed. The intersections of these curves with the critical speed lines define the location of the first three critical speeds.

The curve for mode I can be seen to be almost flat in the stiffness region defined by the x and y support stiffness curves. Therefore, increasing the support stiffnesses will have essentially no effect on increasing the first critical speed above approximately 15,000 rpm. The two bearing locations on the rotor are basically nodal points and the frequency of this mode is governed by the dynamics of the rotor only. Therefore, the higher radial stiffness in the bearings that is available at higher axial preloads will have no effect on this critical speed. The curves for modes 2 and 3 become almost flat at a stiffness of 1.0E6 lb/in and therefore, the maximum values for these modes are approximately 60,000 and 110,000 rpm, respectively, for a rigid bearing configuration.

The mode shapes of the first three critical speeds are plotted in Figure A.8 for a support stiffness of 1.0E5 lb/in, which is a representative stiffness value for the three modes. Note that for mode I the rotor displacement at the bearing locations is very small. The large deflection on the left end of the rotor for mode 3 is due to the coupling mass.

c.3 Response to Unbalance

A forced response analysis has been performed to calculate the rotor response to a specified unbalance. In this analysis, the vibration at specific points along the rotor is calculated at several rotor speeds over a speed range of interest to obtain a vibration vs. speed curve. Since it is difficult to predict the magnitude of the residual unbalance present on an actual rotor, the amount of unbalance to apply to the rotor model for response calculations is based on formulas developed over time that have shown to yield realistic vibration amplitudes. These formulas normally take into account the size and rotational speed of the rotor.

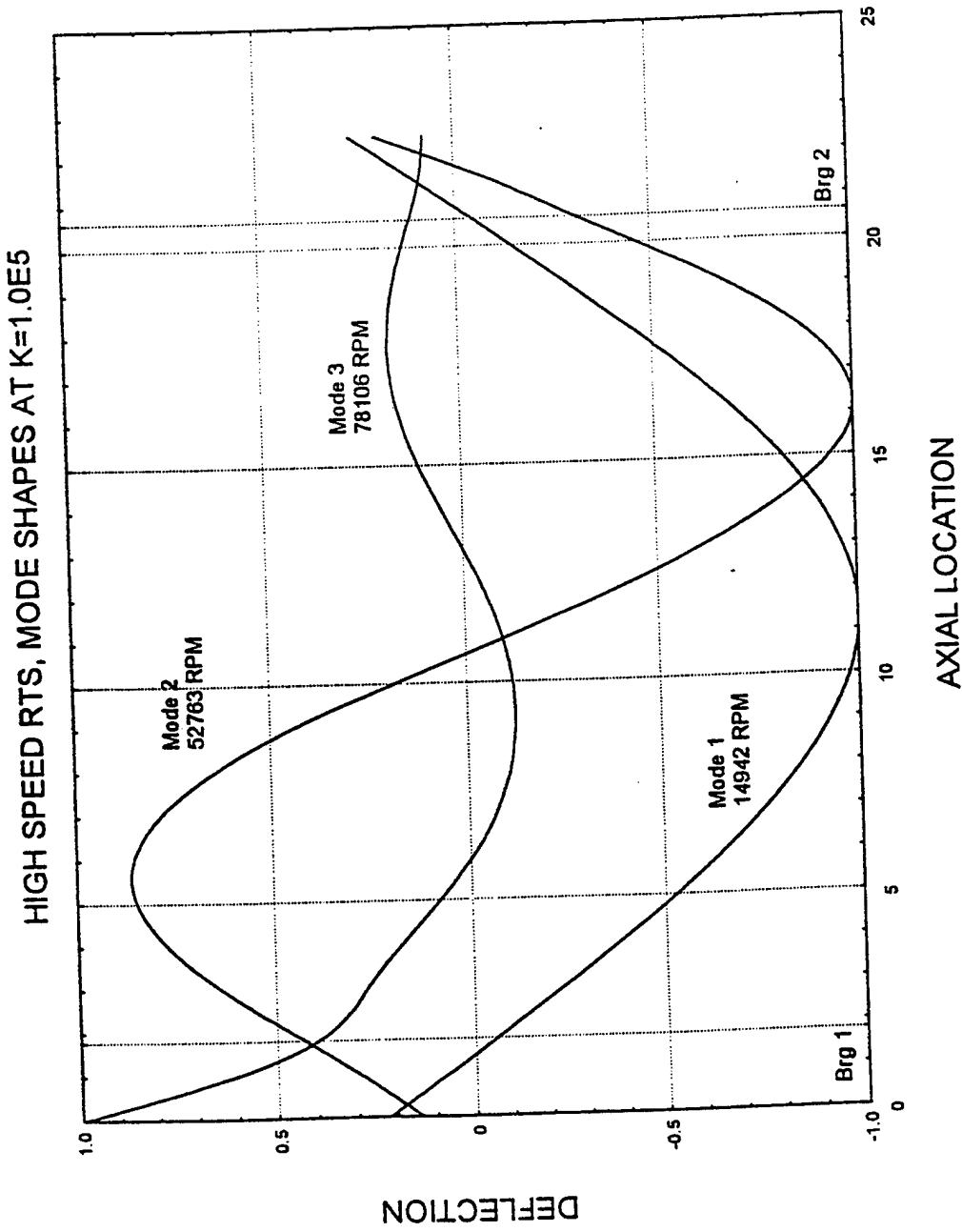


Figure A.8. HSRHP - Mode Shapes at K=1.0E5.

In addition to the magnitude of the unbalance, the distribution of the unbalance along the actual rotor is normally also unknown. The normal procedure for applying the unbalance to the rotor model is to distribute the unbalance in such a way so that the desired mode of the rotor is excited. Using the mode shape information from the critical speed analysis, the first forced response calculation was performed with the unbalance located at the middle of the rotor to excite mode 1. A second forced response calculation was performed to excite mode 2 with unbalances located near each quarter points on the rotor and 180 degrees out of phase. The unbalances applied for the two cases are summarized below.

	Node	Unbalance	Phase
Case 1	15	3. IE-5 lb-in	0.
Case 2	9	1.55E-5 lb-in	0.
	18	1.55E-5 lb-in	180.

The magnitude and phase of the rotor response for the mode I unbalance is plotted up to 80,000 rpm at the drive end bearing, the rotor center, and the opposite drive end (ODE) bearing locations in Figures A.9, A.10 and A.11, respectively. Both the horizontal and vertical responses are shown. The sharpness in the peak of the response at the first mode indicates that the damping for this mode is very low. The vibration amplitude at the rotor center is much larger than the values at the bearings, which is consistent with the mode shapes calculated from the critical speed analysis. The mode 1 unbalance only slightly excites the second mode at approximately 47,000 rpm. However, a large response to mode 3 occurs at both bearing locations at approximately 62,000 rpm.

The rotor response to the mode 2 unbalance at the same three rotor locations is shown in Figures A.12 through A.14. The response to the first mode at both bearing locations is minimal. However, the rotor center shows a very sharp peak with very little damping, which is consistent with the mode I unbalance response results above. For the second mode at approximately 47,000 rpm, the vibration amplitudes are higher at the bearing locations than at the rotor center. Also, the vibration at the two bearing locations is seen to be 180 degrees out of phase. Rotor

RESPONSE TO MODE 1 UNBALANCE, DRIVE END BRG

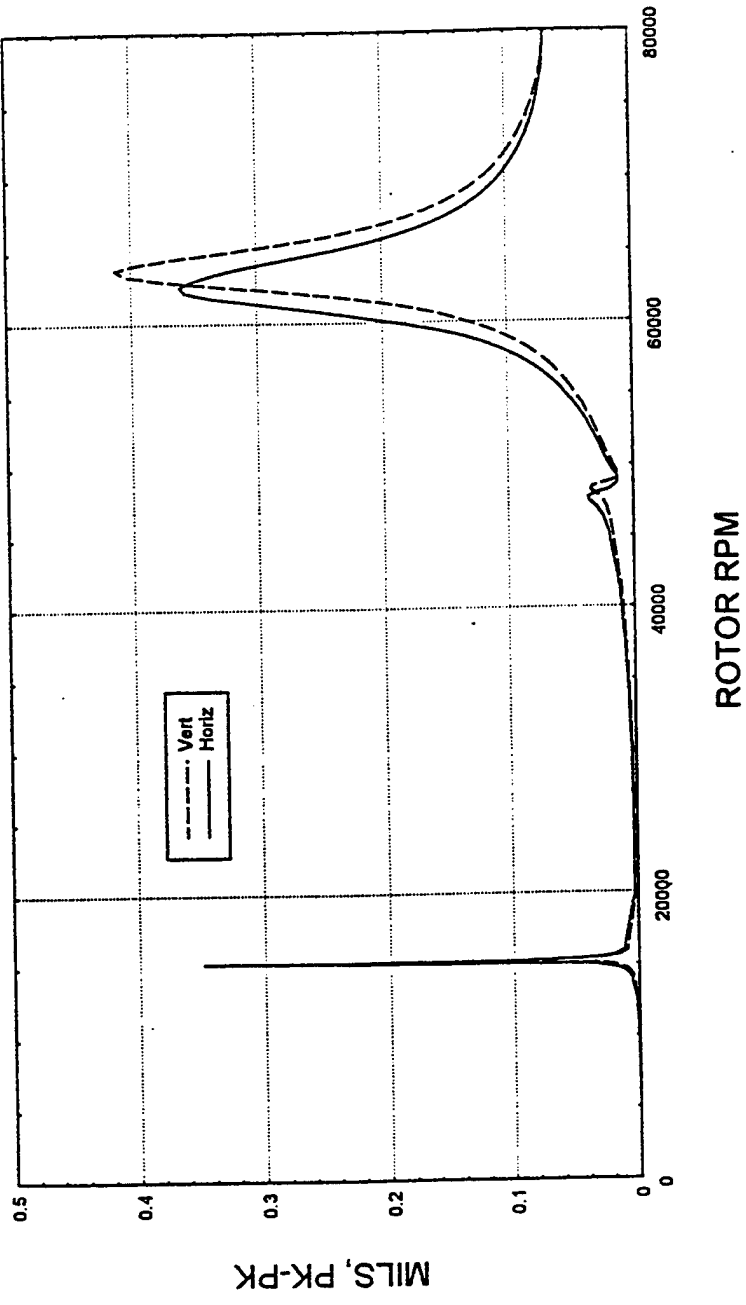
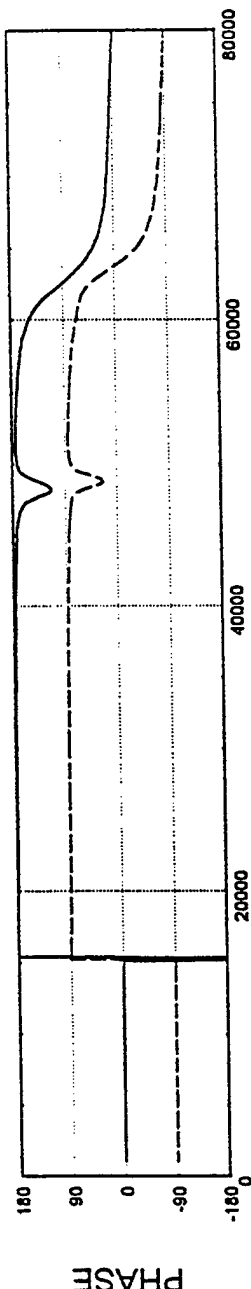
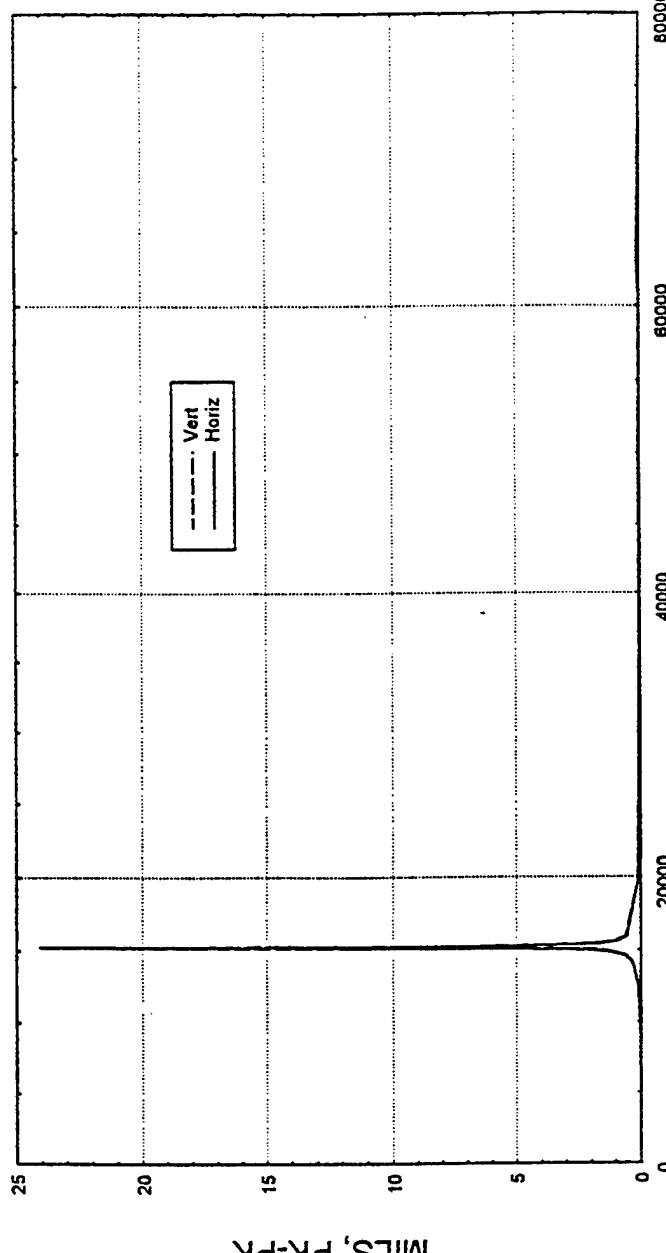
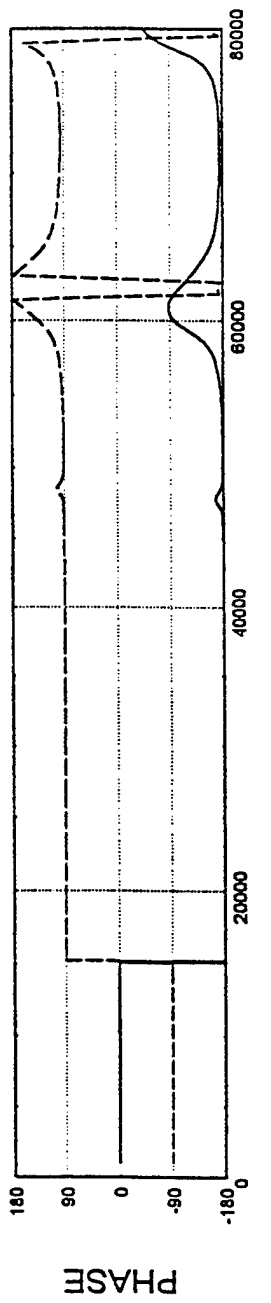


Figure A.9. Response to Mode-1 Unbalance (Drive-end Bearing).

RESPONSE TO MODE 1 UNBALANCE, ROTOR CENTER



ROTOR RPM

Figure A.10 .Response to Mode-1 Unbalance (Rotor Center).

RESPONSE TO MODE 1 UNBALANCE, ODE END BRG

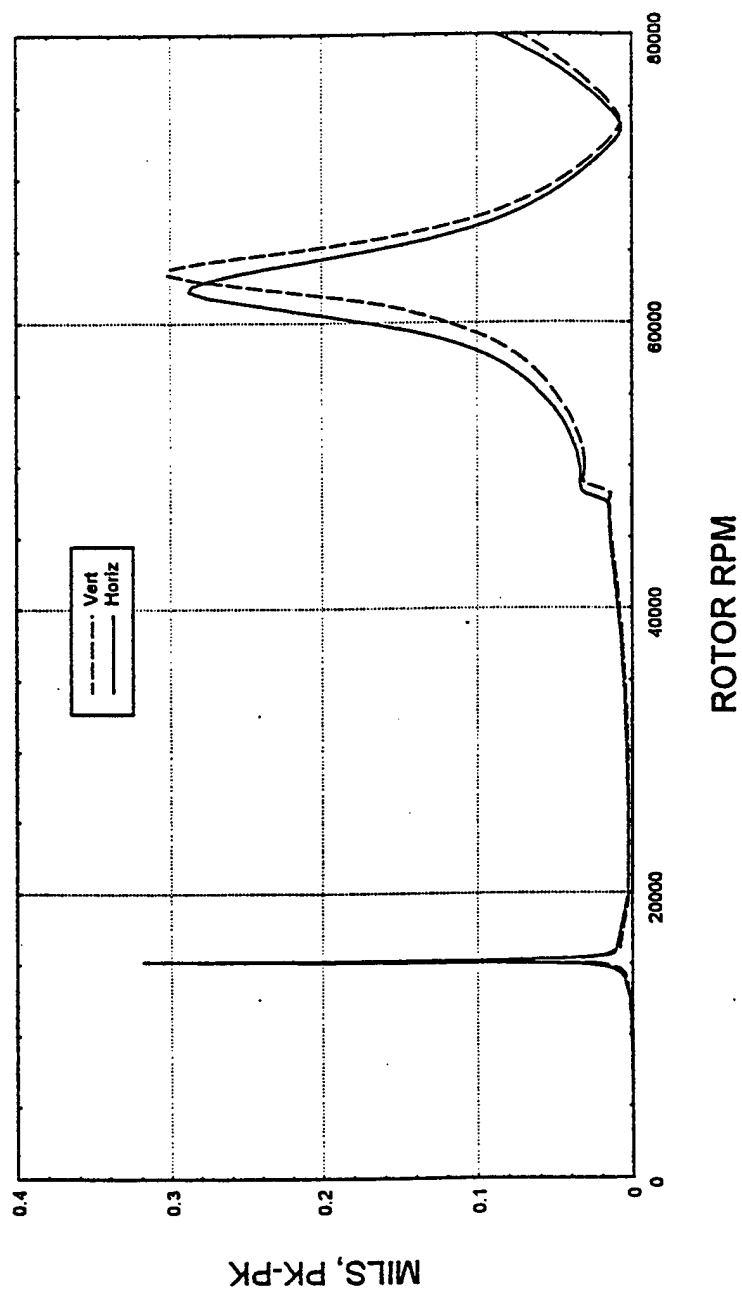
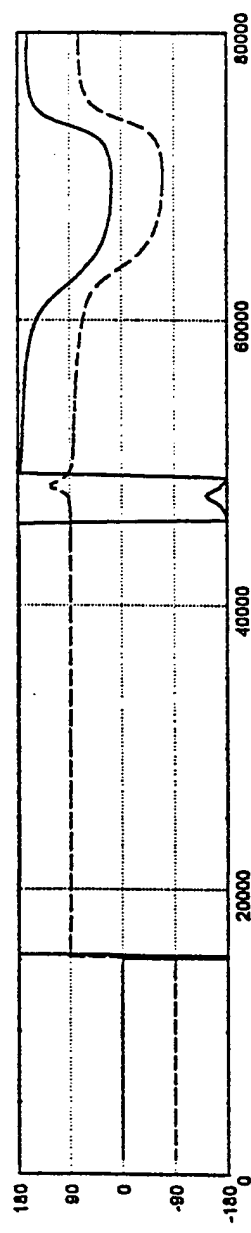


Figure A.11. Response to Mode-1 Unbalance (Opposite Drive-end Bearing).

RESPONSE TO MODE 2 UNBALANCE, DRIVE END BRG

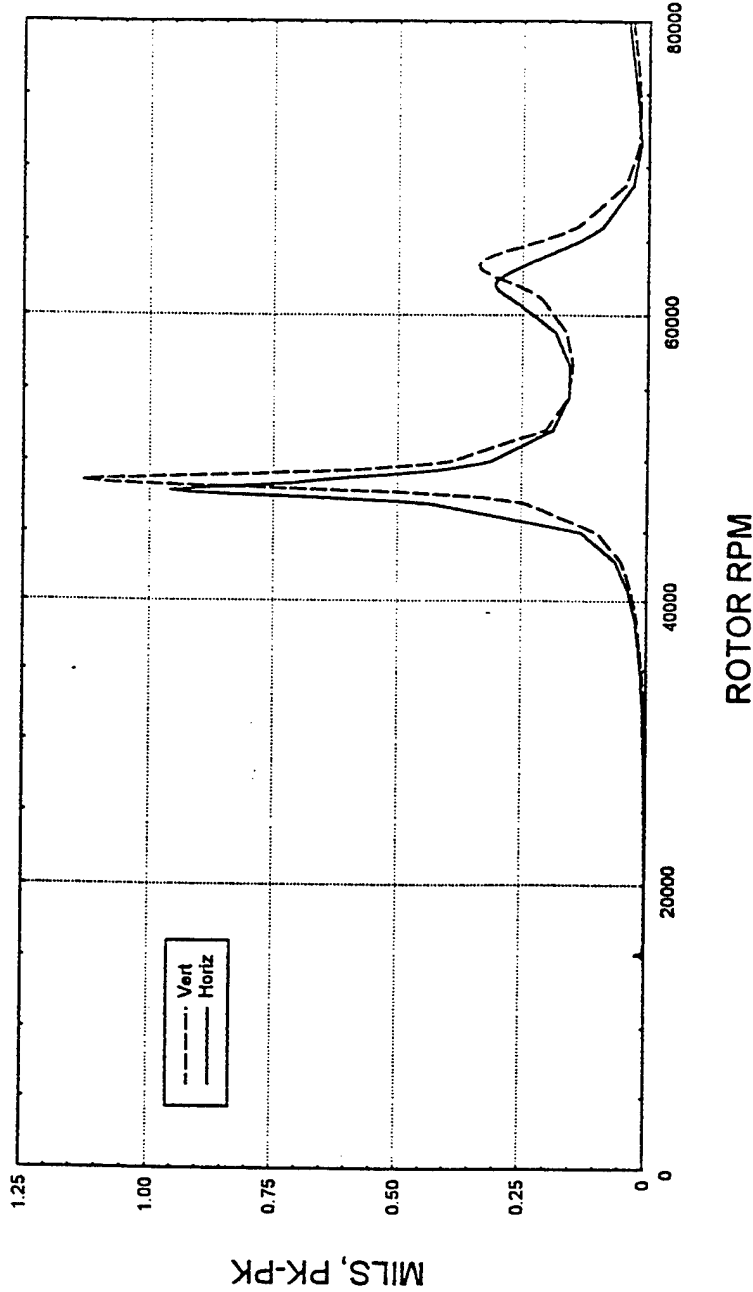
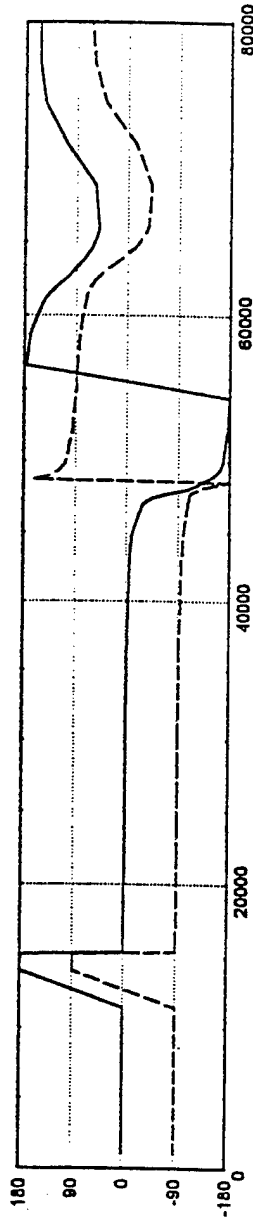


Figure A.12. Response to Mode-2 Unbalance (Drive-end Bearing).

RESPONSE TO MODE 2 UNBALANCE, ROTOR CENTER

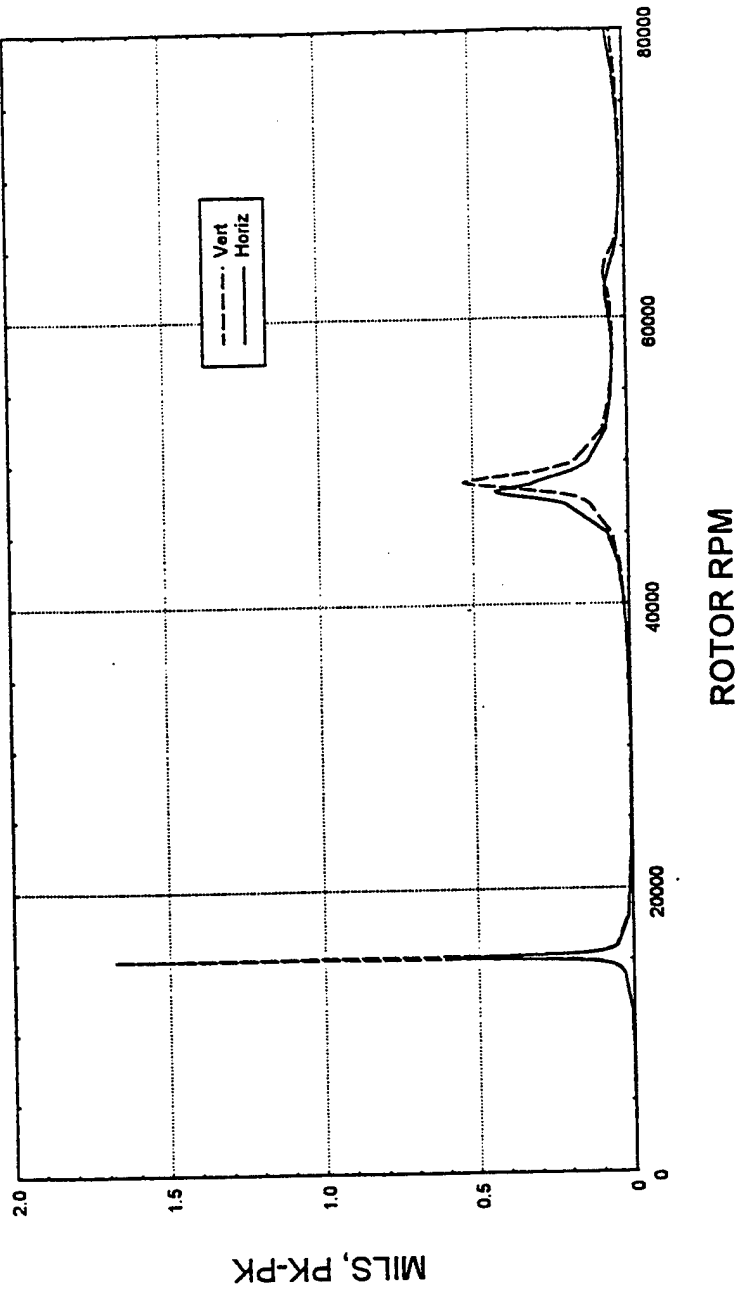
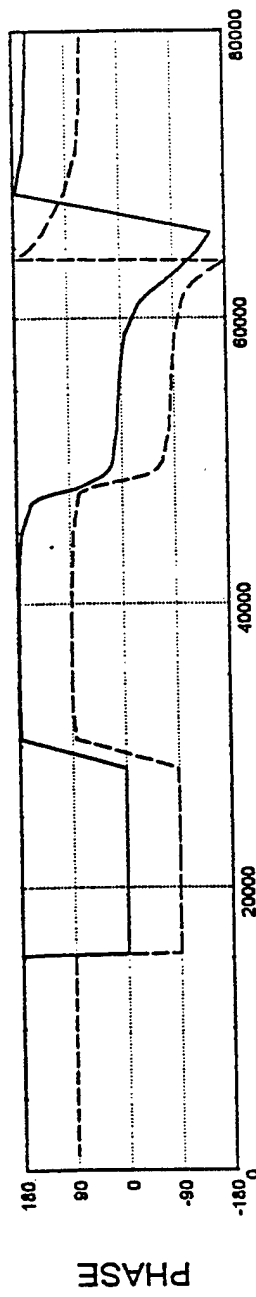


Figure A.13. Response to Mode-2 Unbalance (Rotor Center).

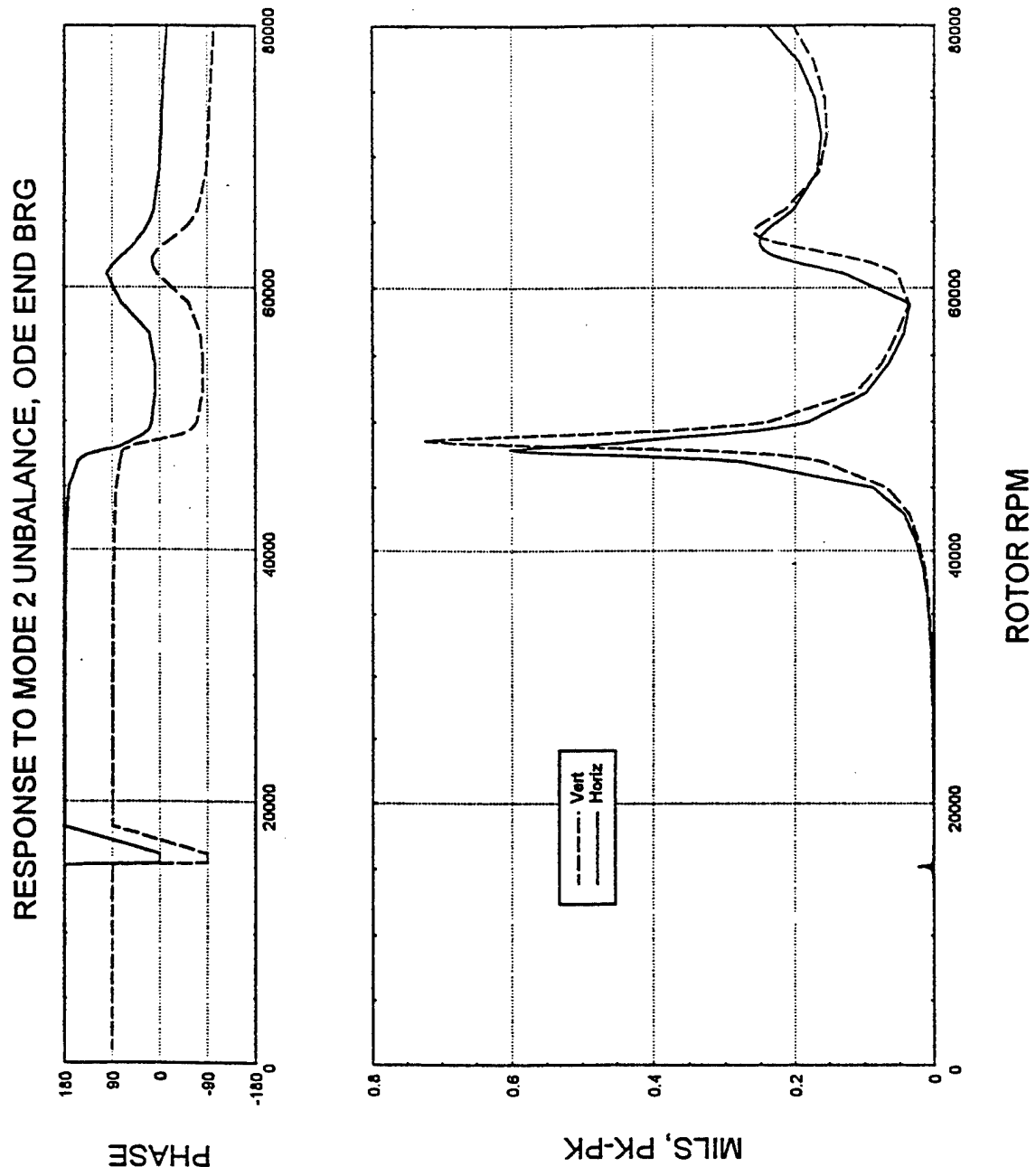


Figure A.14. Response to Mode-2 Unbalance (Opposite Drive-end Bearing).

response to the third mode is shown at the bearings, but the rotor center only shows minimal vibration at this frequency.

It should be noted that the response to unbalance calculation is linear. Therefore, the magnitudes of the vibration amplitudes presented may be directly scaled for different levels of unbalance on the rotor.

The rotor critical speeds and amplification factors calculated for these two unbalance cases using the rotor orbit information are summarized in Table A.3 at the three rotor locations.

A.4 REVISED RHP ROTOR DYNAMICS ANALYSIS

a. **SUMMARY**

The critical speeds and response to unbalance have been calculated for the revised high speed Rhp rotor in which the overall length is 15.74 inches and the maximum outside diameter is 1.1 inches. The first critical speeds is calculated to be at approximately 37,500 rpm. Although this is significantly higher than the first critical speed calculated for the original rotor geometry, this mode is still very lightly damped and large rotor vibration amplitudes are calculated at this speed. The second and third critical speeds are computed at approximately 61,000 and 75,000 rpm, respectively.

The first three modes show some sensitivity to the value of the bearing stiffness and therefore these critical speed values can be expected to increase if higher bearing stiffnesses are used. In addition, the second mode can be increased if a shorter fill tube is used. Since the target maximum operating speed is 60,000 rpm, some reasonable modifications may increase the second mode to provide a margin above this maximum speed. However, the highest value of the first critical speed that is obtainable with this configuration if a bearing and bearing mount stiffness of infinity is assumed is about 43,000 rpm. Therefore, this mode will still be in the operating range if higher bearing stiffnesses are used.

Table A.3. Summary of Response to Unbalance Analysis

Location	Critical Speed RPM	Amplification Factor
Mode 1 Unbalance		
Drive End Bearing	15,238	254
	47,829	28.1
	63,317	17.8
Rotor Center	15,238	254
	48,726	*
	63,756	16.0
ODE Bearing	15,238	254
	48,712	*
	63,092	17.7
Mode 2 Unbalance		
Drive End Bearing	15,220	154
	48,474	35.6
	62,952	18.4
Rotor Center	15,220	165
	48,473	*
	62,723	16.8
ODE Bearing	15,180	156
	48,473	35.8
	63,644	14.0

* Not calculated

Further calculations show that reducing the rotor length by 6.0 inches at the 1.1 inch outside diameter location for this configuration will increase the first critical speed to approximately 57,000 rpm.

b. RESULTS

The analysis method, procedures, and details of the rotor model and bearing data are outlined in the original report. In this analysis of the revised rotor, only the rotor beam element model is changed to reflect the new geometry. The tabulated rotor model used is given in Table A.4. The applied unbalances to the rotor are also unchanged.

The critical speed map is plotted in Figure A.15 and the mode shapes for the first three modes are shown in Figure A.16 for a representative support stiffness of 1.0E5 lb/in. As in the previous report, the coupling end of the shaft is at axial location 0.0 and the fill tube end of the rotor is at 15.74 inches. The first mode shows more deflection at the bearing locations than the original rotor design and therefore the frequency of this critical speed will show some sensitivity to the bearing stiffness used. Note that there is large bending of the fill tube for the second and third modes.

The rotor response results are plotted in Figures A.17 through A.19 for the mode 1 unbalance case at the drive end bearing location, the rotor center, and the opposite drive end bearing location. The three critical speeds are clearly identified. Note that the peaks in the response curves in the horizontal and vertical directions are slightly different since the bearing mount stiffness in the horizontal direction is less than the value in the vertical direction, and therefore the critical speeds occur in pairs. The sharp peaks indicate a lightly damped system and amplification factors are similar to those calculated from the original rotor design.

Table A.4. Summary of Revised Rotor Model

Element Data :

Elem	Type	Matl	Nodes	Len	DK1	DM1	DK2	DM2	ID1	ID2	Cuml
					Mass	[t]	[p]	CX	CY		
1	1	1	1	2	0.4800	0.5000	0.5000	0.5000	0.0000	0.0000	0.480
2	2	1	1	2	0.6600E-01	0.0000E+00	0.0000E+00	0.0000E+00			
3	1	1	2	3	0.4800	0.5000	0.5000	0.5000	0.0000	0.0000	0.960
4	1	1	3	4	0.2640	0.5906	0.5906	0.5906	0.0000	0.0000	0.960
5	1	1	4	5	0.4260	0.5906	0.5906	0.5906	0.0000	0.0000	1.224
6	2	3	5	6	0.3000E-02	0.0000E+00	0.0000E+00	0.0000E+00	0.0000	0.0000	1.650
7	1	1	5	7	0.4500	1.1000	1.1000	1.1000	0.0000	0.0000	2.100
8	1	1	6	7	1.0000	1.1000	1.1000	1.1000	0.6750	0.7100	3.100
9	1	1	7	8	1.0000	1.1000	1.1000	1.1000	0.7100	0.7450	4.100
10	1	1	8	9	1.0000	1.1000	1.1000	1.1000	0.7450	0.7800	5.100
11	1	1	9	10	1.0000	1.1000	1.1000	1.1000	0.7800	0.8150	6.100
12	1	1	10	11	1.0000	1.1000	1.1000	1.1000	0.8150	0.8500	7.100
13	1	1	11	12	1.0000	1.1000	1.1000	1.1000	0.8500	0.8500	8.100
14	1	1	12	13	1.0000	1.1000	1.1000	1.1000	0.8500	0.8500	9.100
15	1	1	13	14	1.0000	1.1000	1.1000	1.1000	0.8500	0.8500	10.100
16	1	1	14	15	1.0000	1.1000	1.1000	1.1000	0.8500	0.8500	11.100
17	1	1	15	16	1.0000	1.1000	1.1000	1.1000	0.8500	0.8500	12.100
18	1	1	16	17	0.4500	1.1000	1.1000	1.1000	0.8500	0.8500	13.100
19	2	17			0.9000E-02	0.0000E+00	0.0000E+00		0.1800	0.1800	12.550
20	1	1	17	18	0.4260	0.5906	0.5906	0.5906	0.1800	0.1800	12.976
21	1	1	18	19	0.2640	0.5906	0.5906	0.5906	0.1800	0.1800	13.240
22	1	1	19	20	1.0000	0.2500	0.2500	0.2500	0.1800	0.1800	14.240
23	1	1	20	21	1.0000	0.2500	0.2500	0.2500	0.1800	0.1800	15.240
24	1	1	21	22	0.5000	0.2500	0.2500	0.2500	0.1800	0.1800	15.740

ROTOR WEIGHT: lbs.

Material 1: 1.6892

Lumped Mass: .34000E-01

Total : 1.7732

Length in inches

REVISED HIGH SPEED RTS CRITICAL SPEED MAP

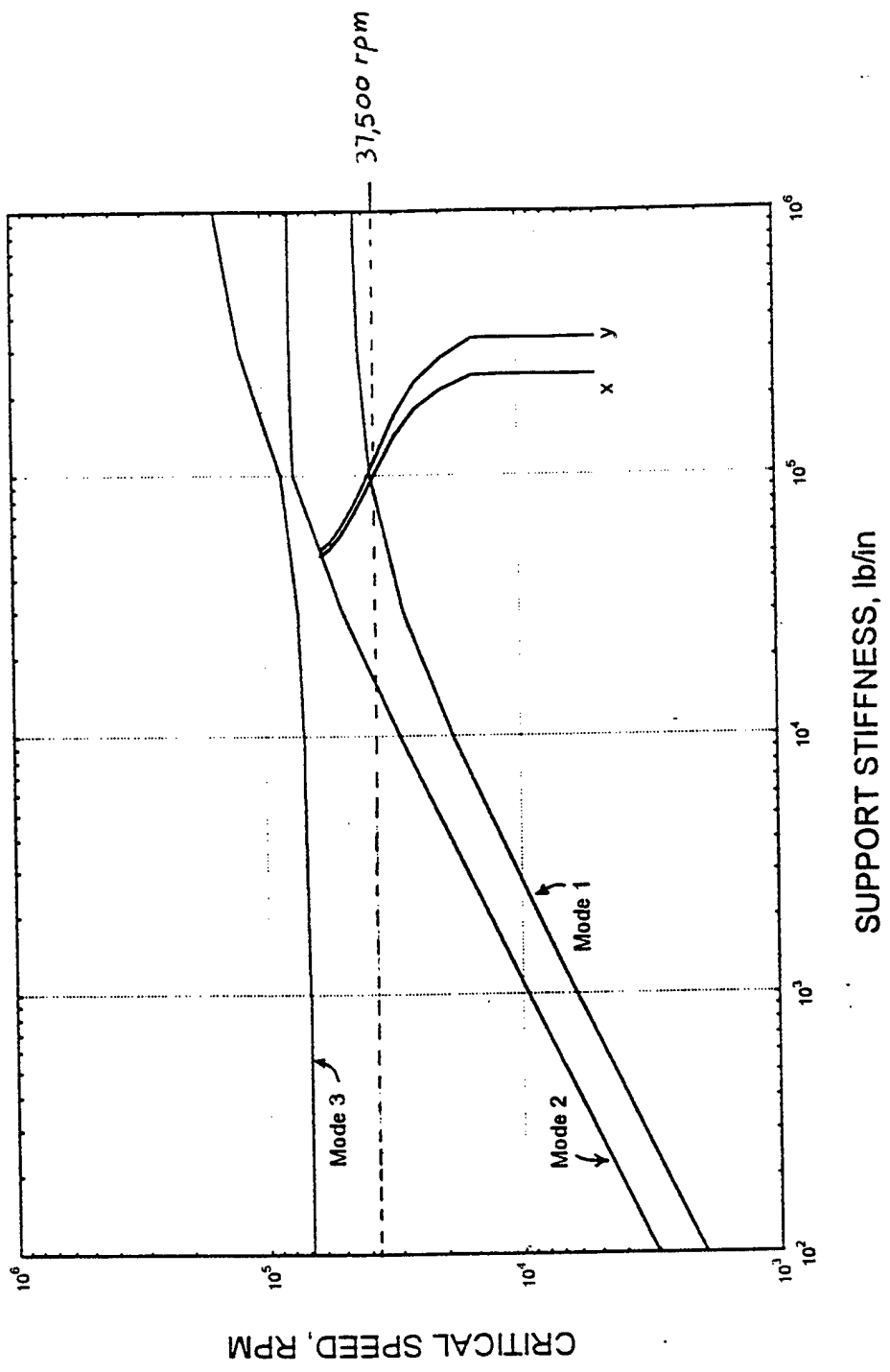


Figure A.15. Revised HSRHP - Critical Speed Map.

REVISED RTS, MODE SHAPES AT K=1.0E5

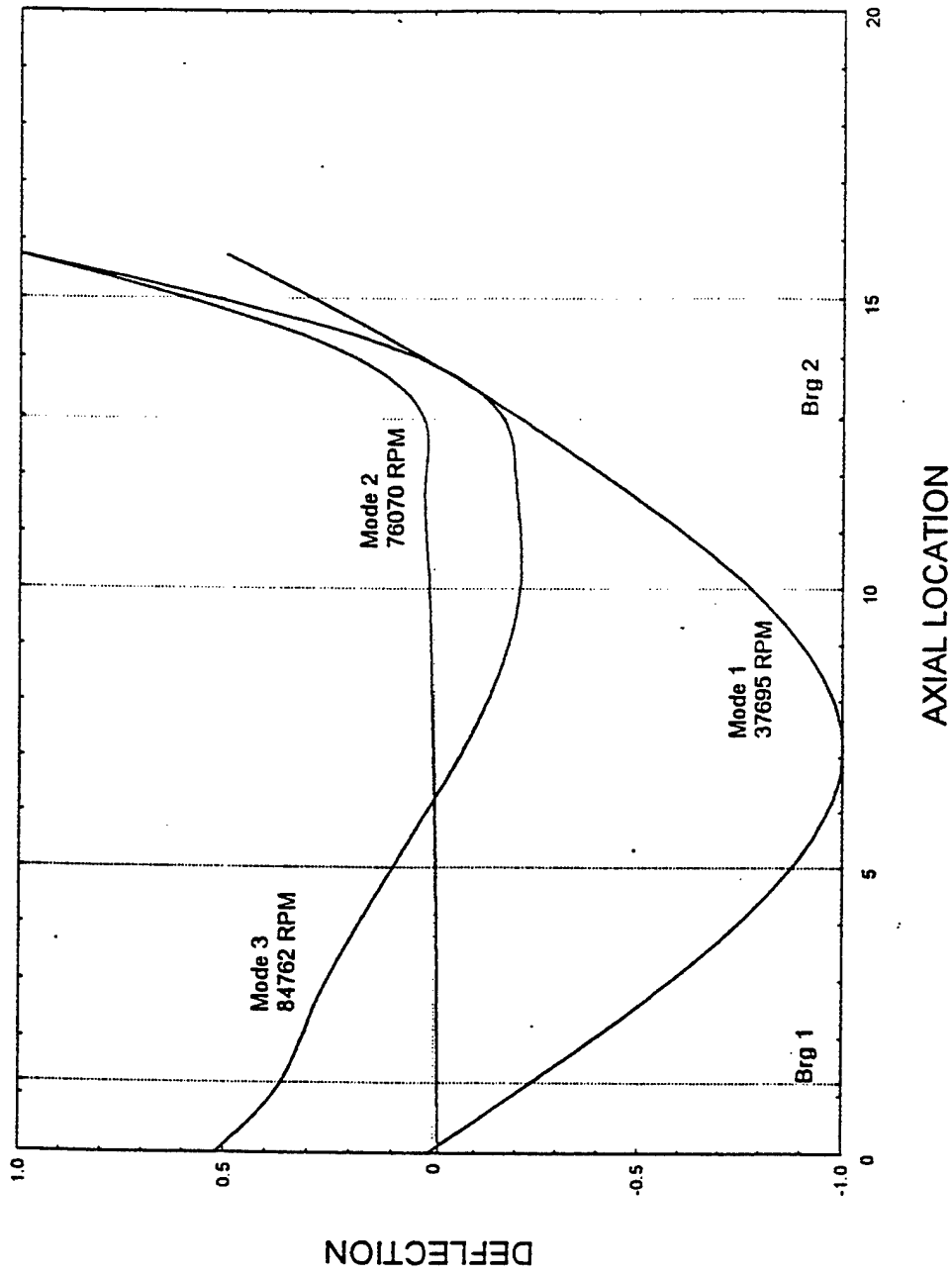


Figure A.16. Revised HSRHP - Mode Shapes at K=1.0E5.

RESPONSE TO MODE 1 UNBALANCE, DRIVE END BRG, REVISED RTS

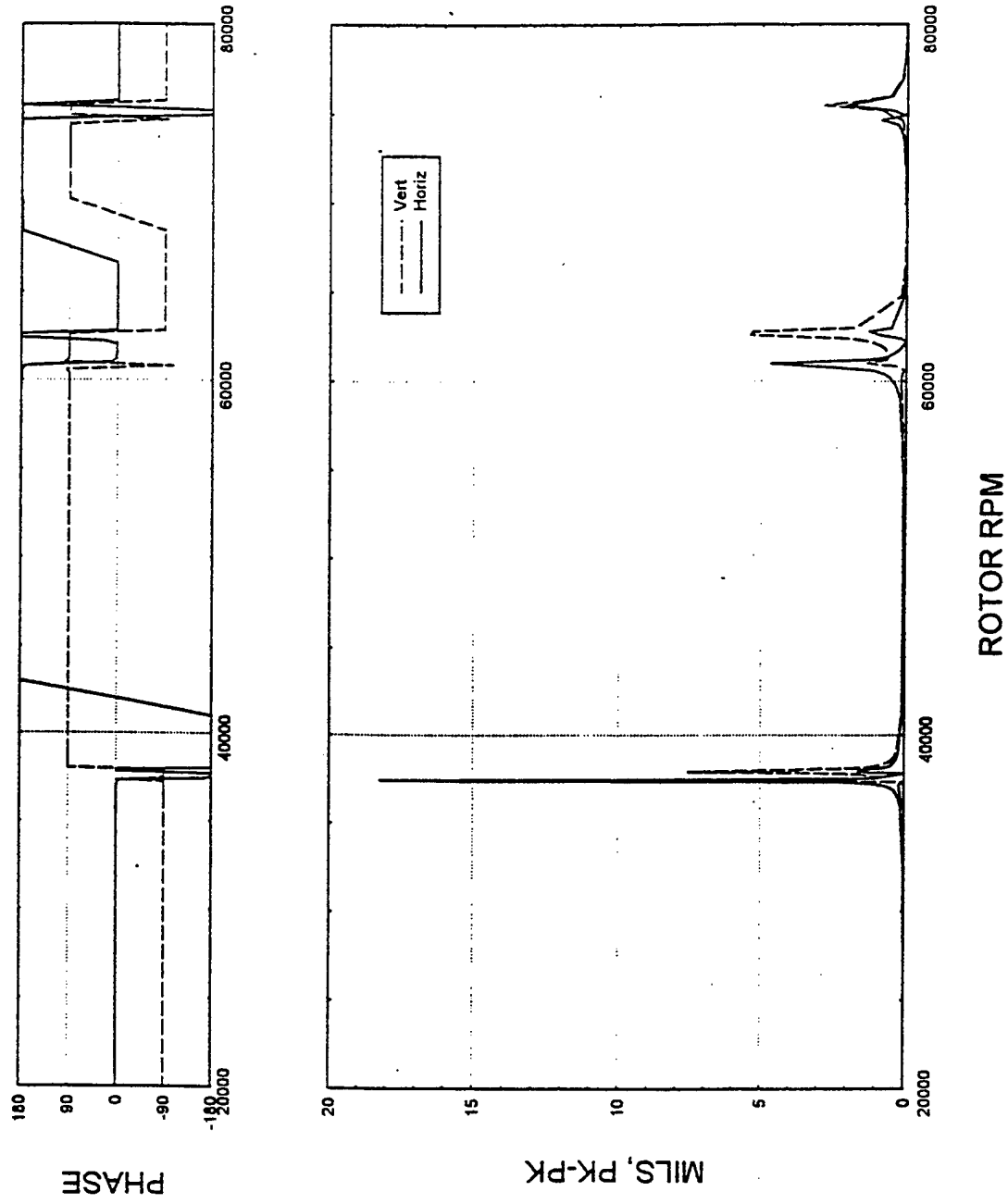


Figure A.17. Response to Mode-1 Unbalance (Driven-end Bearing) - Revised HSRHP.

RESPONSE TO MODE 1 UNBALANCE, ROTOR CENTER, REVISED RTS

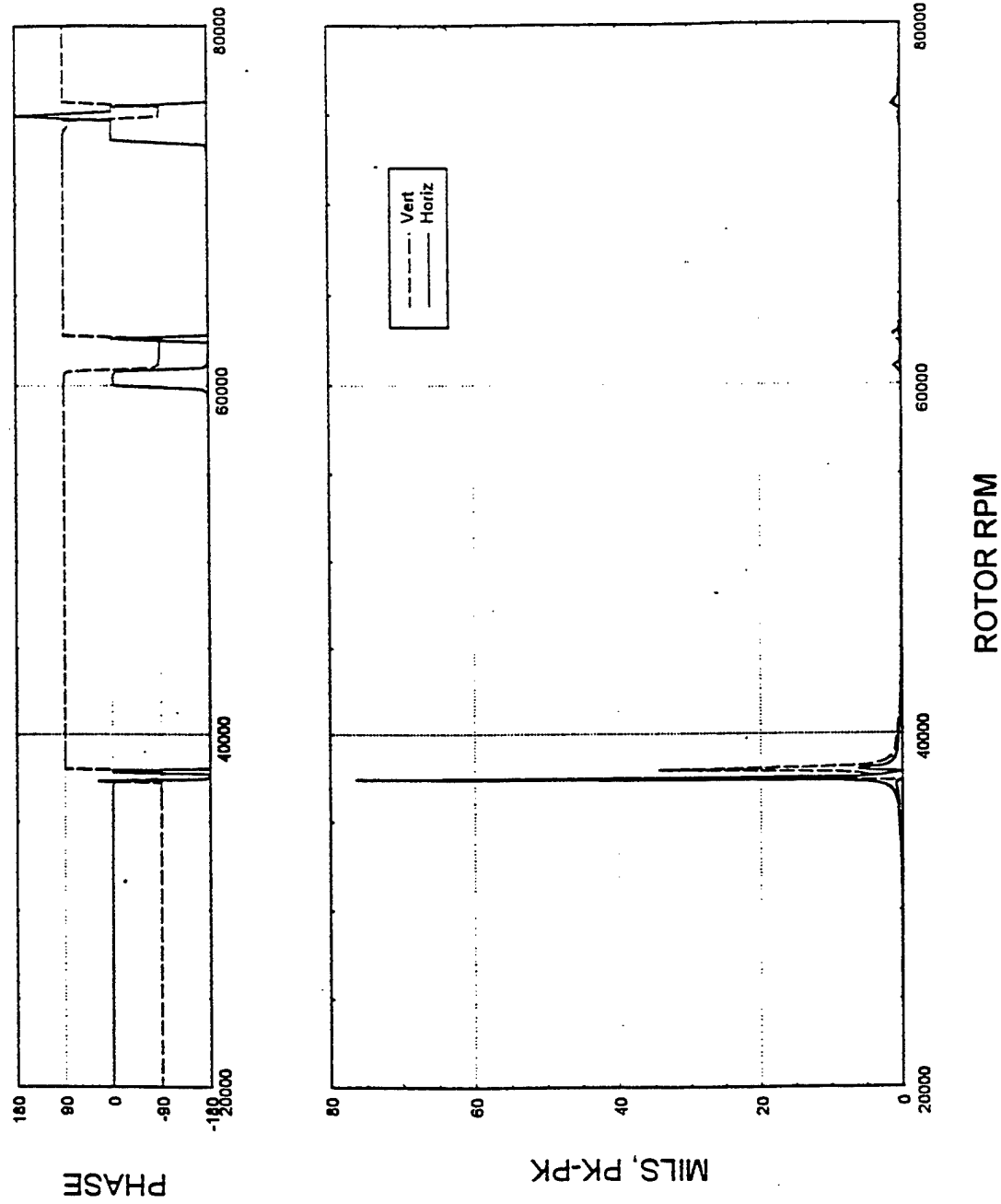


Figure A.18. Response to Mode-1 Unbalance (Rotor Cooling) - Revised HSRHP.

RESPONSE TO MODE 1 UNBALANCE, ODE BRG, REVISED RTS

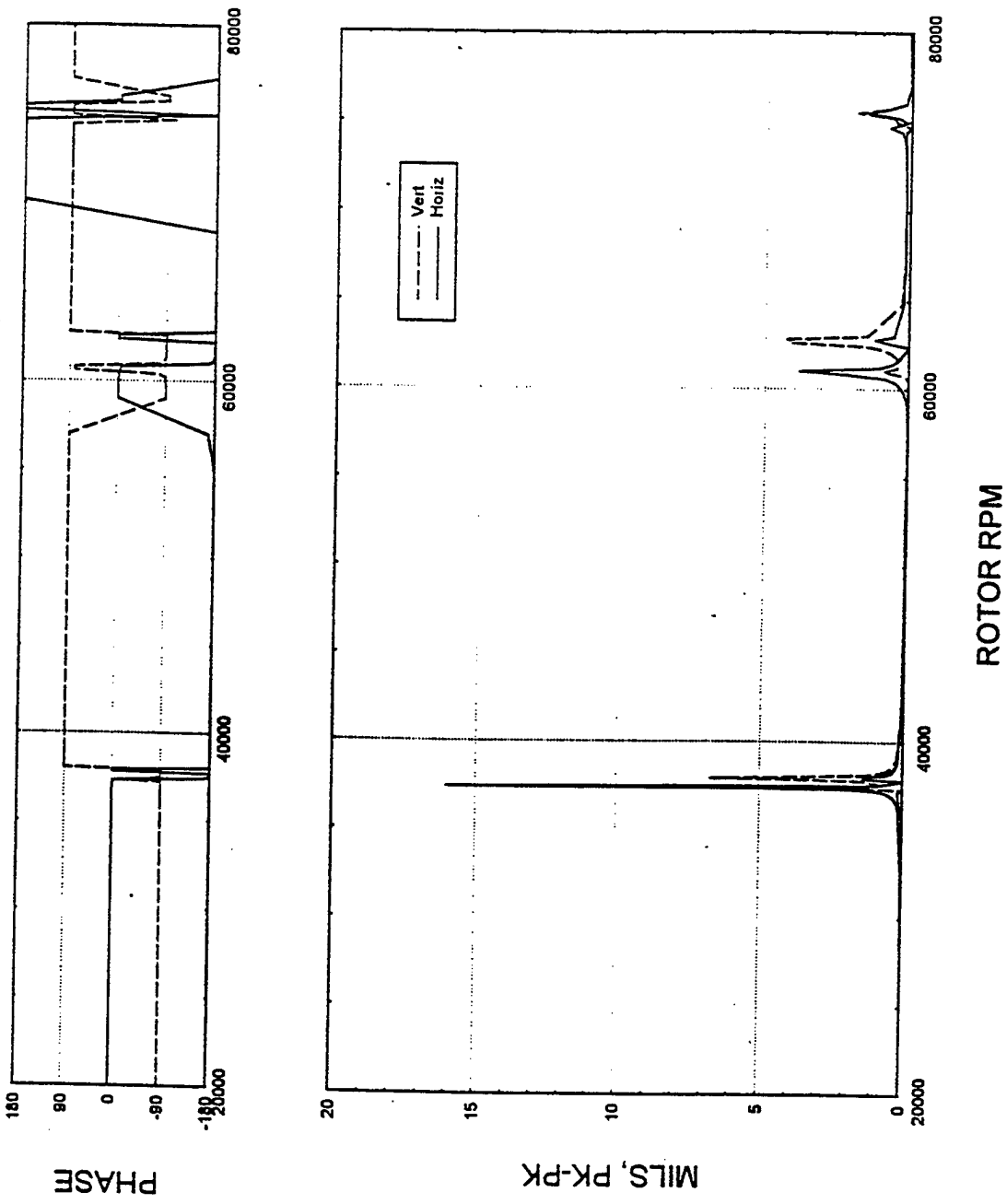


Figure A.19. Response to Mode-1 Unbalance (Opposite Drive-end Bearing) - Revised HSRHP.

A study to determine the required rotor length reduction necessary to increase the first critical speed above 55,00 rpm shows that a 6.0 inch shorter rotor is required for this rotor configuration. The first critical speed calculated for different rotor lengths is tabulated below. In this study, the only parameter modified is the length of the rotor at the 1.1 inch outside diameter section.

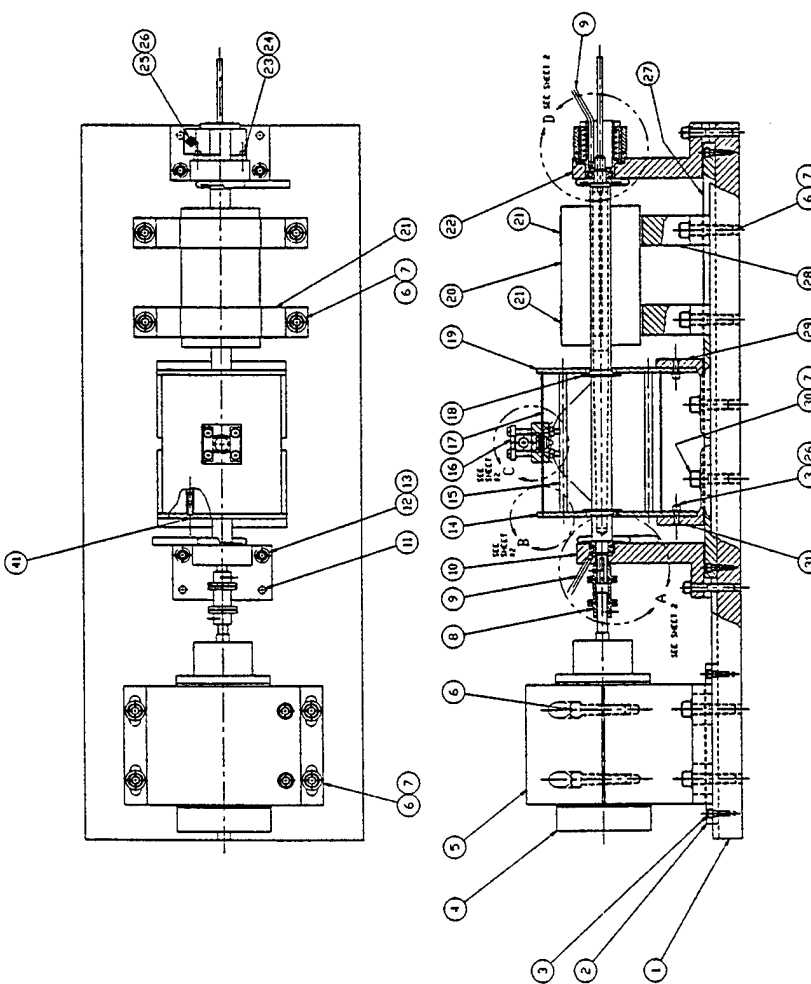
Length Shortened (inch)	Overall Length (inch)	First Critical Speed, rpm
2.0	13.75	45,000
3.0	12.74	48,000
4.0	11.74	51,000
5.0	10.74	53,500
6.0	9.74	56,600

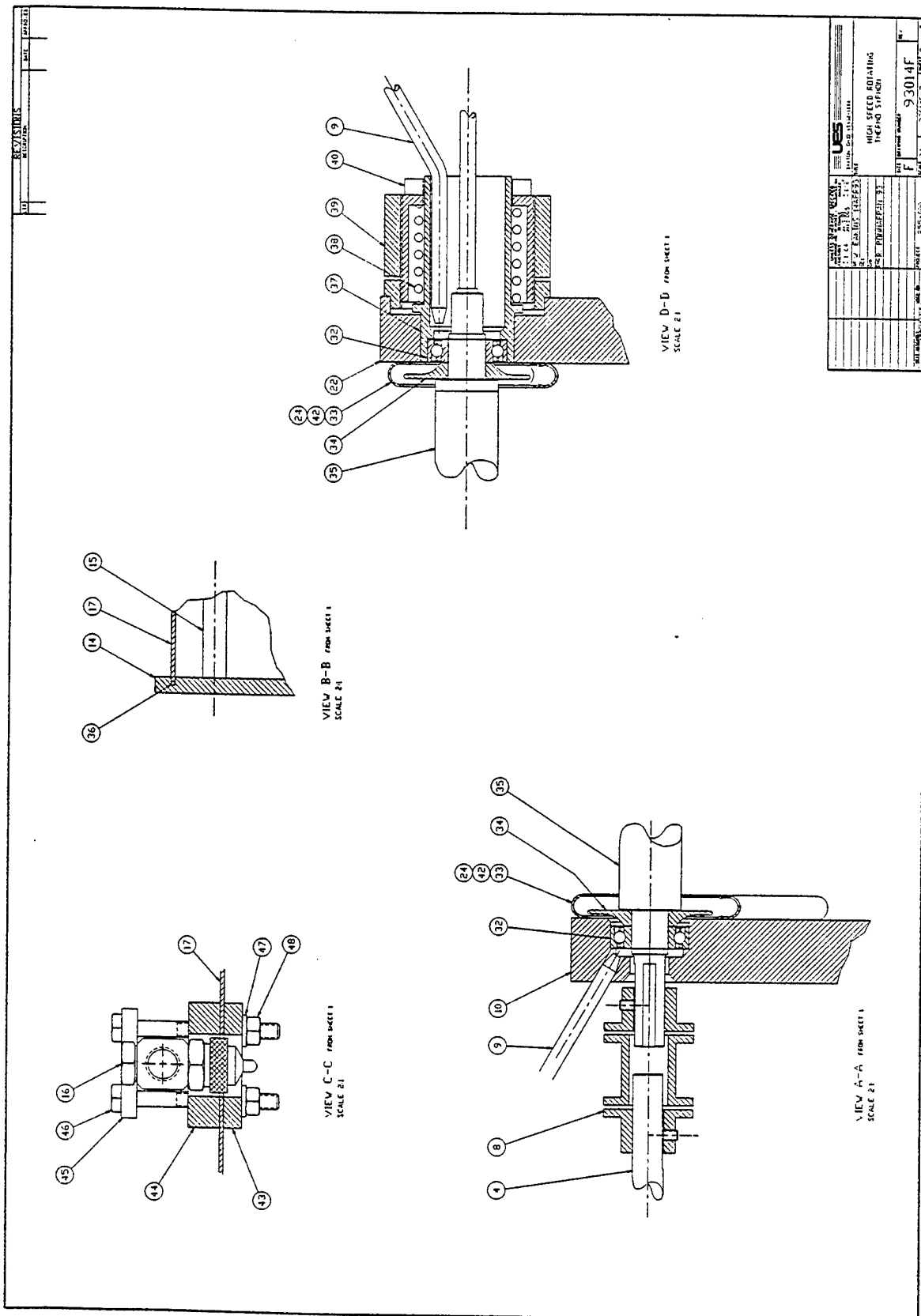
REFERENCES

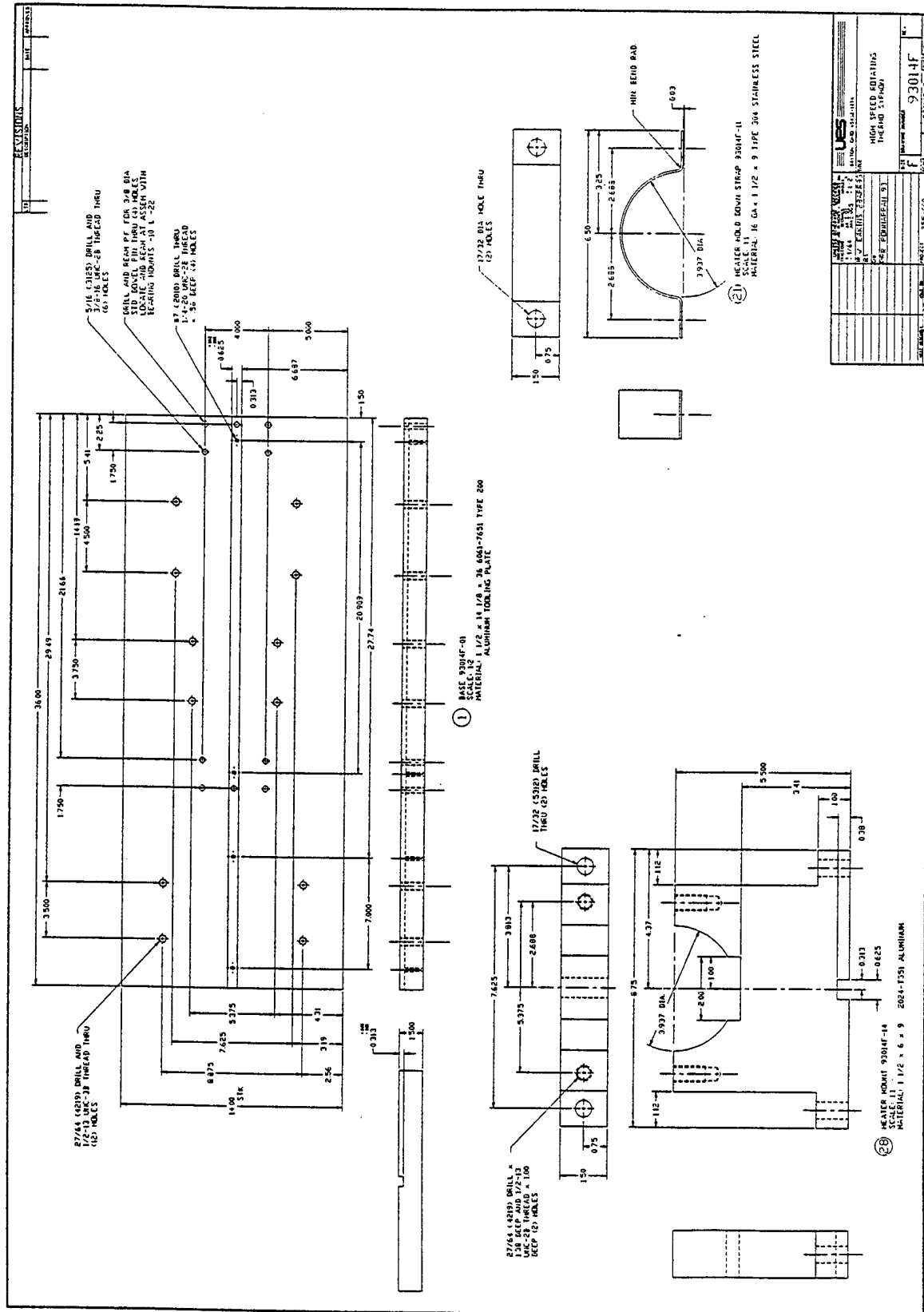
- A.1. Nelson, H.D., "A Finite Rotating Shaft Element Using Timoshenko Beam Theory," ASME Trans., Journal of Mechanical Design, v 102, October 1980, pp. 793-803.
- A.2. Rouch, K.E. and Kao, J.S., "Dynamic Reduction in Rotor Dynamics by the Finite Element Method," ASME Trans., Journal of Mechanical Design, v 102, April 1980, pp. 360-368.

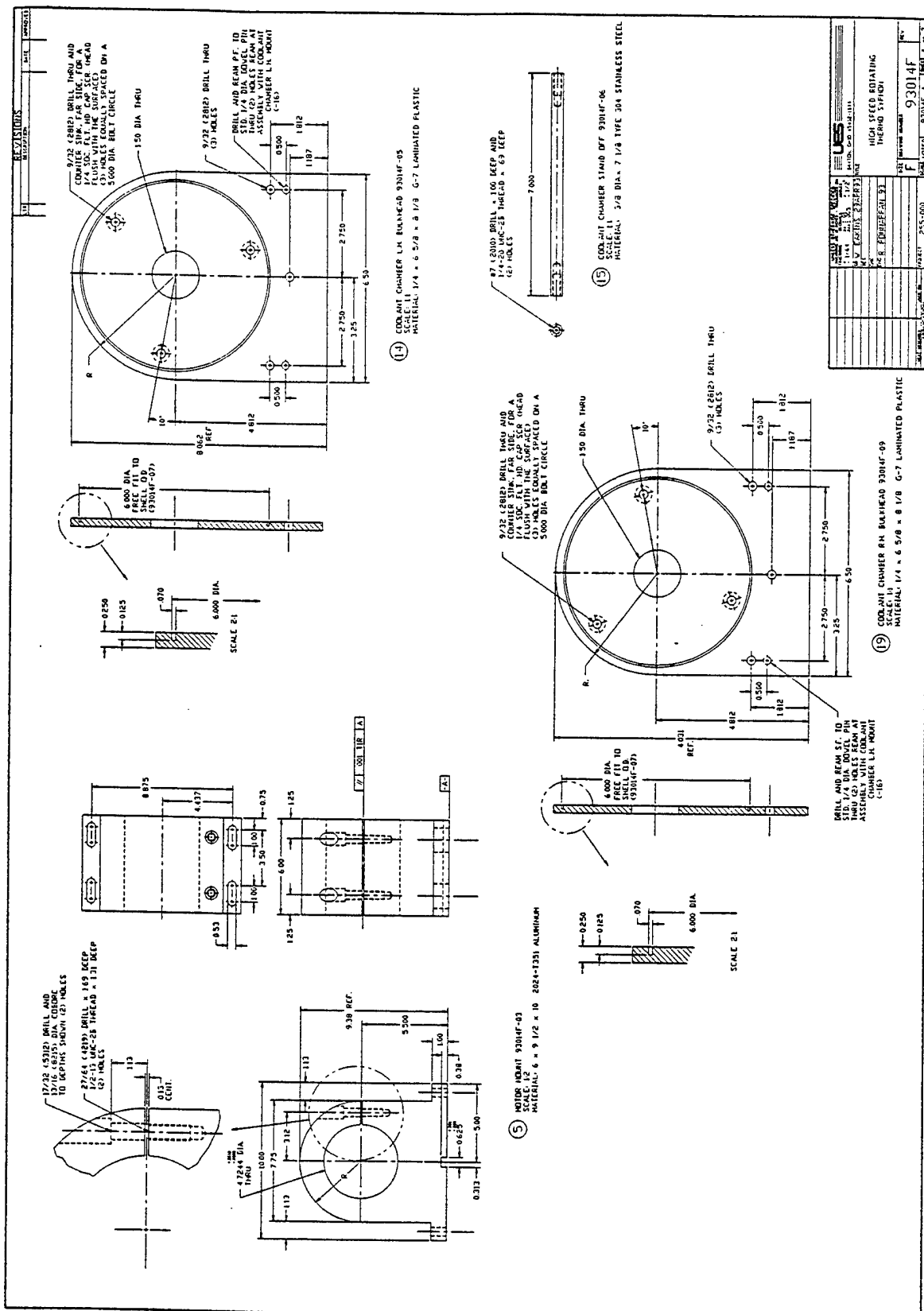
APPENDIX B

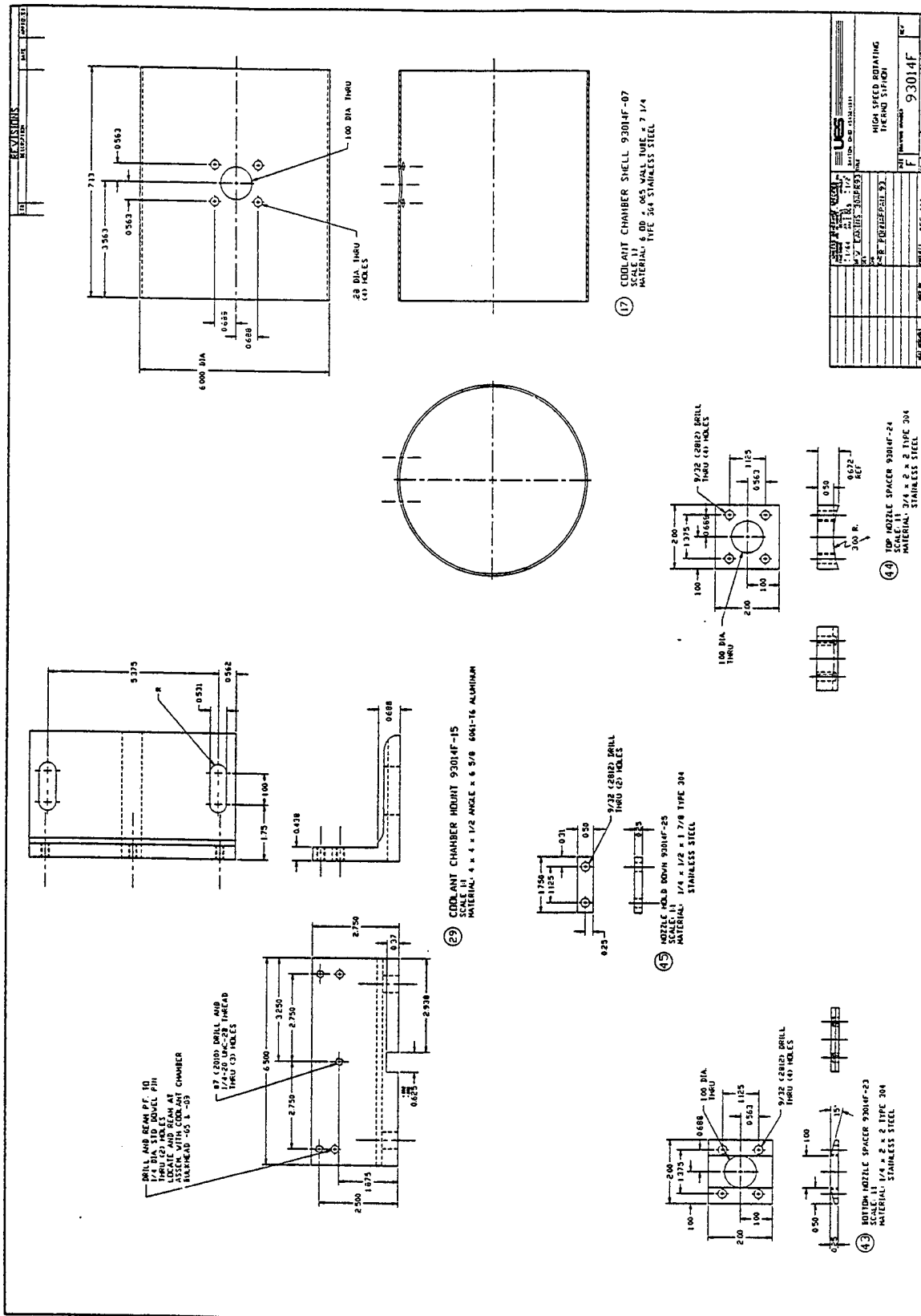
DRAWINGS OF RHP TEST RIG

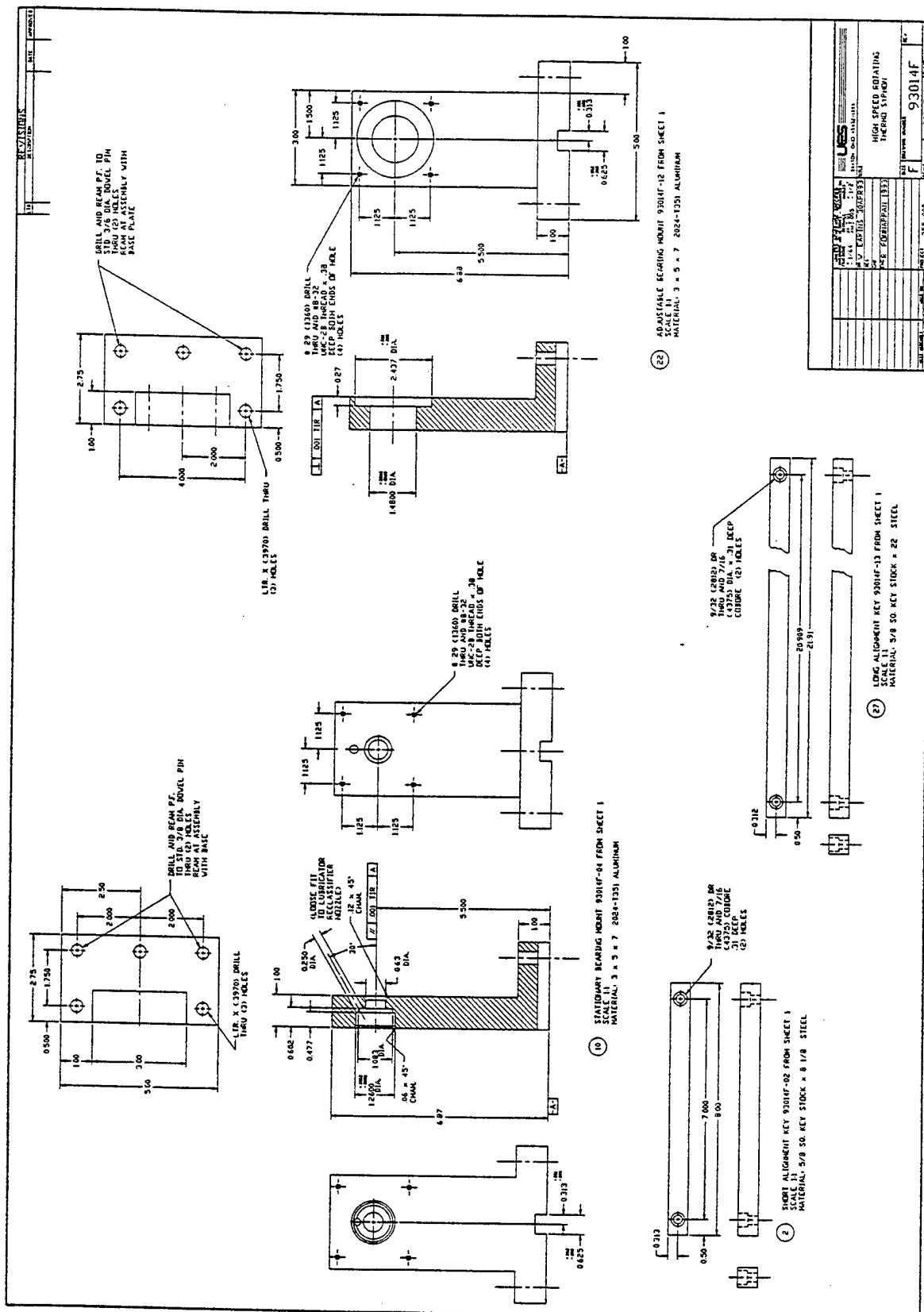


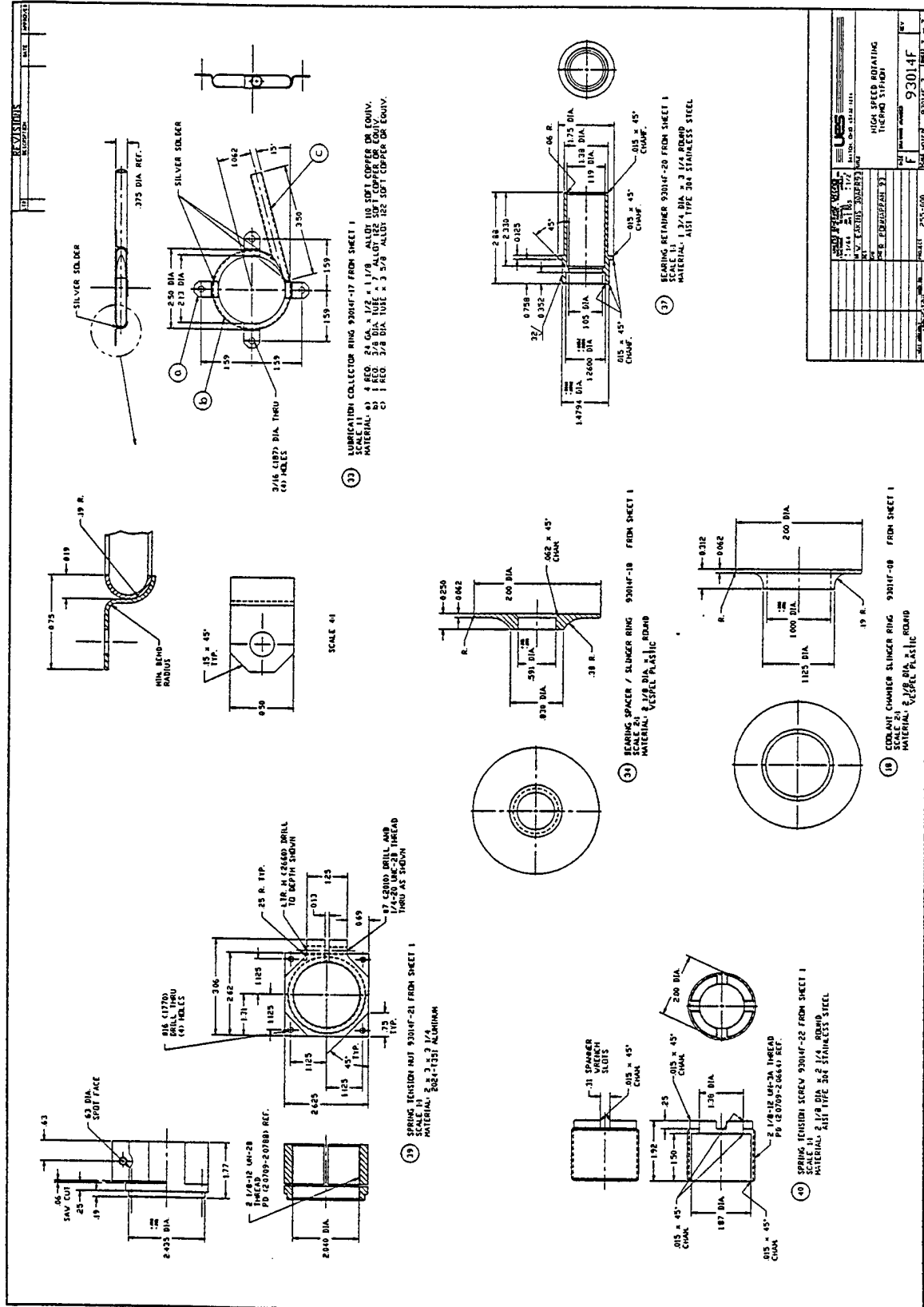












APPENDIX C

RHP INERTIA AND TORQUE CALCULATION

RHP INERTIA AND TORQUE CALCULATIONS

Refer to Figure 15 for dimensions

Mean wall thickness $\approx 3/16"$

Mass estimate:

$$\begin{aligned} M &= \pi/4 (d_o^2 - d_i^2) l \rho \\ \rho_{\text{steel}} &= 490 \text{ lbm/ft}^3 = 0.2836 \text{ lbm/in}^3 (7.86 \text{ g/c.c}) \\ l &= 21" \text{ (fill tube mass is ignored)} \\ M &= \pi/4 [l^2 - (5/8)^2] 21 \times 0.2836 \\ &= 2.85 \text{ lbm} \approx 2.85 \text{ lb}_f \text{ or } 2.85 \text{ lb} \end{aligned}$$

Inertia about the axis (assuming as a solid cylinder):

$$\begin{aligned} J_1 &= \frac{Wr^2}{2g} \\ &+ \frac{2.85 \times 0.5^2}{2 \times 32.2 \times 12} \\ &= 9.2198 \times 10^{-4} \text{ in. lb.s}^2 \end{aligned}$$

Inertia about the axis (assuming as thin hollow cylinder):

$$J_1 = \frac{Wr^2}{g} = 18.439 \times 10^{-4} \text{ in. lb.s}^2$$

We will use this estimate for sizing a motor.

1. Torque due to inertia, $T_J = J_1 a$ where a is shaft spin acceleration rate.

Assume RHP is spun to 60,000 rpm in 30 seconds.

Therefore,

$$a = \frac{2\pi \times 60,000}{60 \times 30} = 209.44 \text{ rad/s}^2$$

$$T_J = 18.4396 \times 10^{-4} \times 209.44 \\ = 0.38619 \text{ in. lb}$$

2. Torque due to windage (T_W)

Windage loss for rotation of the RHP in air has been calculated to be approximately 0.07 h.p.

$$\text{h.p.} = \frac{2\pi N T_W}{33000} \quad N = 60,000 \text{ rpm} \\ T_W = \frac{33000 \times 0.07}{2\pi \times 60,000} = 0.0753 \text{ in. lb}$$

3. Torque due to friction in bearing (T_F)

Per Barden, Inc., frictional torque for 105 B series bearing at 60,000 rpm is 19.99 oz. in. for lube viscosity, $v = 100$ centi stokes. This viscosity number is a conservative value. Actually, it will be lower (≈ 20 CS).

$$T_F = 1.2497 \text{ in. lb per bearing}$$

For 2 bearings, $T_F = 2.494 \text{ in. lb.}$

4. Load torque (T_L)

There is no load torque in our system.

$$T_L = 0$$

Total torque to be delivered by the motor at 60,000 rpm is

$$\begin{aligned}T &= T_J + T_W + T_F + T_L \\&= 0.38619 + 0.07353 + 2.4994 + 0 \\&\quad + 2.95912 \text{ in. lb} \\&\text{or } 47.35 \text{ in. oz}\end{aligned}$$

For steady state operation $T_J = 0$ and $T = 41.2$ in. oz.

Horsepower requirement for motor:

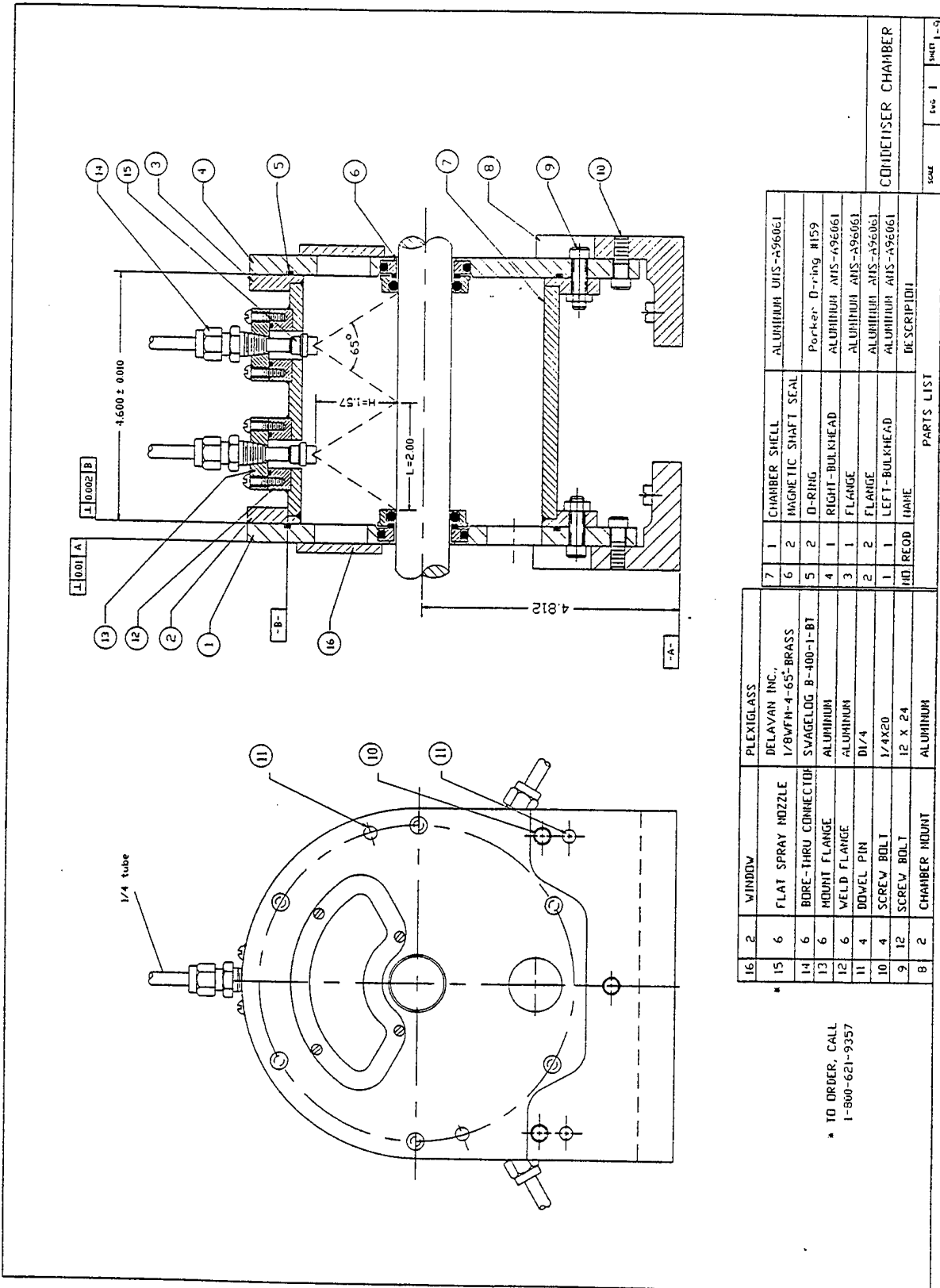
$$\begin{aligned}\text{h.p.} &= \frac{2\pi NT}{33000} && \text{known that} \\&= \frac{2\pi \times 60,000 \times 0.214}{33000} && N = 60,000 \text{ rpm} \\&= 2.45 \text{ or } 1826.5 \text{ W} && T = 41.2 \text{ in. oz (0.214 ft. lb)}$$

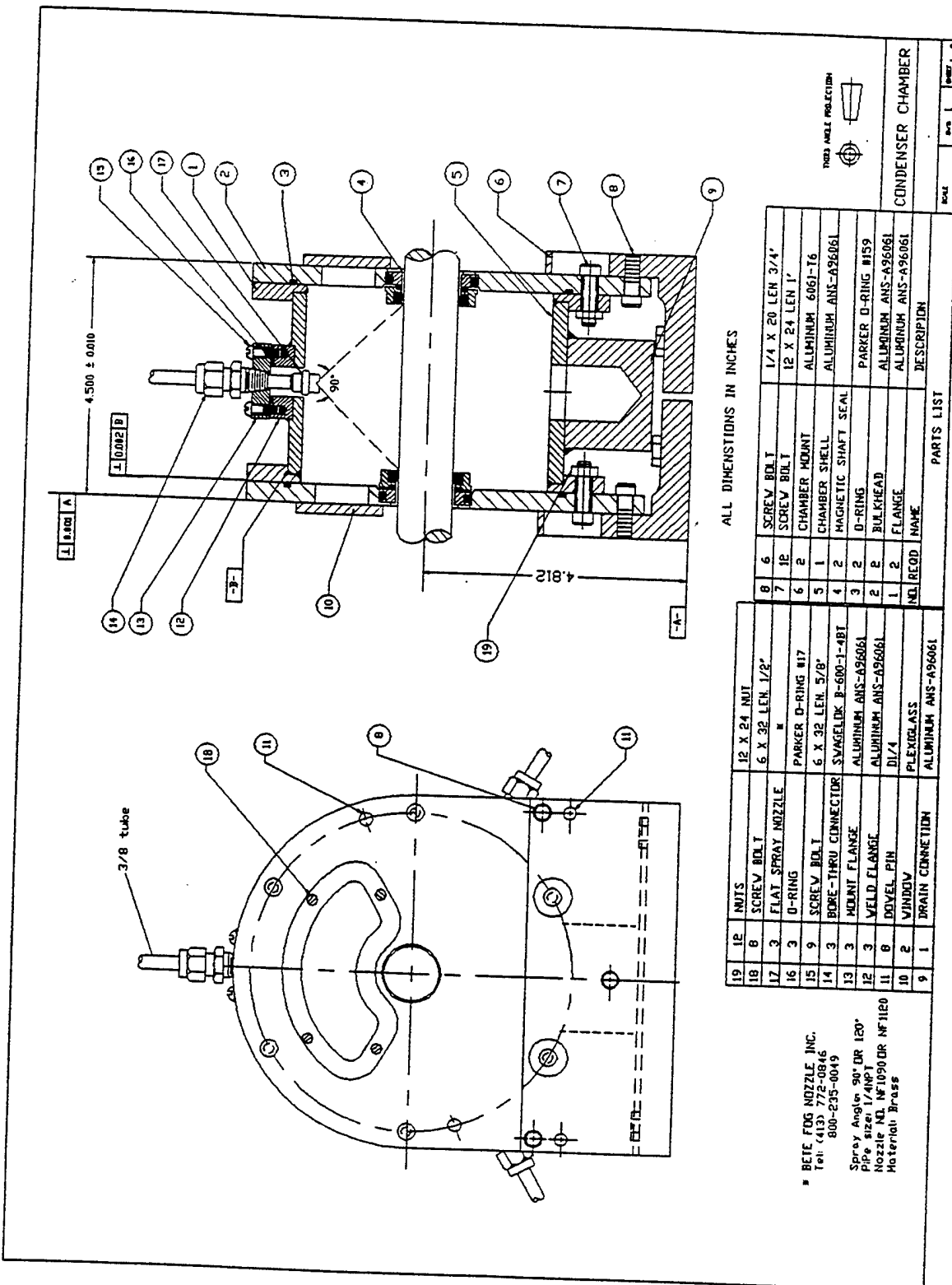
Hence, approximately 3 h.p. motor will be sufficient.

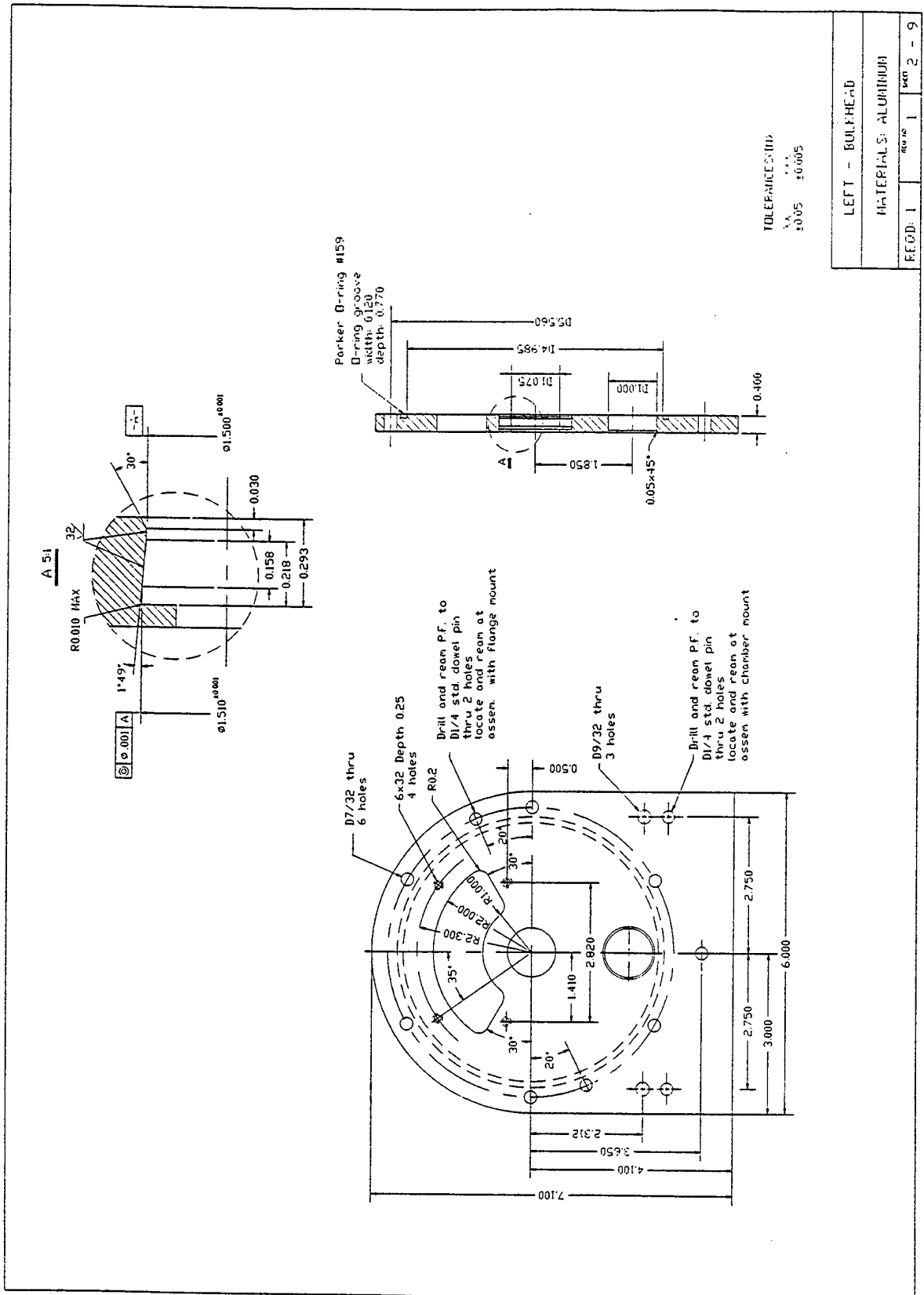
NOTE: If the viscosity of the bearing lube oil is lower than 100 cs, then the h.p. requirement will be correspondingly lower.

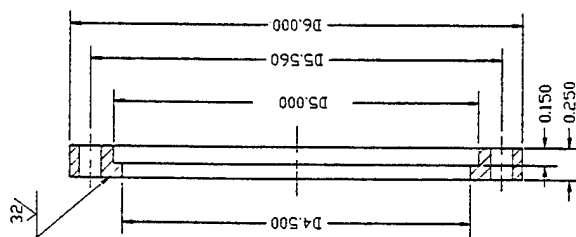
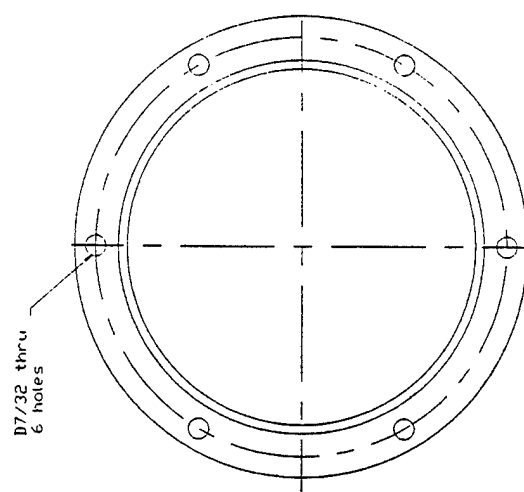
APPENDIX D

DRAWINGS OF CONDENSER COOLING CHAMBER







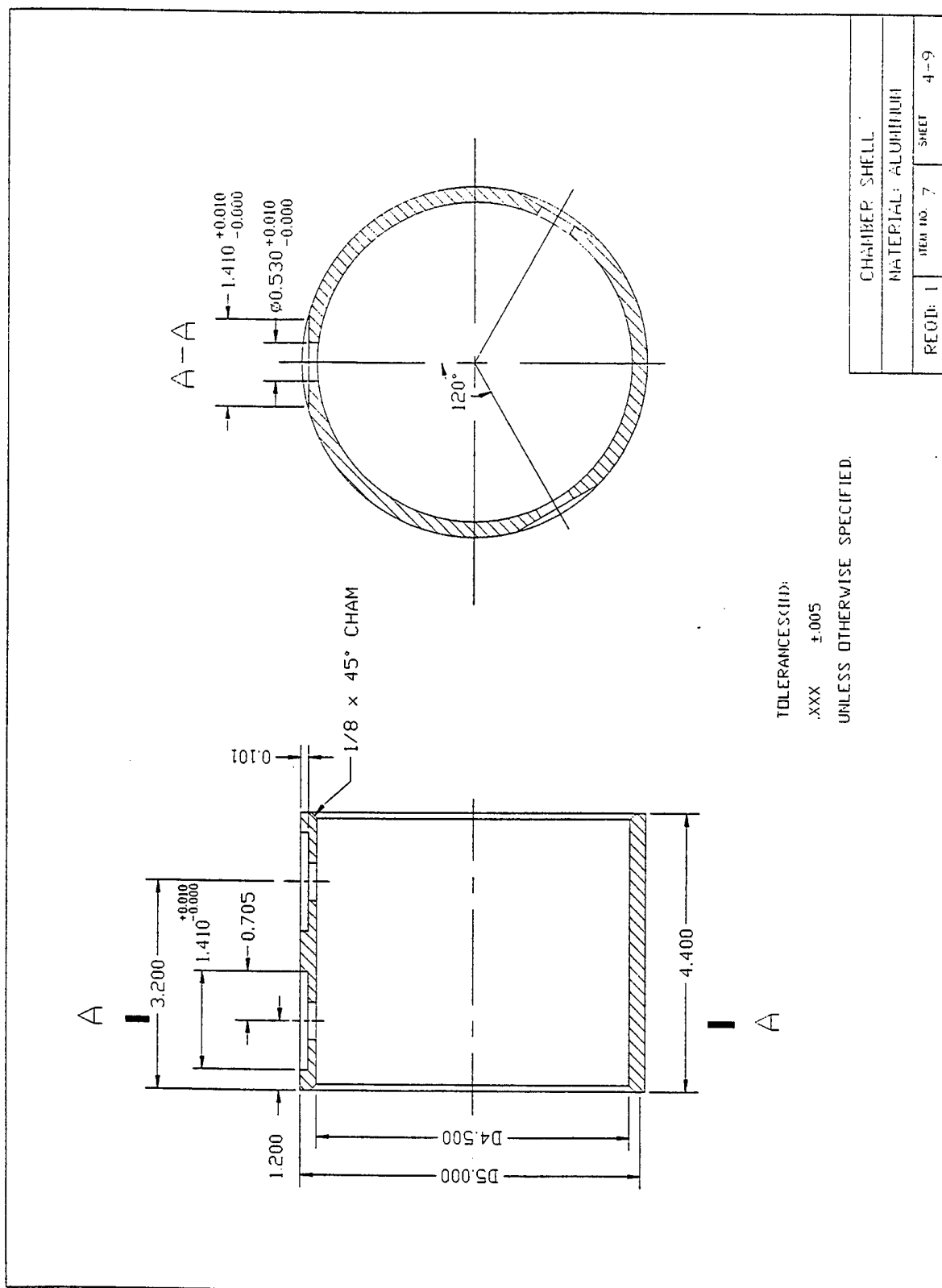


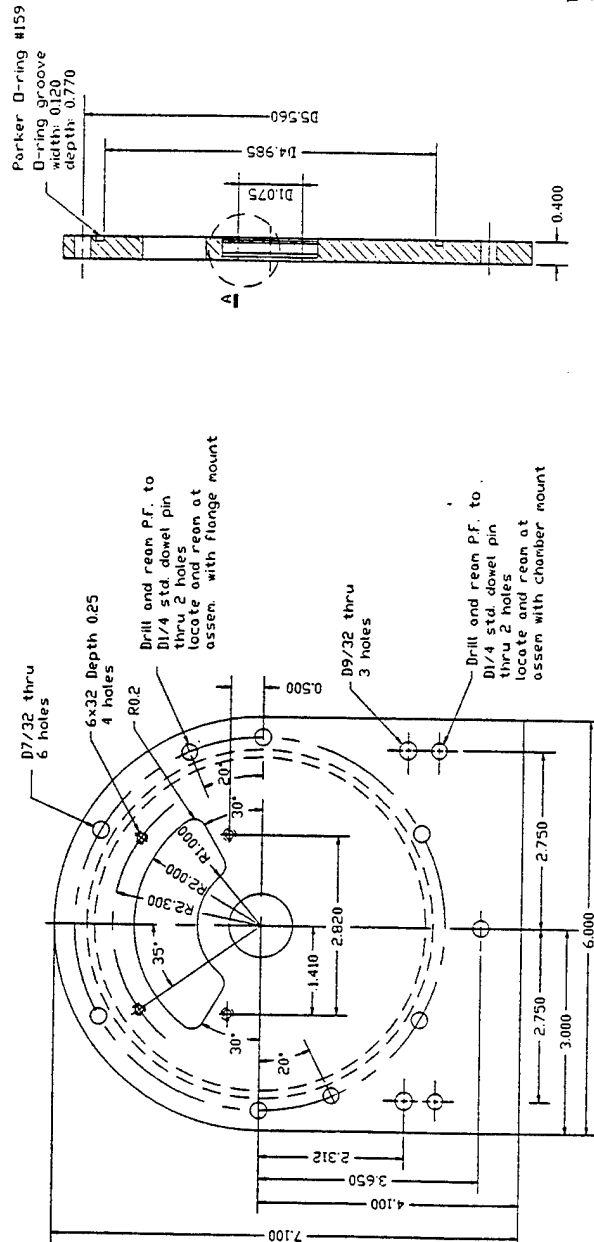
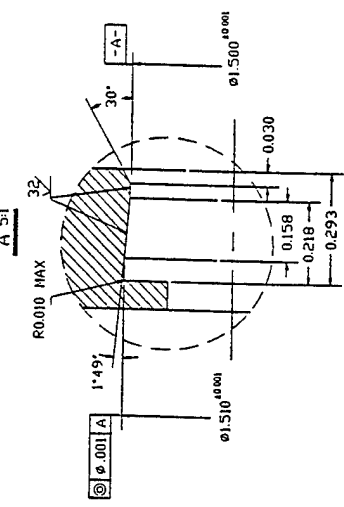
TOLERANCES (IN.)
.005 $\pm .005$

FLANGE

MATERIALS: ALUMINUM

REOD: 2 140° 2 340° 3 - 3

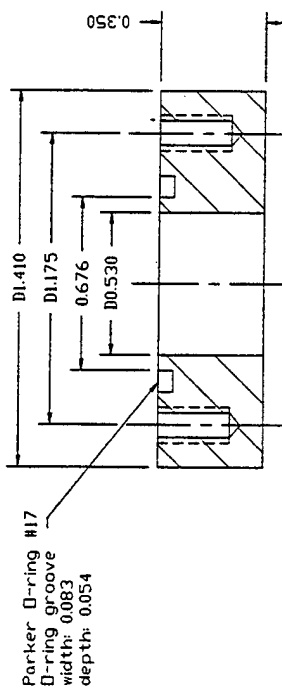
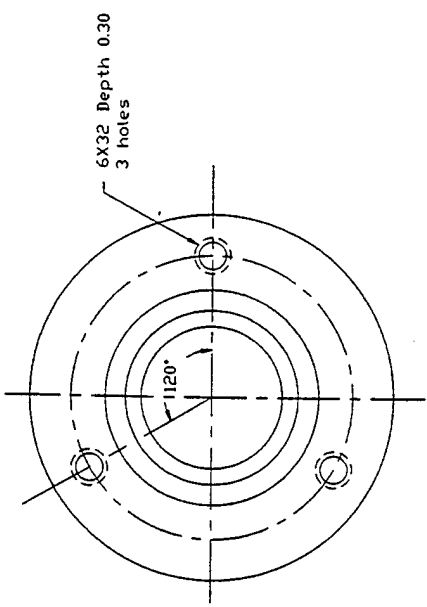




LEFT - BULKHEAD

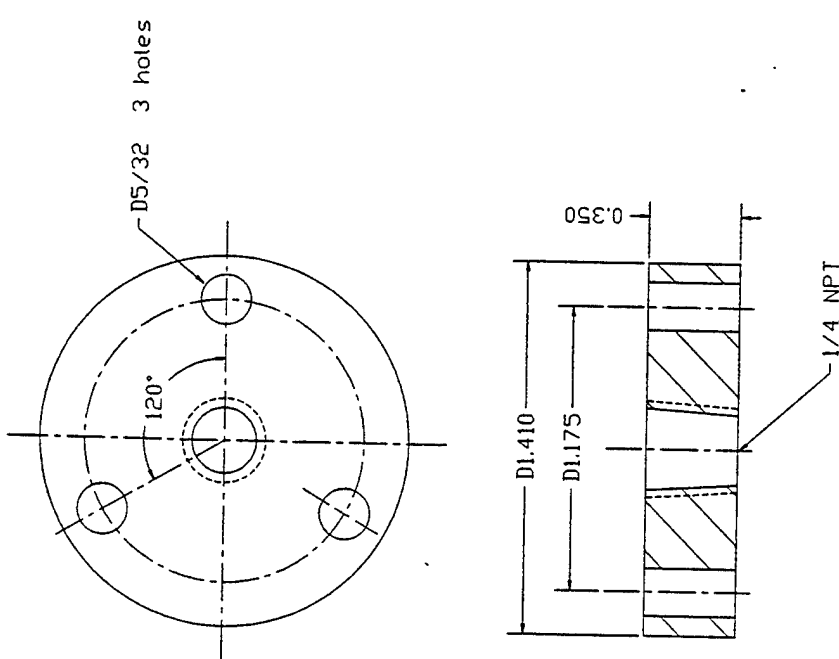
MATERIALS: ALUMINUM

REOD: 1 rev. no. 4 sheet 5 - 9



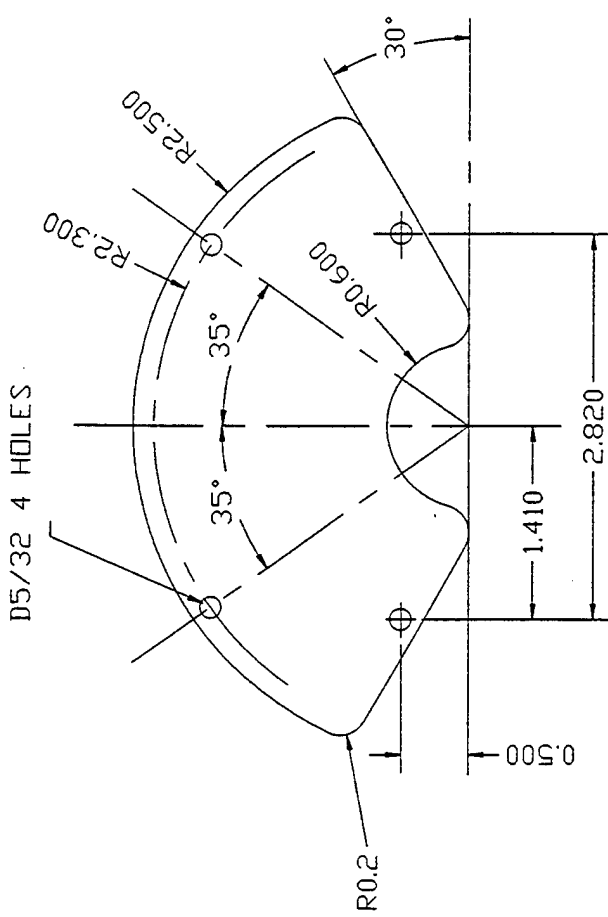
TOLERANCES (IND):
.xxx ±.005

WELD FLANGE		
MATERIAL: ALUMINUM		
REQD	ITEM NO.	SPEC
6	12	7-9



TOLERANCES (IN.)
.005 ± .005

MOUNT FLANGE		
MATERIALS: ALUMINUM		
REQD: 6	ITEM NO. 13	SHEET 8 - 9



TOLERANCES (IN):
XXX ± 0.005

WINDOW		
PLEXIGLASS		
REQD: 2	ITEM NO. 16	SHEET 9 - 9

APPENDIX E

UNCERTAINTY ANALYSIS

E.1 Calibration of RF Power Input to RHP

E.2 Oil-cooled Condenser Calorimeter

E.1 CALIBRATION OF RF POWER INPUT TO RHP

The heat generated in the wall material of the SS316 steel tube by the RF coil and carried away in the cooling water flowing through the tube can be calculated as

$$Q_{\text{Calorimeter}} = \dot{V}\rho C_p(T_{f,\text{out}} - T_{f,\text{in}}) = \frac{V}{t}\rho C_p \Delta T$$

The property data of ρ and C_p are obtained from standard tables with $\pm 0.5\%$ uncertainty. The volume flow rate, \dot{V} is measured using a stop-watch and recording the time for collecting 1 gallon of water. The uncertainty involved is the accuracy of time measurement which amounted to ± 1 s in 41.27 s. The most contributing parameter to the uncertainty is the ΔT measurement. Type K thermocouple and the Fluke datalogger used in this experiment have a combined uncertainty of $\pm 0.3^\circ\text{C}$ in the $19\text{-}26^\circ\text{C}$ range. This level of accuracy was obtained by calibration against an RTD secondary standard, (accurate to within $\pm 0.03^\circ\text{C}$). The measured ΔT varied from 1.25°C for 500 W to 6.5°C for 2500 W. Hence, the uncertainty for ΔT ranges from 24% for 500 W to 4.6% for 2500 W. Summarizing our individual uncertainties, we have:

Volume, V	1%
Time, t	2.4%
Density, ρ	0.5%
Specific heat, C_p	0.5%
Temp. difference, ΔT	4.6 - 24%

Using these individual uncertainty data, the maximum uncertainty of the system is obtained by the Pythagorean summation as described in "Mechanical Measurements," by Beckwith, Buck and Marangoni; Addison-Wesley Publishing Co., 3rd Edition, 1982, pp. 268-273.

$$\begin{aligned} \text{Systematic uncertainty} &= [(1)^2 + (2.4)^2 + (0.5)^2 + (0.5)^2 + (4.6 \text{ to } 24)^2]^{1/2} \\ &= [7.26 + (u_{\Delta T})^2]^{1/2} \end{aligned}$$

For RF power input calibration, the uncertainties at various power levels are as follows:

<u>RF Power (W)</u>	<u>$u_{\Delta T}$ (%)</u>	<u>Systematic Uncertainty (%)</u>
≤ 500	24	24.15
≤ 1000	11.4	11.7
≤ 1500	6.77	7.29
≤ 2000	5.45	6.08
≤ 2500	4.62	5.35

The measurement accuracy is poor at lower power level.

E.2 OIL-COOLED CONDENSER CALORIMETER

The calculation of the quantity of heat carried by the oil sprayed over the RHP condenser length is done exactly in the same manner described in Appendix E.1. The measured and tabulated data are V , t , ρ , C_p , and ΔT . As the oil flow rates used in these tests were less than 1 gpm, the graduated cylinder used for collecting oil was of 1000 ml capacity with 5 ml resolution. Hence, the maximum uncertainty in time measurement based on 0.86 gpm is ± 1 s in 18.4 s which is $\pm 5.4\%$. As before (Appendix E.1), the oil temperature measurement uncertainty in the range 40-62 °C using type K thermocouple and Fluke datalogger system is ± 0.3 °C. The measured ΔT of oil varied from 2.8 °C to 10.6 °C for power level variation from 250 W to 1250 W which translates to the percent uncertainty range of ± 2.8 to 10.7% . Summarizing the individual uncertainties, we have:

Volume, V	0.5%
Time, t	5.4%
Density, ρ	0.5%
Specific heat, C_p	0.5%
Temp. difference, ΔT	2.8 - 10.7%

Hence, the systematic uncertainty of the oil-cooled calorimeter add to,

$$\begin{aligned}\text{Systematic uncertainty} &= \left[(0.5)^2 + (5.4)^2 + (0.5)^2 + (0.5)^2 + (u_{\Delta T})^2 \right]^{1/2} \\ &= \left[29.91 + (u_{\Delta T})^2 \right]^{1/2}\end{aligned}$$

The maximum uncertainty in the oil-cooled calorimeter at various power levels is given below.

<u>Power (W)</u>	<u>$u_{\Delta T}$ (%)</u>	<u>Systematic Uncertainty (%)</u>
250	10.7	12.0
500	6.3	8.3
750	4.3	6.9
1000	3.3	6.4
2000	2.8	6.1

In addition to these measurement related uncertainties, there are other sources of errors to be accounted for. For example, the parasitic heat addition from the magseals and heat losses from the chamber walls also influence the calorimetric data.